

**MODEL BUILDING AND IMAGING
WITH REFLECTION DATA**

Part I

TOMOGRAPHIC DETERMINATION OF SHEAR WAVE VELOCITIES FROM DEPTH MIGRATED CONVERTED WAVE DATA

Part II

STRUCTURAL IMAGING IN COMPLEX GEOLOGICAL AREA: INTEGRATING MODEL-INDEPENDENT AND MODEL-DEPENDENT IMAGING

A DISSERTATION SUBMITTED TO THE
GEOSCIENCE DEPARTMENT OF THE
UNIVERSITY OF HAMBURG
FOR THE DEGREE OF
DOCTOR OF NATURAL SCIENCES

presented by
Elive M. Menyoli
December 2002

Part I

TOMOGRAPHIC DETERMINATION OF SHEAR WAVE VELOCITIES FROM DEPTH MIGRATED CONVERTED WAVE DATA

Part II

STRUCTURAL IMAGING IN COMPLEX GEOLOGICAL AREA: INTEGRATING MODEL-INDEPENDENT AND MODEL-DEPENDENT IMAGING

DISSERTATION
ZUR ERLANGEN DES DOKTORGRADES
DER NATURWISSENSCHAFTEN IM FACHBEREICH
GEOWISSENSCHAFTEN
DER UNIVERSITÄT HAMBURG

Vorgelegt von
Elive M. Menyoli
aus Limbe, Kamerun
Hamburg, 2002

Als Dissertation angenommen vom Fachbereich
Geowissenschaften der Universität Hamburg auf
Grund der Gutachten

von **Prof. Dr. D. Gajewski**
und **Dr. Ch. Hübscher**

Hamburg, den 18.12.2002

Prof. Dr. Ulrich Bismayer
(Dekan des Fachbereiches Geowissenschaften)

THE UNIVERSITY OF HAMBURG

FACULTY OF GEOSCIENCES

The undersigned certify that they have read, and recommended to the faculty of geosciences for acceptance, a dissertation entitled “**MODEL BUILDING AND IMAGING WITH REFLECTION DATA**” submitted by Elive Menyoli in partial fulfillment of the requirements for the degree of Doctor of Philosophy.

Supervisor, Prof. Dr. Dirk Gajewski,
Department of Applied Geophysics,
Institute of Geophysics.

Dr. Christian Hübscher,
Center of Marine Geophysics.

Prof. Dr. Torsten Dahm,
Department of Seismology.

Prof. Dr. Claus-Dieter Reuther,
Department of Geology-Paleontology.

Prof. Dr. How Kin Wong,
Department of Bio-Geochemistry.

TOMOGRAPHIC DETERMINATION OF SHEAR WAVE VELOCITIES FROM DEPTH MIGRATED CONVERTED WAVE DATA

Elive M. Menyoli, Institute of Geophysics, University of Hamburg, Germany

ABSTRACT: PART I

The major task in converted wave processing is to estimate pressure wave (P-wave) velocities, (v_p), and shear wave (S-wave) velocities, (v_s), of geological structures in the Earth. Most S-wave velocity analysis methods are based on the assumption of flat layered geology and mild lateral variations of v_p and v_s . In areas with structurally complex geology, these methods often give unsatisfactory results and more sophisticated techniques are required. One of these techniques, seismic tomography, compares observed traveltimes, measured for each source-receiver pair, with expected traveltimes, computed by ray tracing through an assumed v_p and v_s model; the differences are projected back over the traced ray paths to produce an update of the model.

Travelttime tomography has some drawbacks. First, picking traveltimes of unstacked PS-wave data can be tedious in structurally complex regions. This is particularly difficult in areas where triplications occur. Second, in reflection tomography reflector positions are generally unknown, and ray paths cannot be accurately determined. Third, ray tracing may be difficult in areas with strong lateral velocity variations and large velocity contrasts at structural boundaries. Fourth, even in non-complex areas the quality of unstacked PS data is often poor, therefore, making picking difficult.

To overcome the above difficulties, I use PS-wave prestack depth migration of the Kirchhoff type and migration velocity analysis of the Kirchhoff type. Migration uses a theory of wave propagation in the Earth to convert seismic reflection data to subsurface reflecting horizons. Interval v_p and v_s models are required for the migration. Given an accurate v_p model from analysis of PP data alone, the correct interval shear wave velocities still have to be determined. Migration velocity analysis methods are based on the fact that the migrated common reflection point gathers are flat if the migration velocities are correct. However, for PS data, the common reflection point gathers may be flat even if the S-wave velocities are not correct. In that case comparing the PS and PP common reflection point gathers reveals a depth shift between them, which can be evaluated to update the v_s model.

I use a tomographic migration velocity analysis method to estimate the interval v_s which removes the depth shifts. The tomographic v_s analysis method presented in this thesis overcomes the drawbacks of travelttime tomography. In contrast to classical travelttime tomography, I interpret PS and PP data after depth migration. More specifically, I use both PS and PP common reflection point (CRP) gathers and the reflector structure from a depth migrated PP section. These gathers are easier to interpret than unmigrated prestack PS gathers. I assume that the P-wave migrated section and P-wave velocity are known from a previous migration step and migration velocity analysis. Therefore, the PP CRP gathers are flat and are at the correct depth position. The PS CRP gathers

should be flat and at the same depth position as their corresponding PP gathers after migration if the correct v_s velocity was used. Consequently, discrepancies between the PS and PP CRP gathers indicate errors in the v_s model used for migrating the data. I correct the shear wave migration velocity model by an iterative optimisation technique that minimises the CRP depth discrepancies between the PS and PP gathers. The optimisation scheme is a conjugate-gradient method, where the gradient operator linearly relates the perturbation of shear wave velocities to changes in reflector positions. In calculating this operator, I use reflectors from the interpreted PP section to reconstruct the rays by ray tracing. The perturbations in depth positions are converted to perturbations in traveltimes. Therefore, the shear wave velocity updating scheme is a joint inversion followed by prestack depth migration. For the migration I use Vidale's finite difference algorithm that computes seismic traveltimes on a grid model of the subsurface.

Results from synthetic and field data indicate that the velocity analysis method successfully estimates interval shear wave velocity models that lead to depth migrated PS depth gathers with no depth deviations from their corresponding PP gathers. However, if the PS or PP reflectors are sparse, or the PS data quality is poor, this velocity model will be non-unique. Therefore, additional information about the interval shear wave velocity model or the positions of the reflectors must be supplied to obtain the correct interval velocity model. The method succeeds in estimating structural shear wave velocities for a data set recorded in Southern Bavaria, Germany.

Acknowledgments

I thank my supervisor, Dirk Gajewski, for his guidance and counsel throughout my work. I thoroughly enjoyed the open exchange of ideas and academic freedom that Dirk foster in the institute. I appreciated his pragmatic approach to my research project, especially during the times when progress was slow. I like to thank the German-Kenya Aid Group and the German Research Foundation (grant GA 350/9-1 and Ga 350/10-1) for the financial support of my research. I also like to thank the sponsors of Wave Inversion Technology (WIT) consortium. Without their annual deadlines, this work would not have been completed. I also benefited from fresh insights from the WIT-meetings into all aspects of seismic imaging. I thank all the sponsors of the WIT consortium both for their support and for their advice, criticism, and ideas. In particular, I thank Preussag Energie GmbH and Dr. Paul Krajewski for providing the multicomponent data set used in the first part of this thesis.

I am grateful to Jürgen Mann, from the University of Karlsruhe, Germany, for providing the CRS stack code. Jürgen and the Karlsruhe working group were always open for questions about the running of the code and discussions about theoretical aspects. I am grateful to Dr. Christian Hübscher for his continuous assistance during the seismic processing phase of this work and for the assistance in DISCO/FOCUS and GEODEPTH software.

My office mates Radu Coman and Swetlana Soukina were always a good source of advice, ideas, dissent, general discussion on programming and graphic programs and all other matters of life. I thank every member of the Applied Geophysics Group (AGG) for the continuous discussions during my research. I express my gratitude to the reviewers of this thesis Tina Kaswisch, Axel Ehrhardt and Dr. Claudia Vanelle for their sharp eye and perceptive comments. The Chapters of this work is much improved as a result of their numerous input. Special thanks goes to Dr. Ekkehart Tessmer who provided non-stop help with graphics, and many computer questions. I very much appreciate his open exchange of ideas during preparations for my presentations. Without his excellent computer knowledge, and support this work would have taken a different dimension. I would also like to thank the DOBRReflection Working Team and Ukrgeofiska, Ukraine, for providing the Donbas Foldbelt data set and geological information used in the second part of this thesis.

My special thanks goes to Christel Mynarik who always had some thing positive to tell me. My thanks also goes to Carola Kauhs who in a way promoted this work with constant literature research. Most often she had to look for literature which were not in our geophysics library collections.

Finally, I thank my parents, my sister and especially my girl friend Gudrun Haug and our son Manyacca for their patience, love, and understanding during this period.

Contents

Abstract I	xix
-------------------	------------

Acknowledgements	xxi
-------------------------	------------

I TOMOGRAPHIC DETERMINATION OF SHEAR WAVE VELOCITIES FROM DEPTH MIGRATED CONVERTED WAVE DATA	xxiii
---	--------------

1 Introduction	1
1.1 Background	1
1.2 Dissertation Objectives: Part I	2
1.3 Benefits of Converted Wave Imaging	2
1.4 Assumptions and Terminology	3
1.5 Review of Migration Velocity Analysis	4
1.5.1 Tomography after Depth Migration	5
1.6 Data sets	9
1.7 Dissertation Outline: Part I	9
2 Elastic Kirchhoff Migration	11
2.1 Introduction	11
2.2 Representation of Elastic Kirchhoff Integral (High Frequency)	12
2.3 Implementation of PS Prestack Depth Migration	17
2.4 Traveltime Computation	19
2.4.1 Eikonal Equation	20
2.4.2 Finite Difference Scheme	20
2.4.3 Traveltime Perturbation Method	21
2.4.4 Implementation into Vidale's Algorithm	23
2.4.5 Example	26
2.4.6 Migration Velocity Analysis	28
3 Shear Wave Velocity Estimation	31
3.1 Introduction	31
3.2 Model Parameterisation	32
3.2.1 Parametrising Horizons ?	32
3.3 Linearisation of the PS Traveltime Equation	33

3.4	Objective Function	34
3.4.1	Conversion of Depth Errors to Traveltime Errors	35
3.4.2	Minimising the Objective Function by Least Squares	36
3.4.3	Damped Least-Squares	37
3.4.4	Iterative Optimisation Scheme	37
3.4.5	Structural Velocities	40
3.5	Summary	41
4	Synthetic and Field Data Examples	43
4.1	Description of the Synthetic Data	43
4.1.1	Inversion Results	45
4.2	Field Data Example	48
4.2.1	Data Set	48
4.2.2	Inversion Results	48
4.2.3	Summary	55
4.3	Link between part I and part II	55
II	STRUCTURAL IMAGING IN COMPLEX GEOLOGICAL AREAS: INTEGRATING MODEL-INDEPENDENT AND MODEL-DEPENDENT IMAGING	57
	Abstract II	59
5	Introduction	63
5.1	Background	63
5.2	Dissertation Objectives: Part II	64
5.3	Conventional Stacking	64
5.4	Common Reflection Surface Stack	66
5.5	Depth Imaging	70
5.5.1	An Appropriate Macro-Model	70
5.5.2	Initial Velocity/Depth Model	71
5.5.3	Velocity Analysis for PSDM	72
5.6	Dissertation Outline: Part II	73
6	Model-Independent Time Imaging	75
6.1	Introduction	75
6.2	The NIP- and N-Wave	75
6.3	ZO CRS Stacking Operator	78
6.3.1	Multi-fold Stacking	79
6.4	Stacking Procedure	80
6.4.1	Statement of the Problem and its Solution	80
6.4.2	Search Strategy	82
6.5	Synthetic Example	87
6.5.1	Picrocol Model	87

6.5.2	Results	88
6.5.3	Comments	95
6.6	Summary	97
7	Geological Setting, Data Acquisition and Preprocessing	99
7.1	Location and Geology Setting	99
7.1.1	Pre-rift Sequence	100
7.1.2	Syn-rift Sequence	101
7.1.3	Post-rift Sequence	102
7.2	Data Acquisition	106
7.3	Data Preprocessing	107
7.3.1	Geometry, Trace Editing and Noise Analysis	107
7.3.2	Minimum Delay Transformation	109
7.3.3	Surface Consistent Deconvolution	110
7.3.4	Spectral Balancing	112
7.3.5	Residual statics and CMP sorting	112
8	Field Data: CRS Stacking and Poststack Time Migration	119
8.1	Introduction	119
8.2	Identified Regions on Poststack Time Migrated Sections	119
8.2.1	Small Scale Resolution, Dipping Layers and Anticline Flanks	124
8.2.2	Improved Imaging of Deep Reflections with a poor S/N-ratio	124
8.2.3	CRS Stack plus Poststack Time Migration	127
8.3	Summary	127
9	Velocity/Depth Model and Depth Imaging: Donbas Foldbelt Data	133
9.1	Introduction	133
9.2	Structural Model Building and Updating	134
9.2.1	Initial Model	134
9.2.2	Integrating Migrated CRS Images into Model Building	135
9.2.3	Iterative Prestack Depth Migration and Model Updating	139
9.2.4	Pitfalls of the Depth Imaging	152
10	Dissertation Summary	155
10.1	Part I	155
10.1.1	Future Work	156
10.2	Part II	156
10.2.1	Future Work	158
	Appendix A: Some Assumptions in Kirchhoff Integral	159
	Appendix B: Raypath for a Constant P/S-Velocity Ratio	161
	Appendix C: PS mode offset-limit	163

Bibliography

167

List of Figures

1.1	Sketch of depth errors after prestack depth migration	5
1.2	Depth shift between PP and PS CRP gathers	6
1.3	Sketch of prestack reflection tomography	8
1.4	Velocity analysis after prestack depth migration	8
2.1	Illustration of wavefronts and slownesses at a diffraction point	16
2.2	Example of a migration isochrone	18
2.3	Synthetic depth migrated PS section	19
2.4	Geometry for the main 2D Vidale formula	21
2.5	Grid cell for computing traveltimes using Vidale's algorithm	23
2.6	Computational scheme of expanding squares	25
2.7	A 2D constant gradient S-wave velocity model with a parabolic lens	27
2.8	Relative errors of traveltime computation	27
3.1	Subsurface region and its discretisation into nodes	32
3.2	Schematic of a PS ray	33
3.3	Converting depth shifts to traveltime difference	35
4.1	Seven layer Earth model	43
4.2	Example of PP and PS shot gathers	44
4.3	PP and PS CRP gathers migrated with constant velocity ratio	47
4.4	Comparison of PP and PS gathers after tomography	47
4.5	PP velocity/depth model obtained after prestack depth migration.	49
4.6	Field data example of PS and PP CRP gathers.	50
4.7	Field data example of PS and PP CRP gathers.	51
4.8	Field data example after tomographic updating	52
4.9	A set of PP and PS CRP gathers after tomography	53
4.10	Part of a prestack depth migrated section	54
5.1	Common shot and common midpoint configuration	65
5.2	Dipping reflection events	65
5.3	Dipping layer with CMP rays and normal incidence point	67
5.4	Poststack time migration of an anticline structure after CMP and CRS stacking .	69
6.1	Propagation of the hypothetical wavefront	77

6.2	CRS attributes with a central ray	77
6.3	Curved interface with CMP rays and normal incidence point	79
6.4	Structure of the layers in the Picrocol model	87
6.5	NMO/DMO stack section of the Picrocol data set.	89
6.6	Automatic CMP stack section generated from the first CRS step	91
6.7	CRS stack section.	91
6.8	Coherency section of the CRS stack	92
6.9	Stacking velocity section [m/s] from the q -parameter	92
6.10	Angle section [$^{\circ}$]	93
6.11	Radius of curvature of NIP -wave	93
6.12	Radius of curvature of N -wave [m]	94
6.13	Number of traces that are used to image one particular ZO time sample.	94
7.1	Location map of the survey area with major tectonic zones of the DDB.	100
7.2	Cenozoic subcrop map of the Donets segment of the Dniepr-Donets Basin	103
7.3	Correlation between salt structures of the DDB and the main anticline and synclines	103
7.4	Schematic stratigraphic column	104
7.5	Processing flow for the Vibroseis Donbas Foldbelt data.	108
7.6	Display of the instrument's response	110
7.7	Zero phase wavelet	113
7.8	Minimum phase equivalent of zero phase wavelet.	113
7.9	Shot numbers 345 and 346 before processing	114
7.10	Same shot 345 and 346 after processing	115
7.11	Shot numbers 732 and 733 before processing	116
7.12	Shot numbers 732 and 733 after processing	117
8.1	Stacking velocity model of the Donbas Foldbelt data	121
8.2	Poststack time migration of the seismic line	122
8.3	Interpreted poststack time migration of the seismic line	123
8.4	Unmigrated stacked section of the main anticline	125
8.5	Unmigrated part of the main anticline after CRS stacking	125
8.6	Conventional stack section of the axial part	126
8.7	CRS stack section of the axial part	126
8.8	Poststack time migrated image of the backthrust fault	128
8.9	CRS time migrated image of the backthrust fault	128
8.10	Poststack time migrated section after conventional CMP stacking	129
8.11	Poststack time migrated section after CRS stacking	129
8.12	Poststack migrated CMP stack section	130
8.13	Poststack migrated CRS stack section	130
8.14	Poststack time migrated image after conventional CMP stacking	131
8.15	Poststack time migration after CRS stacking	131
9.1	Time model interpretation of CRS image of the northern flank	137
9.2	Interpretation of migrated CRS time horizons on the faulted syncline	137

9.3	Interpretation of migrated CRS image showing the main backthrust fault.	138
9.4	Interpretation of migrated CRS time horizons on the main anticline.	138
9.5	Scheme with integrated model-independent and model-dependent methods.	139
9.6	CRP gathers with too low velocity	141
9.7	Example of semblance plot for migration velocity analysis	142
9.8	CRP gathers after model updating velocity	143
9.9	Flow chart for obtaining the final model	144
9.10	Final interval velocity/depth section	145
9.11	Depth section after PSDM	146
9.12	Main backthrust fault zone	148
9.13	Northern part of the section	149
9.14	Listric shear zone	150
9.15	Geologic interpretation	151
10.1	Amplitude variation with angle of PP and PS data	164
10.2	An example of a PS shot gather with polarity reversal at zero-offset crossing	165

List of Tables

4.1	Elastic parameters of the 2D synthetic model	44
6.1	Acoustic parameters of the Picrocol model	88
7.1	Seismic data acquisition parameters	107

Part I

TOMOGRAPHIC DETERMINATION OF SHEAR WAVE VELOCITIES FROM DEPTH MIGRATED CONVERTED WAVE DATA

Chapter 1

Introduction

This thesis is divided into two parts. Therefore, there are two introductory chapters. This first part of the dissertation presents research results on seismic converted wave imaging.

The second part deals with the construction of a velocity/depth model and imaging (in time and depth) of data from the inverted Donbas Foldbelt. A new processing flow for integrating model-independent and model-dependent imaging is described. The introduction of this second part will be given in Chapter 5. But note that both parts are linked because both deal with velocity model building and depth imaging.

1.1 Background

In the past decades, there has been a growing interest in shear wave exploration for hydrocarbons. Previous authors (e.g., Tatham and Stoffa, 1976; Tatham, 1992, Mesdag and Helbig, 1982; Garotta, 1985) have shown that the physical properties of rocks, such as lithology, porosity, pore-fill, anisotropy, etc., could be inferred from combined interpretation of multicomponent data.

Although S-wave sections can be generated by S-wave sources, it has also been shown (Tatham and McCormack, 1991) that in practice S-wave images generated from traditional P-wave sources often have resolution and signal-to-noise (S/N) -ratio advantages over those generated by S-wave sources. In addition to difficulties with generating shear wave directly, shear wave source operation is relatively inefficient and expensive, since recording of two perpendicularly polarized emissions are required for each source location (Tatham and McCormack, 1991). Furthermore, SS data have longer recording time than PS data which can be an issue in some recording instruments. In comparison, a P-wave source requires only 3-component geophones to record both PP and PS data. In terms of processing, SS reflection data need a solution for relatively large shot and receiver statics, while the PS data benefit from previously determined P-wave source statics. Another problem with shear wave source as discussed in Tatham and McCormack (1991), is that the frequency content of the SS data is lower than that of PS data, and hence SS data are seriously contaminated by low frequency, source generated noise. Therefore, from an operational point of view (both acquisition and processing), PS data are the preferred data sets for S-wave reflection seismology.

To realize the potential advantages of PS data, it is usual practice to decompose PS reflections from PP reflections. Although some success has been achieved in the separation of P- and S-wave events (Dankbaar, 1985; Tatham and McCormack, 1991), algorithms for handling the asymmetric PS raypath are generally limited to low relief data. For example, common conversion point (CCP) binning (Tessmer et al., 1990) and PS DMO are only partial solutions to the asymmetry problem and face some difficulties in structural data.

Although PS reflection data contain S-wave velocity information, traditional time processing (Tessmer et al., 1990) does not yield direct estimation of the interval S-wave velocity. Usually P-to-S-velocity ratios v_p/v_s are derived by correlating reflection events on both PP and PS sections. However, these values together with the obtained S-wave velocities are root mean square values. Therefore, the most appropriate method for imaging PS data and for estimating interval S-wave velocity is prestack depth migration. Prestack depth migration requires very few assumptions and the results are not affected by the asymmetric PS raypaths. The estimated S-wave velocities and v_p/v_s -ratios during migration directly give the interval values. This information, together with interval P-wave velocity, can then be used for lithology detection.

1.2 Dissertation Objectives: Part I

The main objective of this first part is to develop a tomographic method for estimating shear wave (S-wave) velocities and a v_p/v_s -ratio model from migrated PS and PP data. The method interprets events in depth migrated PS and PP sections and uses discrepancies in the depth sections to update the S-wave velocity model. The method promises to be useful in areas with strong lateral velocity variations because no assumptions about the model complexity are made. The first goal is to develop a fast 2D PS prestack depth migration algorithm which is used for performing the migration and PS migration velocity analysis. A synthetic two component data set was generated using a realistic model to test the inversion algorithm. In addition, a multicomponent data set was provided by Preussag Energy GmbH. These data are used to validate the newly developed tomographic approach of estimating interval shear wave velocities.

1.3 Benefits of Converted Wave Imaging

The propagation of P- and S-waves in sedimentary rocks are affected differently by rock physical properties. S-waves are insensitive to fluids, slower than P-waves, and can be polarised in different directions. The potentials of using S-waves in exploration are based on these three properties. Some of the benefits of interpreting PS and PP data can be stated as follows:

- PS data can be used for imaging below gas clouds and for geological boundaries with low contrast in acoustic impedance for P-waves. Sometimes shale/sand boundaries may produce poor PP-wave velocity contrasts and strong PS-wave contrasts. An example of such a situation is shown in the real data example in Chapter 4, section 4.2 (see also examples in Caldwell, 1999).

- Information from a joint PP and PS data interpretation can be used for lithology as well as a direct hydrocarbon indicator. These benefits exploit the differences in reflectivity response for PP and PS waves at a lithologic change or a fluid reservoir. For bright spots, a strong PP reflection is observed but, because shear waves are essentially insensitive to gas, there is no response on the shear wave reflection.
- PS data can be used to improve imaging in PP due to better azimuthal distribution and more possibilities for removal of receiver ghosts and multiples in marine survey.
- Another potential is to use PS data for estimating anisotropic parameters and fracture detection through analysis of S-wave splitting (see e.g. Gaiser, 2000).

1.4 Assumptions and Terminology

Although waves that propagate through the Earth are inelastic, coupled, anisotropic, and attenuating, throughout this thesis I describe imaging methods for isotropic uncoupled elastic waves. For computational reasons, I discuss only two dimensional (2D) problems in this thesis, but the velocity analysis concepts expounded here also apply to three dimensional velocity analysis.

Prestack multicomponent data always have converted shear waves in the vertical component data and compressional waves in the horizontal component of the data. However, I assume in this thesis that the vertical component (Z-component) of the data has been separated from its shear wave types and the horizontal components (X- and Y-components) of the data have been separated from the compressional wave type. In this situation the vertical component contains only P-waves and the horizontal component contain only PS-waves.

The prestack migration algorithms I use treat the wavefield as if it were composed only of reflection events; multiples and other noise must be removed prior to prestack migration. Moreover, the migration algorithms I use treat the reflected P-wave (PP) and converted S-wave (PS) data using geometric optics which replaces wave calculations with simpler and more economic ray calculations. I use the Kirchhoff integral migration instead of the wave equation migration. The formulation of the migration algorithm is based on high-frequency assumptions, meaning that effects on wave transmission of high wavenumbers in the background medium are neglected. In the migration formulation in Chapter 2, I will mostly use the term “scattered waves” which include reflection, diffraction and refraction waves.

In the tomographic inversion, I assume the knowledge of an accurate P-wave velocity/depth model from a previous migration velocity analysis of PP data. However, the estimation of this model is not trivial and a flow for obtaining it is discussed in the second part of this thesis.

The terms **depth gathers**, **CRP gathers**, and **image gathers** are synonymous. These terms all refer to the gather product of prestack depth migration. These gathers play a key role in the velocity/depth model building process. Depth gather stresses the domain class of this product. The

term **CRP** (common reflection point) gather stresses the nature of this gather as expressing the information that arises from a single subsurface reflection point. Because I compare in the depth domain the PP and PS images after migration, the preferred term used in this work is CRP. It stands in contrast to the reflection point smear of CMP gathers in structured environments. **Image gathers** calls the attention to the fact that these gathers, when stacked, create the final seismic image. The term CMP (common midpoint) gather is not synonymous with these other terms. It represents the collection of traces which share a common midpoint (or bin) location between the surface location and receiver.

1.5 Review of Migration Velocity Analysis

Migration is an operator that suppresses diffraction and other scattering effects by reorganizing the recorded seismic energy so that the data will resemble the reflectivity image of the subsurface over-which it was recorded (Claerbout, 1985). Migration focuses the energy at the apex of the diffraction pattern corresponding to the scattering point. Migration process can be applied to stacked data or to unstacked (prestack) data. Some migration algorithms that work on prestack data output only stacked images; others can output unstacked images. Prestack migration is often applied when a satisfactory stack cannot be made by simple methods because of complex structure and/or lateral velocity variations. Some prestack migration algorithms such as frequency-wavenumber (f-k), frequency-space (f-x) (see e.g., Yilmaz, 2001) and finite difference (t-x), shot/geophone downward continuation and reverse-time migration (Claerbout, 1985) combine the information from all offsets at once. They perform prestack migration and stacking simultaneously.

Other migration algorithms like Kirchhoff prestack migration (common offset or common shot migration) can postpone stacking until after migration. The unstacked output after migration is examined for residual moveout (flatness or non-flatness of events in CRP gathers) and thus, for errors in the velocity model. The idea behind depth migration velocity analysis is that, if the input migration velocity model is correct, events in the CRP gathers will be imaged at the same depth, regardless of their offset (Al-Yahya, 1989; Stork, 1992). If the velocity model is incorrect, events will have residual moveout with the offset (Figure 1.1).

On the other hand, the lack of residual moveout over the offset in a CRP gather is an indication that the input interval velocity model is accurate. Therefore, velocity-dependent residual correction is applied to the migrated common shot/offset sections to remove residual moveout found in the initial migrated images. This principle works very well for monotypic waves (PP or SS) with sufficient spread or cable length. For PS data, and in the short spread limit, the events in the CRP gathers can be flat even though the v_s value is not correct. This incorrectness of the v_s model is “seen” as depth shift when the PS and PP CRP gathers are compared at the same surface location (Figure 1.2).

The question to be solved is how to update the v_s model in a laterally inhomogeneous model such that the PS CRP gathers are flat and tie in depth with their PP counterpart.

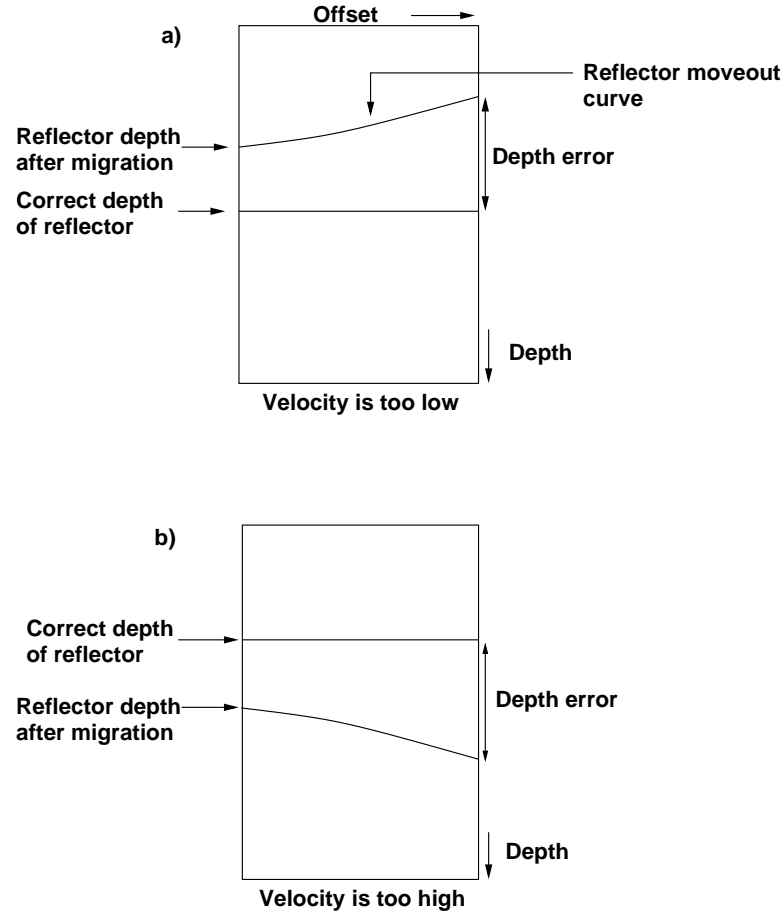


Figure 1.1: a) The CRP pattern when the input migration velocity is too low, b) CRP pattern when the input migration velocity is too high. The velocity errors lead to depth errors and residual moveout of reflection events in the CRP gathers.

Residual moveouts can only be observed, if the offsets are sufficiently large compared to the reflector depth. This is quite often the case for shallow reflectors. For PS data deep reflectors do not often show moveout as a function of offset and S-wave velocity incorrectness. This is because the asymmetrical raypath of the PS reflection emerges almost vertically at the receiver locations. Therefore, instead of using residual moveout analysis I suggest to solve the problem through tomography of depth migrated PS gathers. The depth discrepancies between PS and PP gathers are what I use in this part of the thesis to estimate the interval shear wave velocities and the corresponding v_p/v_s -ratios.

1.5.1 Tomography after Depth Migration

The S-wave velocity estimation method presented in this thesis uses an interactive, event-driven approach, but analyses depth migrated common reflection point gathers. A similar approach for PP data was presented by Kosloff et al. (1996).

The migrated CRP gathers are better suited for interpretation than the unmigrated gathers are. First, they closely resemble the geology, so geological constraints can guide the interpretation.

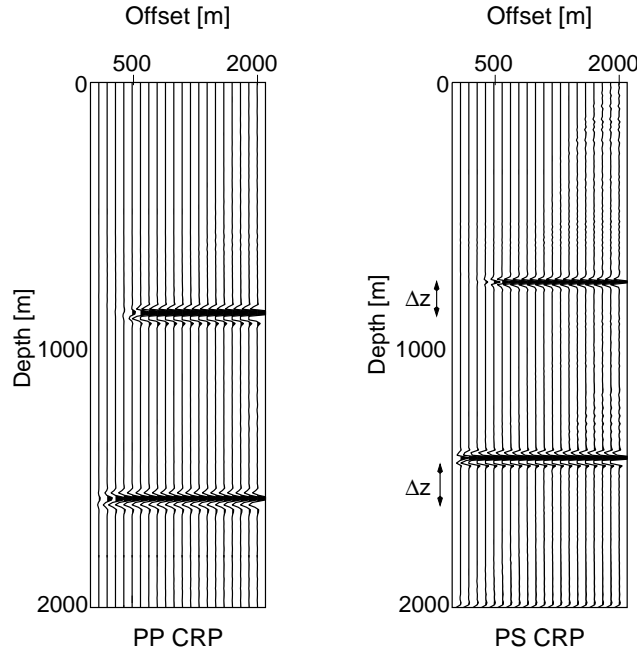


Figure 1.2: PP and PS CRP gathers at the same surface location. The PP gather was generated using the correct v_p model, therefore, the events are flat. The PS gather was generated using the correct v_p and an incorrect v_s model. Both the PS and PP events are flat, however, a depth shift Δz exist between them.

Second, seismic energy is focused by migration, so that the local signal-to-noise (S/N)-ratio is improved. Migration collapse diffractions; the residual depth shift or residual moveout effects that are left after migration are clearer and easier to analyse. Thus, migration greatly simplifies the picking of the events in the data and thereby solves one of the main problems of tomography.

The method used in this work is an iterative optimisation scheme that tries to find an S-wave velocity model for which all PS and PP reflectors are imaged at identical positions on different common reflection point panels. For this purpose, I pick reflectors in the PS and PP migrated panels, and from the picks I estimate perturbations in reflector depth. The optimisation then determines how the shear wave velocity model should be updated so that the perturbations are minimised. The minimisation is carried out by a conjugate gradient algorithm, where the calculation of the gradient (or back projection) operator is based on a linearisation of the relation between the positions of the migrated reflectors in the PS and PP section and the velocity model.

1.5.1.1 Comparison with Prestack Traveltime Tomography

The objective of tomography is to update the initial parameters of an Earth model that has already been estimated. Reflection tomography is an inversion method for estimating the Earth model parameters from the reflection traveltimes associated with the observed seismic data. The reflection

traveltime from a source at the surface to a reflection point and back to the surface is represented by an integral of the traveltime segments along the raypath that depends on the parameters of the Earth model. This makes the direct inversion of the reflection traveltimes for the estimation of the model parameters a non-linear problem (Tarantola, 1984). Nevertheless, with Fermat's principle small changes in the reflection traveltimes are linearly related to small changes in the Earth model parameters. Therefore, tomography is not used to estimate an initial Earth model, but to update a previously estimated model.

Although the S-wave velocity estimation method described here can equally well be implemented in prestack traveltime tomography there is one fundamental difference: in prestack traveltime tomography the reflection events are picked in the unmigrated data, whereas in prestack migration tomography the reflection events are picked after depth migration. As a consequence, picking traveltimes in the unmigrated prestack domain must be done on events clearly identifiable on both PS and PP data. Depending on the data quality, the identification, pairing and picking of PS and PP events may be very difficult. Furthermore, using migrated data allows direct incorporation of geological interpretation in the model updating process.

There is another important reason why I prefer using migration in the velocity analysis. In conventional tomography traveltime observations would be independent of the velocity model, whereas here the depths found after migration depend on the velocity model. It is this dependency and the fact that migration is supposed to produce identical images at all offsets, that provide the ingredients for an efficient optimisation scheme. In other words, unlike in prestack tomography, my optimisation does not minimise the mismatch between modelled and observed events, but instead uses the unique relation between the migrated reflectors and the S-wave velocity model to check the validity of the S-wave velocity model. Therefore, migration is important not only as a tool for imaging and aiding interpretation, but also in providing a consistent framework for verifying seismic velocities. Figure 1.3 and 1.4 shows the differences in approach between prestack tomography and tomography after migration.

There also exist similarities between my depth domain tomographic approach and prestack reflection tomography. First, both use picked events and project perturbations of these events back onto the velocity models. Second, both use the fact that the reflector position is fixed and is held fixed during the computation of the back projection operator. This assumption is justified since the reflector geometry is known from previous inversion of the PP wave data section. With this I assume that the PS reflection and the PP reflections come from the same interface. Third, tomography generally does not assume hyperbolic moveout (characterised by zero-offset traveltime and stacking velocity).

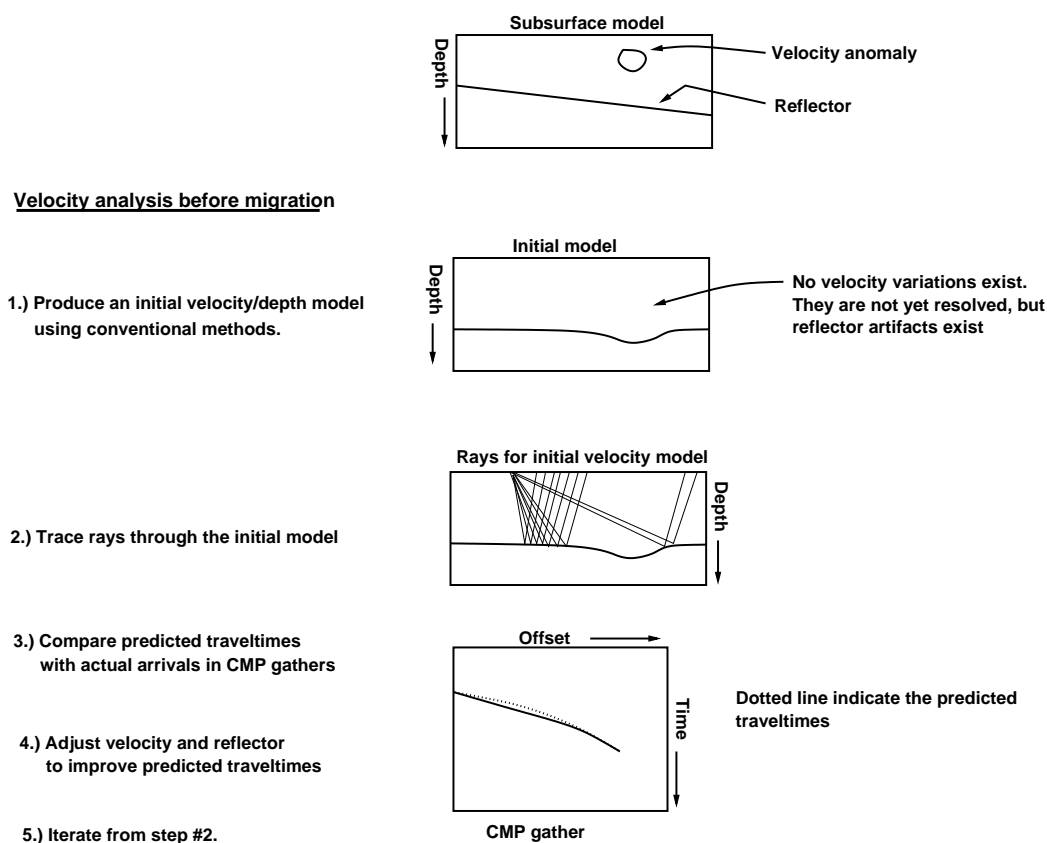


Figure 1.3: A sketch of reflection tomography. Predicted traveltimes are computed through an initial velocity/depth model. The differences between the predicted traveltimes of the reflection events (dotted lines) and the actual traveltimes represent errors in the initial model. Reflection tomography adjust the model to optimize the predicted traveltimes.

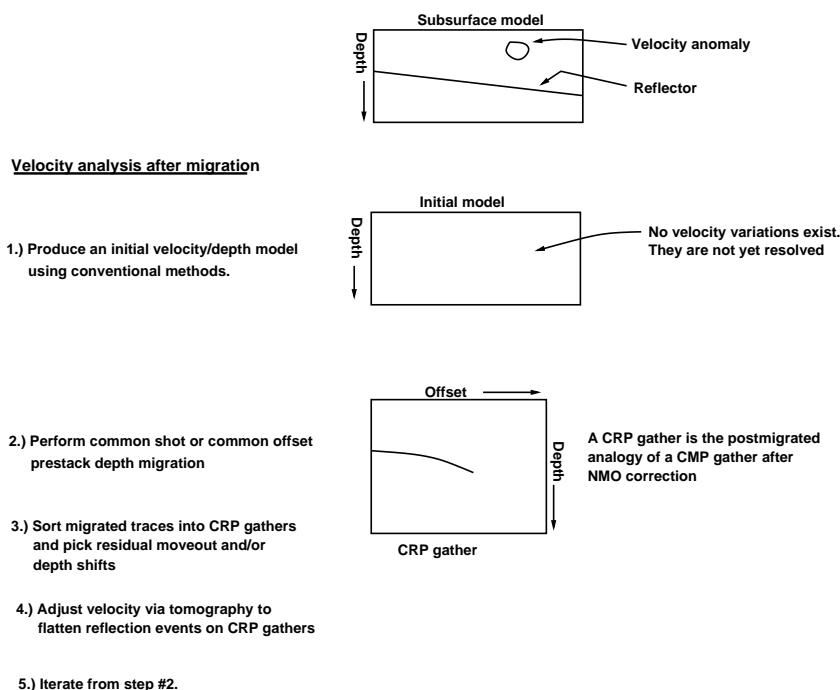


Figure 1.4: A sketch of tomography after prestack depth migration. The prestack data are migrated through the velocity field but not stacked. CRP gathers are sorted from the migrated traces and residual moveouts are picked. The residual moveouts are then used for tomographic inversion. The postmigrated tomography generates a model which flattens the events on the CRP gathers.

1.6 Data sets

Synthetic data

The two component synthetic data used in this dissertation were generated by the ray tracing elastic modelling program (Seis88) (Červený and Pšenčík, 1984) which simulates a 2D Earth, three component (3C) recording (vertical and two radial) with a line source. Since the data were generated for prestack depth migration, surface multiples and direct waves were avoided.

Field data

A 2D multicomponent seismic profile was acquired by Preussag Energie GmbH in South East Bavaria (Germany). The line consisted of three independent measurements. For two of them, three P-wave vibrators with a sweep of 17-100 Hz were used as a source. A well drilled up to 4.7 km depth was used to estimate the P-wave velocity. Preprocessing of the PP and PS data was already applied by Preussag Energie GmbH.

1.7 Dissertation Outline: Part I

Chapter 2 reviews the formulation of the elastic Kirchhoff depth migration. The implementation of the derived integral formula for common shot converted wave depth migration is described. The implementation is very similar to that for PP-waves, with the only difference being that the ray branch from the reflector to the receiver is an S-ray and therefore, requires S-wave traveltimes. A synthetic example shows the validity of the algorithm.

Chapter 2 also discusses the finite difference Vidale's method (Vidale, 1988) for computing seismic traveltimes. Traveltimes are important for both migration and migration velocity analysis. I implemented the perturbation method into Vidale's algorithm for computing traveltimes simultaneously for more than one model. This is important for the migration velocity analysis described in Chapter 3. The finite difference traveltime algorithm is fast and accurate for tomographic applications.

Chapter 3 is devoted to the new solution of the tomographic inverse problem of estimating the S-wave velocities from depth migrated horizons. I discuss the linearisation of the PS traveltime and show how PS and PP depth shifts are converted to traveltime differences. This chapter ends with a discussion on structural velocity models. The application of the tomographic method to synthetic and real data is discussed in Chapter 4.

Chapter 2

Elastic Kirchhoff Migration

2.1 Introduction

The main objective of seismic imaging is to use reflection events (Sheriff and Geldart, 1982) to reconstruct a plausible subsurface geological model. For this purpose it is common practice to use seismic migration. Migration is a process that corrects for effects of wave propagation (e.g. diffraction) that often distort the reflection events. In the past decades, numerous migration methods have been developed (see Gray et al., 2001, for a review of methods). The different methods can be classified into finite difference (wave equation), and integral (Kirchhoff) techniques. Each technique has certain advantages and disadvantages with respect to computational speed and capability to handle irregular geometries or strong variations in subsurface velocity. In practice, finite difference (FD) migration suffers some limitations. First, this migration requires regularly sampled offsets therefore, its application requires trace regularization (especially in 3D). Moreover, its application to real-size data sets is usually limited by the present computer power. However, the FD migration has the advantage that its application is based on the full wave equation and not on an asymptotic assumption based on ray theory. On the other hand, Kirchhoff migration has the advantages that first, it is faster than the FD migrations. Second, its by-products (the CRP gathers) are used as the most important input into migration velocity analysis. Third, its application do not necessarily require trace regularization.

Therefore, in this thesis, I use the Kirchhoff prestack depth migration method (Schneider, 1978). Because converted waves are involved, the migration is called elastic migration as opposed to the acoustic migration where only P-waves are migrated. In this chapter, I review the mathematical formulation of the elastic Kirchhoff migration and later discuss the practical implementation of the migration algorithm for PS-waves. The major input into the migration and the subsequent velocity analysis after migration is the computation of traveltimes tables. Because migration followed by velocity analysis is an iterative process, a fast traveltimes computation algorithm is essential. Section 2.4 is devoted to Vidale's traveltimes algorithm (Vidale, 1988) and I will show how to implement the perturbation method into the traveltimes algorithm. This perturbation method allows for a simultaneous migration of PS data within a range of P- and S-wave velocity models. This method ensures that migration velocity analysis becomes faster.

2.2 Representation of Elastic Kirchhoff Integral (High Frequency)

Migration involves two major steps, namely, a wave-extrapolation technique to back-propagate the seismic data recorded at the surface, and secondly an imaging condition. The Kirchhoff-Helmholtz integral for elastic waves (Pao and Varanharajulu, 1976) ¹ is used to downward continue the total displacement wave field. This integral is expressed in its general form in the frequency domain as:

$$U_m^g(\mathbf{r}, \omega) = \int_s \left\{ t_i(\mathbf{r}', \omega) G_{im}(\mathbf{r}; \mathbf{r}', \omega) - U_i^s(\mathbf{r}', \omega) \Sigma_{ijm}(\mathbf{r}; \mathbf{r}', \omega) \right\} dS', \quad (2.1)$$

$$\mathbf{r}, \mathbf{r}' \in V,$$

where $U_m^g(\mathbf{r}, \omega)$ ² is the scattered displacement vector field emitted by the Huygen's secondary sources, (denoted as $U_i^s(\mathbf{r}', \omega)$), interior to a volume V bounded by a closed surface S' , and ω is angular frequency. Note that the integral extends from $-\infty$ to $+\infty$. $G_{im}(\mathbf{r}; \mathbf{r}', \omega)$ are the components of the Green's displacement tensor. The summation convention is implied over repeated sub-indices. Physically, $G_{im}(\mathbf{r}; \mathbf{r}', \omega)$ represents the m -th component of the displacement at \mathbf{r} due to concentrated force applied at \mathbf{r}' in the i -th direction with a delta function. Likewise, $\Sigma_{ijm}(\mathbf{r}; \mathbf{r}', \omega)$ represents the stress tensor field at \mathbf{r} generated by three mutually perpendicular concentrated forces at \mathbf{r}' . Both tensors satisfy the symmetry relations. The traction stress t_i and the Green's traction tensor $\Sigma_{ijm}(\mathbf{r}; \mathbf{r}', \omega)$ are:

$$t_i(\mathbf{r}; \mathbf{r}', \omega) = n_j C_{ijkl}(\mathbf{r}') \frac{\partial U_l^s(\mathbf{r}; \mathbf{r}', \omega)}{\partial x_k}, \quad (2.2)$$

and:

$$\Sigma_{ijm}(\mathbf{r}; \mathbf{r}', \omega) = n_j C_{ijkl}(\mathbf{r}') \frac{\partial G_{lm}(\mathbf{r}; \mathbf{r}', \omega)}{\partial x_k}, \quad (2.3)$$

where $C_{ijkl}(\mathbf{r}')$ represent the elastic parameters of the medium (a fourth rank tensor) and n_j is a component of the unit vector.

Assuming the seismic measurements are made over a free-surface S , the following traction-free boundary condition will be satisfied (Eskola, 1992):

$$\mathbf{t} = 0, \quad \mathbf{r} \in S. \quad (2.4)$$

Using equation (2.4) and (2.1), the surface integral representation of the displacement field can be rewritten in the form:

¹Appendix A gives some assumptions required in deriving the Kirchhoff integral.

²Although the implementation of the Kirchhoff integral is in the time domain, I use the frequency domain for mathematical clearness.

$$U_m^g(\mathbf{r}, \omega) = - \int_s U_i^s(\mathbf{r}', \omega) \Sigma_{ijm}(\mathbf{r}; \mathbf{r}', \omega) dS' \quad z > 0. \quad (2.5)$$

Equation (2.5) is the Kirchhoff-Helmholtz integral. This integral allows the computation or forward propagation of the displacement field anywhere inside the earth (i.e., in the region $z > 0$) from the measurements of the displacement field on the free surface S ($z = 0$), provided a suitable expression of the Green's tensor is available. However, in the process of seismic migration (time or depth) the recorded wavefield needs to be backward propagated in time into the medium where it will focus at the scatterers (Huygens' secondary sources) and consequently form an image of the subsurface. For migration purposes a major assumption is that the point scatterers in the medium are excited at the arrival time of the incident wave from the source. This is usually called the excitation time imaging condition.

Therefore, to change Equation (2.5) from the forward propagation to a backward propagation, the Green's tensor in the Kirchhoff-Helmholtz integral is replaced by its inverse. The inverse Green's tensor is approximated as the complex conjugate of the forward Green's tensor. Therefore, the back-propagated wavefield is given by:

$$U_m^g(\mathbf{r}, \omega) = - \int_s U_i^s(\mathbf{r}', \omega) \Sigma_{ijm}^*(\mathbf{r}; \mathbf{r}') dS' \quad z > 0, \quad (2.6)$$

where $*$ denotes complex conjugate. Note that expression (2.6) is not the true back-propagated displacement field because a conjugate operator is used instead of a "true" inverse operator. However, it is accurate enough for practical applications. For a given source-receiver pair, the Green's tensor G_{im} for a smooth medium can be approximated by the high frequency approximation (Červený, 2001). In this approximation the total Green's tensor from the source to the receiver can be expressed as:

$$G_{im}(\mathbf{r}; \mathbf{r}', \omega) = G_{im}^{source}(\mathbf{r}; \mathbf{r}', \omega) + G_{im}^{receiver}(\mathbf{r}; \mathbf{r}', \omega), \quad (2.7)$$

whereby (Pao and Varantharajulu, 1976; Kuo and Dai, 1984):

$$G_{im}(\mathbf{r}; \mathbf{r}', \omega) = \sum_{L=1}^3 A_{im}^L(\mathbf{r}; \mathbf{r}') e^{i\omega\tau_L(\mathbf{r}; \mathbf{r}')}, \quad (2.8)$$

$$G_{im}^*(\mathbf{r}; \mathbf{r}', \omega) = \sum_{L=1}^3 A_{im}^L(\mathbf{r}; \mathbf{r}') e^{-i\omega\tau_L(\mathbf{r}; \mathbf{r}')}, \quad (2.9)$$

where A_{im}^L and τ_L are the ray amplitude and traveltime³ for wave mode L , respectively. Equation (2.8) and (2.9) give the general high frequency, HF, Green's tensor for all possible wave modes from the source. Using Equations (2.8) and (2.3), and dropping lower order terms, the Green's

³In the high frequency, HF, assumption the phase information in seismic waves is simplified to traveltimes (Aki and Richards, 1980, p. 416). This is because the phase term $i\omega\tau$ is mostly governed by the traveltime. Along a raypath, the variation in $e^{-i\omega\tau}$ is much greater than the variation in A . Thus the first term in the derivative of G (i.e. $\partial_n G = (\partial_n A)e^{-i\omega\tau} - Ae^{-i\omega\tau}(\partial_n \tau)$) is small compared to the second term and can be neglected.

stress tensor becomes:

$$\Sigma_{im}(\mathbf{r}; \mathbf{r}', \omega) = \iota\omega \sum_{L=1}^3 C_{ijkl}(\mathbf{r}') A_{im}^L(\mathbf{r}; \mathbf{r}') \cdot p_k^L(\mathbf{r}; \mathbf{r}') e^{\iota\omega\tau_L(\mathbf{r}; \mathbf{r}')} n'_j, \quad (2.10)$$

where

$$p_k^L(\mathbf{r}; \mathbf{r}') = \frac{\partial \tau_L(\mathbf{r}; \mathbf{r}')}{\partial x'_k} \quad (2.11)$$

is the k -component of the slowness vector corresponding to the wave mode L . Substituting Equation (2.10) into equation (2.6) gives the back propagated elastic Kirchhoff wavefield:

$$U_m^g(\mathbf{r}, \omega) = \iota\omega \sum_{L=1}^3 \int_s U_i^s(\mathbf{r}', \omega) C_{ijkl}(\mathbf{r}') A_{im}^L(\mathbf{r}; \mathbf{r}') p_k^L(\mathbf{r}; \mathbf{r}') e^{-\iota\omega\tau_L(\mathbf{r}; \mathbf{r}')} n'_j dS'. \quad (2.12)$$

It is usually assumed that the Kirchhoff wavefield propagates in a background medium in which the amplitude and the direction of propagation of the wavefield vary only slightly over distances of the order of a wavelength (see Appendix A). Geologically, these conditions mostly prevail in areas with sedimentary depositions and marine environments.

To generate an image or reflectivity function $R(\mathbf{r}, \omega)$ of the subsurface, Keho and Beydoun (1987) defined the image function as the ratio of the back propagated wavefield from the receivers, $U_m^g(\mathbf{r}, \omega)$, to the forward propagated wavefield from the source, $U_m^{inc}(\mathbf{r}, \omega)$. $U_m^{inc}(\mathbf{r}, \omega)$ should not be confused with $U_i^s(\mathbf{r}', \omega)$. For multicomponent data I express $R(\mathbf{r}, \omega)$ in the following matrix form (imaging matrix):

$$R(\mathbf{r}, \omega) = \begin{pmatrix} R_{11}(\mathbf{r}, \omega) & R_{12}(\mathbf{r}, \omega) & R_{13}(\mathbf{r}, \omega) \\ R_{21}(\mathbf{r}, \omega) & R_{22}(\mathbf{r}, \omega) & R_{23}(\mathbf{r}, \omega) \\ R_{31}(\mathbf{r}, \omega) & R_{32}(\mathbf{r}, \omega) & R_{33}(\mathbf{r}, \omega) \end{pmatrix}, \quad (2.13)$$

where the correspondence $1 \Leftrightarrow P$, $2 \Leftrightarrow SV$, $3 \Leftrightarrow SHhold$. For example, the PP and PSV reflection coefficients are given as:

$$R_{11}(\mathbf{r}, \omega) = \frac{U_p^g(\mathbf{r}, \omega)}{U_p^{inc}(\mathbf{r}, \omega)}, \quad R_{12}(\mathbf{r}, \omega) = \frac{U_{sv}^g(\mathbf{r}, \omega)}{U_p^{inc}(\mathbf{r}, \omega)}. \quad (2.14)$$

The incident wavefield $U_m^{inc}(\mathbf{r}, \omega)$ in its HF form can be expressed as:

$$U_m^{inc}(\mathbf{r}, \omega) = S(\omega) B_{mq}^M(\mathbf{r}; \mathbf{r}_o) e^{\iota\omega\tau_M(\mathbf{r}; \mathbf{r}_o)}, \quad (2.15)$$

with $S(\omega)$ being the source function and B_{mq}^M the amplitude of the incident wave mode M . I consider that the incident wavefield is generated by a point source in the q -direction at the position \mathbf{r}_o .

Therefore, the general expression for the M to L reflection coefficient takes the form:

$$R_{ML}(\mathbf{r}, \omega) = \frac{\iota\omega}{B_{mq}^M(\mathbf{r}; \mathbf{r}')} \int_s U_i^s(\mathbf{r}', \omega) C_{ijkl}(\mathbf{r}') A_{lm}^L(\mathbf{r}; \mathbf{r}') p_k^L(\mathbf{r}; \mathbf{r}') e^{-\iota\omega(\tau_L(\mathbf{r}; \mathbf{r}') + \tau_M(\mathbf{r}; \mathbf{r}_o))} n'_j dS'. \quad (2.16)$$

In Equation (2.16) I assume that $S(\omega)$ has a unit value. Next, Equation (2.16) is transformed into the time domain via the Fourier transform. This will result in Equation (2.17):

$$R_{ML}(\mathbf{r}, t) = \frac{-1}{2\pi B_{mq}^M(\mathbf{r}; \mathbf{r}')} \int_s \frac{\partial}{\partial t} U_i^s(\mathbf{r}', t + \tau_L(\mathbf{r}; \mathbf{r}') + \tau_M(\mathbf{r}; \mathbf{r}_o)) \cdot C_{ijkl}(\mathbf{r}') A_{lm}^L(\mathbf{r}; \mathbf{r}') p_k^L(\mathbf{r}; \mathbf{r}') n'_j dS'. \quad (2.17)$$

Note that $\int (\iota\omega) U(\omega) e^{-\iota\omega\tau} e^{-\iota\omega t} d\omega = \frac{\partial U^s}{\partial t}$. Finally, the image, $I_{ML}(\mathbf{r})$, of the medium is obtained by setting $t = 0$ in Equation (2.17); i.e., by applying the excitation time imaging condition with the consideration that the wave starts propagating from the source at the time $t = 0$ (causal signal). This gives:

$$\text{image} = I_{ML}(\mathbf{r}) \equiv R_{ML}(\mathbf{r}, t = 0). \quad (2.18)$$

Further simplification of Equation (2.17) is achieved by assuming the recording surface is the plane $z = 0$ such that the unit vector $\mathbf{n}' = (0, 0, -1)$ and that the boundary conditions on the interface allows for decoupling of the wave modes (e.g the region around the scatterer is smooth and homogeneous). In isotropic elastic media the elastic constant is expressed as:

$$C_{ijkl}(\mathbf{r}') = \delta_{ij}\delta_{kl}\lambda(\mathbf{r}') + (\delta_{ik}\delta_{jl} + \delta_{il}\delta_{kj})\mu(\mathbf{r}'), \quad (2.19)$$

where $\lambda(\mathbf{r}')$ and $\mu(\mathbf{r}')$ are the Lamé parameters at the free surface and δ_{ij} is the Kronecker's symbol. Using Equations (2.18) and (2.17), the image of the subsurface takes the form of Equation (2.20). For clarity I omit the position vectors $(\mathbf{r}; \mathbf{r}')$ and $\tau(\mathbf{r}; \mathbf{r}')$;

$$I_{ML} = \frac{1}{B_{mq}^M} \int dS' \left\{ (\lambda + 2\mu) \frac{\partial U_z^s}{\partial t} A_k^L p_k^L + \mu \left(\frac{\partial U_x^s}{\partial t} (A_z^L p_x^L + A_x^L p_z^L) + \frac{\partial U_y^s}{\partial t} (A_z^L p_y^L + A_y^L p_z^L) \right) \right\}, \quad (2.20)$$

where $k = x, y$, or z . The first term in Equation (2.20) is the P-wave contribution while the second and third terms are the S-wave contributions. Equation (2.20) gives the general elastic wave image for various combinations of wave types, and the traveltime function $\tau(\mathbf{r}; \mathbf{r}')$ satisfies the eikonal equation (see Section 2.4). Therefore, elastic migration should be performed by using Equation (2.20) without any decomposition of the recorded wavefield. However, because of practical rea-

sons the recorded wavefields are always decomposed into their various components (Dankbaar, 1985). In the case of a decomposed PS migration only the second and third term are used for the migration algorithm, while only the first term is used for PP-wave migration.

The combination of the amplitude terms and the slowness vectors in Equation (2.20) give the weighting function W_{ML} (required for common shot preserved amplitude migration):

$$W_{ML}(\mathbf{r}; \mathbf{r}') = \left| \frac{A_{im}^L(\mathbf{r}_g, \mathbf{r}') \mathbf{n}' \cdot \nabla \tau(\mathbf{r}; \mathbf{r}')}{2\pi B_{mq}^M(\mathbf{r}; \mathbf{r}') \mathbf{q}} \right|. \quad (2.21)$$

For a monotypic wave e.g PP reflection, $\mathbf{n}' \cdot \nabla \tau = \mathbf{n}' \cdot \mathbf{q}'/v_p = 2 \cos \theta/v_p$; θ is the angle between the normal to the surface and the emerging ray ($\mathbf{r}_g, \mathbf{r}'$) and \mathbf{q} is the unit tangent vector for the emerging ray. For PS data $\mathbf{n} \cdot \nabla \tau_{ps} = (\cos \theta_p/v_p + \cos \theta_s/v_s) = \mathbf{p}_p + \mathbf{p}_s$ (see Figure 2.1). Expressions for the ray amplitudes (A^L and B^M) are given in Keho and Beydoun (1987) and Čer-

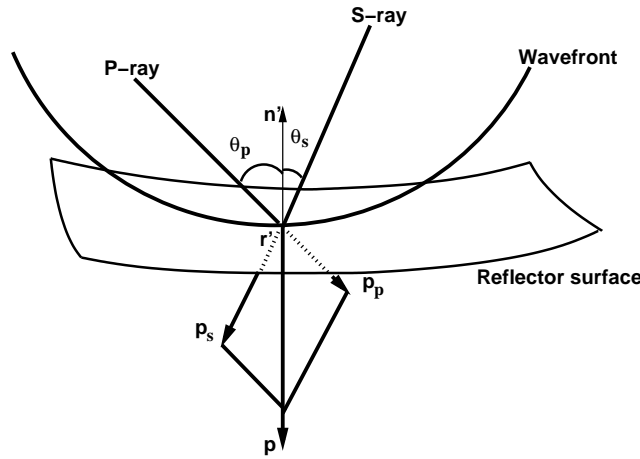


Figure 2.1: Schematic illustration of a wavefront and the slownesses of the corresponding P- and S-ray at a point of incidence \mathbf{r}' . The symbols \mathbf{p}_p , \mathbf{p}_s , and \mathbf{p} represents the corresponding P-ray slowness, S-ray slowness and the sum of the two slownesses, θ_p and θ_s are respectively, the incidence and reflection angles. Note that for reflected ray \mathbf{p}_s takes the opposite direction.

vený (2001).

Equation (2.20) contains the time derivative of the recorded wavefield, $\frac{\partial U^s}{\partial t}$. This time derivative of the wavefield is given as (Bleistein, 1987):

$$\begin{aligned} i\omega U^s & \quad 3D, \\ \sqrt{|\omega|} \exp(i\pi/4 \text{sign}(\omega)) U^s & \quad 2.5D, \\ |\omega| U^s & \quad 2D. \end{aligned}$$

The time derivative field is usually described as the filtered wavefield. The migration surface in Equation (2.20) extends from $-\infty$ to $+\infty$ in the horizontal direction. However, practical limits are placed upon the extent of the surfaces since the measured data are band limited. The practical procedure is to restrict the horizontal extent of the surfaces to a distance known as the migration

aperture. This will result in limiting the number of traces that should be summed over for each migrated point.

The computation of the Green's function (see Equation(2.8)) and the estimation of the appropriate velocity field through which the wavefield propagates are the key in all prestack migration algorithms. The amplitude terms of the Green's function equation determine the dynamic part of the migration while the traveltime terms determine the kinematic part. If the purpose of the migration is for preserved amplitude migration, then the amplitude terms have to be computed. A description of preserved amplitude migration is given in the literature (see e.g. Schleicher et al., 1993a; Hanitzsch et al., 1994; Hanitzsch, 1997). In this work I use only the kinematic part since my objective is focused on imaging.

2.3 Implementation of PS Prestack Depth Migration

In practice migration is rarely implemented as expressed in Equation (2.20). Instead, the 3-component recorded data are separated and each component is migrated individually. It is assumed that each component is free from the other wave modes. In this section I describe the implementation of Equation (2.20) for PS data based on migration of individual shot gathers.

The migration process consists of two steps: (1) traveltime calculation and (2) Kirchhoff summation. The imaging condition for each depth point (considered as a possible scatterer) requires that I know the traveltimes from the source and from the receiver to the depth point under consideration. The traveltimes are computed for the background velocity models (v_p and v_s). For 2D PS data the discretised form of Equation (2.20) is rewritten as (without the amplitude terms):

$$I_{ps_{out}} = \frac{1}{2\pi} \sum_a \mathbf{n}' \cdot \nabla \tau_{ps} \frac{\partial U_{ps_{in}}(\mathbf{r}, \tau_{ps})}{\partial t} \Delta x, \quad (2.22)$$

where Δx represents the trace intervals and $I_{ps_{out}} = I(x, z; \tau_{ps})$ is the output of the migration using the input wave field $U_{ps_{in}}$, a indicates the migration aperture. Traveltimes from the source position to the scattering point are computed using the discretised background P-wave velocity field while traveltimes from the receiver positions to the scattering points are computed using the discretised background S-wave velocity field. The sum of these two traveltimes give the arrival time of the scattered wavefield as recorded by the receiver. Note that the scattering points can be either a reflection point or any arbitrary diffraction point. I will now demonstrate the implementation of Equation (2.22) by using a constant velocity medium as a simple example for a general background medium.

Assuming a constant P- and S-wave velocity model, prestack depth migration will map a time sample recorded at the time τ and the shot-receiver pair (x_s, x_g) onto a semi-ellipse in depth (Figure 2.2), where the foci of the ellipse are determined by the shot and geophone position. The depth points (x, z) on the ellipse satisfy :

$$\tau_s(x, z) + \tau_g(x, z) = \tau(x, x_s, x_g), \quad (2.23)$$

with τ_s and τ_g being the traveltimes from the depth point to the source and geophone respectively. For non-constant velocity, the ellipse (in 3D it an ellipsoid) becomes distorted; Equation (2.23) will then describe a general curve in the subsurface. The seismic energy from each sample on

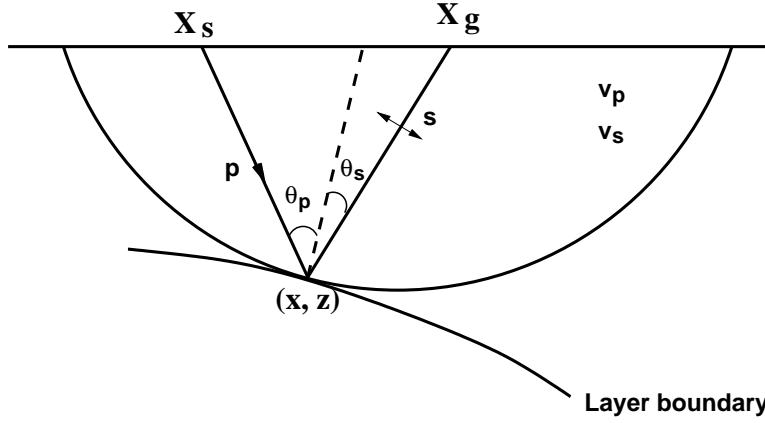


Figure 2.2: Migration maps a data point recorded at time τ with shot at x_s and geophone at x_g onto a semi-ellipse in depth. The shape of the ellipse is determined by the migration velocity model (v_p, v_s) .

each trace (x', τ) is distributed over an array of output points (x, z) in the depth domain. While constructive interference of the values in any particular (x, z) -point gives a strong response, destructive interference gives a weak response in others points. This leads to the reconstruction of reflectors in the resulting image. Note that, on each trace, the sample to be picked at time $\tau(x')$ is chosen according to the computed traveltimes $\tau(x, x_s, x_g)$ given in Equation (2.23). The summation is carried out over all of the traces in the aperture, with the filtered data on each trace picked out at the appropriate time $\tau(x, x_s, x_g)$.

Each common shot gather is migrated individually. The final migrated section is obtained by sorting the migrated common shot gathers into CRP gathers and summing the traces in each CRP gather. Figure 2.3 shows a synthetic example of a migrated PS section. The synthetic data were generated using ray tracing (Seis88) from a model consisting of seven curved interfaces. A description of the model and the data acquisition parameters are given in Chapter 3. After migration with the true velocity models, the six reflectors are properly imaged. Note that due to the limited extent of the illumination area the seventh layer is only partly imaged. Note also the strong migration artifacts on the last two layers. These artifacts are due to the limited extent of the migration aperture.

As mentioned earlier, the computation of traveltimes from the source to the scatterers and back to the receivers is one of the keys issues in Kirchhoff migration algorithms. The accuracy of the traveltimes depend on the traveltimes computational algorithm and on the accuracy of the velocity models. In the next section I will discuss the finite difference eikonal solver method for computing seismic traveltimes and in Chapter 3 I will describe a method for estimating the velocity models.

2.4 Traveltime Computation

Background

For migration purposes traveltimes have to be computed from the source and receiver locations to each grid point in the model. Traditionally, traveltimes are computed by ray tracing (see e.g. Ettrich, 1997; Červený, 2001) and because velocity values and the array of subsurface points are usually distributed on a regular grid, the traveltimes along the rays must be interpolated onto the grid. For complicated velocity models, rays may cross each other. Also, rays may not penetrate shadow zones; the interpolation may then become cumbersome and computationally expensive.

Several other methods have been introduced to compute traveltimes directly on a regular grid. In calculating the depth gradient of traveltimes, Reshef and Kosloff (1986) use a finite difference

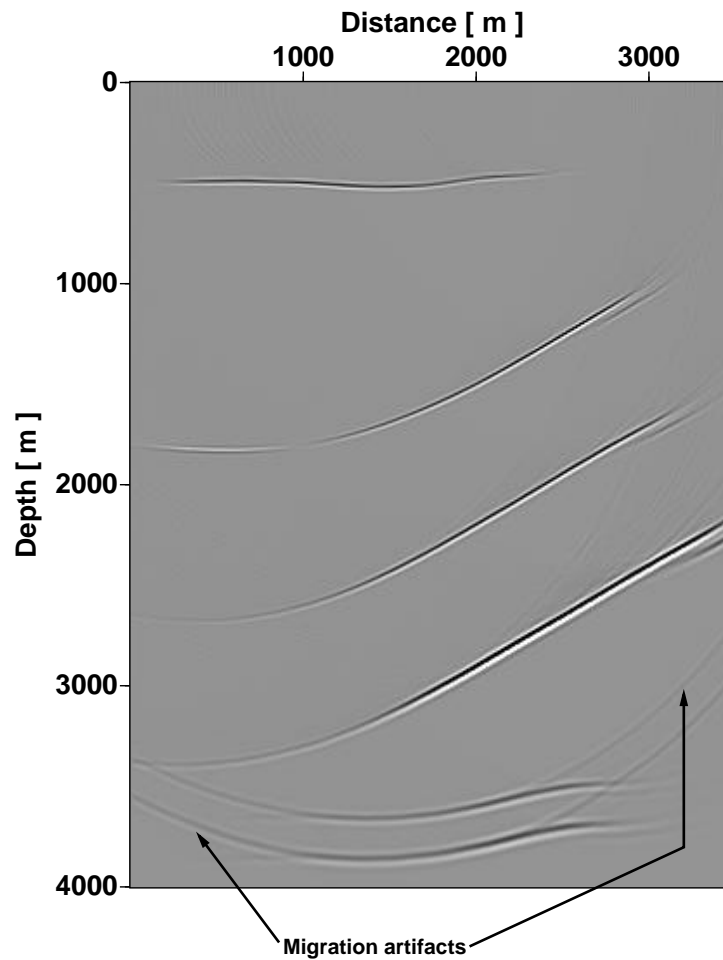


Figure 2.3: Depth migrated PS section using the correct v_p and v_s models. All six reflectors have been properly imaged. The complete lateral extents of the last layers are not reproduced due to the limited illumination of these layers. The migration artifacts are due to the limited extent of the migration aperture.

(FD) approximation to the eikonal equation, which is then integrated with a Runge-Kutta method. Other methods which compute traveltimes directly on regular grid points include wavefront construction methods (Vinje et al., 1993; Ettrich, 1997; Coman and Gajewski, 2001). The advantages and disadvantages of using wavefront construction methods and FD methods have very well been documented and demonstrated by many other authors (e.g. Geoltrain and Brac, 1993; Audebert et al., 1997). In this work I used Vidale's method (Vidale, 1988).

Vidale's method approximates the eikonal equation by finite differences and solves directly for traveltimes at regular grid points using a planar wavefront extrapolation. The traveltime computed by this method is the shortest possible; the first arrival traveltime. This is a property common to all FD methods (Leidenfrost, 1998). For the tomographic application presented in Chapter 3, these first arrival traveltimes are sufficient. An in-depth review of Vidale's scheme is discussed in Vidale (1988). In this section I only describe the relevant FD scheme and the implementation of the perturbation method into Vidale's scheme. I demonstrate the computation of S-wave traveltimes with the perturbation method on a synthetic example. Other examples are given in Menyoli and Gajewski (1999). For a collection of different traveltime computation methods see, e.g. Leidenfrost (1998).

2.4.1 Eikonal Equation

The central formula related to the computation of seismic traveltimes is the eikonal equation and in 2D it follows (Aki and Richards, 1980, Ch. 4):

$$(\nabla\tau)^2 = \left(\frac{\partial\tau}{\partial x}\right)^2 + \left(\frac{\partial\tau}{\partial z}\right)^2 = s^2(x, z), \quad (2.24)$$

where $s(x, z)$ is the 2D slowness model (reciprocal velocity) and $\tau = \tau(x, z)$ is the traveltime field through the slowness model. The slowness model can either be a P-wave model or an S-wave model,⁴ considered here for an inhomogeneous isotropic medium.

2.4.2 Finite Difference Scheme

The 2D Vidale algorithm is based on a calculation scheme of expanding squares, starting at a given source location with a given source velocity. The velocity model is discretised into grid points. Within each square cell wavefronts propagate as plane waves. Because the slowness is perpendicular to the wavefront, the direction of propagation can be estimated, thus the wavefront is known. The actual traveltime computation within a cell (Figure 2.4) is performed with formulas derived from Equation (2.24) by using finite differences.

The partial derivatives in Equation (2.24) are approximated with the second order finite-differences as:

⁴Note that under the assumption of the validity of the HF approximation two independent wave types (P- and S-wave) can exist.

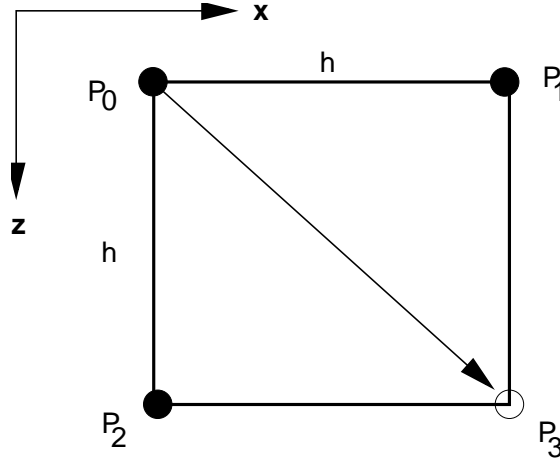


Figure 2.4: Geometry for the main 2D Vidale formula. A ray is considered to propagate from P_0 through the cell to P_3 .

$$\frac{\partial \tau}{\partial x} = \frac{1}{2} \left(\frac{\tau_3 - \tau_2}{h} + \frac{\tau_1 - \tau_0}{h} \right), \quad (2.25)$$

$$\frac{\partial \tau}{\partial z} = \frac{1}{2} \left(\frac{\tau_3 - \tau_1}{h} + \frac{\tau_2 - \tau_0}{h} \right). \quad (2.26)$$

In Figure 2.4, the velocity values are given at grid points and τ_3 , τ_2 , τ_1 , and τ_0 are traveltimes at grid points P_3 , P_2 , P_1 , and P_0 , respectively, and h is the grid spacing. Knowing τ_2 , τ_1 , and τ_0 , the goal is to compute the traveltime τ_3 at grid point P_3 . Inserting equations (2.25) and (2.26) into equations (2.24) gives an implicit FD scheme which is solved for τ_3 :

$$\tau_3 = \tau_0 + \sqrt{2h^2 s^2 - (\tau_2 - \tau_1)^2}, \quad (2.27)$$

with s being the slowness value within the cell under consideration. The slowness value is obtained by linearly interpolating the slownesses at the grid points, $s = (s_0 + s_1 + s_2 + s_3)/4$, and are considered to be constant within each cell. The computation of the traveltime for one cell is usually known as the **local scheme**, while computing traveltimes for all grid points and all cells in the model is usually known as the **global scheme**.

2.4.3 Traveltime Perturbation Method

The motivation for implementing the perturbation method into the Vidale algorithm is to compute traveltimes simultaneously for different velocity models (v_p and v_s). If two velocity models deviate only slightly from one another, then the traveltimes need to be computed only in one model and for the other models, the perturbation theory is applied to obtain their corresponding traveltimes (Ettrich and Gajewski, 1996, 1998). In tomographic model updating, the first arrival traveltimes given by the FD method are usually sufficient. This method increases the computational speed of traveltime tools for applications in tomography and PS prestack velocity estimation. Various v_p and v_s velocity models which cover the range of the most likely velocities of the subsurface are used for the migration.

2.4.3.1 Perturbation equation

Using Taylor series expansion, I express the traveltimes and slowness up to first order as:

$$\tau(x_i) = \tau_o(x_i) + \epsilon_\tau \tau_1(x_i) + \dots \quad (2.28)$$

$$s(x_i) = s_o(x_i) + \epsilon_s s_1(x_i) + \dots \quad (2.29)$$

The symbol ϵ_τ and ϵ_s denote constants $\ll 1$, τ_1 and s_1 are perturbations in traveltimes and slowness, respectively. Substituting equation (2.28) and (2.29) into equation (2.24) and equating terms with the same order leads to:

$$(\nabla \tau_o)^2 = s_o^2, \quad (2.30)$$

$$2(\nabla \tau_o \nabla \tau_1) = s_o s_1. \quad (2.31)$$

Equation (2.30) is the eikonal equation for the traveltimes τ_o in an initial reference medium with the slowness s_o . In equation (2.31), I substitute $\nabla \tau_o = p_i$ (p_i is the slowness vector which is perpendicular to the wavefront) and use the kinematic ray tracing equation that $s_o dx_i / dl_{(o)} = p_i$ (Aki and Richards, 1980). Integrating the result along the initial ray path (l_o) gives:

$$\tau_1 = \frac{1}{2} \int_{l_{(o)}} s_1 dl. \quad (2.32)$$

Equation (2.32) is the first order correction along the unperturbed ray (i.e. the ray through the initial model). In a similar manner, the second order correction can be derived. Next, subtracting τ_o from both sides of equation (2.28) gives the first order difference:

$$\delta\tau = \tau - \tau_o = \tau_{pert} - \tau_{ini}, \quad (2.33)$$

between the traveltimes τ_{ini} in the initial reference medium with velocity $v_{ini} = 1/s_o$ and in a perturbed medium τ_{pert} with velocity $v_{pert} = v_{ini} + \epsilon v_1$ (from $s = s_o + \epsilon s_1$). This first order traveltimes difference can be expressed as:

$$\delta\tau(P, S) = \int_{ref} \left(\frac{1}{v_{pert}} - \frac{1}{v_{ini}} \right) dl, \quad (2.34)$$

with P being a point in the model and S being the source point. The implementation of equation (2.34) in a ray tracing algorithm is straight forward since the corresponding raypaths are already known and the integration follows along these raypaths (see Ettrich and Gajewski, 1996). In the following section the integral in equation (2.34) is implemented into the FD algorithm without any explicit knowledge of the ray path.

2.4.4 Implementation into Vidale's Algorithm

In terms of the FD perturbation, τ_3 computed in equation (2.27) is the reference traveltime at point P_3 (Figure 2.5).

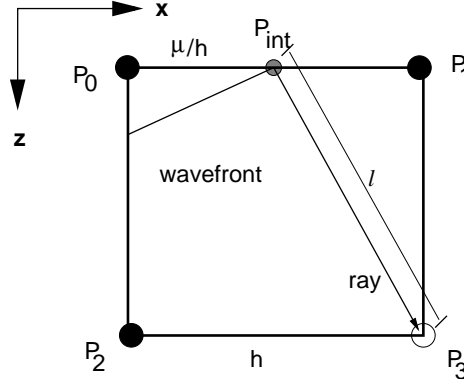


Figure 2.5: Grid cell with known traveltimes at P_0 , P_1 and P_2 . A local plane wavefront is assumed to propagate from P_0 through the cell to calculate τ_3 at point P_3 . The direction of the ray is known from the slowness ($\partial\tau/\partial x$ and $\partial\tau/\partial z$). The length of the corresponding raypath in the cell between the intersection point P_{int} and P_3 is l . The parameters required at point P_{int} for the perturbation are interpolated from neighbouring points P_0 and P_1 with μ being the interpolation factor.

The velocities v_{ini} and v_{pert} are defined at the same grid points. The effective length of the corresponding straight raypath in the cell is denoted as l and let P_{int} be the point of intersection of the plane wavefront at side $\overline{P_0P_1}$. Therefore, within a cell the traveltime difference $\delta\tau'(P_3, P_{int})$ between the medium v_{ini} and v_{pert} can be expressed as:

$$\delta\tau'(P_3, P_{int}) = \left(\frac{1}{v_{pert}} - \frac{1}{v_{ini}} \right) l, \quad (2.35)$$

whereby all the parameters required in equation (2.35) are constant along the ray. Equation (2.35) is the local traveltime difference within the cell. It is the contribution to equation (2.34) of the ray segment within the cell. Therefore, the total traveltime difference at P_3 from the source, S , is given as the sum of the local traveltime difference and the traveltime difference from the source to the point P_{int} ($\delta\tau(P_{int}, S)$). This sum is given as:

$$\delta\tau(P_3, S) = \delta\tau(P_{int}, S) + \delta\tau'(P_3, P_{int}), \quad (2.36)$$

and $\delta\tau(P_{int}, S)$ is obtained by linear interpolation of $\delta\tau$ between the neighbouring points P_0 , and P_1 or P_0 and P_2 . Note, that it is important to consider from which side of the cell the plane wave enters into the respective cell (i.e. $\overline{P_0P_1}$ or $\overline{P_0P_2}$; $\tau_1 < \tau_2$ or $\tau_1 > \tau_2$). In Figure 2.5 the wave enters the cell at side $\overline{P_0P_1}$. However, if τ_2 is smaller than τ_1 , then the plane wave will enter the cell at side $\overline{P_0P_2}$ and P_{int} will be situated between P_0 and P_2 . The ray enters the cell from the side with the minimum traveltime as required by the Vidale's scheme. As shown in equation (2.33) the perturbed traveltime τ_{pert} at P_3 is now given by:

$$\tau_{pert}(P_3, S) = \tau_{ini} + \delta\tau(P_3, S). \quad (2.37)$$

The ray segment within each cell can be approximated as $l = \frac{h}{v_{ini}p_z}$ if $\tau_1 < \tau_2$ (Ettrich, 1997), with p_z being the z -component of the slowness. Inserting the ray segment into equation (2.35) gives:

$$\delta\tau' = \frac{2h^2}{v_{ini}} \left(\frac{1}{v_{pert}} - \frac{1}{v_{ini}} \right) \frac{1}{t_z}, \quad (2.38)$$

where $t_z = 2p_z h$. t_z as well as t_x are obtained from the traveltimes τ_o , τ_1 , τ_2 and τ_3 :

$$t_x = (\tau_1 - \tau_o) + (\tau_3 - \tau_2), \quad (2.39)$$

$$t_z = (\tau_2 - \tau_o) + (\tau_3 - \tau_1), \quad (2.40)$$

which are known from application of Vidale's method.

2.4.4.1 Implementation into the Global Scheme

Figure 2.6 shows how the local scheme described above is embedded into the global scheme. Black circles indicate points where traveltimes and traveltime differences are already known. The computation continues for the outer gray shaded grid points. Assuming the traveltimes for the grid points around the source have been computed, then the solution continues by solving for grid points at increasing radius around the source. As an example, the traveltimes of the four corner points (labelled A_1 , A_2 , A_3 and P_o) are computed from the times of their neighbours. Traveltimes at each side of the proceeding computational square are extrapolated onto the corresponding current side separately; the current sides are connected by the final computation of traveltimes at the four corner points. Because the computation is carried out along wavefronts, it is not necessarily causal. The algorithm will fail for velocity contrasts larger than $1 : \sqrt{2}$ in 2D and even only $1 : \sqrt{3/2}$ in 3D. This means that, e.g., head waves or turning rays (in case of a smooth model) with an angle $< 45^\circ$ to the vertical axis are not properly handled (Vidale, 1988). Therefore, to guarantee stability Vidale (1988) implements an alternative formula. For this purpose, points of the preceding sides with minimum traveltimes are considered first. If A_3 (Figure 2.6) is such a point, and assuming a plane wavefront approximation between P_o and A_4 , a modified noncentered finite difference version of equation (2.27) is obtained (Vidale, 1988):

$$\tau_{A_5} = \tau_{A_3} + \sqrt{(h/v_{ini})^2 - 0.25 (\tau_{P_o} - \tau_{A_4})^2}, \quad (2.41)$$

with τ_{A_3} being the minimum time, τ_{P_o} and τ_{A_4} are the times on either side of τ_{A_3} . Velocities v_{ini} (and for the perturbation method also v_{pert}) are obtained by averaging values of the two cells separated by $\overline{A_3 A_5}$ and $\overline{A_3 A_4}$. Applying the perturbation equations (2.33) and (2.34), the

intersection point P_{int} is between P_o and A_4 . With known traveltime quantities at A_5 , the local scheme is successively applied to its neighbours.

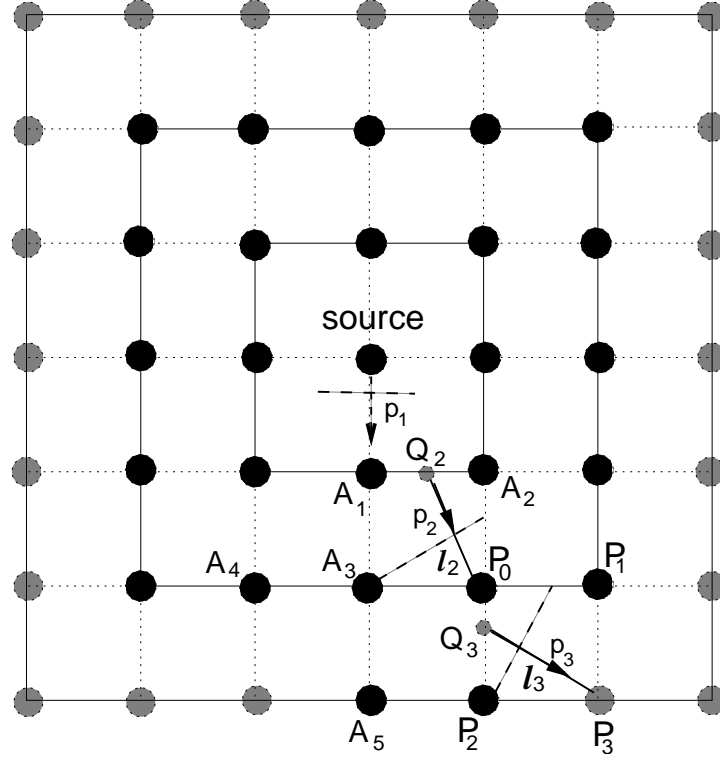


Figure 2.6: Computational scheme of expanding squares starting from the source. Traveltimes at black circles are assumed to be known. The interpolated values at points Q_i are added to the local values $\Delta\tau'$ along the ray paths l_i . This sum gives the traveltime difference $\Delta\tau$ at the point P_3 . \mathbf{p}_i are the slowness vectors.

Therefore, following equation (2.41) the reference traveltime in P_3 is determined by the reference traveltimes at P_o , P_1 , and P_2 . Vector $\overline{\mathbf{s}_3}$ is the slowness vector of the local plane wavefront passing through P_3 and intersecting side $\overline{P_oP_2}$ in Q_3 . The local traveltime difference between the perturbed and the initial reference model is, thus, given by equation (2.35) with $l = l_3$ and the total traveltime difference in P_3 given by equation (2.37), where $\delta\tau(Q_3)$ is obtained by interpolating between $\delta\tau(P_o)$ and $\delta\tau(P_2)$. The traveltime differences are computed for each cell before moving to the next cell. Note that, for a set of perturbed models the ray segment in each cell is computed only once. Depending on the structure of the model, there may exist points where computation of initial traveltimes would usually stop due to acausality. This occurs generally, if rays point into inner computational squares and result in negative arguments of square roots in equation (2.41). However, Ettrich and Gajewski (1998) showed how the computation can still be forced for such cases.

2.4.4.2 Computing S-wave traveltimes

I use the perturbation technique described above for a simultaneous computation of S- and P-wave transmission traveltimes. Note that for a constant v_p/v_s -ratio the transmission P- and S-waves

propagate along the same ray path (see Appendix B).

In order to run the simultaneous algorithm, I first consider to have a range of v_p/v_s -ratio models. Next, I assume that the true v_p/v_s -ratio ($\gamma(\mathbf{x})$) deviates only slightly from an average value γ_{ave} . This difference is $\delta\gamma$, i.e. $\gamma = \gamma_{ave} + \delta\gamma$. Since P-wave velocities are often better known than S-wave velocities, I scale the P-wave model with the initial γ_{ave} of the whole model to obtain a reference model ($v_{ref} = v_p/\gamma_{ave}$). This model is the reference model used for S- as well as for P-wave perturbed models. This initial reference model determines the ray paths of the S-wave which is the same as in the P-wave model. Now, other possible S-wave models are considered as perturbed models with:

$$v_{pert} - v_{ini} = \frac{(\gamma - \delta\gamma)v_s - v_p}{\gamma_{ave}} = \left| \frac{v_s\delta\gamma}{\gamma_{ave}} \right|. \quad (2.42)$$

The P-wave traveltimes in the reference model are obtained by scaling the reference traveltimes by γ^{-1} .

2.4.5 Example

The example illustrates the traveltime computation for a 2D gradient model with a parabolic lens in the centre. The values of the model are P-wave velocities. First, the model is multiplied with an average v_p/v_s -ratio of $1/\sqrt{3}$ to give the reference S-wave model. Next, I perturbed the S-wave velocity model in the lens by 10% of its original value. The S-wave velocities around the lens are kept unchanged. In this way I introduced a vertical as well as a lateral change in the v_p/v_s -ratio in the model.

The model dimension is 0.6 x 0.6 km and it consists of 301 x 301 grid points arranged in a rectangular grid with 2 m grid spacing. The source is located at 0.3 km on the surface of the model. In the unperturbed lens $v_p = 1.0$ km/s and $v_s = 0.58$ km/s, while in the perturbed lens $v_p = 1.0$ km/s and $v_s = 0.52$ km/s and the surrounding P- and S-wave velocities are unchanged with the initial S-wave velocity being $v_{s_{ini}} = 1.15$ km/s. Figure 2.7 shows the gradient model and traveltime contour lines computed using Vidale's method for the reference S-wave model. The FD perturbation algorithm is applied to compute S-wave traveltimes in the perturbed model. I also computed S-wave traveltimes in the perturbed model directly using Vidale's method and compared the relative errors. Figure 2.8 shows the absolute value of errors in [%]. Overlaid on the error plot are directly computed traveltime isochrons (white lines) and isochrons computed by perturbation (dashed lines). The relative errors range from 0.0 – 1.0%.

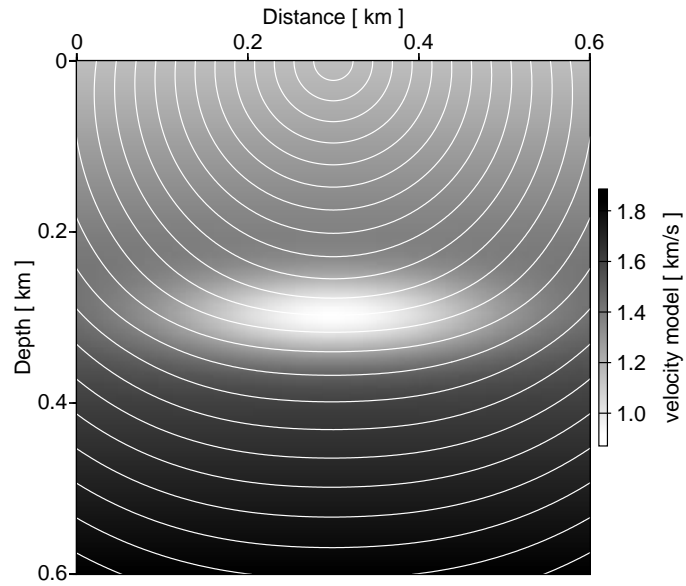


Figure 2.7: A 2D constant gradient S-wave velocity model with a parabolic lens at the centre (used as reference model). Overlaid are traveltimes isochrons directly computed using a 2D-Vidale FD-algorithm

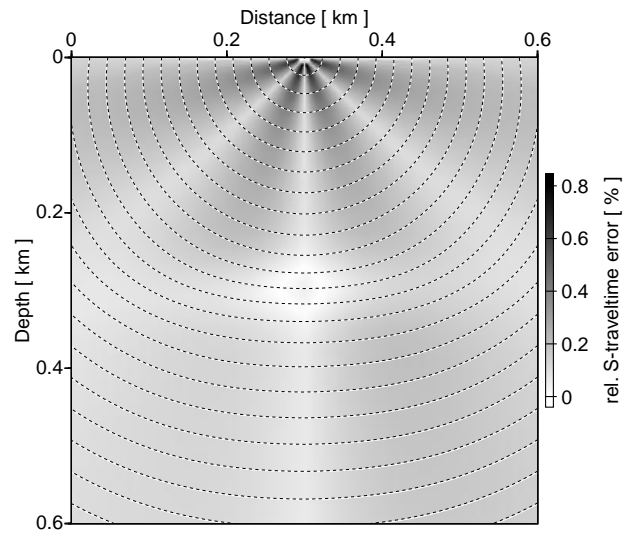


Figure 2.8: Absolute values of the relative error [%] of directly computed traveltimes using the FD-method and the FD-perturbation method for a perturbed S-wave velocity model. Overlaid are the directly computed traveltime isochrons (white lines) and the isochrons computed by perturbation (dashed lines).

2.4.5.1 Limitations

The main limitation of using perturbation methods in traveltime computation comes from the general limitations in using FD methods for computing traveltimes. FD methods compute only first arrival traveltime fields. However, in complex geology, reflection events can be multi-valued, having triplications. The recorded seismic energy can come from the later arrivals and not only from the first arrivals. In such a situation, using maximum energy arrival or multivalued arrival algorithms such as the wavefront construction (WFC) methods can provide more appropriate results.

In FD methods, the choice of the computational front poses another limitation: the solution evolves in time, but it is computed by rectangular fronts that expand in space. If the time field to be computed does not have an outward-pointing gradient at each front i.e., if the time gradient becomes parallel to the computational front (a turned ray), then the calculations stop.

Another limitation is the use of first order perturbation. The effect of considering a linear relation i.e., first order for the velocity variation rather than the more accurate nonlinear form will generally result in a slight decrease of accuracy. Furthermore, if the velocity variation deviates substantially from the reference value, then raypaths will deviate and the perturbation principle will break down.

2.4.6 Migration Velocity Analysis

After describing the traveltime computation tools, the next step is to use them for PS migration velocity analysis. PS prestack depth migration will construct an accurate image if accurate background velocities are known. Usually, the correct background model is hardly known. This section describes how I can use the FD perturbation algorithm described above to estimate the velocity models.

The simultaneous computation of traveltimes from more than one model allows to estimate the best velocity model which gives optimum flat PS CRP gathers. First, a background S-wave velocity model is defined as $v_{s_o}(\mathbf{x}) = \gamma_{ave}^{-1} v_p(\mathbf{x})$, with γ_{ave} being constant. This model is used as a reference model for computing S-wave and P-wave traveltimes. The v_p model can be obtained from PP data analysis, and γ_{ave} can be obtained from time domain analysis. Note, that the v_p model used in PP migration need not be the same v_p model to be used in migrating PS data. However, in this example I assume it is the same.

Next, the velocity field is expressed as the sum of the smooth background velocity field v_{s_o} and a small-scale perturbation δv_s . I describe a set of small scale perturbations δv_{s_i} such that $i = 1, \dots, n$ with n being the total number of perturbed models. Therefore, the current migration velocity is given as $v_{s_i}(\mathbf{x}) = v_{s_o}(\mathbf{x}) + \delta v_{s_i}(\mathbf{x})$. The model perturbation can be performed at any place in the model as required necessary. Using the background velocity models $v_p(\mathbf{x})$, $v_{s_o}(\mathbf{x})$ and $v_{s_i}(\mathbf{x})$, for every source s_i , I obtain a prestack depth migrated image. The PS CRP gathers selected at surface locations for each $v_{s_i}(\mathbf{x})$ model are analysed. The desired $v_s(\mathbf{x})$ value is the one which

best flattens the corresponding events on the analysed CRP gather.

After the migrated CRP gathers are formed at the selected surface location, v_s (as a function of depth, z_{ps}) is picked, based on the flatness of each event. If v_s is too low, the events curve upwards as the offset increases. If v_s is too high, the events curve downwards. v_s can also be assessed by using the ensembles of perturbed gathers to create a velocity spectrum (e.g. semblance) from which the update velocities with depth can be picked directly. The initial model $\gamma_{ave}^{-1}v_p$ can also be used for computing new P-wave traveltimes for other ranges of v_p values in the same run. The P-wave traveltimes in the initial reference model are obtained by just scaling the reference traveltimes by γ_{ave}^{-1} . In this way both v_p and v_s can be updated. A similar method called common conversion point scan (CCP scan) was introduced by Audebert et al. (1999).

This method of estimating migration S-wave velocity is accurate if the background velocity model depends only on depth, i.e., the model in the survey area has only little or no lateral variations. In Chapter 3, I will show that flat events in PS CRP gathers do not necessarily imply that the migration v_s model is correct. However, the S-wave velocity model estimated by the described method can nevertheless be used as an initial model for the tomographic model updating.

Chapter 3

Shear Wave Velocity Estimation

3.1 Introduction

So far, I have discussed how to perform PS and PP prestack depth migration using the Kirchhoff formalism and traveltimes computation methods. After depth migration, CRP gathers are sorted for migration velocity analysis purposes. CRP gathers contain traces that sample the same subsurface area. Bearing in mind the discrepancies due to limited coverage, noise problems, shadow zones, AVO effects (Castagna, 1993), etc, the traces in a migrated CRP gathers, which are images of the subsurface, should be identical to each other if the migration velocities are correct, i.e., all events should appear at the same depth. In reality they hardly ever are, because the velocity models needed for the migration of the sections are inaccurate; the migrated gathers are therefore incorrectly positioned. For PS depth migration in addition to v_p , an accurate interval v_s is required. However, P-wave migration velocity analysis can be performed from PP data.

The analysis of migrated PS and PP CRP gathers reveals the correctness of the shear wave velocity model. As discussed in Chapter 1 I assume that the P-wave velocity model is known and that the mode conversion occurs at the same horizon. PS migration with incorrect S-wave velocity model gives incorrect depth positions of the PS CRP gathers as compared to the PP CRP gathers even if the PS CRP gathers are flat. This observation serves as the basis for the inverse problem: how to find the correct S-wave velocity model to use in migrating the PS data such that PS and PP CRP gathers will have the same depth position. In this chapter a tomographic inversion is formulated to solve this problem. The inversion is formulated as an interactive optimisation process, in which success in the optimisation is measured by a function that quantifies discrepancies in depth between PS and PP CRP gathers. The objective function is calculated after reflection events have been converted to time differences. I start this chapter by describing how I parameterise the velocity model. I then discuss the objective function, after which I present the optimisation scheme itself. Because the method requires interpretation of geologic horizons, I discuss geological constraints and the problem of finding a structural velocity model.

3.2 Model Parameterisation

When a PS ray travels through several structures in the Earth, its traveltime is an integral measure of v_p and v_s velocities in the structure that the ray encounters. Resolving the exact velocity of a structure from PS traveltime observations therefore, requires that the structure is penetrated by a large number of rays over a wide range of angles. In PS reflection, where the S-ray branch travels nearly vertically and for the short spread limit such a situation is highly unlikely.

In view of this limitation, I choose to parameterise the v_s velocity model by 2D cubic spline functions that are intrinsically smooth. The depth model is considered to consist of N regions. Inside each region velocity is a smooth varying function. The interpolation function is built as the tensor product of basic spline functions $f_i(x)$ and $g_j(z)$ (Inoue, 1986) as:

$$v_s(x, z) = \sum_{i=0}^3 \sum_{j=0}^3 c_{ij} f_i(x) g_j(z), \quad (3.1)$$

where c_{ij} are spline coefficients. The local velocity values are given at equidistantly spaced nodes, while the values between the nodes are interpolated. Figure 3.1 shows an illustration of parametrising a model in regions and nodes. For a practical implementation the distance between two nodes is chosen to be equal to the shot receiver spacing. Since the reflector structure is known from the

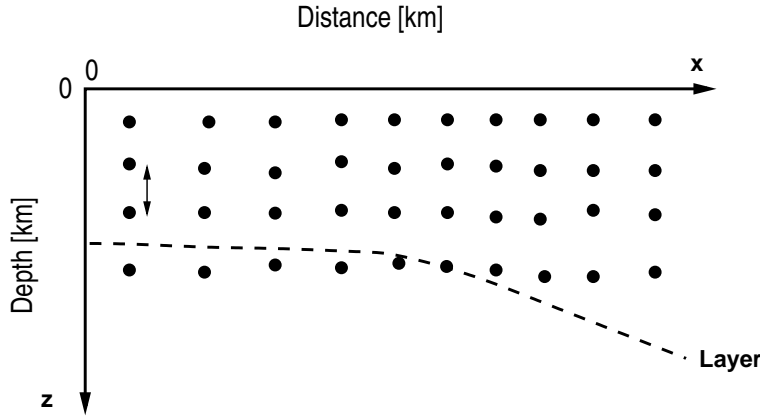


Figure 3.1: Subsurface region and its discretisation into nodes. The arrow shows the distance between two nodes.

interpretation of the PP data, only the velocity values are interpolated from values at the node points.

3.2.1 Parametrising Horizons ?

Many tomographic methods try to invert for the depth interfaces apart from the velocity model (Bishop et al., 1985; Stork and Clayton, 1987; Williamson, 1990; Kosloff et al, 1996). I choose not to parametrise both velocity and depth in the optimisation. Instead, I obtain the reflector depths from a previous migrated PP data and use them only in the computation of the back projection operator.

Avoiding the use of reflector depths as model parameters in the inversion has some advantages. First, specifying horizons and velocity contrasts without any information other than seismic traveltimes may be unwarranted because this can make the inversion algorithm unstable. Second, both velocity and depth of a structure control the position of a reflector after migration. This velocity-depth ambiguity can lead to instabilities and non-convergence of the solution in the optimisation (Stork and Clayton, 1991). Finally, velocity and depth are two different physical parameters that need to be scaled differently in the optimisation. The scaling factors are not straight forward to be determined in advance.

3.3 Linearisation of the PS Traveltime Equation

In ray theory, the reflection of a PS-wave is divided into two ray branches; the P-ray branch traveling from the source to the reflector with the compressional velocity, v_p , and the reflected S-ray branch traveling from the reflector to the receivers with the shear velocity, v_s (Figure 3.2).

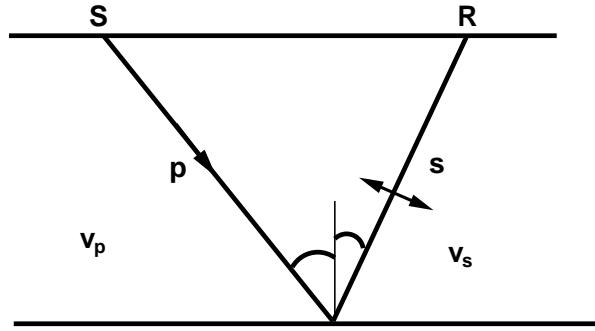


Figure 3.2: Schematic sketch of a PS ray which begins at the source S as a P-ray traveling with the velocity v_p and is reflected at the interface and travels with the velocity v_s to the receiver at R as an S-ray.

The total transient traveltimes associated with the ray can be expressed as a function of integrated velocities:

$$t_{ps}(\mathbf{x}) = \int_{R_p} \frac{1}{v_p(\mathbf{x})} dl_p + \int_{R_s} \frac{1}{v_s(\mathbf{x})} dl_s, \quad (3.2)$$

where R_p and R_s denotes the integral along the P-raypath and S-raypath respectively, \mathbf{x} is the position vector and dl_p and dl_s are the differential distances along the raypaths. Because migrated image positions depend on the traveltimes of the ray, Equation (3.2) shows that the migrated image position and focusing of the image are sensitive to changes in the v_p and v_s . A change in v_p with constant v_s will change the image position, or a change in v_s with constant v_p or both concordantly will change the migrated image positions. Because I assume that v_p is already known from the PP section therefore, only a change in v_s will be considered to affect any change in the migrated image position.

The S-raypath, l_s , in Equation (3.2) depends on the unknown v_s field. However, like in standard reflection/transmission tomography (e.g., Bishop et al., 1985; Chiu and Stewart, 1987; Stork and Clayton, 1991), Equation (3.2) can be linearised about some initial or reference value. That is instead of solving Equation (3.2) for v_s , I solve an approximation to Equation (3.2) for the perturbation in v_s from an initial model. Next, I assume that an initial shear wave velocity model (v_{s_o}) is known and that this model is close to the true model. The PS traveltimes in the initial and a perturbed S-wave model ($v_{s_{pert}}$) are expressed as:

$$t_{ps_o}(\mathbf{x}) = \int_{R_p} \frac{1}{v_p(\mathbf{x})} dl_p + \int_{R_{s_o}} \frac{1}{v_{s_o}(\mathbf{x})} dl_s, \quad (3.3)$$

$$t_{ps_{pert}}(\mathbf{x}) = \int_{R_p} \frac{1}{v_p(\mathbf{x})} dl_p + \int_{R_{s_{pert}}} \frac{1}{v_{s_{pert}}(\mathbf{x})} dl_s. \quad (3.4)$$

The difference between the PS traveltimes computed in the perturbed and the initial model is given in a discrete form as:

$$\delta t_{ps}(\mathbf{x}) = \mathbf{D} \delta \mathbf{u}_s, \quad (3.5)$$

where $\mathbf{u} = 1/v_s(\mathbf{x})$ is the slowness (reciprocal velocity) and $\delta \mathbf{u}$ is the vector whose components are the differences in shear wave slowness between the perturbed and initial model along the individual raypath, and $\delta t_{ps}(\mathbf{x})$ is the vector of traveltimes deviations. \mathbf{D} is a matrix whose elements are the derivatives of the CRP ray traveltimes with respect to the model parameter (v_s). In this study, I estimate this matrix using ray tracing. Note that Fermat's principle is applied to account for the difference in raypaths in the initial and the perturbed models. Equation (3.5) is the linearised version resulting from Equation (3.3) and (3.4). It can also be used in prestack PS reflection tomography.

For tomographic inversion Equation (3.5) requires the knowledge of δt_{ps} , which is the function to be minimised. However, after prestack depth migration I do not directly have δt_{ps} . Instead I observe changes in depth positions of PS CRP gathers. Therefore, in the next section, I describe the function to be minimised and show to convert the depth perturbations to δt_{ps} . Instead of using slowness, I will continue to use v_s because geophysicists make use of velocity and not slowness.

3.4 Objective Function

If the v_s migration model is not correct, the same reflector will appear at different depth positions on PS and PP sections (Figure 1.2). In principle, I determine the differences between the PS and PP migrated depths of the reflector at each offset and surface location and translate these depth perturbations (depth shifts) into velocity perturbations in the inversion method. I will consider the depth of the reflector from the P-wave migrated section as the true depth z_{tr} . At each surface location x_r , the depth shifts δz_r can vary as a function of offset (h) and velocity:

$$\delta z_r(x_r, h; v_s(\mathbf{x})) = z_{tr}(x_r) - z_r(x_r, h; v_s(\mathbf{x})), \quad (3.6)$$

where z_r is the PS migrated reflector depth as a function of surface location, offset, and migration S-wave velocity, $v_s(\mathbf{x})$. Note that the PS and the PP reflections are assumed to originate from the same horizons. Therefore, the function to minimise is $\delta z_r(x_r, h; v_s(\mathbf{x}))$

3.4.1 Conversion of Depth Errors to Traveltime Errors

In the standard reflection tomography, traveltime perturbations from an arrival between the prestack data and that predicted from a reference model are input to Equation (3.5) and the traveltimes are then optimised. Instead of optimising traveltimes, I optimise depth shifts of the PS CRP gathers. Therefore, I call the method *depth shift tomography* of PS data in order to emphasis that I minimise perturbations in depths instead of traveltime perturbations. To use the depth shifts in tomography I have to convert δz to δt_{ps} . Figure 3.3 shows a schematic of the vicinity of a reflection point of a PS ray showing the quantities needed for converting depth shifts to traveltime perturbations. From this figure the traveltime perturbation can be deduced as:

$$\delta t_{ps}(\mathbf{x}) = \delta z \left(\frac{\cos(\theta_p - \phi)}{v_p(\mathbf{x})} + \frac{\cos(\theta_s + \phi)}{v_s(\mathbf{x})} \right), \quad (3.7)$$

$$= \delta z (p_{zp} + p_{zs}), \quad (3.8)$$

where ϕ is the angle of the reflector slope; θ_p and θ_s are the angles of incidence and reflection of the ray on the reflector measured against the reflector's normal; p_{zp} and p_{zs} are the vertical slownesses of the P- and S-ray branches. To compute δt_{ps} , rays need only to be traced to compute

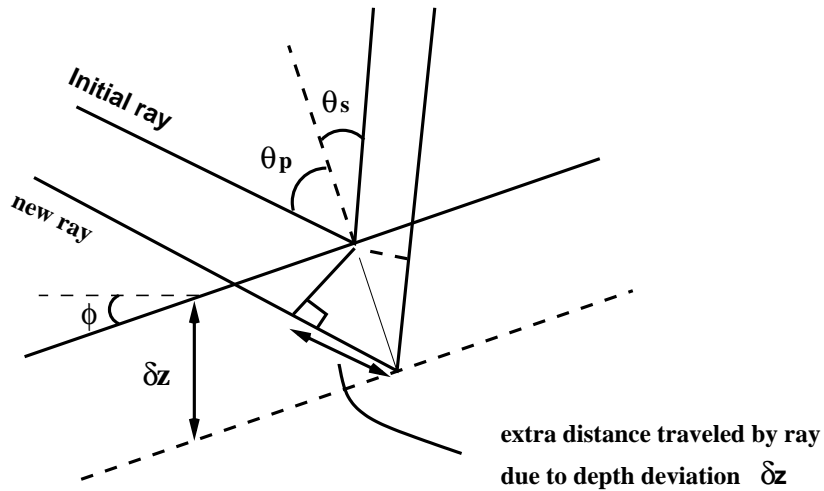


Figure 3.3: Ray diagram for PS wave reflection tomography, showing how changing the traveltime along two rays moves their specular reflection point. Traveltime is the integral of slownesses along the raypath, so the P- and S-wave velocity values along an entire raypath joining the source and receiver with an image point influence the image. The δz perturbation values from PS CRP gathers in the vicinity of the reflector are converted to δt_{ps} perturbation values used by reflection tomography, following Fermat's principle.

the $\tilde{\mathbf{D}}$ matrix. These rays correspond to the path taken by the arrivals on the traces of the CRP gathers. For this purpose I use the ray tracer as described by Červený and Pšenčík, (1984).

3.4.2 Minimising the Objective Function by Least Squares

The goal of the optimisation is to minimise perturbations in depths. As shown in Section 3.4.1, the depth shifts have been converted to time perturbations, therefore, I minimise $\delta t_{ps}(\mathbf{x})$. Note that from Figure 3.3, $\delta t_{ps}(\mathbf{x})$ is the difference in traveltimes between the old ray t_{ps_o} in the initial model and the new ray $t_{ps_{pert}}$. A common choice for the objective function, J , to be minimised is the Euclidean or L_2 -norm of the perturbations:

$$J(v_s(\mathbf{x})) = \sum_{x_r, h} |\delta t(x_r, h; v_s(\mathbf{x}))|^2 = \sum_{x_r, h} |t_{true}(x_r) - t_{pert}(x_r, h; v_s(\mathbf{x}))|^2. \quad (3.9)$$

In this equation I denote $t = t_{ps}(\mathbf{x})$. The problem of finding a solution that minimises this L_2 -objective function is called a **least-squares problem**, and its solution is named the least-squares solution.

A first step towards finding the least-squares solution is to linearise equation (3.9) with respect to the model parameter, $v_s(\mathbf{x})$. Assuming small model perturbations $\delta v_s(\mathbf{x})$, the objective function can be evaluated for a perturbed model $v_s(\mathbf{x}) + \delta v_s(\mathbf{x})$ since the problem is linearised around the correct solution v_s (for clarity I drop out the vector \mathbf{x}):

$$\begin{aligned} J(v_s + \delta v_s) &= \sum_{x_r, h} |t_{true}(x_r) - t_{pert}(x_r, h; v_s + \delta v_s)|^2 \\ &= \sum_{x_r, h} \left| t_{true}(x_r) - t_o(x_r, h; v_s) - \frac{\partial t_{pert}(x_r, h; v_s)}{\partial v_s} \delta v_s \right|^2 \\ &= \left\| \delta t - \tilde{\mathbf{D}} \delta v_s \right\|^2, \end{aligned} \quad (3.10)$$

$\delta t(\mathbf{x})$ is a vector consisting of the traveltimes perturbations $\delta t(x_r, h; v_s(\mathbf{x}))$; if N is the number of CRP locations, then $r = 1, N$; $\|\cdot\|$ denotes the vector norm. $\tilde{\mathbf{D}}$ is an $N \times M$ matrix, with M the number of model parameters (i.e. number of cells in the model). Note, that generally the model parameters are the velocity and the reflector positions. Because I do not parameterise the reflector positions the only model parameter is v_s . The elements of $\tilde{\mathbf{D}}$ are the first-order derivatives of traveltimes with respect to the model parameter:

$$\tilde{\mathbf{D}}_{rc} = \frac{\partial t(\mathbf{x})}{\partial v_s}, \quad (3.11)$$

$$r = 1, N; \quad c = 1, M$$

A row of the matrix $\tilde{\mathbf{D}}$ is calculated for each CRP point, hence the index r . To be consistent, I index each column by c . The matrix $\tilde{\mathbf{D}}$ is also called the backprojection operator because it projects perturbations in traveltimes back onto the model. Because I do not consider traveltimes changes due to horizon movements, the backprojection operator consists only of derivatives of traveltimes with respect to the model parameter, v_s , for a fixed reflector position. This is very similar to traditional tomography, in which reflector positions normally are assumed to be fixed (Chiu and Stewart, 1987). Bishop et al. (1985) showed that this gradient operator is equal to the raypath of the i -th ray in the j -th cell. The raypaths are computed by tracing rays through the initial reference model from shot locations through the conversion points to the receiver locations.

To find the least-squares solution δv_s that minimises J , I solve $\partial J / \partial v_s = 0$, which yield the normal equations:

$$\tilde{\mathbf{D}}^T \tilde{\mathbf{D}} \delta v_s(\mathbf{x}) = \tilde{\mathbf{D}}^T \delta t(\mathbf{x}). \quad (3.12)$$

In a general case the effect of changes in reflector position on the traveltimes perturbation should be taken into account and reflector interfaces must also be parameterised. Nevertheless, a method for including this is given in Stork and Clayton (1991) and Kosloff et al. (1996).

3.4.3 Damped Least-Squares

In practice, Equation (3.12) is often under-determined (Chiu and Stewart, 1987) and the least-squares problem usually must be damped in order to update the model parameter. This damping can be done by computing the least-squares of a modified system of equations:

$$\begin{pmatrix} \tilde{\mathbf{D}} \\ \tilde{\mathbf{K}} \end{pmatrix} \delta v_s(\mathbf{x}) = \begin{pmatrix} \delta t(\mathbf{x}) \\ \mathbf{0} \end{pmatrix}, \quad (3.13)$$

where $\tilde{\mathbf{K}}$ is a damping matrix. The least-squares solution of this system minimises:

$$\left\| \delta t(\mathbf{x}) - \tilde{\mathbf{D}} \delta v_s(\mathbf{x}) \right\|^2 + \left\| \tilde{\mathbf{K}} \delta v_s(\mathbf{x}) \right\|^2 \quad (3.14)$$

(Tarantola, 1984). $\tilde{\mathbf{K}}$ adds a penalty term to the objective function, and can thus be used to constrain the model according to a priori knowledge. $\tilde{\mathbf{K}}$ is often called the model-covariance matrix.

3.4.4 Iterative Optimisation Scheme

The back projection operator described above is used in an optimisation scheme that iteratively updates the velocity model until the depth shifts are minimised. The algorithm consists of two main loops and is displayed in the scheme below.

The input to the inversion is a set of common reflection points, picked depth shifts, v_p and an initial v_s model (the same model that is used in the initial migration), and damping matrix \mathbf{K}_{\sim} (see section 3.4.5.1, page 41).

Input:

1. CRP locations along the horizons
2. picked depth shifts
3. v_p and initial v_s model
4. Geological constrains: damping matrix $\tilde{\mathbf{K}}$

```
{
  Migrate the data with  $v_p$  and initial  $v_s$  model
  Check for convergence: no remaining depth shifts -> done; if yes
  Pick depth deviations    }
  For each surface CRP location {
    DO {
      Determine traveltimes perturbations  $\delta t_{ps}(\mathbf{x})$ 
      Compute row of matrix  $\tilde{\mathbf{D}}$ 
    }
  }
```

Inner loop: DO {

```
  Invert for  $\delta v_s(\mathbf{x}) = \left( \tilde{\mathbf{D}}^T \tilde{\mathbf{D}} + \tilde{\mathbf{K}}^T \tilde{\mathbf{K}} \right)^{-1} \tilde{\mathbf{D}}^T \delta t_{ps}(\mathbf{x})$  using conjugate gradient method
  Update model:  $v_s = v_s + \delta v_s$ 
```

```
} until convergence in  $v_s$ 
```

Outer loop:

```
{ For each shot and receiver location around target zone compute traveltimes and repeat migration }
```

Output:

1. Updated v_s model
2. Updated v_p/v_s -ratio
3. PS migrated section

The algorithm consists of two major parts: in the first part, model perturbations are determined by an inversion of the gradient operator. The perturbations in the model are found by solving the damped system of equations (3.15) by least-squares:

$$\delta v_s(\mathbf{x}) = \left(\tilde{\mathbf{D}}^T \tilde{\mathbf{D}} + \tilde{\mathbf{K}}^T \tilde{\mathbf{K}} \right)^{-1} \tilde{\mathbf{D}}^T \delta t_{ps}(\mathbf{x}) \quad (3.15)$$

The inverse matrix in the expression (3.15) is not explicitly calculated; instead I use a conjugate gradient method to find the least-squares solution. I use the conjugate gradient routine of Paige and Saunders (1982). In the second part, the data is re-migrated with the updated v_s model, and depth shifts in CRP gathers are picked again until convergence is achieved.

3.4.4.1 Stopping criteria

A final aspect of the inversion algorithm is the stopping criterium. I use an empirical approach based on observations. The convergence criterion is given as:

$$C = 1 - \frac{\Delta z^2}{z_{tr}^2}, \quad (3.16)$$

where z_{tr} is the true depth position of the reference PP CRP gather and Δz is the depth shifts between PS and PP CRP gathers. The coefficient C is 1 if PP and PS image depths are equal. For any other velocity model, the coefficient is less than 1. Therefore, I stop the iteration for values of C close to 1.

3.4.5 Structural Velocities

Traveltime or moveout analysis (tomography, normal moveout) can determine only the long wavelength component of the velocity model. These models are generally smooth. However, a smooth velocity model can sometimes limit the interpretation of the migrated data because interpretation is usually easier in a structural velocity model that can directly be related to geological features in the seismic image. In addition, finding a structural model and locating boundaries is important for exploration targets.

Given that tomography can determine only smooth velocity models, information about structural velocities has to come from other sources. If the PP migrated section is already interpreted then the interpretation of the v_s model and the PS section can be straight forward.

If available, well logs probably provide the most important source of information. In most cases well logs allow the determination of reflector depths and velocities of major stratigraphic structures. Furthermore, they reveal the lithology of sediments in the region. This is a knowledge that is useful in interpreting seismic data away from the well location, and in constructing a structural velocity model.

If no well logs are available, the seismic image itself provides a good base in deriving a structural model. Although structural boundaries may be mispositioned after depth migration, the image is generally focused enough so that major structures can be identified. For example, salt structures are normally easy to recognise on the migrated image, and the velocity of salt formations in certain sedimentary basins is often known. How structural models are used in migration and interpretation is discussed in details in the second part of this thesis (Chapter 9).

Finally, general geological knowledge does help to shape the structural model. Examples are constraints on fault dip, section balancing, basin reconstruction, etc. Structural geological maps of the near surface outcrop structures can be very helpful in constraining seismic models since seismic images of the near surface are hardly present. However, most of the techniques employed in the field of geological balancing determine structural models by trial-and-error: they forward model the deformation of an assumed structural model in geological time, rather than invert this

model from the current geology. The treatment of these methods is beyond the scope of this thesis; I refer the interested reader to the work of Woodward et al. (1989) and Dahlstrom (1969).

3.4.5.1 Constraining the Optimisation

The input of constraints comes from a priori knowledge about the PP structural model, and it is entered in the damping or model-covariance matrix $\tilde{\mathbf{K}}$ (Tarantola, 1984). Another source of constraints comes from the average v_s of the area, and the P-wave velocity model. In the case of no a priori information and as long as the quality and acquisition of the PS data leave the velocity-inversion problem under-determined, and given that geological constraints cannot be easily quantified, I recommend to trust an interpreter rather than a poorly understood damping matrix.

3.5 Summary

The velocity analysis is formulated as an iterative optimisation process, in which the objective is to minimise discrepancies in depth between PS and PP CRP gathers. The optimisation algorithm consist of two loops; the inversion loop and the outer migration loop. In the inversion loop, model perturbations are determined from the minimisation of the objective function by a conjugate-gradient algorithm. In the migration loop, the data are re-migrated with the updated model parameter. Reflector positions are not updated because they are known from the PP section. This is advantageous because only one parameter (layer velocities) is iteratively updated. Updating only the layer velocities leads to a fast convergence of the solution than if both layer geometry and layer velocities are to be updated.

The computation of the $\tilde{\mathbf{D}}$ -matrix is performed by ray tracing through the initial model. I used the ray tracing algorithm of Červený and Pšenčík, (1984) (Seis88). The ray tracing is performed only once and it is assumed that the raypaths do not vary as the model is updated (Fermat's principle). However, in case of strong variations an update of the ray paths is necessary.

Even though the velocity analysis involves repeated prestack depth migration and inversion, it is still fast enough because the finite difference eikonal Solver (Chapter 2, page 19) used to compute traveltimes is very efficient. Secondly, with Kirchhoff migration, I do not need to re-migrate the complete data but only particular target zones. After obtaining the final velocity model I can then use other traveltimes methods (e.g. Wavefront construction method) which include maximum energy arrivals to migrate the complete data.

Chapter 4

Synthetic and Field Data Examples

4.1 Description of the Synthetic Data

In this section, I present a 2D isotropic data example to test the validity of the tomographic method developed in Chapter 3. Figure 4.1 shows the Earth model used for the test. It consists of seven homogeneous layers separated by smooth curved interfaces. The elastic parameters of the model are given in Table 4.1. The source signal is a zero-phase Ricker wavelet of 20 Hz maximum frequency. Figure 4.2 shows an example of ray synthetic PP and PS shot gathers generated from the model

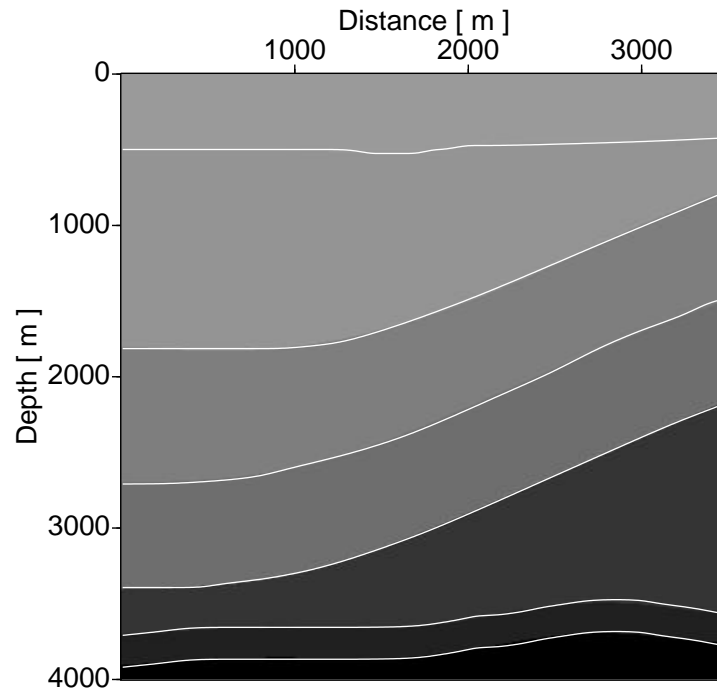


Figure 4.1: Layered model used for generating synthetic data. The model parameters are given in Table 1.

with the Seis88 code. In generating these data two basic simplifications were made. First, no direct

Layers	v_p	v_s	ρ	v_p/v_s
1	2075	1383	2.12	1.50
2	2200	1272	2.14	1.73
3	2655	1475	2.23	1.80
4	3000	1734	2.30	1.73
5	4202	2322	2.54	1.81
6	4608	2664	2.62	1.73
7	5285	3055	2.76	1.73

Table 4.1: Elastic parameters of the 2D synthetic model in Figure 4.1. Velocities are in m/s and densities in g/cm^3 .

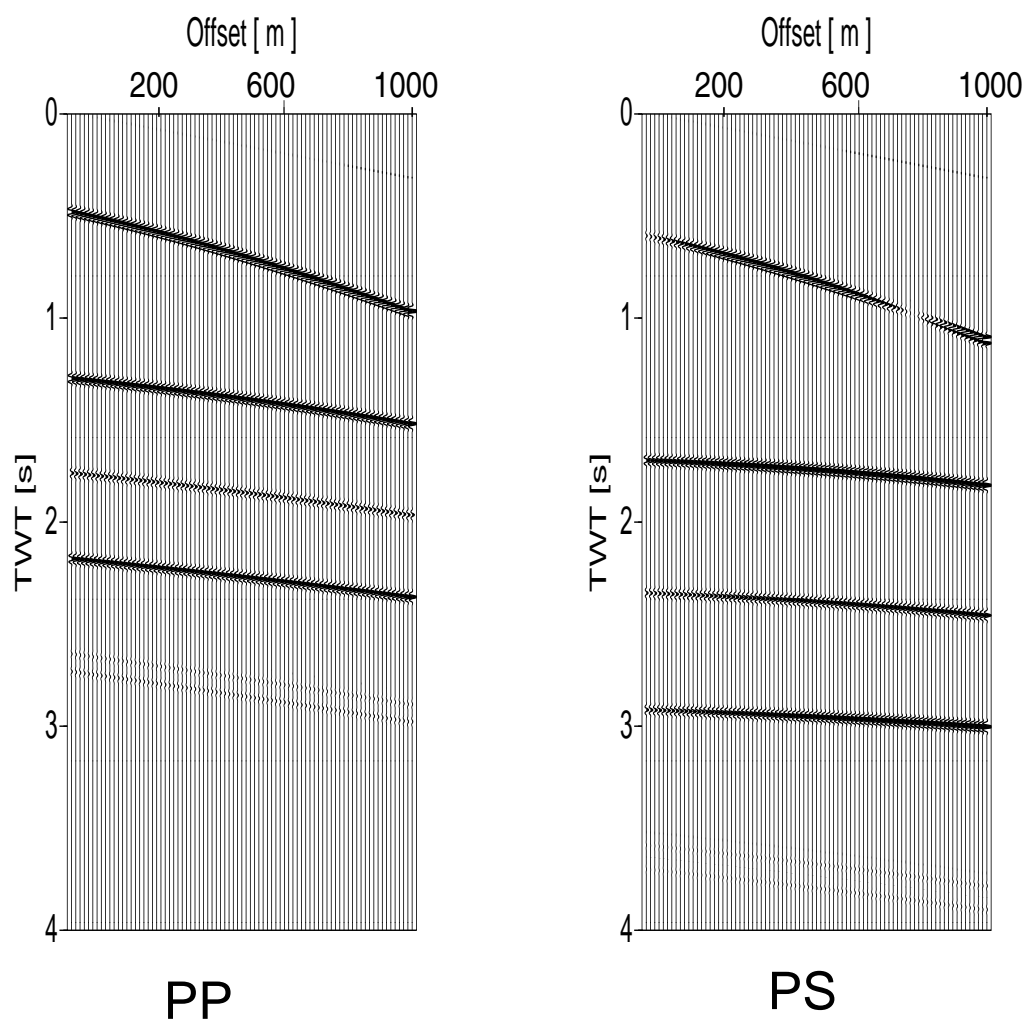


Figure 4.2: An example of a PP and PS shot gather generated by a ray tracing code using the model in Figure 4.1. In the PS shot gather, a phase reversal occurs for the first horizon at an offset of 800 m. This phase reversal is discussed in Appendix C

waves were included. Second, the PP waves are completely free from PS wave modes, likewise the PS waves are free from PP wave modes. These simplifications are justified because for the model building algorithm I assume that preprocessing has been correctly carried out on the data. These preprocessing steps include the suppression of the direct waves, the wavefield decomposition into PP and PS components (Dankbaar, 1985) and P- and S-wave residual static corrections.

I generated a total of 20 shot records for a regular receiver spacing of 10 m and shot spacing of 100 m with 200 m as nearest offset and 1000 m as far offset. The acquisition was designed to acquire PS data mainly within the PS mode offset-limit (see Appendix C). Note that in the PS data in Figure 4.2 a phase reversal appears at an offset of 800 m for the first reflecting horizon. The reason for this phase reversal is discussed in Appendix C.

4.1.1 Inversion Results

First, the PS data are migrated with a v_s model generated from v_p and a constant v_p/v_s -ratio for the entire model ($v_p/v_s = 1.99$). This is about 13% higher than the average value. A pair of selected PP and PS CRP gathers which have been sorted from the depth migrated common shot gathers is shown in Figure 4.3. These example gathers were collected at surface location $x=1500$ m. In the inversion I analysed a series of CRP locations but as an example only one is displayed here. As expected the events in the PP CRP gathers are flat and horizontal (no residual moveout) since the correct P-wave interval velocity is used. The traces in this CRP gather will interfere constructively if the traces are stacked to obtain the final migrated section. Except for the first layer, the events in the PS CRP gather are equally flat and horizontal even though the shear velocity (v_s) is incorrect. If stacked, the PS CRP traces would also sum up constructively in the final migrated section.

However, comparing the depth positions of both the PP and PS CRP gathers at the same locations we see that the PS images are not tied to the PP images, even though they are all flat in the range of the considered offsets. Therefore, if flatness of the PS CRP gathers is the only criterion for determining which shear wave velocity model is accurate, the resulting model can always have wrong interval shear velocities as well as wrong P-to-S-velocity ratios. Therefore, a necessary and sufficient condition for estimating the accurate v_s and v_p/v_s model is the same depth position in PS and PP gathers in addition to flatness of the gathers.

In Figure 4.3 the PS images are shifted upward. This upward shift is an indication of a lower migration v_s (higher migration v_p/v_s -ratio) than the true values. A downward depth shift would indicate a higher v_s (lower v_p/v_s -ratio). I picked the depth shifts and used them as input into the tomographic inversion. For this example eight CRP gathers along the profile were analysed. Figure 4.4 displays the resulting PP and PS CRP gathers after four iterations for each layer stripping procedure. In the layer stripping process, the first layer is migrated using the initial v_s and depth shifts are picked from a set of CRP gathers. This velocity is then updated. After the first layer is done I proceed to the next layer and the process is repeated for the next layer. I inverted directly the interval v_s since the reflector positions are already known from the P-wave model. This is the major advantage because I do not need to update simultaneously for depth and v_s , thereby reduc-

ing the number of parameters to determine. Knowing the v_p distribution and the v_s distribution, the v_p/v_s -ratio distribution is directly obtained. This ratio is a very important elastic parameter in hydrocarbon exploration.

4.1.1.1 Migration noise

In Figure 4.3 and 4.4 the PP and PS CRP gathers show migration noise. Residual moveouts in the gathers are not present but strong migration artifacts (migration smiles) are present. These migration artifacts should not be confused with residual moveouts. The artifacts are caused by data truncation due to the limited aperture of the migration. The artifacts are eliminated when the CRP gathers are stacked to obtain the final migrated section since they will interfere destructively. Sometimes it is necessary to mute the CRP gathers before stacking. This has the advantage that the artifacts are not included in the stacked image and the risk of some constructive artifacts interference is avoided. In addition, after muting, some weak signals in the stacked section can be better enhanced. Therefore, some interpretation is required in order to recognize “real flat events” and distinguish them from artifacts which are to be muted. Also note that other conventional processing techniques such as filtering can be applied to the CRP gathers in order to improve the appearance of the final migrated section.

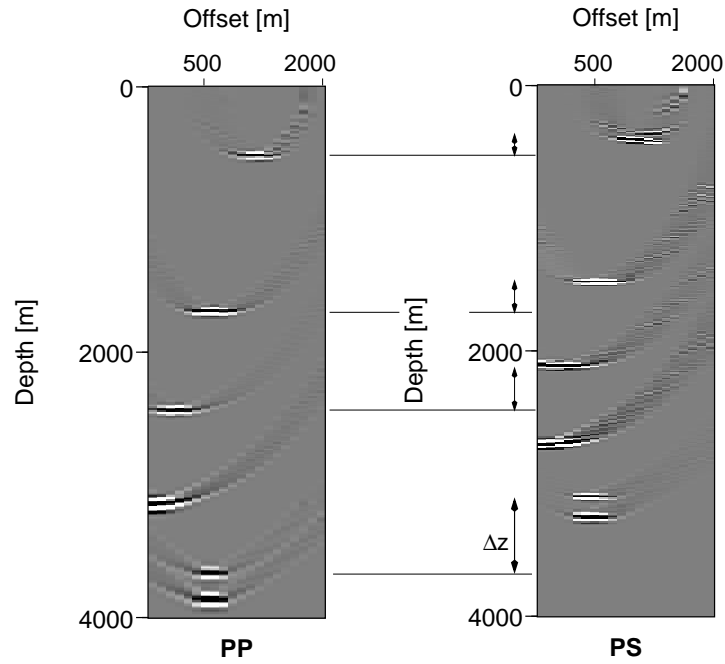


Figure 4.3: PP (left) and PS (right) CRP gathers at surface location 1500 m. An initial migration velocity ratio of 1.99 was used for the entire model. The PP gather was generated using the correct v_p model. The PS gather was generated by using the constant migration v_p/v_s value. Despite this incorrect migration v_p/v_s value, the events in the PS gather are flat, however, they clearly show substantial depth shifts Δz when compared to their PP counterpart.

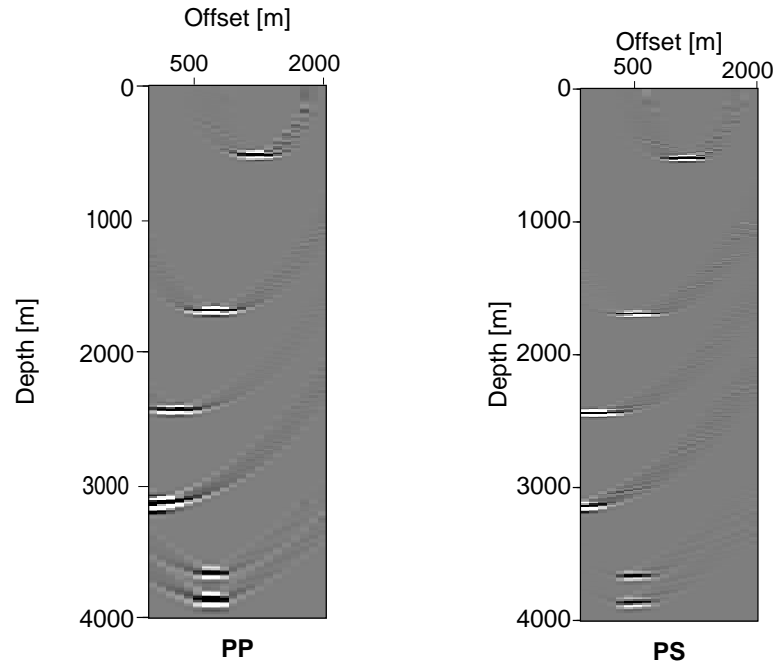


Figure 4.4: Comparison of the same situation as in Figure 4.3 after tomographic updating (PP and PS CRP gathers at surface locations 1500 m). This result is obtained after four iterations.

4.2 Field Data Example

4.2.1 Data Set

The joint process of imaging and interval shear wave velocity inversion was applied to a 2D on-shore data set acquired in South Eastern Bavaria (Germany) by Preussag Energie GmbH. The PS-wave reflections were recorded together with PP wave reflections. The line consisted of three independent measurements. For two of them, three PP wave vibrators with a sweep of 17-100 Hz were used as a source. Because the PS data survey was independently measured, a smaller vibrator spacing of 30 m was chosen in order to obtain a high coverage and to avoid the zone of uncertainty polarity (see Appendix C). For the PP data a vibrator spacing of 60 m was used. No wavefield separation was required with this measurement geometry. However, both PP and PS records could have equally been combined in one survey as it is routinely done, using the same source but recording on different geophone lines. An SH wave survey was also carried out on the same line using a single SH wave vibrator as source and horizontal geophones orientated perpendicular to the line as receivers. The PS prestack data contain 76 shot records while the PP data contain 120 shots. Each shot record consists of 120 traces. The data was recorded up to 8 s with a sample rate of 2 ms. The source to source and receiver to receiver separation was not constant but had an average distance of 30 m; the nearest offset was 90 m and the maximum offset was 3690 m. A well drilled down to 4700 m depth was also available with log information. Examples of the PS and PP shot gathers are given in Tessmer et al. (1990).

Before passing both PP and PS data to the migration and inversion algorithm several preprocessing steps like spherical divergence correction, minimum-delay transformation, spectral balancing, spiking deconvolution, scaling and static corrections were carried out (see Tessmer et al., 1990).

4.2.2 Inversion Results

Because the tomographic inversion method relates PS CRP gathers to PP CRP gathers in the depth domain, I chose only the central part of the data where best illumination was achieved. First, I generated a P-wave velocity/depth model. The data from the sonic log served as a starting model. I updated the P-wave velocity/depth model using iterative prestack depth migration until the PP CRP gathers were flat (e.g. in Figure 4.6 and 4.7 left panels). The CRP gathers were computed at 200 m intervals, giving a total of 17 CRP gathers along the selected part of the profile. The reflector positions from the PP depth section were interpreted and kept unchanged (Figure 4.5).

The second major step is to generate the best initial average v_s model. For this purpose, I first migrated the PS data with a range of possible initial v_s models using the algorithm described in Chapter 2. From the results of these migrations the best possible initial v_p/v_s -ratio of 1.85 was chosen for the entire model. Figure 4.8 and 4.7 show PP and PS CRP panels at surface locations 12000 m and 13600 m after migration with this initial constant v_p/v_s model and v_p model. Upward shifts as well as downward depth shifts of PS reflection events are seen. Figure 4.8 shows the CRP gather at the same location as in Figure 4.7 after migrating with the updated v_s field. A display of a

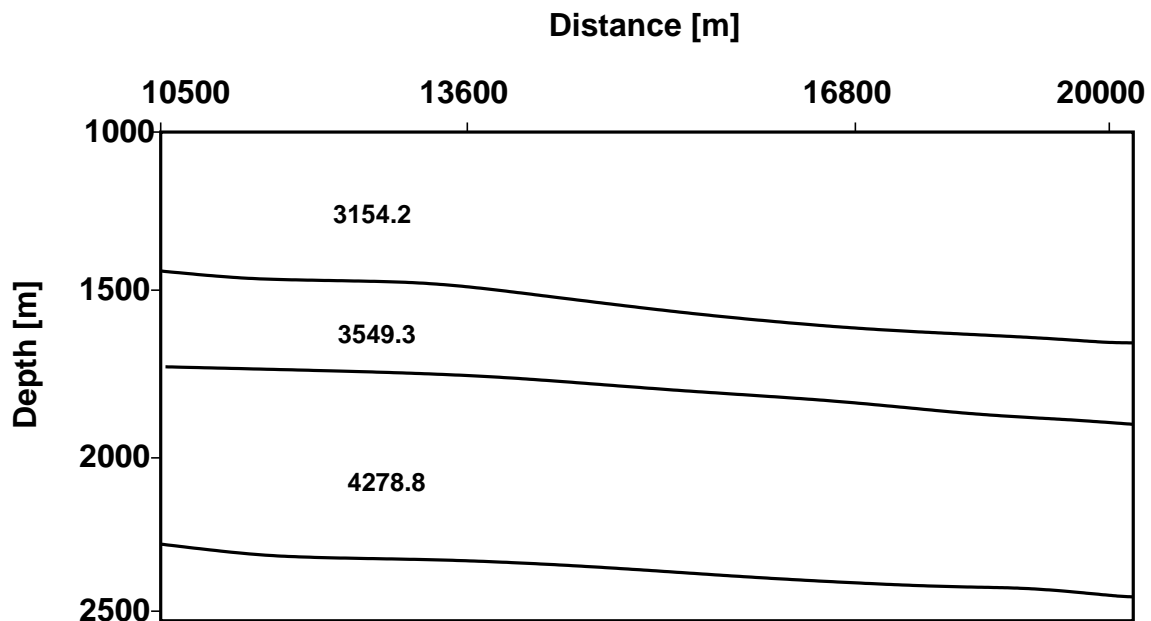


Figure 4.5: PP velocity/depth model obtained after prestack depth migration. The depth migration section is given in Figure 4.10. The velocity values are in m/s.

set of PS CRP gathers is shown in Figure 4.9. The right panel is a PP gather for comparison. Each PS gather was matched with its corresponding PP gather at the same surface location. Note that as the PS and PP depth shifts decreases, the PS reflection events becomes more focused. This is due to the fact that as the velocity model is improved a better focusing is achieved. Figure 4.10 shows part of the PP and PS 2D Kirchhoff prestack depth migrated section. The PS section was migrated using the final S-wave velocity. For the three main interpreted horizons, the final updated interval velocity values are $v_p = 3154.2, 3549.3, 4278.8$ m/s; $v_s = 1502, 2151, 2625$ m/s; and the velocity ratios are 2.1, 1.65, and 1.63. Good reflection continuity and event character are observed on both data sets, and reliable correlations can be made between the P- and S-wave data. The reflectivity in the PP section is much higher than that of the PS section. This can simply be attributed to the fact that the data quality of the PS prestack data was poorer. Generally environmental background noise levels are often higher in S-wave data than in P-wave data. The increase in noise level in the PS section is clearly seen.

It can be observed that in the PP section the reflector continuity of the third layer (at 2.4 km depth) is disrupted. This can be attributed to possible gas cloud which might be present in the overlying layers. Gas clouds usually scatter P-wave energy thus reducing the amount of transmitted P-wave energy. In the PS section the reflector is continuous with other structures present in the “empty PP area”. This demonstrates the fact that S-wave can travel through gas clouds without being affected.

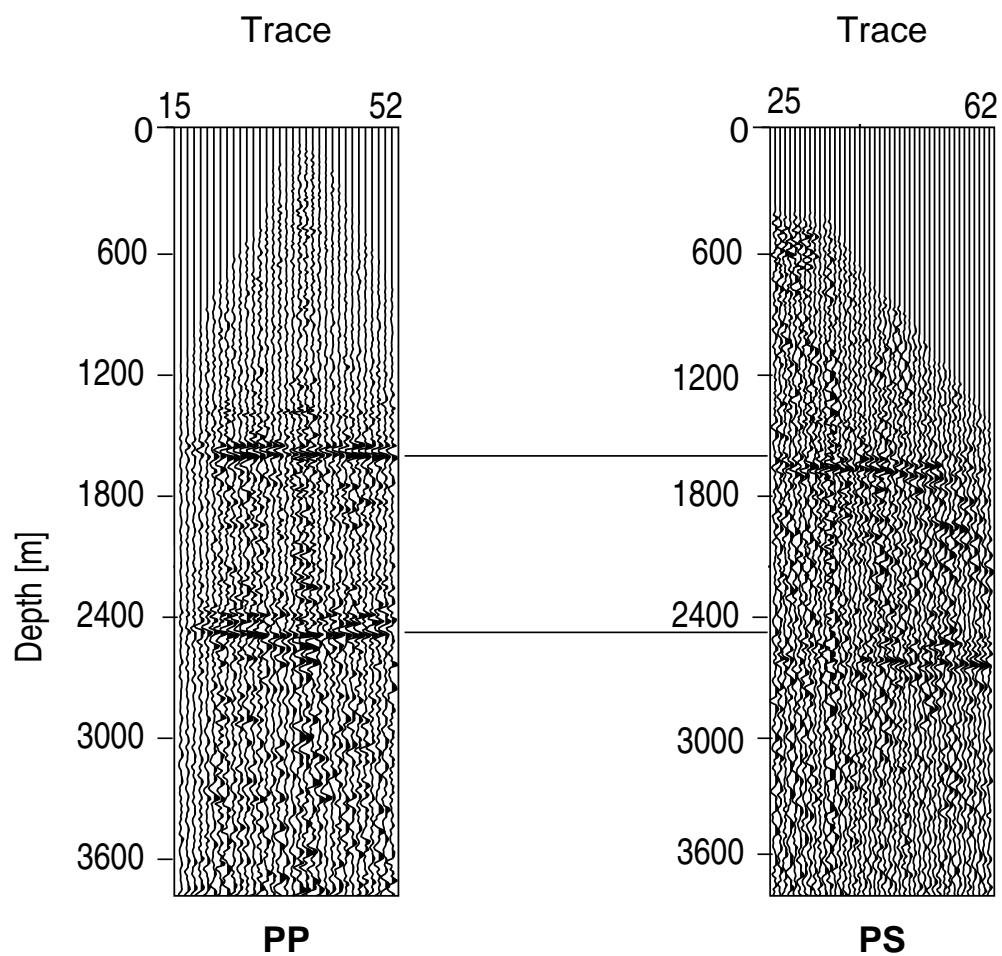


Figure 4.6: PP (left) and PS (right) CRP gathers at surface location $x=12000$ m before tomographic inversion. Downward depth shifts indicate that the initial input migration velocity ratio of 1.85 is too low.

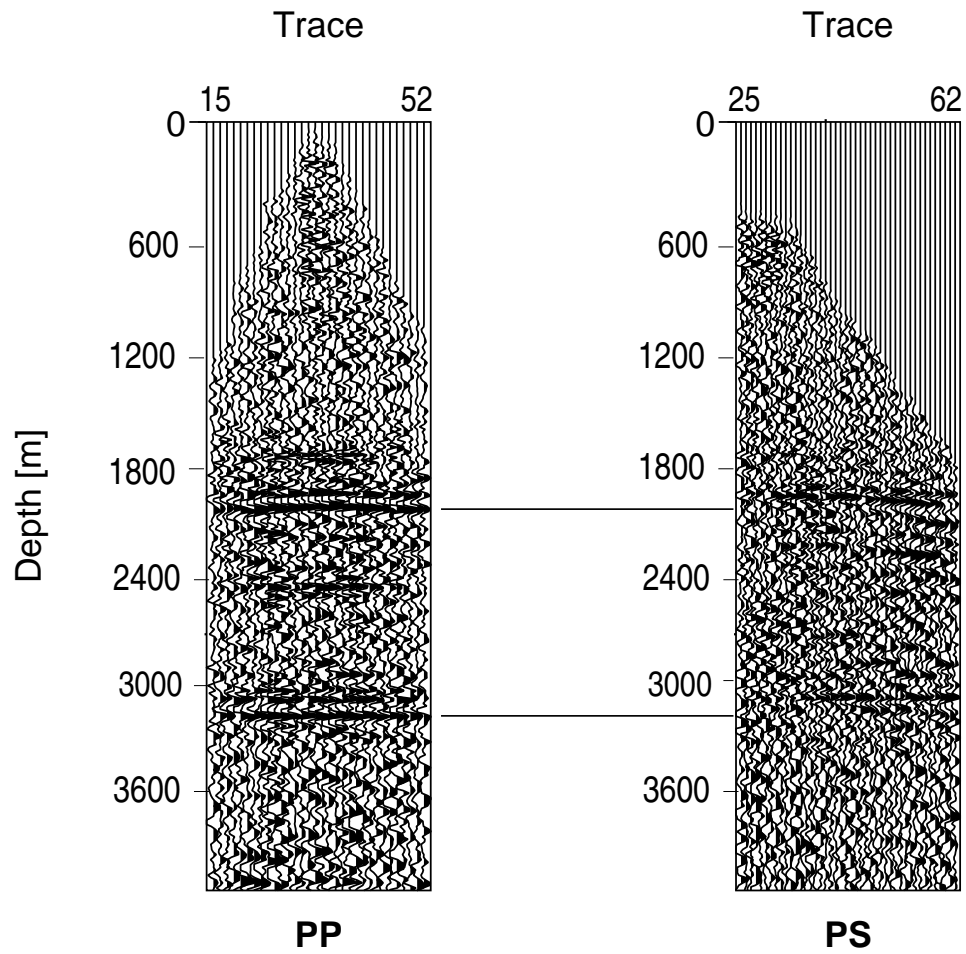


Figure 4.7: A different pair of PP (left) and PS (right) CRP gathers at surface location $x=13600$ m with an upward depth shift. This indicates that the migration velocity ratio in this region was too high and therefore v_s too low.

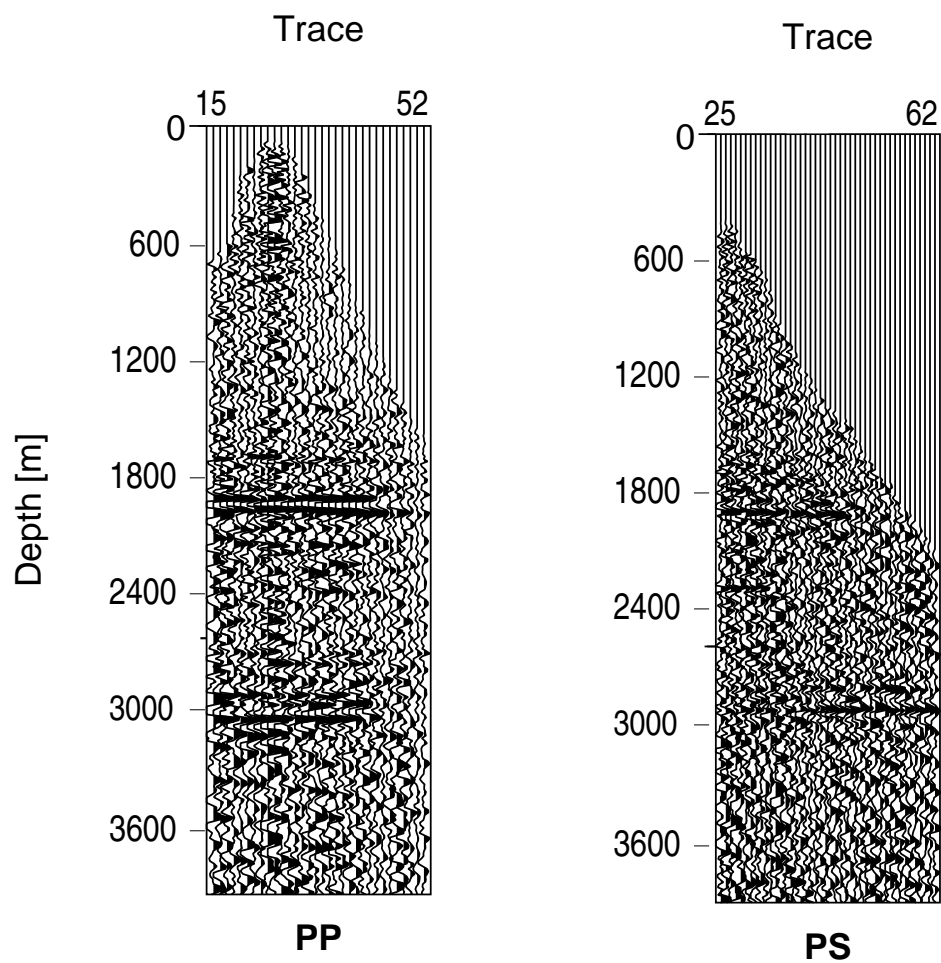


Figure 4.8: A pair of PP and PS CRP gather after tomographic updating ($x=13600$ m). While the first layer tie in both PP and PS data the second layer still require some adjustment.

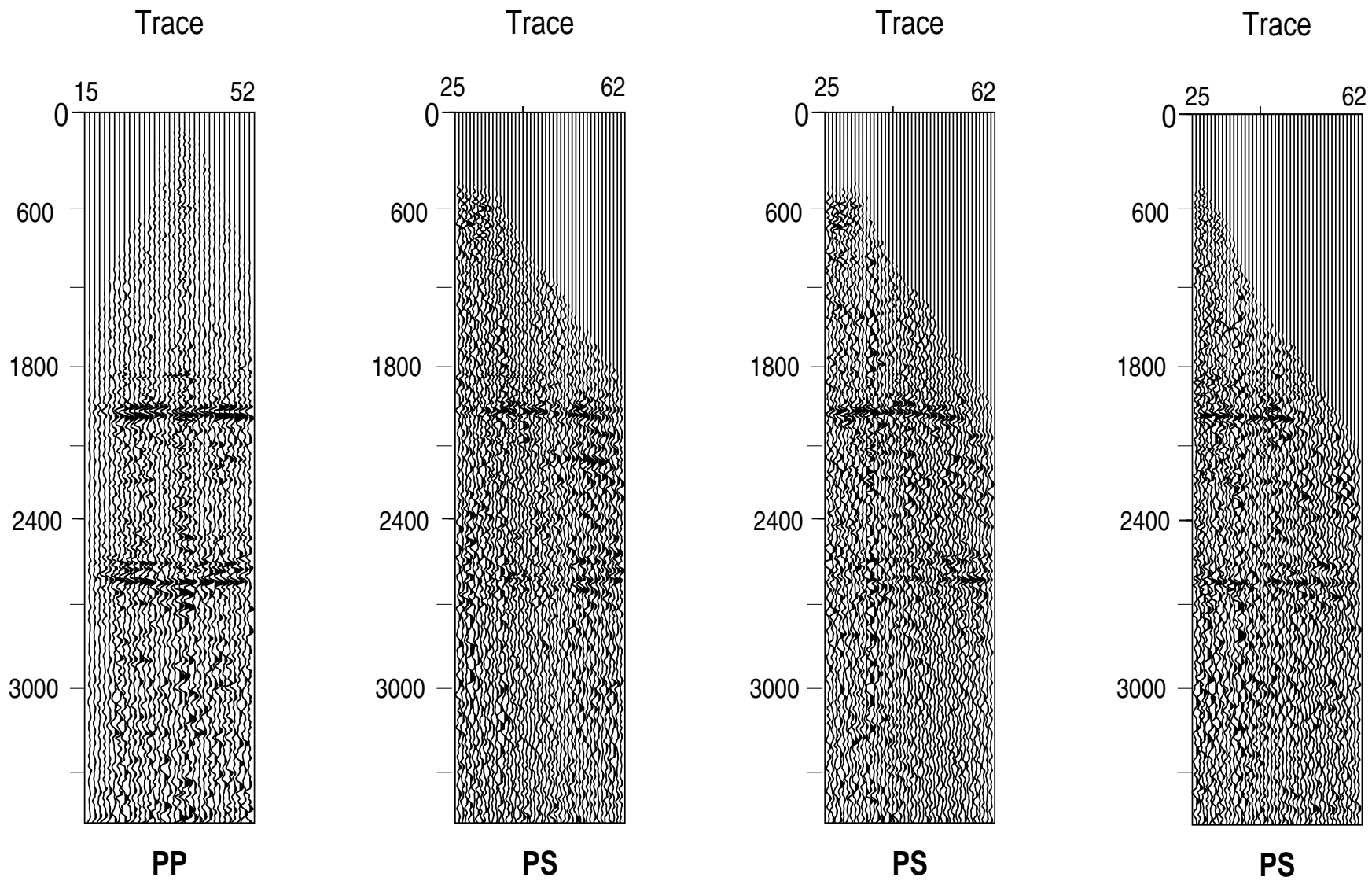


Figure 4.9: The right panel is a PP gather and the other panels are updated PS panels at different surface locations.

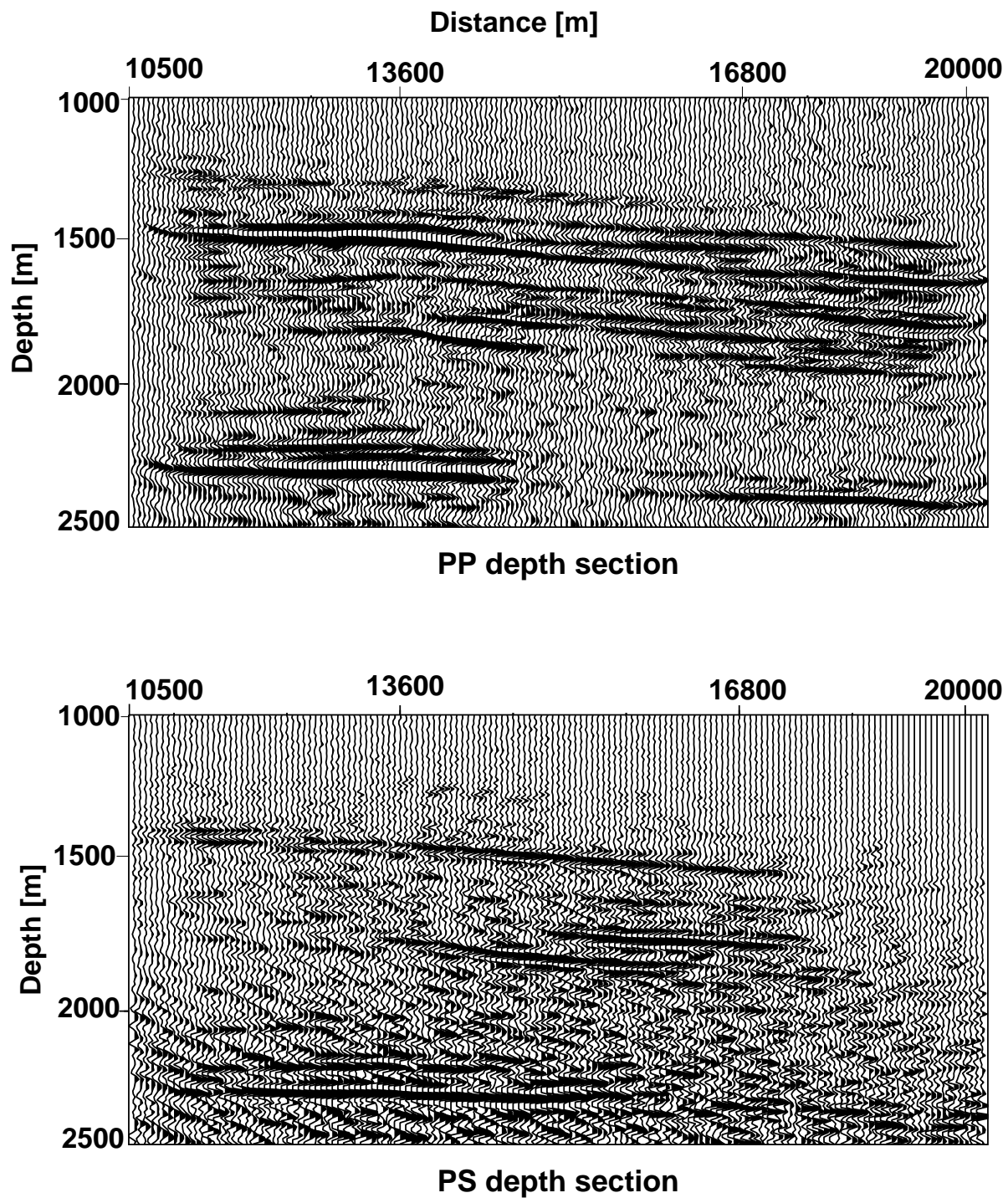


Figure 4.10: Part of a prestack depth migrated section. The upper section is the PP section and the lower section is the PS section after using the updated v_s model

4.2.3 Summary

The tomographic scheme developed and applied in this part of the thesis can be applied to both prestack PS and postmigrated PS data. The coupled problem of simultaneously inverting for the velocity values and reflector position is avoided because I use the depth structure previously determined from the PP wave section. Since I fix the depth structure, no inversion of reflector depth is required. This reduces the number of inverted parameters. The inversion procedure presented here has three major stages:

- The generation of a PP velocity/depth model.
- The generation of an initial v_s velocity model. I use the simultaneous migration scheme (Section 2.4.6, page 28) to determine the initial model. Because the initial model is already close to the final model, only a few iterations are needed in the tomographic inversion.
- Tomographic inversion.

For the inversion, it is critical that the depth intervals between PP and PS section are identical. Not all interfaces produce good reflections on both PS and PP sections, so care must be taken to select appropriate events. Also note that sometime there is not a one-to-one correspondence between all the events in the initial and final gathers; events can move laterally as well as vertically after re-migration, and they may therefore, move to different surface locations.

After inverting for interval v_p , v_s and v_p/v_s -ratios, other elastic parameters such as Poisson's ratio and the bulk modulus-to-shear-modulus-ratio can directly be estimated. These are important hydrocarbon indicators.

4.3 Link between part I and part II

In part I of this thesis, I have shown how S-wave interval velocities can be estimated from converted waves. Before continuing to part II of this work, I will describe the link between the two parts. The general objective of the whole thesis is to develop methods for velocity/depth model building and seismic imaging.

The tomographic method in part I can (with small modifications) very well be applied to single component data (i.e., PP or SS data). In part II another model building strategy and imaging method are described. While the strategy for model building in Part I directly works in the depth domain, the strategy in part II include both time and depth domain imaging. Part II will demonstrate that a properly stacked time domain seismic section will facilitate any further depth domain imaging. Therefore, part I and part II are connected in the sense that the methodologies which are described all aimed at handling imaging problems. While part I was focused more on describing a new method, part II will be focused on application and validation of existing methods on real seismic data acquired over a tectonically complex area.

Part II

STRUCTURAL IMAGING IN COMPLEX GEOLOGICAL AREAS: INTEGRATING MODEL-INDEPENDENT AND MODEL-DEPENDENT IMAGING

STRUCTURAL IMAGING IN COMPLEX GEOLOGICAL AREA: INTEGRATING MODEL-INDEPENDENT AND MODEL-DEPENDENT IMAGING

Elive M. Menyoli, Institute of Geophysics, University of Hamburg, Germany

ABSTRACT: PART II

As exploration targets become complex, velocity analysis which is a central part of seismic data processing becomes even more difficult. An example for such a complex target is the imaging of Foldbelt data. Because of the complex tectonics and steeply dipping layers in Foldbelt areas, the common reflection point assumption usually breaks down. Usually, prestack depth migration is required for imaging in complex areas. However, prestack depth migration itself requires an accurate velocity/depth model as input. For this reason most research work has been focused on methods and strategies for estimating accurate velocity/depth models. Even with new sophisticated methods like reflection tomography, velocity models in complex geological areas are still not accurate enough to give a “perfect” image of the subsurface.

Therefore, during the last 8-12 years alternative technologies to image the subsurface without the velocity model were developed. I suggest to integrate the information from this new model-independent methods with the already existing model-dependent methods in order to improve the accuracy of the velocity/depth model estimation. Model-independent imaging has the advantage that the results are purely data-driven, i.e they are free from any error due to wrong interpretation or picking of reflection events. Errors due to velocity models are avoided. Model-independent methods like the common reflection surface (CRS) stack also produce wavefield attributes, which embody characteristics of the background model through which the wavefield propagates.

The CRS stack technique simulates a zero-offset section by summing along stacking surfaces in the multi-coverage prestack data. In 2D the stacking formula depends on three parameters associated with the reflected wavefronts, in contrast to the standard CMP stack which depends only on one parameter (stacking velocity). The three parameters are obtained by a coherency analysis. Coherency analysis is performed along the various test stacking operators within a specified test range. The stacking operator yielding the highest coherency is used to perform the actual stacking on the original prestack data.

In this thesis the CRS stack method and prestack depth migration are integrated in order to estimate an accurate velocity/depth model of a Foldbelt data set. The CRS stack method can produce only stacked time sections (unmigrated or migrated). Because a depth section of the data set is required, model-dependent prestack depth migration is applied. First an appropriate velocity/depth model is needed. The generation of the interval velocity/depth model is iterative. The number of iterations depends on the accuracy of the initial model. In this work I use coherency inversion as a method for generating the initial velocity/depth model. However, coherency inversion requires accurately picked time horizons. The high quality results from the CRS stack method are, therefore, advantageous at this stage in order to obtain correctly picked time horizons. The results of

the CRS stack images are migrated and the main time horizons are interpreted.

To produce the final depth section of the Foldbelt data, I used the iterative prestack depth migration (PSDM) of the Kirchhoff-type. Residual moveout analysis is applied to update the initial velocity model. I use the procedure of iterative and interpretive adjustment of the velocity and depth model. In this phase structural geological information and migrated CRS stack information are incorporated. The combination of the model-independent and model-dependent imaging proved to be a powerful strategy for imaging the complex geological structures in the Donbas Foldbelt area. The examples in this thesis show that this strategy leads to a more reliable estimation of the subsurface velocity/depth model of the complex geological structures.

Chapter 5

Introduction

5.1 Background

Seismic imaging methods aim at reconstructing a “mirror image” of the subsurface geology (in the time or depth domain). For this, multi-coverage seismic traces are transformed to zero-offset sections. These sections give the structural image of the subsurface. Because the true geology in all details can never be completely recovered, it is rather aimed for the recovery of a suitable subsurface model that, when used in seismic migration, provides the desired information, which is reasonably consistent with other available surface or bore hole measurements (Fagin, 1998). Deriving such an accurate subsurface model from surface measurements is practically difficult where the geology is complicated. The geology of the Donbas Foldbelt is an example of a complex terrain because of the complexity of thrust faulting and folding of Paleozoic and younger sedimentary layers. Thrust faulting and folding produces locally very steep dips and strong lateral velocity variations, thus violating the assumption of common reflection point traces which is used in conventional common midpoint (CMP) stacking. Therefore, in Foldbelt areas conventional seismic methods such as normal moveout (NMO)/dip moveout (DMO) stacking usually give unsatisfactory imaging results.

In the past 8 - 12 years many complementary methods have evolved, all aiming for improving images of complex areas in a fast and robust manner. These methods can be categorised into model-independent and model-dependent methods. Model-independent methods such as the common reflection surface (CRS) stack (Müller, 1998; Mann et al., 1999; Jäger et al., 2001) or the multi-focusing method (Gelchinsky et al., 1999) are data-driven and require little or no user intervention. On the other hand model-dependent methods such as conventional CMP stacking and prestack depth migration (PSDM) require an accurate velocity/depth model in order to produce accurate images of the subsurface (see e.g. Gray et al., 2001). Both model-independent and model-dependent methods might give different information about the subsurface since they rely on different stacking operations. The challenge to exploration geophysicists, therefore, is to utilise both techniques to extract as much detailed information as possible from the seismic data.

5.2 Dissertation Objectives: Part II

The main objective of this part of the thesis is to investigate how the model-independent CRS stack method and the model-dependent PSDM can be integrated in estimating an accurate structural velocity/depth model of the Donbas Foldbelt data for an improved understanding of basin evolution. The first goal is to validate the model-independent CRS stack algorithm on synthetic data. The CRS stack produced images are compared with images produced through standard velocity analysis and stacking. Assessment of the differences is carried out, with the objective of understanding the working principles of the CRS stack method and its strength as well as its weaknesses.

The final purpose of the work is to develop a complete and consistent workflow in which CRS stacking and PSDM are incorporated. This new workflow includes a solution for estimating a structural velocity/depth model. It is hoped that by integrating model-independent and model-dependent methods, the flow proposed is general enough to apply to data from any complex terrain and not only to Foldbelt data.

5.3 Conventional Stacking

On the field, seismic data are acquired as common source gathers (CSG) and are sorted into common midpoint (CMP) gathers in the processing centres. Figure 5.1 displays a CSG and a CMP gather for the same profile. A CMP gather consists of an equal number of shots and receivers placed symmetrically on a line about the common midpoint. In a constant velocity and horizontally layered model, all rays in a CMP gather are reflected from the same depth point. If a coincident source and receiver location existed in the acquisition geometry, then a CMP gather will also contain a zero-offset ray that originates from the coinciding source/receiver pair at the CMP location. With respect to this zero-offset ray the depth point can also be referred to as normal incidence point *NIP*.

In a CMP gather, the reflection events appears as a set of responses aligned along a moveout curve (see Yilmaz, 2001). Conventional CMP stacking involves summing the primary reflections along the interpreted moveout curves which best approximate the actual reflection time curves. The traveltimes are approximated as (Yilmaz, 2001):

$$t^2(\mathbf{x}) \approx t_0^2 + \frac{\mathbf{x}^2}{v_{rms}^2}, \quad (5.1)$$

with $t(\mathbf{x})$ being the total traveltimes from source to receiver and \mathbf{x} is the offset vector between source and receiver, v_{rms} is the root-mean square velocity of the medium. The primary reflections in an optimum stacked trace are enhanced against the background noise. The stacked trace approximates a noise- and multiple-free zero-offset trace. The degree to which an actual stacked trace approximates the desired result depends upon various parameters such as the number of traces in the CMP gather (coverage), spread length, and complexity of subsurface geology. The hyperbolic traveltimes curve (Equation (5.1)) depends only on the unknown velocity v_{rms} . This velocity is obtained through velocity analysis (either automatic or manually).

Standard velocity analysis applies normal moveout (NMO) to the CMP gathers with several velocity values and finds the one that best corrects the moveout events. After NMO correction with the appropriate stacking velocity, the CMP gathers are straightened and are summed to give the stacked image. The procedure of NMO velocity analysis is repeated for CMP gathers located at intervals (usually every 200 CMP gather) along the seismic line and the results are interpolated in time and space.

In a horizontally and constant velocity layered medium the velocity which gives the “best” stacking results is the rms-velocity (v_{rms}). When the subsurface geology (velocities and structure of the medium) becomes complex, the optimum stacking velocity (v_{stk}) deviates significantly from the rms-velocity. Sometimes the optimum stacking velocity does not have any geological significance because in a complex medium the velocity additionally becomes dependent on the structure of the reflectors- the dip of a plane reflector, the radii of curvature of a curved boundary, and its depth. Figure 5.2 shows an example of a moderately complex medium (a dipping layer model) with a constant velocity. The source-receiver combinations having a common midpoint do

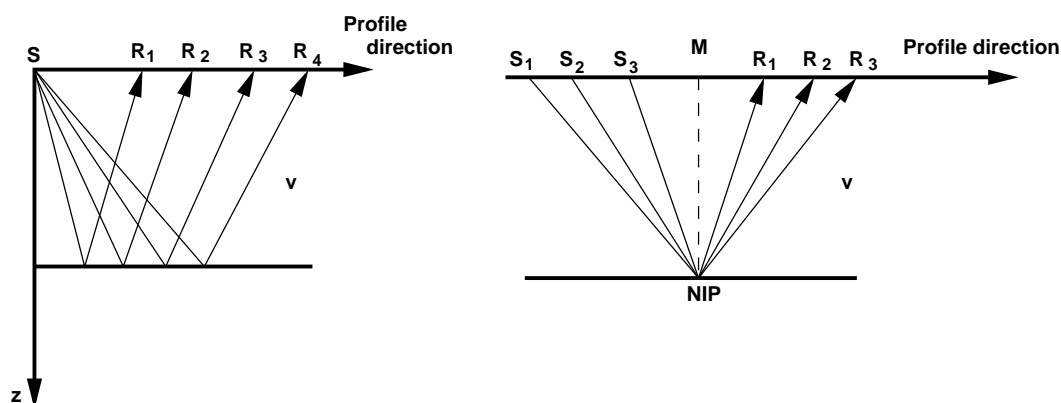


Figure 5.1: Common shot and common midpoint configuration. A common shot illuminates a region of an interface and a CMP configuration multiply illuminates a point of the reflector. Strictly speaking, the region of illumination is not a point but mainly the first Fresnel zone.

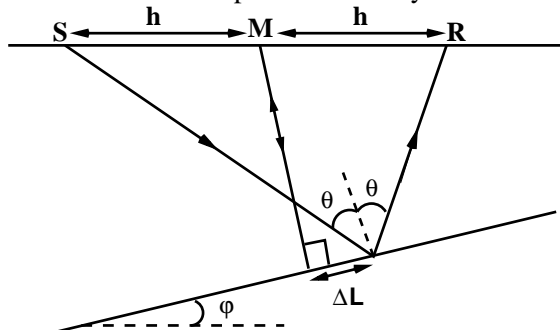


Figure 5.2: Dipping reflection events suffer from reflector point dispersal. Even for constant velocity, the reflection point moves up-dip with increasing offset in a CMP gather. Conversely, for a fixed reflection point, the corresponding midpoints will be distributed over the distance ΔL . h is the half-offset and M is the midpoint between source and receiver, and φ is the dipping angle of the reflector.

not share the same common reflection point as in Figure 5.1. The reflection points are variable and move up-dip with increasing offset (reflection point dispersal) and are distributed over a segment ΔL along the interface. Conversely, for a fixed reflection point, energy reflected at this point will correspond to midpoints distributed over ΔL . Therefore, summation of the CMP gathers would involve reflection energy originating from different subsurface points. Reflection point dispersal leads to a decrease in S/N-ratio in steep dip flanks and reduction in lateral resolution (Deregowski, 1990). The reflected waves from different reflection points will not necessarily stack together coherently, therefore, velocity analysis without true common reflection point gathering can degrade velocity analysis, leading to a poorly interpreted velocity field. A poorly interpreted velocity field may result in failure to optimally stack the data with the loss of valuable signal and subsequent mispositioning when the data are imaged. Usually, the remedy to reflection point dispersal is to apply dip moveout (DMO) correction after NMO correction and repeat the velocity analysis again (Deregowski, 1990). DMO attempts to correct for the geometrical effect of CMP smearing observed for dipping reflectors and converts CMP gathers to common reflection point gathers. After a perfect DMO the stacking velocities for dipping layers should be dip-independent. However, velocity analysis and DMO is not trivial in Foldbelt areas with complex tectonics, high reflector dips and strong lateral velocity variations. Besides, in a medium with strong lateral velocity variations, even after DMO, conventional stack still have limited chances to stack the traces constructively. Note that DMO is usually applied with a constant velocity medium or if the vertical velocity gradient is moderate. Poorly stacked images will eventually lead to poor poststack migration results since the success of poststack migration (time or depth) strongly depends on the quality of the poststack seismic data rather than on the accuracy of the migration rms-velocities. DMO cannot solve stack imperfections caused by lateral velocity variations.

Therefore, from the discussion above the image quality of standard processing strongly depends on the velocity model used for stacking. Because it is not always trivial to find the appropriate velocity model, I use in this thesis a velocity independent imaging method as an alternative in order to reach maximum improvement of the unmigrated stacked section. One of this model-independent methods is the CRS stack method. Nevertheless, equation (5.1) in its so simple form, is by a wide margin the most common velocity analysis estimator applied to seismic data and still enjoys great success.

5.4 Common Reflection Surface Stack

Chapter 6 describes the common reflection surface (CRS) stack technique. In the CRS stack approach (Hubral et al., 1998; Müller, 1998; Mann et al., 1999; Perroud et al., 1999; Jäger et al., 2001) each zero-offset (ZO) trace is constructed (simulated) by stacking traces which need not belong to the same CMP gather but whose sources and receivers are in a certain vicinity of a central ZO ray. Since the traces being stacked do not belong to the same CMP gather, such a procedure requires a more general moveout expression than equation (5.1). Because a central ZO ray is considered, the CRS stack as implemented in this work is known as ZO CRS stack.

Figure 5.3 shows an illustration of CMP ray distribution as “seen” in the CRS stack method. In a general background medium CMP rays with finite offset, x , do not reflect at the normal incidence point (NIP). However, Hubral and Krey (1980) showed that up to second order (i.e.,

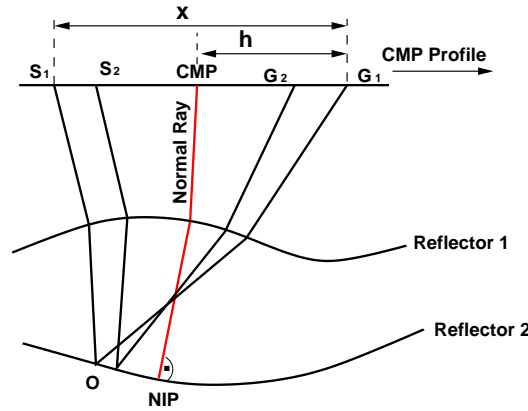


Figure 5.3: A 2D curved layer model with a normal ray (central ray) and two CMP rays. The source-receiver separation is assumed small. The traveltime along the CMP ray S_1G_1 can be approximated, up to second-order, by the sum of the times from S_1 to NIP and from NIP to G_1 . The same also applies for the ray from NIP to G_1 .

for small offsets) approximations of CMP reflection time curves, it can be assumed that all CMP rays (Figure 5.3) pass through the NIP . That means the traveltime along the CMP ray S_1G_1 can be approximated by the sum of the traveltime from S_1 to NIP and from NIP to G_1 . In this approximation, the CMP rays are considered to agree sufficiently well with a ray family belonging to a hypothetical wave propagating away from a point source at the NIP . The wavefront of this hypothetical wave is referred to as NIP -wavefront. Therefore, the principle of CRS stacking involves summing traces in CMP gathers as if the rays originate from NIP and belong to the NIP -wavefronts. Traces are summed along a number of test hyperbolae (given by the CRS stacking operator) for specified ZO , and two-way reflection times. The test hyperbolae are characterised by parameters which determine the hypothetical wavefront. For 2D these parameters are the angle of emergence (α) of the NIP -wave at the surface and the radii of curvature of two hypothetical wavefronts (R_N , R_{NIP}). In Chapter 6, I will discuss the two hypothetical wavefronts and show their physical visualisation.

The set of parameters (α , R_{NIP} , and R_N) which are used for CRS stacking is determined through a coherency measure. The absolute value of a stacked trace is a measure of the coherency of trace amplitudes. A hyperbola for which coherency is locally a maximum is assumed to characterise the moveout of the primary reflection. The optimum stacking hyperbolae are determined for all primary reflections in the CMP gathers.

Unlike in standard processing, the CRS stack method takes into account the characteristic of the curved reflector interfaces over which energy can be smeared. It delivers wavefront attributes (α , R_{NIP} , and R_N) which characterise the orientation of the interfaces and the reflector curvature. The wavefront attributes can be used to derive an approximation of the macro-model (Hubral and

Krey, 1980). In the stacking process, in contrast to conventional NMO correction, normal moveout stretching is avoided. Note that NMO stretching occurs during stacking velocity analysis in the far offset traces.

Synthetic and experimental results have shown that the CRS stacking surface approximates seismic events in the prestack data better than conventional stacking techniques such as the NMO/DMO/Stack process. Figure 5.4a shows an example of CMP stack data that displays a poorly imaged anticline structure constructed through standard processing. The flanks and top of the anticline structure are barely imaged. Figure 5.4b shows the corresponding section after CRS stack. After CRS stacking and poststack time migration with a reasonable velocity model, the events will be more properly focused (see also Chapter 7, page 99).

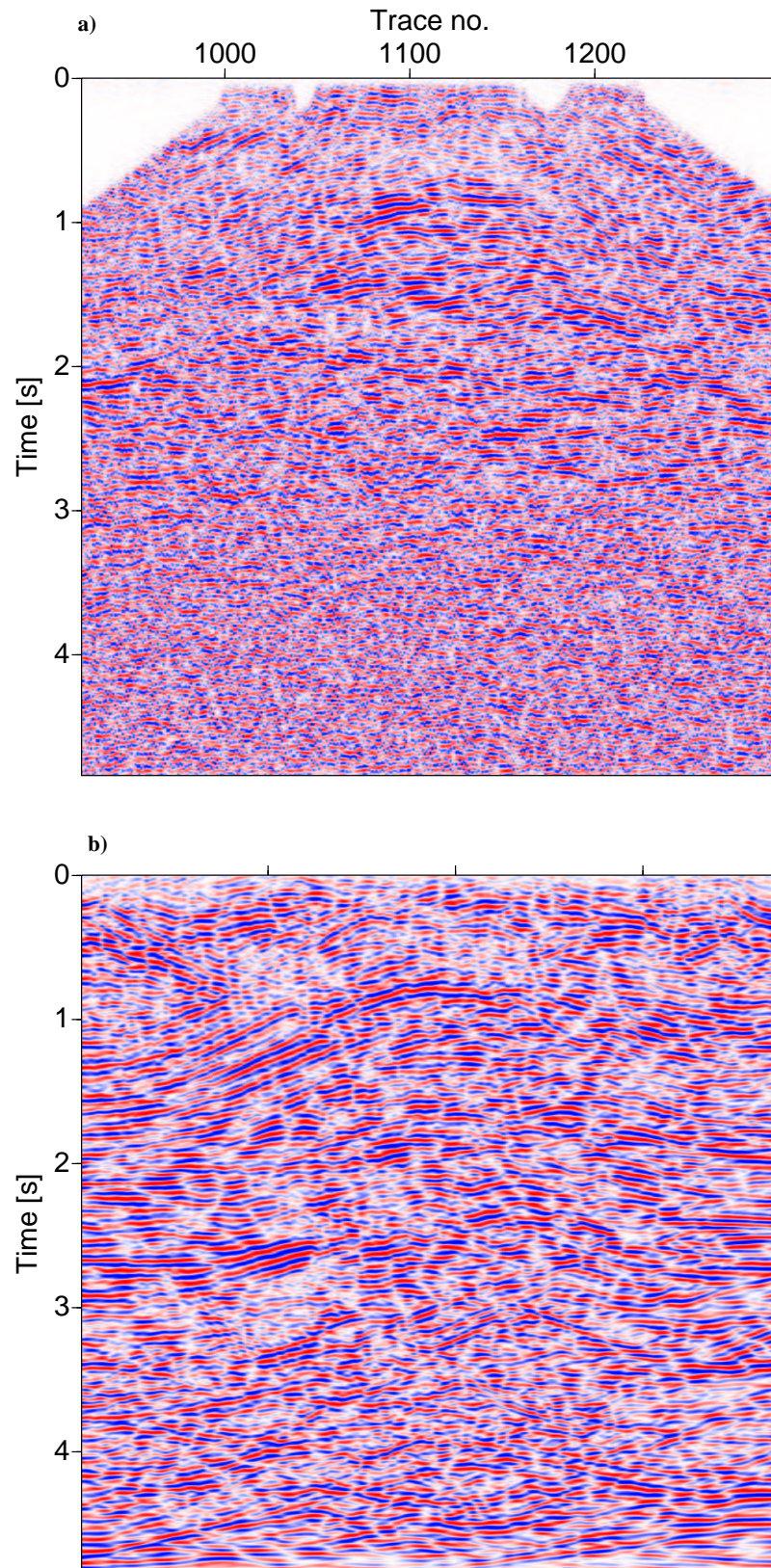


Figure 5.4: Poststack time migration of an anticline structure after conventional CMP stacking (a). The top of the anticline is poorly imaged. b) shows the corresponding CRS image displaying more continuous events.

5.5 Depth Imaging

If a coherent stacked section can be formed, time-to-depth conversion with a geologically derived velocity model (i.e. velocity model from well log) is sometimes sufficient to image horizontal or nearly horizontal structures with mild lateral velocity variations. If more dipping structures are apparent and with moderate lateral velocity variations, depth conversion after DMO, poststack time migration, poststack depth migration or prestack time migration are often needed to stack all events coherently. One successful imaging method in areas of moderate lateral velocity variation and dipping structure is to use CRS to stack the data coherently followed by poststack depth migration with a geologically derived interval velocity model (Trappe et al., 2001).

What happens when there are dipping structures and strong lateral velocity variations (such as thrust belts, salt domes etc.) and the velocity model is not known? Prestack time migration gives only approximate common reflection point gathers and reflector positions. DMO followed by poststack migration can give correct reflector positions, but only approximate common reflection point gathers (Deregowski, 1990); so it can be difficult to get a coherent stack or reasonable stacking velocity estimates. Within small offset limits, zero-offset CRS stacking followed by poststack depth migration can correctly position reflectors, give improved results, and deliver correct geometry of an interface. However, the CRS stack does not output common reflection point gathers which are needed for estimating and verifying the interval velocity model. Prestack depth migration performs true common reflection point gathering, correctly positions reflectors in depth, and output common reflection point (CRP) gathers. Therefore, if the subsurface structure is complicated and there are strong lateral velocity variations, prestack depth migration has proven to be the preferred imaging tool. CRS stacking plus poststack depth migration as discussed by Trappe et al. (2001) can also be an alternative with great potentials in 3D velocity determination. However, poststack migration of CRS images and depth imaging (PSDM) requires an appropriate interval velocity model. Therefore, obtaining an accurate estimates of the interval velocity model is the core for an accurate horizontal and vertical positioning of reflectors in structural targets.

5.5.1 An Appropriate Macro-Model

In the real world, geology is made up of layering of depositional units having variable thickness. Thin strata which are hardly a few meters of thickness are commonly observed. In geophysics the most accurate investigation of geological units in depth is achieved via well logging experiments. However, such accurate measurements are quite sparse and do not meet all exploration needs and targets (Fagin, 1998). Furthermore, they give only accurate information around the wells. Therefore, surface seismic imaging is used for investigating the geological units on a large scale.

To produce an image of the subsurface seismic methods use the kinematic information present in reflection data. Only the main velocity contrasts, which govern the wave propagation, are estimated and positioned in space. In principle vertical velocity contrasts correspond to the interface between the main geological units and horizontal contrasts correspond to the lateral velocity variations within these units. Because traveltimes do not carry enough information to produce a detailed

image of the velocities down to the scale of thin strata, geophysical models are usually subdivided into so-called **macro-layers** and major faults. Each macro-layer corresponds to a series of strata with similar stratigraphical and lithological characteristics. The fault model is an integral part of the macro-model and contains only those faults with significant throws. Minor faults are usually not included since they would only complicate the model.

Therefore, in designing the appropriate geological model from the surface seismic data, I select parameters that describe sharp velocity contrast between the main geological units, with smooth lateral variations within the units (see Chapter 9). I use the fact that the seismic reflectors set the limits of the main geological units. Therefore, the number of macro-layers are close to the number of seismic reflectors that contributes to the model inversion. Generally, other surface boundaries for which no reflection data are interpreted are illuminated by transmission wavefields only. This occurs when the contrasts in elastic parameters are too small.

As an input to prestack depth migration, two types of macro-models are generally in common place. They are categorised as structural models and smooth models. As described above, I define the structural model as a set of surfaces that separate the geological macro-layers and major faults. As such, these surfaces coincide with the main vertical velocity contrasts within the model. Fagin (1998) showed on field data examples that the macro-model which works best for prestack depth migration depends on the geologic factors that control velocity variations. If the velocity variation is most influenced by age, lithology or pressure then structural models are preferred. If the velocity is most influenced by depth, then a smooth model is desirable. Smooth models are generally used if the sediments are geologically young (Cenozoic period), or in crystalline areas where we cannot define boundaries (see Chapter 9).

Note that smooth macro-models are always produced from moveout analysis (tomography, normal moveout). Smooth models do not show any sharp boundaries of geological units. The velocities from one unit to the other are continuous. Using field data examples from the Gulf of Mexico, Egozi (1998) showed that smooth velocity models gave much better images than structural models. I note that there is a difference between a smoothed structural model and a smooth model obtained from methods like tomography. In the Donbas Foldbelt data, I use a structural model framework and its smoothed version for the prestack depth migration in Chapter 9.

5.5.2 Initial Velocity/Depth Model

Iterative prestack depth migration requires that an initial velocity/depth model be generated. The number of iteration depends on how well the initial model is close to the final model. Furthermore, the final result will depend on the initial model if no other a priori information such as well log data are available (like with the Donbas Foldbelt data). Therefore, the method used for estimating the initial model need to be carefully selected. Coherency inversion (Landa et al., 1988, 1991) is an accurate method for estimation initial interval velocities from prestack data especially in areas where there are no well information. It has the advantage that it does not require event picking as in stacking velocity analysis. However, time horizons from unmigrated stacked sections are re-

quired. The picking of wrong time horizons will lead to wrong interval velocities. Therefore, for its success a good unmigrated stacked section is necessary. Picking unmigrated stacked sections can be difficult in Foldbelt areas with forward and reverse thrust. Therefore, in this work I first perform poststack time migration and pick time horizons on the migrated sections. These horizons are then demigrated to give unmigrated picks. On the other hand, the results of poststack migration strongly depends on the rms velocity and the quality of the unmigrated stacked section. In poor quality data areas I use the model-independent CRS stack method to produce unmigrated stacked sections. These high quality sections are then poststack migrated; interpreted and integrated into the coherency inversion process.

Most often initial estimates of interval velocity sections are obtained by converting rms-velocity sections into interval velocities via Dix's formula (1955). The rms-velocity is generated from the stacking velocity model and modified to give the best migration section (prestack time or poststack time migration). Main horizons that corresponds to macro-layers can be interpreted. The interpreted time migrated horizons can be converted to depth via an image ray migration using the Dix transformed interval velocity (Fagin, 1998). In 3D this is known as map migration. In this way an initial velocity/depth model with structural framework can be obtained. This type of transform may not yield correct results for horizons with steep dips or complex structures where raypath bending is predominant (Note, that Dix formalism does not take ray bending into account).

A more accurate possibility of estimating velocities is from well log information. Sonic logs give the most accurate means of obtaining interval velocities locally. Usually poststack or prestack time migrated horizons are given sonic log interval velocities (constant or with gradients). Like in the previous possibility, the time model is converted to a depth model (using the sonic log velocities) via image ray migration (Yilmaz, 2001). After obtaining the initial depth model prestack depth migration is applied to produce the depth section and to verify and update the model. However, the upscaling of sonic logs to surface seismics is not trivial and can sometimes lead to misties.

5.5.3 Velocity Analysis for PSDM

The velocity analysis method applied for the field data in this work is an integration of CRS imaging, iterative prestack depth migration (analysis of CRP gathers and migration), structural interpretation of the migrated images and geological constraints. Since prestack depth migration cannot be used directly as a velocity analysis tool, velocity analysis is performed after the initial prestack depth migration using an initial velocity/depth model. In constructing this initial velocity/depth model I integrate information gained from migrated CRS stack sections (Chapter 9). Therefore, in building the velocity/depth model, I start by using CRS stacking and poststack time migration. This is followed by coherency inversion to give a close starting model. Thereafter I proceed to update the velocity field for a given layer using residual moveout analysis, and then delineate reflector geometries for the horizon under consideration using the depth migrated section, CRS migrated images and surface structural geology model. In essence this processing flow comprises a part for the interval velocity update (using PSDM) and another part for the horizon

geometry update (using migrated CRS stack and structural geology). The integration of model-independent and model-dependent methods yield more accurate and stable velocity/depth models. After performing the initial prestack depth migration, I used coherency analysis (i.e. observing the variation of residual moveout in CRP gathers with offset) to upgrade the model.

Another velocity updating method which is commonly used in the seismic industry is migration focusing time (Faye and Jeannot, 1986). This method combine depth-focusing analysis with downward continuation prestack depth migration. The method detects average velocity errors by imaging downward continued data not just at imaging time $t_i = 0$ but in a range $-t < t_i < +t$. If the velocity model is in error, events focus best at imaging times other than $t_i = 0$ and at depth other than their true depths $z = z_r$. The depth error measured from the focusing analysis are then related to an error in the average velocity.

Other interval velocity analysis methods are based explicitly on traveltimes tomography. As described in Chapter 1, conventional traveltimes tomography uses the traveltimes of picked events and ray tracing to find a velocity model and reflector positions that agree with the picked traveltimes. The velocity-reflector ambiguity problem (Stork and Clayton, 1991) makes solving for both, velocities and reflector depth, difficult. To get more coherent images of reflectors, Bording et al. (1987) used traveltimes tomography combined with depth migration to estimate velocity models (see also Part I of this work). Using tomography after depth migration, as is implemented in Part I, makes reflector-depth location easier or more stable.

5.6 Dissertation Outline: Part II

Chapter 6 gives a description of the common reflection surface stack method and shows its application to synthetic data. Even though physically only three parameters are required, to obtain the optimum results some other input parameters for running the algorithm are very vital. Therefore, the objective is to understand the various aspects of the CRS algorithm and its applicability under more realistic but “controlled” conditions. Furthermore, the essence of the synthetic test is to acquire a better understanding of the input control parameters. The synthetic test include data derived from the relatively complex Picrocol model.

The first part of Chapter 7 discusses the geology of the Dniepr-Donets-Basin where the field data was acquired. Because the objective of this part of the thesis is to construct an accurate structural velocity/depth model of the Donbas Foldbelt data, it is necessary to have an understanding of the geology in the survey area. Such a geological understanding aids in interpreting the depth migrated section. However, before migration the seismic data had to undergo some preprocessing in order to suppress noise and other unwanted signals. Therefore, this chapter also contains a description of the data and the major preprocessing steps.

Chapter 8 is devoted to the application of the CRS stack to the preprocessed data. The results of the CRS stack are compared to those obtained from standard CMP stacking processes.

Time migrated images of the CRS sections of certain key areas are shown to have improved image quality. The results of the CRS stacking are used for constructing the velocity/depth model. The implemented strategy for this process is described in Chapter 9.

Chapter 9 describes the construction of the structural framework of the velocity/depth model of the Donbas Foldbelt. This involves an iterative prestack depth migration and structural interpretation. Geological constraints are highly required at this level. Finally, Chapter 10 gives a summary of the dissertation with an outlook for future research.

Chapter 6

Model-Independent Time Imaging

6.1 Introduction

While depth imaging continues to play a major role in velocity/depth model estimation in complex areas, accurate imaging in time is still an important step prior to depth imaging. From the time images initial velocity models are constructed which can later be converted to depth. Therefore, this chapter describes a model-independent method which aims at improving the image quality of unmigrated time sections. The model-independent CRS stack method runs completely automatic with less or very little user intervention. Since my emphasis here is the application of the CRS stack, I will only briefly describe particular aspects of the method and I refer the reader to other publications on the subject for a detailed theory of the CRS stack method. The CRS algorithm applied in this work is the zero-offset CRS stack (ZO CRS), and it is different from the finite-offset (CO) CRS stack (see Zhang et al., 2001). To understand the algorithm I first apply it to synthetic examples and show some practical aspects. First, I will start by reviewing the so-called hypothetical eigenwave wave (*NIP*- and *N*-wave) concept (Hubral and Krey, 1980; Hubral, 1983) which is fundamental in understanding the CRS stacking technique.

6.2 The *NIP*- and *N*-Wave

In Hubral (1983) two hypothetical experiments were constructed in order to obtain true amplitude zero-offset traces. The nomenclature *NIP*-**wave** and *N*-**wave** describes hypothetical eigenwaves from these experiments. Mathematically, the wavefront curvatures of the eigenwaves are related to the second order derivatives of the Taylor expansion of traveltime function (Hubral and Krey, 1980; Jäger, 1999). A detailed mathematical background of the wavefronts is given in the above mentioned literature. In the following section I will describe *NIP*- and *N*-waves from a physical point of view. For this purpose I assume the Earth's surface is densely covered with coincident source/receiver pairs.

A ray from a source location hits a reflector at 90° and travels back along the same path to the receiver. The two-way path of the normal ray at the surface to a reflector can be associated with a ray of a hypothetical wavefront that originates at the normal incidence point (*NIP*) on the reflector (Figure 6.1a). The traveltime of the hypothetical ray is half the time of the actual

normal ray recorded at the coincident source/receiver location. Therefore, in a horizontal layer CMP experiment, all rays that connect surface points with the common subsurface depth point can subsequently be associated with the hypothetical wave that originates at the common depth point. The radius of curvature of this hypothetical NIP -wave is denoted as R_{NIP} . On a curved interface where the common midpoint and the common depth point do not coincide the situation is similar (see section 6.3.1, page 79). Each ray of the CMP gather can be viewed upon as passing through point NIP instead of through its real reflection point. Figure 6.1a shows that if the wavefront at the coincident source/receiver points propagate downwards, it will focus at NIP . Practically, the NIP -wavefront emerging at the coincident source/receiver point is approximated by a quadratic surface (Jäger, 1999). This approximation of the wavefront by a quadratic surface is valid because only the second order approximation of the traveltimes function is considered (Jäger, 1999).

In the second experiment which is illustrated in Figure 6.1b, I start by considering that when seismic data are properly stacked, the stacked primary reflection times closely approximate two-way normal times. Thus, the stacked primary reflections can be simulated with the help of normal-incidence ray modelling (exploding reflector model). If through ray modelling two-way normal times of a selected reflector element are plotted as a function of the surface coordinates, it will result in a two-way normal reflection time function (or time map in 3D). The time function can be single-valued or multi-valued (e.g. in a triplication). The normal reflection time functions can be looked upon as representing the traveltimes of hypothetical waves that originate at time zero with unit amplitude at the various reflector points and travel to the surface with half the actual local velocity of the layers (Hubral, 1983). For comparison, poststack migration can be viewed as the inverse process by which such hypothetical wavefronts at the surface are propagated back down to those reflecting interfaces using the local velocity of the layers. This type of hypothetical wavefront is referred to as the normal wavefront (N -wavefront) with the radius of curvature R_N (see Figure 6.1b). The radius of curvature of the N -wave is a function of the reflector curvature, because the N -wave originates from the reflector element.

In these experiments both NIP and N -wavefronts propagate along the normal ray and emerge with the same surface location at the same angle α_o (Figure 6.2). Figure 6.2 shows the wavefront attributes, also known as the CRS attributes or parameter triplets. The radius of curvature (R_{NIP} and R_N) and the angle of emergence (α_o) form the wavefront attributes or CRS attributes. These are the attributes that build the CRS stacking operator. In the following sections the term parameter triplets, CRS attributes or wavefield attributes are synonyms and all refer to the set (α_o, R_{NIP}, R_N) .

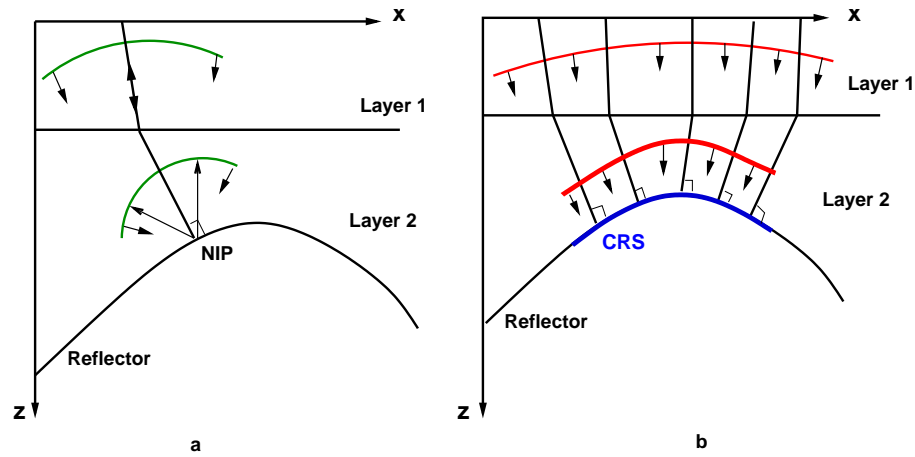


Figure 6.1: Propagation of normal incidence ray a), and normal ray b). The green curves are the wavefronts of the NIP-wave, and the red curves are the wavefronts of the N-wave. The normal incidence wave originates from a point on the interface and propagates with a velocity which is half the velocity of the overburden layers. The normal wave originates from a segment of the interface and propagates with half the overburden velocity. The normal rays are perpendicular to the segment of the interface from which they originate. The blue segment is the common reflection surface (CRS).

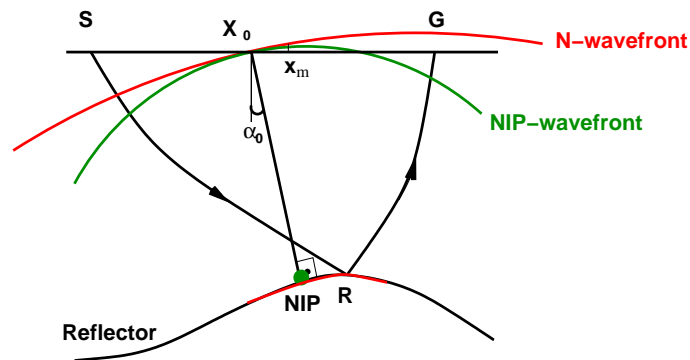


Figure 6.2: CRS attributes for a normal central ray X_0 NIP X_0 : the emergence angle α_0 and the NIP- and N-wavefront curvatures. X_0 is the central point coordinate, and S and G are the source and receiver positions for a ray reflecting at R with the midpoint x_m .

6.3 ZO CRS Stacking Operator

In the framework of zero order ray theory Hubral and Krey (1980), Schleicher et al. (1997b) and Tygel et al. (1997) described how to derive traveltimes of rays in the paraxial vicinity of a fixed central ray and they showed that the traveltime can be described by a certain number of parameters that refer to the central ray only. The approximations are correct up to the second-order of the distances between the paraxial and central ray at the corresponding initial and endpoints (Tygel et al., 1997). Assuming that the primary ZO ray of a CMP gather is the central ray, the number of parameters are three for 2D and eight for 3D wave propagation, respectively. The fixed central point X_o (Figure 6.2) on a seismic line is considered to be the location of a coincident source- and receiver pair ($S_o = G_o = X_o$) with the corresponding ZO ray, $X_o NIP X_o$, being the central ray. With this configuration Hubral and Krey (1980) derived two formulae that exactly describe the properties of the CRS stack. These formulae describe the traveltime of rays in a CMP experiment thereby taking into account the orientation of the reflector element. The formulas are the parabolic and hyperbolic traveltime formulae (see e.g., Hubral and Krey, 1980; Hubral, 1983; Tygel, 1997; Müller, 1999; Schleicher et al., 1997b; Mann, 1999). The hyperbolic formula, which is derived from the parabolic formula, is given as:

$$t_{hyp}^2(x_m, h, P) = \left(t_o + 2 \frac{\sin \alpha_o}{v_o} (x_m - x_o) \right)^2 + 2 t_o \frac{\cos^2 \alpha_o}{v_o} \left(\frac{(x_m - x_o)^2}{R_N} + \frac{h^2}{R_{NIP}} \right), \quad (6.1)$$

where t_o is the two-way normal time for a coincident source/receiver pair (ZO traveltime), v_o is the velocity at the coincident source/receiver location X_o that is defined by its coordinate x_o . If s and g are the coordinates of the shot S and receiver G on the seismic line, then $x_m = (s + g)/2$ is the common midpoint coordinate and $h = (g - s)/2$ is the half-offset coordinate; $(x_m - x_o)$ denote the relative midpoint; P abbreviates the dependence of t on the angle of emergence α_o of the ZO ray, the radius of curvature of the NIP -wave, R_{NIP} , and the curvature of the N -wave, R_N . The parameter triplet $P = (\alpha_o, R_N \text{ and } R_{NIP})$ defines the stacking surface with respect to a specific two-time ZO traveltime t_o (i.e., at each sample time). Equation (6.1) is the CRS stack operator and apart of v_o it is explicitly macro-model-independent. However, it is implicitly model dependent because the curvatures R_{NIP} , R_N and the angle α_o depend on the velocity model through which these waves propagate, but when searching for these parameters, the velocity model is not needed in order to find these parameters.

Note that Equation (6.1) is the second order approximation for the traveltime of the wavefront in the vicinity of X_o along the seismic profile. It approximately describes the traveltimes of all reflections that originate from the considered reflector element in the vicinity of NIP , i.e., that originate from an approximate quadratic reflector mirror that has the same orientation and curvature as the reflector in NIP . Therefore, the CRS stacking surface describes the multi-coverage traveltime response of the reflector mirror. As the CRS stack takes the local shape of the reflector into consideration the corresponding stacking surface fits best to the multi-coverage CMP reflection data.

6.3.1 Multi-fold Stacking

A strength of the CRS stack method is its multi-fold stacking and its ability to produce the wave-field attributes. The multi-fold advantage is schematically shown in the CMP gather in Figure 6.3. For small offsets, x the traveltime along the reflected CMP ray between source S_1 and receiver G_1 is approximated by the sum of the traveltime from S_1 to the NIP and from the NIP to G .

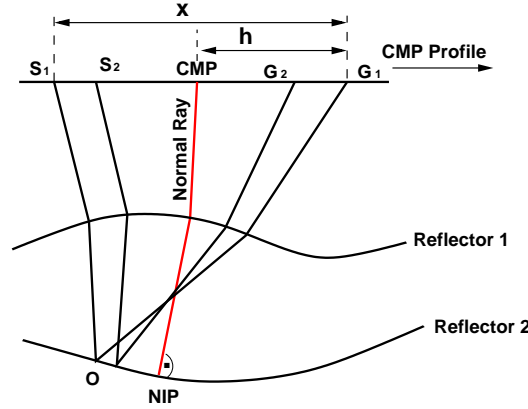


Figure 6.3: A 2D curved layer model with a normal ray (central ray) and two CMP rays. The source-receiver separation is assumed small. The traveltime along the CMP ray S_1G_1 is approximated, up to second order, by the sum of the times from S_1 to NIP and from NIP to G_1 (Hubral and Krey, 1980). Knowing the times of the normal ray, Equation (6.1) is used to approximate the time from S_1 to the NIP , i.e. S_1 is in the vicinity of the normal ray. The same is also applied for the ray from NIP to G_1 . In the CRS stack method the two-way times for the normal ray are picked for each time sample.

Hubral and Krey (1980) showed that to second order and for small values of x the raypath difference between the non-Snell's ray S_1NIPG_1 and the reflected CDP ray S_1OG_1 can be neglected. Therefore, within this approximation, rays in the CMP gather are associated with rays belonging to the hypothetical NIP -wavefront. Note that, there is a lateral displacement between the NIP from the actual reflection point. Likewise there is also a lateral displacement between the CMP ray reflection points across the reflector. Now, taking into account the NIP - and N -waves, traces from more than one CMP gather with midpoints lying in the vicinity of NIP are considered to belong to the family of hypothetical non-Snell's rays originating from NIP . The summing of all the rays (Snell's and non-Snell's rays) leads to the multi-fold stacking. Therefore, depending on the distance of the lateral displacement ($x_m - x_o$) the CRS stacking operator (Equation (6.1)) will implicitly increase the stacking fold. Practically, this distance is determined by the aperture h . The increased stacking fold eventually lead to an improvement in the S/N-ratio of the CRS images. While DMO tries to remove reflection point dispersal so that conventional stacking should stack the traces constructively, CRS stacking do not need to remove reflection point dispersal. Instead the traces are summed over the surface which contains the reflection points. Therefore, the reflector surface over which the CMP rays are distributed is imaged. Since the imaging is based on the radii of curvature, it directly preserves dipping events which is the key property of DMO

correction (see Yilmaz, 1987).

After describing the hypothetical waves and the CRS stacking operators, the most crucial part is the determination of the wavefield attributes. These wavefield attributes have to be determined for each sample (x_o, t_o) in the stacked section to be generated.

6.4 Stacking Procedure

6.4.1 Statement of the Problem and its Solution

In CRS stack the basic problem to be solved can be formulated as:

We consider a dense grid of points (x_0, t_0) , where x_0 locates a central point X_o on the seismic line and t_0 is the zero-offset traveltime. For each central point X_o , and a given near surface velocity $v_0 = v(x_0)$, the question is to determine the corresponding parameter α , R_N , R_{NIP} , from multi-coverage seismic data for any given point (x_o, t_o) .

This problem is solved by computing synthetic reflection surfaces for all possible orientations and curvatures in every subsurface point. The optimal parameter triplets are those for which the traveltime surface “best” correlates to the CMP reflection events.

6.4.1.1 Coherency Measures

The approach used to solve the above problem is the application of automatic coherency measures to the multi-coverage data. We use the traveltime formula (Equation (6.1)) for a number of selected traces, $U(x_m, h, t)$, in the vicinity of the normal incidence ray X_o and for a suitable time window around the time t_o . Unlike in standard stacking velocity analysis, the human eye for picking coherent reflection events is replaced by automatic picking. The output map (i.e., the parameter(s) spectrum) is a surface representing coherency measure versus two-way ZO time and stacking parameters.

Practically, at particular two-way time, t_o , a coherency measure is computed for various hyperbolic trajectories corresponding to a specified series of test stacking parameters, e.g. the emergence angle such that $-\pi/2 \leq \alpha \leq \pi/2$. A coherency value is computed for each of the test stacking parameter at the fixed chosen time t_o . The position of the maximum value of coherency determines the optimum stacking parameter of a particular event. By increasing t_o by an appropriate amount (usually by the sample rate, Δt), the search is repeated for different t_o -values over the entire target length of interest. From this principle, the optimum stacking parameters are estimated as a function of two-way ZO time.

Different coherency criteria can be applied along the respective stacking trajectories. The commonly used coherency measure is semblance, as introduced by Taner and Koehler (1969). The semblance is defined as:

$$S_c = \frac{\sum_{t=t(i)-w/2}^{t(i)+w/2} \left(\sum_{i=1}^M U_{it} \right)^2}{M \sum_{t=t(i)-w/2}^{t(i)+w/2} \sum_{i=1}^M U_{it}^2}, \quad 0 \leq S_c \leq 1, \quad (6.2)$$

where $w + 1$ is the width of a symmetric temporal window and M is the total number of selected traces; the seismic trace is denoted as U_{it} , where i refers to the trace index, and t is the time index (sample number $j \Delta t$, j is an integer). The inner summation is performed over all selected traces, and the outer one is performed over the given time window around t_o . To account for temporal extension of the wavelet, the coherency criteria are applied to a temporal window centred around the stacking trajectory. The size of this window is given as the coherency band. Therefore, for each given pair (x_o, t_o) , the objective is to find the maximum of the semblance function with respect to the parameters α , R_N , R_{NIP} . The parameters are restricted to the range $-\pi/2 < \alpha < \pi/2$, $-\infty < R_N, R_{NIP} < \infty$. With the correct parameter triplets the stacked amplitude of M input traces is given by:

$$s = \sum_{i=1}^M U_{it}. \quad (6.3)$$

The absolute value of s exhibits a maximum when the stacking trajectory corresponds to the maximum stacking parameter, i.e., when the CMP events are properly aligned. In the semblance spectrum the optimum parameters are automatically picked and validated. The picking and validation is described in the next section.

6.4.1.2 Automatic Picking and Validation

The strength and at the same time weakness of the CRS stacking method is that it is automatic, i.e it requires very limited user intervention. A stacking parameter function is constructed by connecting those peaks in a spectrum which are considered to represent primary reflection energy buildups. To handle large amounts of data, automatic picking of semblance maxima is advantageous. Another advantage is that the optimum stacking parameters are data-driven instead of interpreter controlled. However, in such automatic picking, all possible semblance maxima can be picked. This will result in both valid and spurious picks. The valid picks will result from those with high probability of being primary events. The spurious ones will result from picking minor lobes, multiples, diffractions, and aliases. For example, problems of maximum semblance picking occurs in areas where the stacking parameters of primaries does not increase monotonously with depth. Here multiples may have higher stacking parameters than do primaries at equal times. Therefore, the automatic picks have to be validated. One possibility to validate the picks is to observe the by-products of the CRS algorithm (high density stacking velocity and coherency sections). The coherency sections and stacking velocity sections must interactively be interpreted in order to discriminate true reflection events from noise or possible multiples. The semblance maxima should coincide in time with the peak energy concentration of the reflection events.

6.4.1.3 Stability of parameters

To ensure stability in stacking parameter estimates, the temporal windows which account for the wavelet extension are chosen such that they overlap by about half their window length. They should not be shorter than about the dominant period of the coherent wavelets of a reflection event. For this reason the default value is given as $1/(f_{main} \cdot \Delta t)$, with f_{main} being the main frequency of the signal. Broadening the window length leads to loss in resolution.

Furthermore, it is required that the wavelet character be more or less constant with offset. Like in conventional stacking velocity analysis, muting reflections on the far offset traces is preferable because the wavelet character often changes with increasing angle of reflection. Both offset dependence of wavelet character and possible interference with mode-converted waves can bias the stacking parameter picking. Therefore, it is recommended to choose the stacking aperture (see Section 6.5.3, page 95) such that very far offset traces will not be included in the analysis. To ensure stability in R_{NIP} and R_N , the offsets, whether between source and receiver or between the normal incident ray location and the neighbouring positions, must be small relative to the distances travelled along the reflected ray paths.

6.4.2 Search Strategy

As described previously, the CRS stack basically consists of a measure of the coherency of the multi-coverage prestack data along all operators given by Equation (6.1) for any possible combination of values of α , R_{NIP} , and R_N within a specified test range. In practice, one has to determine the global maximum of the parameter triplets in the domain, in which α_o , R_{NIP} and R_N are distributed along the corresponding axes (see e.g Müller, 1999). However, the determination of the global maximum is too time consuming in a simultaneous three-parametric search strategy and therefore, unpractical. Such a simultaneous three-parametric search was proposed by Landa et al. (1999). Müller (1999) and Mann et al. (1999) proposed to split the three-parametric search problem into three one-parametric searches and an optional three-parametric optimisation. The first search step produces a preliminary ZO section (automatic CMP stack) and the search parameter is the stacking velocity. The next two steps are applied to the ZO section from the first step. The search parameters in this second step are α , and R_N . Because R_{NIP} and α are directly linked R_{NIP} is obtained after α is known. After obtaining the parameters on each individual search step, they are then input into Equation (6.1) to produce the final stack. In the next section I will describe each step of the search strategy.

6.4.2.1 Automatic CMP Stacking

The first step in the search strategy is the automatic CMP stack. This automatic CMP stack is similar to conventional CMP stacking. In the conventional CMP stacking process stacking velocities, v_{stk} , are determined by means of semblance velocity analysis, whereas in CRS a q -parameter scan is automatically performed by means of the coherency analysis. For this reason the simulated ZO section is referred to as the automatic CMP stack. The stacking trajectory is obtained by setting in Equation (6.1) $x_m = x_o$:

$$t^2(h, q) = t_o^2 + \frac{2t_o h^2}{v_o} q, \quad (6.4)$$

where

$$q = \cos^2 \alpha / R_{NIP}. \quad (6.5)$$

In this step the search parameter is the stacking velocity which is written in terms of the CRS wavefield attributes, R_{NIP} and α , as:

$$v_{stk}^2 = \frac{2v_o R_{NIP}}{t_o \cos^2 \alpha} = \frac{2v_o}{t_o} \frac{1}{q}. \quad (6.6)$$

Comparing Equation (6.4) with the CMP hyperbola in its classical representation (Equation (5.1)), it is directly seen that the q -parameter is related to the normal moveout or rms velocity in the form: $q = 2v_o/t_o v_{stk}^2$. For a horizontally layered medium the rms velocity is therefore directly related to R_{NIP} ($v_{rms}^2 = 2R_{NIP}v_o/t_o$).

Therefore, scanning for the q -parameter is equivalent to scanning for v_{stk} . The search for q is performed on the prestack CMP gathers according to Equation (6.4). The generated automatic CMP stack section is considered as an approximate ZO section. The result from the automatic CMP stack and conventional CMP stack usually do not differ very much. Therefore, the automatic CMP stack section can be replaced by the stack section obtained after standard velocity analysis.

Apart of the automatic CMP stacked section, other important by-products of this first step are the square of the stacking velocity section and a coherency section. Note that every ZO sample carries a stacking velocity value. This of course leads to a high density and high resolution stacking velocity section. If the CRS stacking velocity section is to be used for further processes, then one has to interpret the velocity section. One can pick velocity functions of main reflectors from the CRS stacking velocity section. The picking of stacking velocity functions should be combined with interpreting the coherency section. The coherency section provides a confidence criterium for identifying reflection events. One has to be aware of the fact that the automatic CMP stack will sum up all coherent events within a CMP gather which can approximately be described by hyperbolae. This is true for primaries as well as multiples (see Section 6.4.2.4).

6.4.2.2 Second Step: Scan for Parameters α , R_N and R_{NIP}

This is the most critical step because all three parameters (α , R_N , R_{NIP}) are obtained in this stage. The results of the simulated ZO section (i.e. the automatic CMP stack and q -parameter) from the first step are submitted into this step for the wavefront attribute analysis. The analysis is performed with Equation (6.7):

$$t^2(x_m, \alpha, R_N) = \left(t_o + \frac{2\sin\alpha}{v_o} (x_m - x_o) \right)^2 + \frac{2t_o \cos^2 \alpha}{v_o} \frac{(x_m - x_o)^2}{R_N}. \quad (6.7)$$

Equation (6.7) is obtained by setting $h = 0$ in Equation (6.1). This equation is a shifted hyperbola because the apex of the hyperbola is shifted with respect to the location of the considered point

(x_o, t_o) in midpoint time direction. In the ZO section, the traveltime hyperbola (Equation (6.7)) depends only on α and R_N . These two parameters are searched for in a one-dimensional search procedure. First we set $R_N = \infty$ in Equation (6.7) and determine α according to (plane wave equation):

$$t(x_m, \alpha) = t_o + \frac{2 \sin \alpha}{v_o} (x_m - x_o) \quad (6.8)$$

This is a linear expression in $(x_m - x_o)$ (see Müller, 1999), and setting $R_N = \infty$ implies the reflector is a plane surface. Therefore, to take into account this linear expression in the search for α -parameter, a relatively small stacking aperture has to be chosen in the ZO section. In will come back to this in Section 6.5.3.

After obtaining the α -parameter with the maximum coherency, R_{NIP} is obtained through Equation (6.5). Next, α is directly substituted into Equation (6.7) and the next one-parametric search for R_N is performed. As Equation (6.7) provides a second-order approximation, a larger aperture is used during the search for R_N . The choice of the aperture size is critical at this stage (see Section 6.5.3, page 95).

The search for α , and R_N using the automatic CMP stack section is directly related to the theory of the hypothetic normal incidence and normal wave. Because the result of the automatic CMP stack is input for the second search step, the generation of an “accurate” automatic CMP stack section in the first step is vital for the results of α , and R_N .

6.4.2.3 Initial and Optimised CRS Stack

Finally, for every ZO time sample in the target zone to be imaged, initial values of the stacking parameter triplets are available. Each triplet combination defines a CRS stacking surface in the (x_m, h, t) domain. Summing up the CMP prestack data along these surfaces (using Equation (6.1)) and assigning the summation result to the respective ZO time sample yields the Initial CRS stack section. The word “Initial” is used because the CRS stack attributes used for the stacking serve as initial values for an optional optimisation process. Coherency analysis of the initial CRS stacking surface with the prestack data provides its own coherency section. This section is used to estimate the quality of the fitting of the CRS stacking surfaces to events in the prestack data. Contrary to the automatic CMP stack, the simulated ZO-stack of step II is not used in subsequent steps. It can only be used for quality control purposes.

Usually after obtaining the initial values, an optimisation of these values follows. There are different optimisation algorithms which can be used (Jäger, 1999). In the framework of the CRS stack, the flexible polyhedron search is applied as a local optimisation algorithm. For details interested readers should refer to the work of Jäger (1999) and Perroud et al. (1999). The optimal stacking parameter triplets are finally used for stacking the prestack CMP gathers. This yields the final CRS stack section. Note that like any optimisation process, the optimised parameter triplets are confined within the vicinity of the initial estimates. Therefore, sometimes the initial values are

good enough. In the examples of this work, I did not apply the optimisation process since it was too time consuming. However, my experience with a smaller data volume shows that the results of both initial and optimised CRS stack are very similar.

6.4.2.4 Near Surface Velocity and Constraints

As given in Equation (6.1) the only required model parameter is the near surface velocity, v_o and it is assumed to be constant. In a marine environment the water velocity of 1500 m/s is always available. For land data an average near surface velocity is used. Because refraction statics (field statics) are usually performed, the average near surface velocity is readily known. With the correct near surface velocity, the CRS stacking parameters give rms measures for the angular orientation of the reflection surface (via α_o , the distance and the local curvature of the reflector (via R_{NIP} and R_N). If v_o is not known or an arbitrary value is assumed the CRS stacking still give stacking parameter triplets that maximise the CRS objective function. In such a case, the output parameter triplets should be interpreted with care. From my experience if imaging is the only goal of the CRS stacking, the knowledge of the exact near surface velocity is not necessary. Any arbitrary value other than zero can be used since the value of v_o does not affect the quality of the stacked image. On the other hand, if the parameter triplets are to be used for other inversion purposes e.g. inverting for the macro interval velocity model, then an accurate v_o value should be estimated. Given v_o the data driven CRS stack automatically searches for stacking surfaces in the time domain that fits in an optimal way to the reflection events in the prestack data.

As discussed in Section 6.4.1.2 the automatic CRS stacking method can easily stack coherent events as well as spurious events. Multiples are stacked if not previously suppressed through deconvolution and/or other processes. In conventional stacking methods, stacking velocity models can be chosen such that multiples are rejected. If multiples can be described by the hyperbolic moveout formula given in Equation (6.1), the CRS stack would also find stacking parameter triplets for these multiples. However, the search parameter space can be constrained in order to suppress multiples. Note that primaries usually have less moveout (i.e. higher stacking velocity) than multiples therefore, the multiples can be identified and suppressed during the automatic CMP stack. For the purpose of suppressing CRS parameters which describe multiples, a rough estimate of the stacking velocity of the survey area is necessary.

The stacking velocity field from conventional NMO analysis can be used as a minimum velocity limit to build a constrain function for the q -parameter. Using Equation (6.5) the regional stacking velocity can be transformed into q -values. This constraint is the upper limit for q -parameter and has the same effect of suppressing multiples. Therefore, CRS stacking parameters that correspond to surface or water bottom multiples can easily be rejected. If no stacking velocity field is available the minimum and maximum stacking velocity values are sufficient. Using a minimum and maximum stacking velocity leads to the name “constrained automatic CMP stack”.

The minimum, average and maximum stacking velocities can be obtained iteratively during the fast automatic CMP stack. In the initial stacking velocity section, v_{stk}^{ini} , determined by the automatic

CMP stack, multiples and other coherent noise are identified in a similar manner as in velocity spectra of conventional velocity analysis. This information is used to set up the constrained search function. The process can be repeated until an optimal automatic CMP stack section is obtained without multiples. Another alternative is to use the CRS attributes as proposed by Zaske et al. (1999) or to replace the automatic CMP stack by standard velocity analysis and a standard CMP stack. Thus commonly used techniques to suppress multiples could be applied.

6.5 Synthetic Example

This section describes the application of the CRS algorithm to synthetic data derived from the complex Picrocol model. The aim is to understand the various aspects and applicability described in the previous section under realistic but “controlled” conditions. Furthermore, the essence of the synthetic test is to acquire a better understanding of the input control parameters, which frequently require some fine tuning. Some comments on the input parameters are given in Section 6.5.3 The generated CRS stack results are compared to the results after conventional NMO/DMO stack.

6.5.1 Picrocol Model

A 2D PP structural synthetic data set computed for the Picrocol model (from Brokešova et al., 1994) is used. The model was designed at the French Petroleum Institute (Institute Français du Pétrol, IFP). It was designed to be a nontrivial model but with less complexity than the Marmousi model (Versteeg and Grau, 1991). Figure 6.4 shows the structure of the model. The model parameters (velocity and density) for generating the synthetic data are given in Table 6.1.

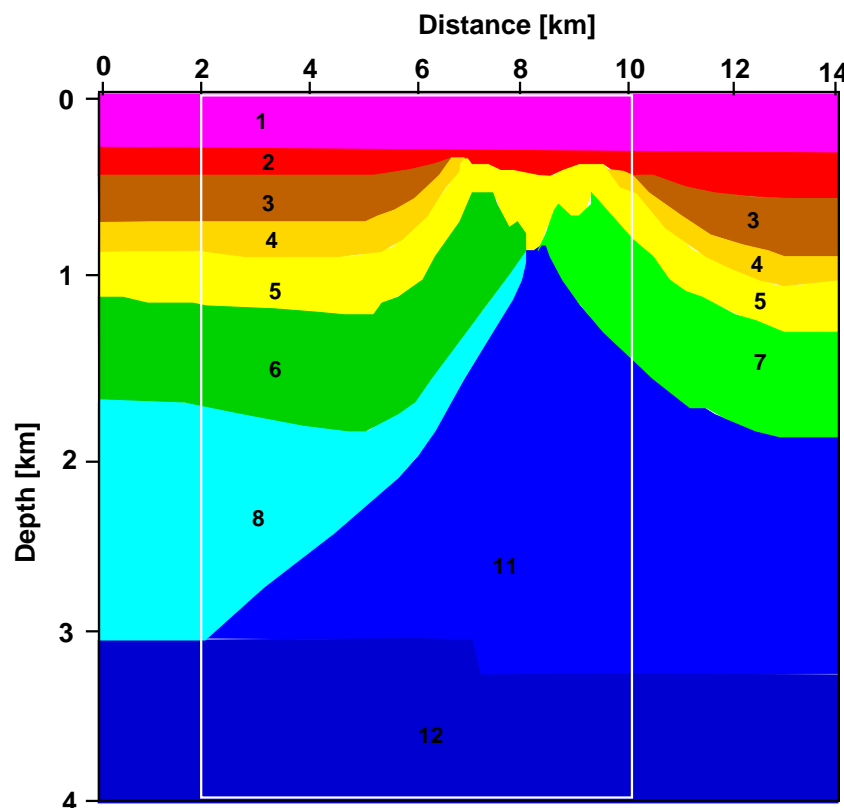


Figure 6.4: 2D structure of the layers in the Picrocol model. The model contains a salt diapir that pierces horizontal layers, folding and uprising them near the flanks and breaking them in and above the cap rock. The white box indicate the area of acquisition.

The model contains a salt diapir that pierces horizontal layers, folding and uprising them near the flanks and breaking them in and above the cap rock. The base of the salt is horizontal and slightly faulted and situated at about 3.5 km depth. The synthetic data were generated at the Institute of Geophysics, University of Hamburg, Germany, for experimental purpose, using the acoustic ray tracing algorithm of the Norsar software. The source wavelet was a Ricker wavelet with a

Layer	Density	Velocity
1	2.0	1.70
2	2.1	1.80
3	2.1	2.00
4	2.2	2.20
5	2.2	2.31
6	2.25	2.45
7	2.3	2.80
8	2.4	3.20
9	2.45	3.50
10	2.55	4.20
11	2.2	4.50
12	2.7	5.00

Table 6.1: Acoustic parameter of the model "Picrocol". Density values are given in g/cm^3 , and the velocity values are given in km/s

main frequency of 25 Hz and maximum frequency of 50 Hz. An end-on-spread of 4 km was chosen with 200 receivers. The acquisition geometry did not cover the whole model but was limited to 2 - 10 km (white box in Figure 6.4). The total number of shots required for a 20 fold coverage was 81 with 100 m shot interval and 10 m receiver spacing.

Before the CRS stack imaging, the data were passed through some preprocessing steps such as spherical divergence compensation, muting of first break arrivals and spiking deconvolution. The preprocessing and the conventional NMO/DMO stack were performed using FOCUS 2D software of Paradigm Geophysical. A constant velocity fk-DMO algorithm was used. The result of the conventional NMO/DMO stack is shown in Figure 6.5. Velocity analysis was performed via standard methods at every 10 CMP gather interval.

For the CRS stacking, rather than trying all possible combinations of stacking parameter triplet simultaneously (Landa et al., 1999), I applied the one parametric search approach. This approach proved to be efficient and fast. The results produced by the CRS stack are usually contaminated by some high frequency noise. Therefore, after CRS stack I applied a trapezoid bandpass filter (3/10 - 40/55 Hz) in order to remove the high frequency noise.

6.5.2 Results

Figure 6.5 displays the stacked image of the data set after applying NMO/DMO. This Figure is used as a comparison for the CRS stack images. This horizons seems to be rough with small fluctuations. On the model in Figure 6.4 no such fluctuations are present. Therefore, it is probable that this is due to the coarse velocity sampling. The CRS stacking process starts with the estimation of the combined parameter q which is related to the stacking velocity (Equation (6.5) and (6.6)). This step performs a one-parameter q -search on the prestack CMP gathers. For each midpoint x_o , taken as a central point (representing the response of the central ray), the corresponding CMP gathers

are considered.

For each (x_o, t_o) in the automatic CMP stack to be generated a coherency value is computed along the hyperbolae given by Equation (6.5) for a given range of q -values. The q -value with the highest coherency is selected. The above procedure leads to the construction of three auxiliary CMP related sections, namely, the q -section, the square stacking velocity section and the coherency section. The q -search is performed iteratively within the given range. The search range may be refined for greater accuracy with the maximum number of iterations being three. Higher number of iterations gave no further improvements. Within the search range the search step sample rate can take the value 1, 2 or 3. Figure 6.6 shows the result from the automatic CMP stack process. This section is generated without any use of velocity information apart of the near surface velocity ($v_o = 1.7$ km/s). Note that this result does not depend on the given value of v_o . The automatic CMP stack section is an intermediate result and is used as input to the subsequent angle and N -wave curvature search. Note that the accuracy of the automatic CMP stack determines the accuracy of the estimated parameter triplets.

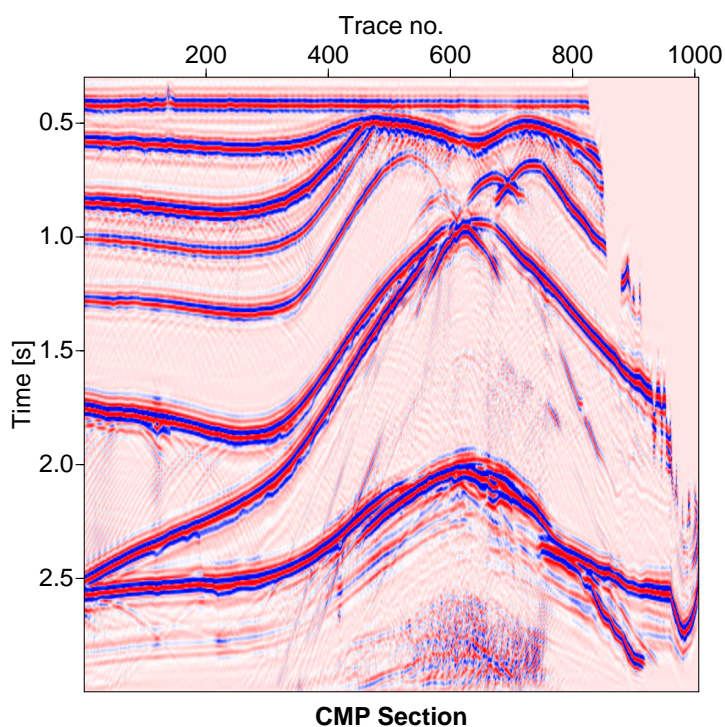


Figure 6.5: NMO/DMO stack section of the Picrocol data set. Note the pull-up of the faulted base of salt at about 2.2 s due to the high salt velocity.

Figure 6.7 shows the zero-offset section of the CRS stack. As compared to Figure 6.5 the reflector continuity is highly improved. This is especially observed on the reflector which maps the flanks of the salt dome structure. In Figure 6.5 the reflector seems to have flexure and small faults even though there were no such features on the model. The triplicated features and diffractions in

Figure 6.7 are very well focused. This is an indication of the good fit of the CRS stacking surfaces to the prestack data. The surface-wise summation guarantees a larger fold, since the summation surface extends over more than one CMP gather. In case of noisy data this will lead to an increase of the S/N-ratio (see examples in Chapter 7). The coherency section (Figure 6.8) displays consistency with Figure 6.7. The reflectors stand out significantly from the noisy part. This section is used to estimate the quality of the fitting of the CRS stacking surfaces to events in the prestack data. The generated coherency section needs to be interpreted in order to identify detected coherent events. It represents a confidence level, since it is a direct indicator of the reliability of the generated stacked section. High semblance values in the coherency section are associated with strongly correlated events. Around the reflectors the semblance values are in the order of 0.8 to 1.0, while in the noise they are up to about 0.2. Low coherency values indicate that no events with moveouts according to Equation (6.1) are detected. Low coherency values also imply that the corresponding attributes at this location have less significance and can be cut out.

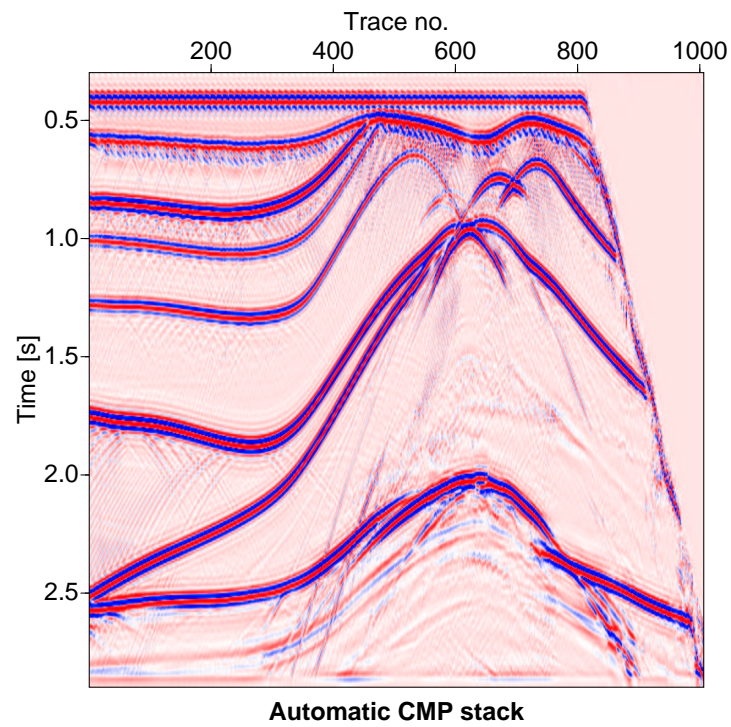


Figure 6.6: Automatic CMP stack section generated from the first CRS step

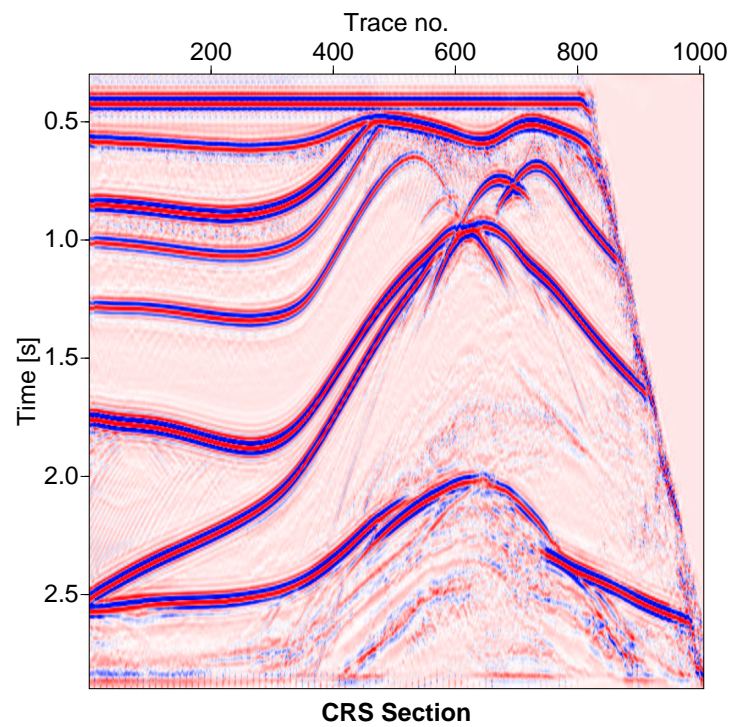


Figure 6.7: CRS stack section. The most significant difference between this figure and Figure 6.5 is the S/N ratio and the smooth character of the reflectors. The S/N ratio is much larger for the CRS stack image.

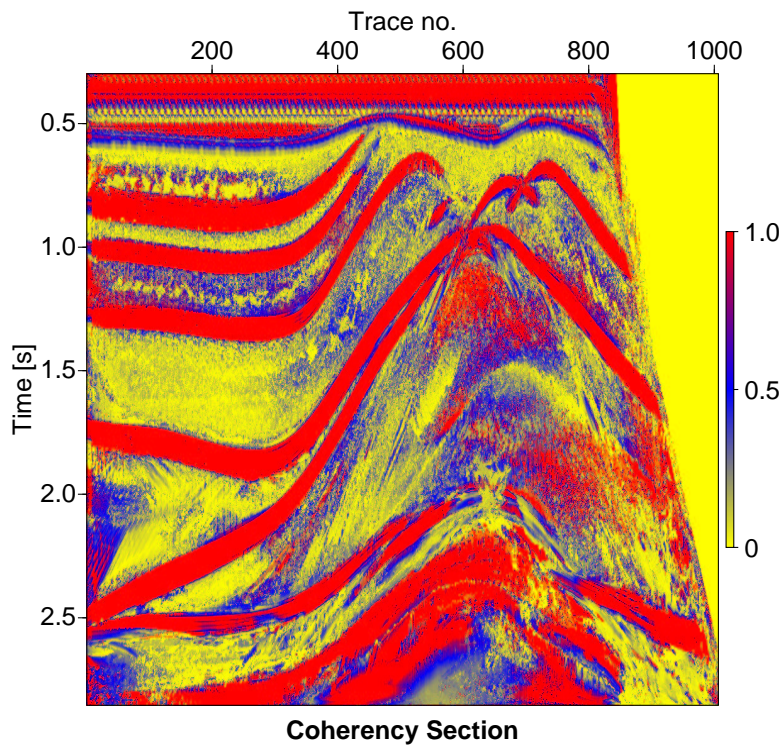


Figure 6.8: Coherency section (semblance) of the CRS stack. The reflectors stand out significantly from the background noise. Around the reflectors the semblance values are in the order of 0.8 to 1.0, while in the noise they hardly exceed 0.2.

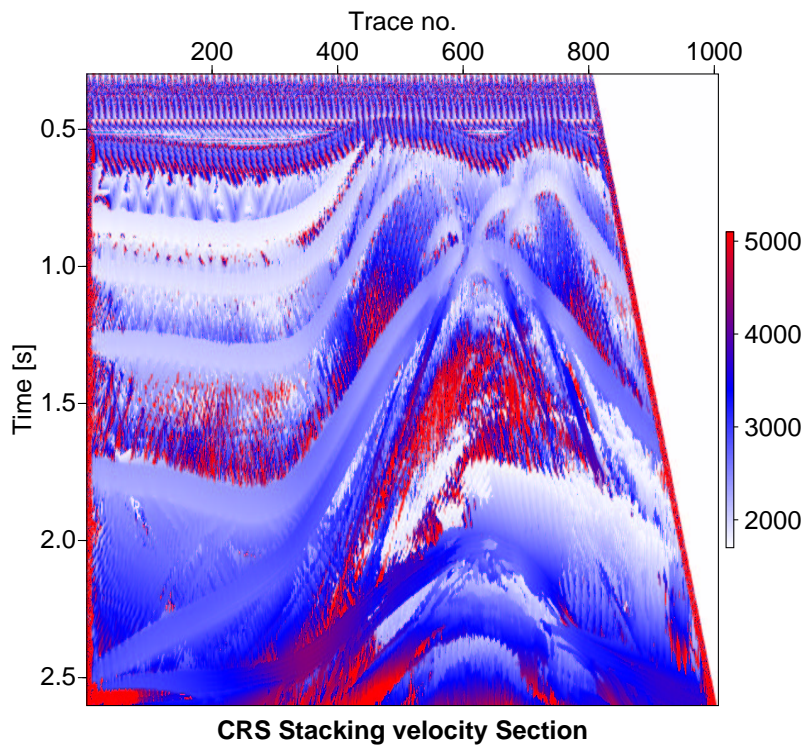


Figure 6.9: Stacking velocity section [m/s] from the R_{NIP} section and the α section.

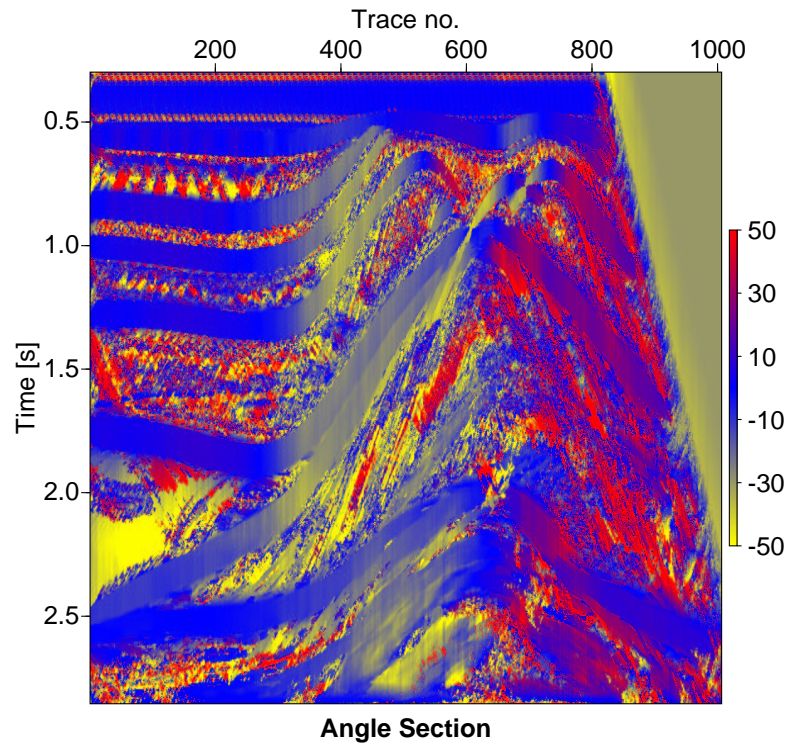
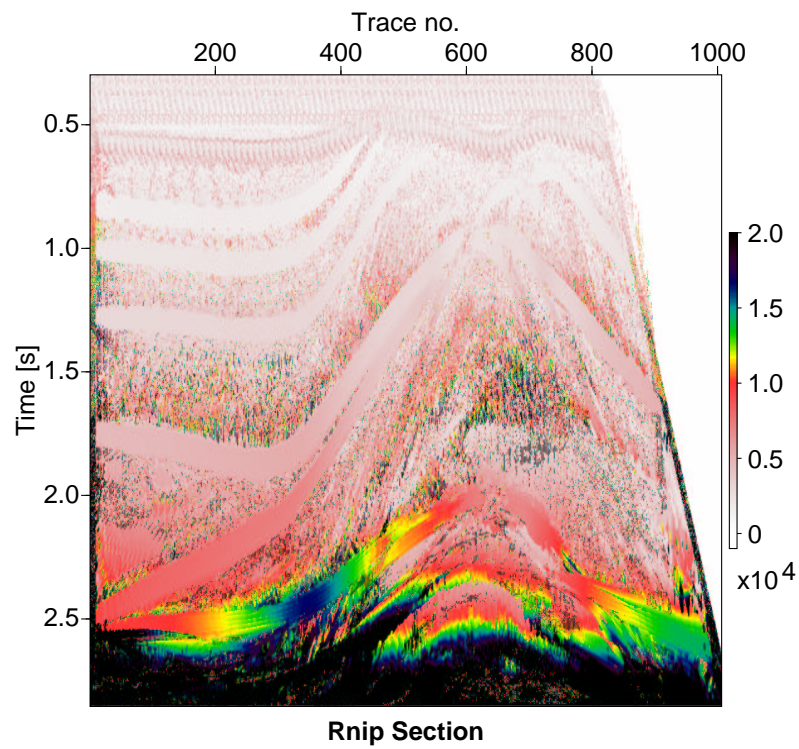
Figure 6.10: Angle section [$^{\circ}$]

Figure 6.11: Radius of curvature of NIP -wave [m]. This CRS stacking parameter shows a smooth behaviour similar to the stacking velocity and the angle of emergence.

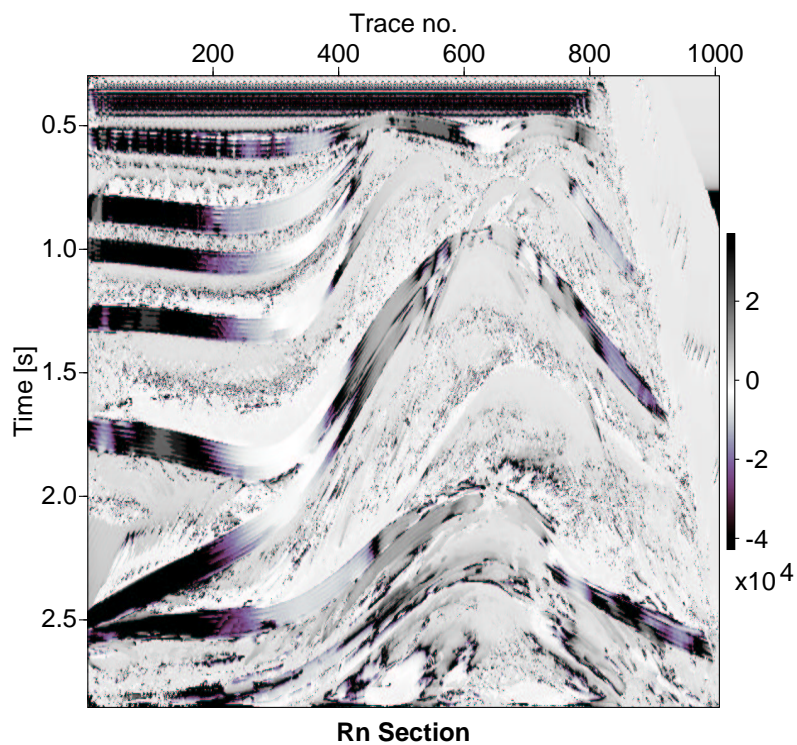
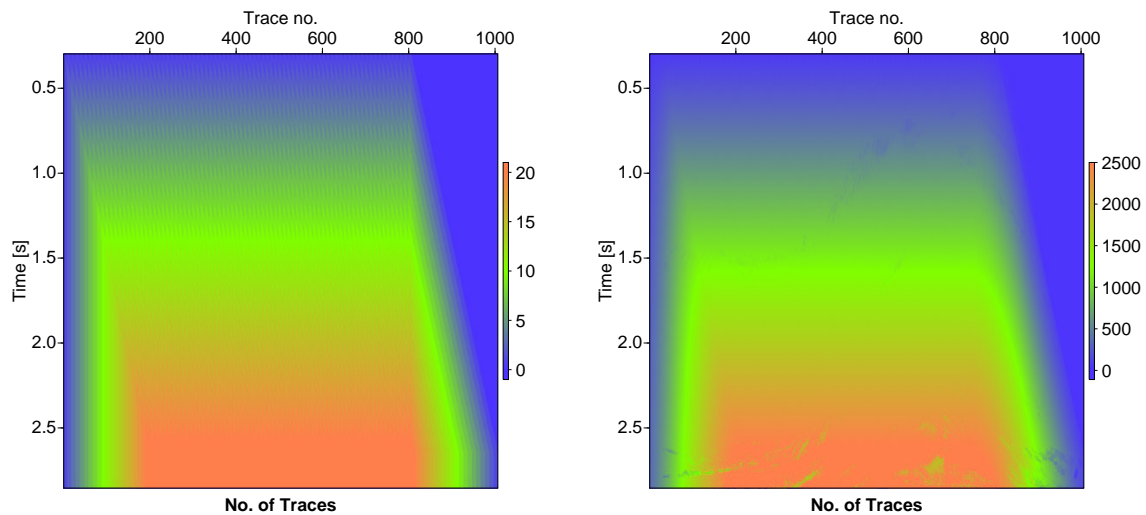
Figure 6.12: Radius of curvature of N -wave [m]

Figure 6.13: Number of traces used to image one particular ZO time sample for the automatic CMP stack (left) and the CRS stack (right).

In the coherency sections, the semblance values are plotted as a function of trace number and the ZO traveltime. In Figure 6.8 all of the reflection events, starting from the first reflector are identified. In this synthetic test the semblance values are very high with a maximum value of 1.0 and decreases with increasing ZO traveltime. This is due to the decreasing S/N ratio that goes along with increasing geometrical spreading loss. However, the semblance values along the horizons are clearly distinguishable from the surrounding noise. It is seen that the low coherency values belong to the noisy part of the section. The high coherency values are along the reflectors. This coherency section is usually interpreted together with the section in Figure 6.7.

Figure 6.9 shows the generated stacking velocity section. This section is generated during step I. The values range from 1700 to 5000 m/s. It is computed from Equation (6.5) using the parameters α and R_{NIP} which are shown in Figure 6.10 and 6.11. In Figure 6.10 the emergence angle section is displayed. This parameter is displayed in the range from -50° to $+50^\circ$. The negative values indicate the change in ray direction on emergence at the surface. Figure 6.11 and Figure 6.12 are the R_{NIP} and R_N sections. As expected, the NIP -wave radius of curvature increases with increasing ZO traveltime since it is an rms-measure for the distance of a potential reflector segment to the surface. The CRS stacking parameter R_{NIP} and α contain all important information of the velocity distribution. These information are used for obtaining the required stacking velocity shown in Figure 6.9. From the stacking velocity section Dix's interval velocity and reflector depth can be inverted. The R_N -wave radius can take values between $\pm\infty$. Note that a value of $R_N = \pm\infty$ would correspond to plane reflectors. In Figure 6.12 large values of R_N can be seen along events that correspond to almost plane layered structures. Using Equation (6.7) the angle of emergence α is determined for every ZO time sample. In analogy to the automatic CMP stack, a discrete number of α -values between -60° to 60° is scanned. For each value of α , Equation (6.7) is computed and correlated with zero-offset data. The value that yields the highest correlation is selected. A summation of the ZO data along Equation (6.7) into the ZO-time sample yields the ZO stack section. This name is so chosen because only ZO data are used in the stacking process. Similar to the automatic CMP stack, a coherency section is obtained. The ZO stack is only used as a quality check.

It is clear from this section that the accuracy of the ZO section generated in the first step determines the accuracy of the values obtained for the parameter triplets. Therefore, a requirement is that the automatic CMP stack result should be accurate enough and show the main reflectors. The N -wave radius of curvature is the most sensitive parameter, and can be very unstable. Finally, Figure 6.13 shows the number of traces that were used by the automatic CMP stack and the CRS stack to image one time sample. For this example the CRS stack uses a maximum of about 2500 traces to simulate one ZO time sample. The CMP stack uses a maximum of 30 traces.

6.5.3 Comments

As it has been shown in section 6.4, the CRS stacking operator uses three wavefront attributes (α , R_{NIP} , R_N). The accuracy of estimating these attributes depend on the input parameters of the algorithm. Most of the input control parameters require fine tuning and readjustment in order to

lead to optimal attribute sections. I discuss now some main input parameters which can strongly influence the results.

One parameter controls the temporal window within which semblance analysis is performed (see Section 6.4.1.1). In this window, attributes with high coherency are automatically picked and stored. Note, that a coherency section is produced by all the search steps as well as in the final CRS stacking itself. Therefore, the value of this input parameter can be used through out the algorithm. Because the data volume and quality changes during the different search steps, this parameter can be adjusted before starting each search step. The size of the temporal window is given as $2 \cdot cohband + 1$. My experience shows that a value within $5 \leq cohband \leq 8$ gives good results for all α , R_N , and R_{NIP} parameters.

Generally, the prestack multi-coverage seismic data can be transformed before they are input into semblance analysis. The input parameter *convop* in the algorithm determines the type of seismic traces to be used during the semblance coherency computation. The different possibilities are to:

- Use the original traces,
- Use analytical traces (i.e, trace envelopes),
- Use normalised traces
- Use normalised analytical traces.

Note that after the best stacking parameter is obtained, the stacking is performed on the original traces. I recommend not to use analytical traces in the semblance analysis. In the current version of the algorithm this led to some errors. For crustal data normalised traces are also recommended in order to avoid signal variations within the stacking aperture (Mann, personal Communication).

Another important parameter which affects the results is the size of the summation aperture. The parameter h in Equation (6.1) defines the aperture within which the trace stacking is performed. The aperture size plays the most important role on the speed of the algorithm as well as for the quality of the result. The aperture is defined in terms of the trace distance from the central ray at position x_o . Only those traces within the aperture are summed. Therefore, if the aperture is small only a small number of traces are stacked. This definitely will lead to a fast run of the algorithm. On the other hand, a too large aperture implies that a larger number of traces be summed and thereby leading to a more computer intensive run of the algorithm. Note that large aperture size brings with it more noise into the summation process and will break the limits of Equation (6.1). As a rule of thumb, the size of the aperture should be chosen such that the last target reflector is within the first Fresnel zone. This limit of the Fresnel zone is an acceptable interval for which the Taylor expansion of the traveltimes function is valid.

It can be expected that, summing over more than one CMP locations as is done in the CRS stack method (see Section 6.3.1) should smooth or even hide local discontinuities. My experience

shows that this was not the case in most areas. The extent of the summation aperture would influence this phenomenon.

6.6 Summary

There is one major drawback in the CRS stack method, and it is called “TIME”. The increased amount of information required for the CRS stack involves a larger computing effort than the conventional NMO/DMO stack processing. In 2D three wavefield attributes need to be determined, while 3D ZO CRS stack results in five wavefield attributes. However, with the continuous growing strength of computing systems the gains of CRS imaging will be higher than its costs. The main advantages can be summarized as follows:

- The application of the CRS stack requires little or no human interaction. The parameter triplets are determined automatically without any velocity model and are data-driven. Therefore, errors which might be due to velocity analysis and wrong event picking by the processor are avoided. The automatic picking could be of particular advantage for 3D data.
- Stacking a large number of traces spanning over many CMP gathers increases the stacking power as compared to the conventional CMP stack. In the conventional CMP processing, the stacking power is defined by the number of traces in a CMP gather, and, primarily, by the acquisition fold. In the CRS stack the number of traces to be stacked is determined by the user through the extent of the aperture. However, this aperture cannot be chosen too wide because of the paraxial approximation involved in the theory. The example in this chapter has clearly expressed the multi-fold advantage of the CRS method (see also examples in Chapter 8). This is particularly advantageous in Foldbelt data with steep dipping flanks, where the picking of reflection events for stacking velocity analysis is very tedious and always prone to errors.
- Because the CRS stacking is over a reflector element or surface, dipping events, if present, are preserved. The preservation of dipping events has been one of the key properties of the DMO process. Therefore, the CRS imaging directly incorporates this feature. Also note that DMO cannot solve stack imperfections caused by strong lateral velocity variations.
- The determination of the wavefront curvatures and the emergence angle makes it possible to recover high density and high resolution rms or stacking velocities of the subsurface (Equation (6.6)). These velocities may be used for migration.

After testing and understanding the working principles of the CRS stack algorithm on synthetic data, the next logical step is to apply the algorithm to the Donbas Foldbelt data. However, before applying the algorithm I will first describe the location, geological setting and scientific interest of the survey area. This will be followed by a description of the seismic data and the preprocessing steps I applied on the seismic data. Because the preprocessing was not a major part of this research, its description will be very brief. Chapter 8 will then follow with the results of the CRS stack on the field data.

Chapter 7

Geological Setting, Data Acquisition and Preprocessing

7.1 Location and Geology Setting

In this section I present a brief description of the geology of the Dniepr-Donets Basin (DDB). A more complete description and discussion of the geology of the Basin is given by Chekunov et al. (1992), Stovba et al. (1996), Stovba and Stephenson (1999), Ulmishek et al. (1994) and listed literature therein. My description is based mainly on the above listed literature.

The DDB is a late Devonian rift basin located in the southeastern Ukraine, lying between the Ukrainian Shield and the Voronezh High in Ukraine and Belarus and extending from the Donbas in the east to the Pripyat basin in the west (Figure 7.1). The word Donbas is an abbreviation for Donets Basin. The DDB strikes in a Southeast-Northwest direction from Belarus through Ukraine. It is usually subdivided from northwest to southeast into the relatively shallow Pripyat basin, the much deeper central Dniepr-Donets basin and the mildly to strongly inverted Donets segment, with the latter also including the Donbas Foldbelt (DF).

The DDB, like most intracratonic rift basins, formed as a consequence of the isostatic response of the lithosphere to crustal thinning and geothermic perturbation following lithospheric extension (Chekunov, 1992). Rapid syn-rift subsidence occurred during lithospheric extension as the result of crustal thinning induced by lithosphere geothermic increase. After the lithospheric extension had ceased, thermal re-equilibration and cooling resulted in slower, exponentially decaying post-rift thermal subsidence. The main regional faults, dipping at $70 - 80^\circ$, are called the northern and southern marginal faults. The rift itself has a symmetric structure and is subdivided into an axial (the deepest part) and adjacent southern and northern preflank zones (Stovba and Stephenson, 1999). The axial zone of the basin is ca. 650 - 700 km long, and extends from the structural Bragin-Loev high separating the Pripyat basin through southeast to the Donbas margin (Figure 7.1). The axial zone ranges in width of ca. 70 - 140 km, and increases in the southeast. The preflank zones are separated from the axial zone either by a pair of large displacement faults or by a system of obliquely dipping blocks separated by faults with moderate throw (Stovba et al., 1992).

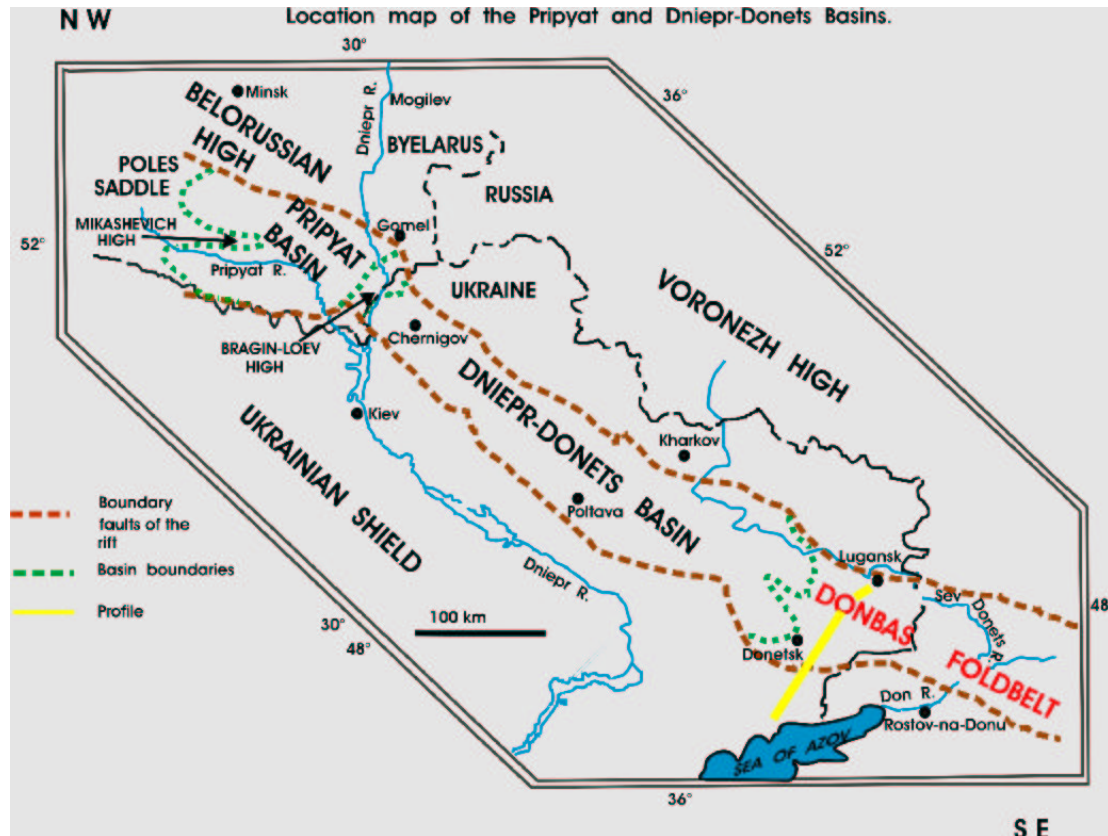


Figure 7.1: Location map of the survey area with major tectonic zones of the DDB.

The preflank zones are in turn separated by the regional extensive, large amplitude main boundary faults from the southern and northern rift shoulders. Therefore, over this entire segment the rift basement is broken into blocks of various size by disruptive faults with amplitudes in the range of about 100 m - 2.0 km forming characteristic large, rotational fault blocks and half grabens. As a result of the effects of the overlying post-rift sedimentary successions, most of the half-grabens are flattened with respect to the modern relief of the basin bottom (Chekunov et al., 1992).

This late Devonian intracratonic basin is characterised by linear bounding faults penetrating much of the crust, substantial crustal thinning, and syn-rift volcanic activity (Chekunov et al., 1992). It is filled with pre-rift and syn-rift, Middle and Late Devonian sequences, overlaid by Carboniferous, Permian, Mesozoic and Palaeogene sediments (Figure 7.2). Within the rift boundaries the crystalline basement is overlaid by Devonian sediments, while on the rift shoulders the Devonian sediments are generally absent, and Carboniferous sediments are unconformably overlying the basement. Upper and Middle Carboniferous sediments are present within the axial zone of the Donbas Foldbelt; near the Ukrainian Shield margin, pre- and syn-rift Devonian sediments are exposed. Note that in the Donbas Permian to Jurassic sediments, Upper Cretaceous and Cenozoic sediments are completely absent, due to basin uplifting (inversion) and erosion.

7.1.1 Pre-rift Sequence

Prior to the initiation of the basin subsidence, the Ukrainian Shield and Voronezh High, between which the rift basin developed, had been subject to erosion (Chekunov et al., 1992). The main

stage of the Devonian rifting occurred during the Frasnian and Famennian. Figure 7.4 shows the timetable of the DDB evolution, identifying pre-rift, syn-rift and post-rift stages of basin formation. This main stage of the rifting was immediately preceded by a pre-rift stage which lasted from Middle Devonian to Lower Frasnian. The pre-rift stage was characterised by the development of a vast smooth sag basin without evidence of substantial vertical movements of the basement blocks (Stovba and Stephenson, 1999). Volcanic activity gradually increased and reached a maximum at the end of this stage. Pre-rift Devonian depositions in the basin commenced in the Middle Devonian (383 Myr) and are characterised by shallow marine deposition. The crustal-scale marginal and axial faults with large throws formed between Late Frasnian (370 Myr) and the end of the Devonian and were accompanied by rapid subsidence producing grabens and half-grabens within the basin, and uplift and erosion of the rift shoulders especially on the southern side of the rift (the Donbas). The reason for this is not clearly documented. Faulting fractured the crystalline basement into small-scale blocks of dimensions of about 2-5 km or less. Major depositional centres separated by uplifted blocks formed during this time (Stovba et al., 1999). On some of the largest intra-basin highs there are very little or no syn-rift or pre-rift Devonian sediments. Pre-rift sediments, which appear to have been deposited in a platformal environment were presumably eroded during the syn-rift phase. The duration of the rifting stage is estimated to be between 7 and 9 Myr, extending from within Frasnian through the Famennian to the end of the Devonian.

7.1.2 Syn-rift Sequence

In the lower part of the syn-rift sequence substantial deposits of salt are found. Figure 7.3 shows the distribution of salt in the DDB. The salt alternates laterally with clastic-carbonate rocks. Salt diapirs and salt pillows are mainly distributed along the axial part of the basin. It is suggested that structural reactivation including salt tectonics have played a major role in forming the present day basin (Stovba and Stephenson, 1999). The salt bodies occur on localised zones and in local anticlinal uplifts. Most of the salt are Frasnian age. Salt of Famennian age has more limited occurrence in the DDB with only small thickness in the northwestern part of the basin (towards the Pripyat basin). The evaporitic rocks of the Frasnian were modified by diapirism during the post-rift stage.

The northwestern part of the Dniepr-Donets Basin was the most volcanically active. Two main phases of volcanism occurred; the first in the late Frasnian and the second in the late Famennian. They consist predominantly of alkaline-ultramafic lavas, alkali basalts and their differentiates (note that alkaline lavas are formed only through melting of subducted oceanic plate). Magmatic activities continued until Tournaisian time and volcanic products are found within the basin fill. Within the basin, the thickness of the first volcanic series is 100 - 900 m and that of the second series is about 300 - 500 m, increasing to 1500 - 2700 m in regions of volcanic build-ups. Smaller thicknesses of volcanic series are also found inter-bedded within Upper Devonian sediments. A correlation between volcanism and uplifted areas of the rift and between volcanism and deep basement faults has been noted (see e.g. Stovba and Stephenson, 1999).

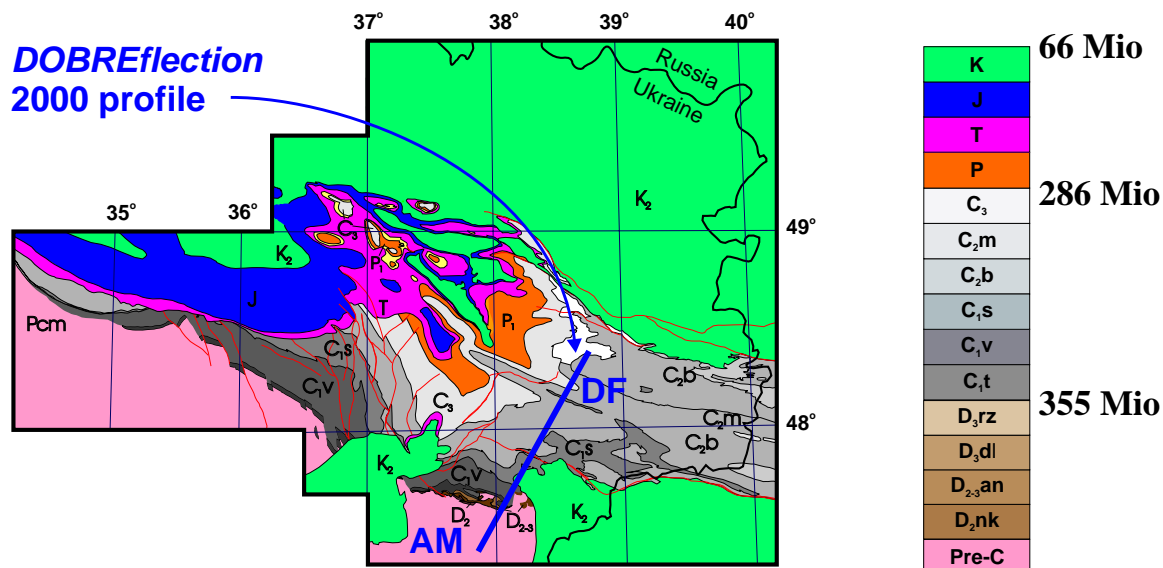
Due to the active tectonic processes at this time, the basin experienced frequent transgressions and regressions at either a regional or local scale. As a consequence there are frequent changes

in the palaeogeographic environments both in time and space. Famennian successions contain interbedded clastic and carbonate rocks, together with effusive, pyroclastic rocks and salt. Along the southern margin of the Dniepr-Donets Basin, immediately adjacent to the rift margin fault, the amount of clastic material increases, and contains unsorted and irregularly grained material frequently with large blocks of crystalline rock without any sign of weathering (Stovba et al., 1996). Similar units but of smaller thickness and better sorted were observed in some areas along the northern marginal faults. Coarse-grained rocks gave way laterally to finer grained rocks towards the axial part of the basin.

7.1.3 Post-rift Sequence

Post-rift basin development is characterised by the formation of vast synclines, set on the rift and its shoulders, commencing in Tournaisian time (Stovba et al., 1992; Chekunov, 1992; Ulmishek et al., 1994). Devonian sediments are absent on the flanking shoulders of the rift basin and also on some of the intra-basin highs. Tournaisian and lower Visean sediments are present as a nearly continuous blanket and lie unconformably upon eroded Devonian sediments and crystalline basement on the intra-basinal highs. Sedimentary deposition of Tournaisian to Early Visean through the remainder of the Carboniferous are shallow-water sediments and in some places continental deposits. The Tournaisian-Lower Visean sequence has a uniform thickness towards the Ukrainian Shield and Voronezh Massif. These sediments transgress onto the rift shoulders (in some areas onto crystalline basement, e.g. in the northern part of the study area). A distinctive feature of the Tournaisian-Early Visean succession is a relatively low rate of deposition (shallow water sedimentation). These relatively thin stratigraphic units of Tournaisian and Lower Visean age are interpreted to represent the earliest part of the post-rift fill in the basin (Stovba et al., 1996). Therefore, the main rift stage is assumed to have terminated in late Famennian (ca. 363 Myr). Above the Tournaisian-Lower Visean is a very thick, finely layered clay-sandstone succession which continues into the Upper Carboniferous. A succession of sediments with different composition and facies was laid down in a general background of basin subsidence with some influence of wave activity. The Carboniferous and Mesozoic sediments cover the rift flanks and increase in thickness towards the rift axis. Maximum thickness of the sedimentary successions within the DDB accumulated during late Paleozoic and Mesozoic times ranging from 2-6 km in the northwest to 15-21 km on the southeast and in the Donbas. The thickness of the Devonian succession often shows substantial variations over very short distances with maximum thickness of about 4 km.

During the late Carboniferous the depositional environment of the basin changed. The lateral extent of the basin became smaller and shallow-marine deposition gave way to continental and lagoonal sedimentation, leading to evaporitic conditions in the Early Permian. In the northwestern part of the basin the duration of hiatuses in the sedimentation increased.



Cainozoic subcrop map of the Donets segment of the Dniepr-Donets Basin (DDB) and Donbas Foldbelt (DF). AM symbolize the Azov Massif

Figure 7.2: Cenozoic subcrop map of the central part of the Dniepr-Donets Basin (DDB) and Donbas Foldbelt (DF). AM symbolises the Azov Massif, and the thick black line indicates the DOBREflection-2000 profile.

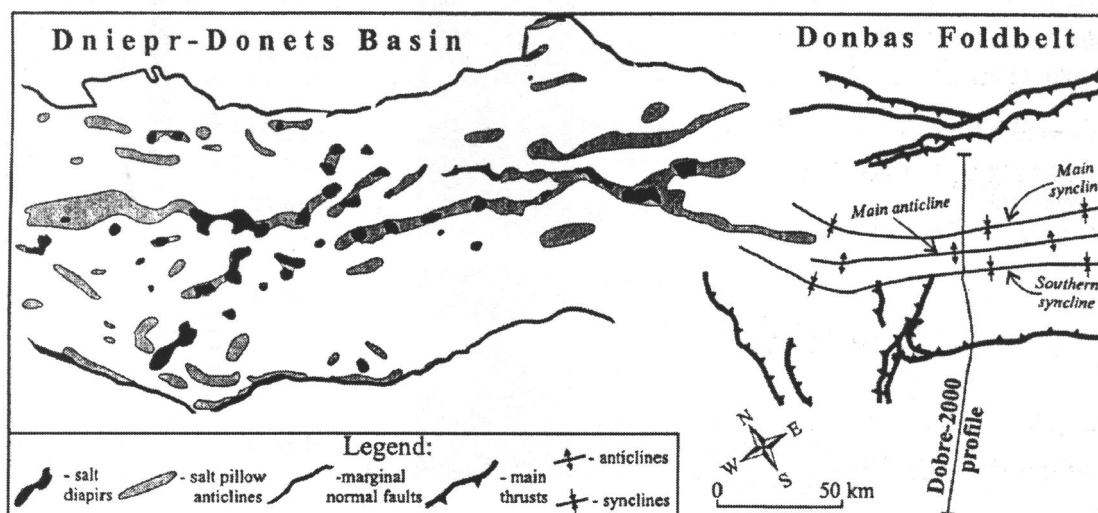


Figure 7.3: Correlation between salt structures of the DDB and main anticline and synclines of the DF. The distribution of salt is taken from interpreted industrial lines

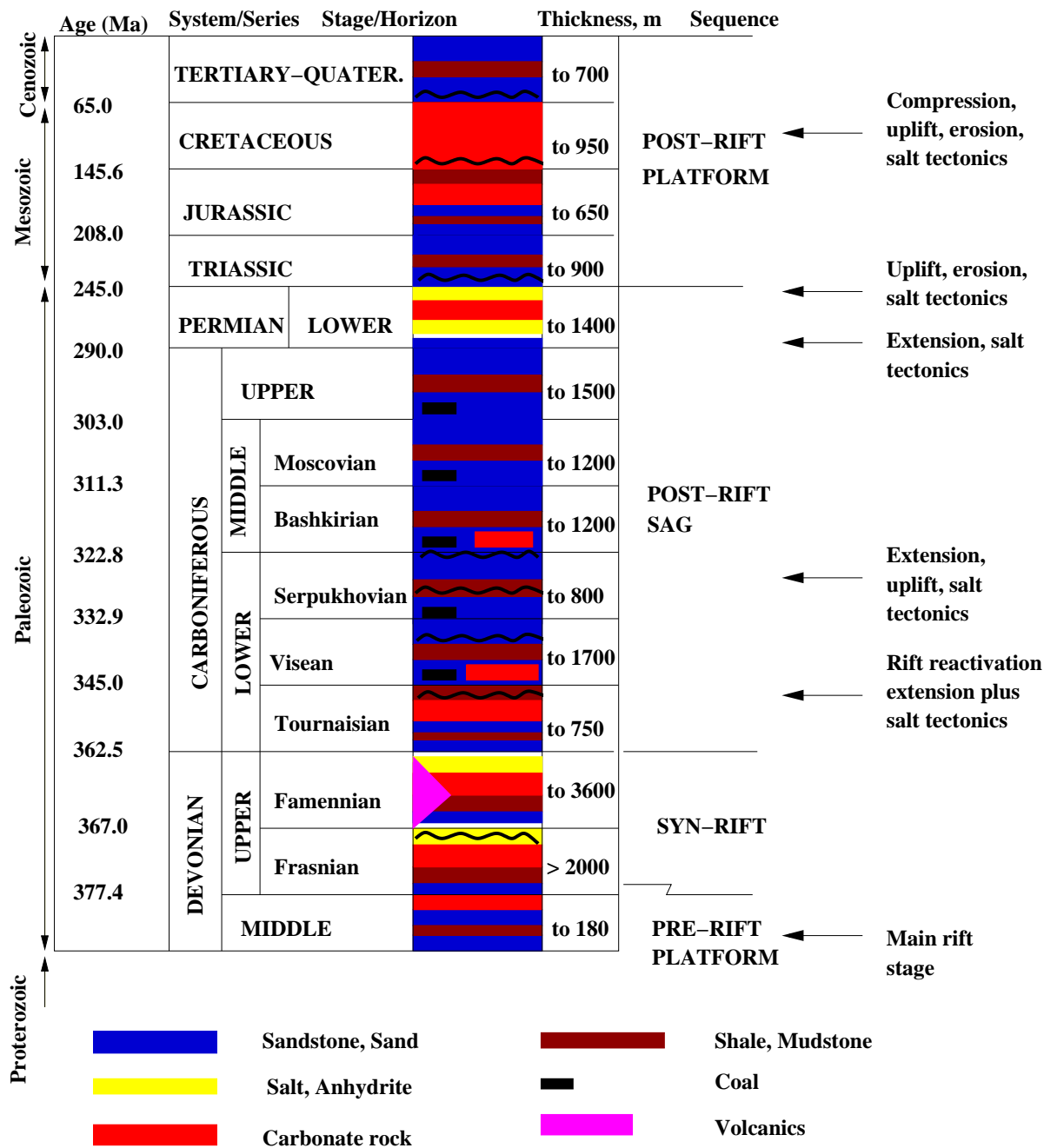


Figure 7.4: Schematic sedimentary column (indicating dominant lithologies in the DDB) with the main tectonic phases. The table is from Ulmishek et al. (1994) and modified.

7.1.3.1 Major Scientific Interests

- The goal of the DOBRReflection 2000 project is subdivided into several parts. The geological (basin infill and basin evolution) and geophysical (crustal structure and imaging of sedimentary infill) characteristics of the Pripyat basin and Dniepr segment of the DDB are explicable similar to that of most other intracratonic rifts and passive continental margins (Stovba et al., 1996). However, the integration of basin infill with what is known of crustal structure becomes increasingly difficult when passing from the Dniepr to the Donets segment of the DDB and by extrapolation into the Donbas Foldbelt (DF). As described in section 7.1, the thickness of the sedimentary fill and tectonic activities in the Donets segment of the DDB and the DF are different. Therefore, one of the objectives is to study the southeastern continuation of the Dniepr-Donets basin into the coal mining areas of the DF, including the sedimentary infill and its deformation.
- It is known from surface geology that the DF is more strongly inverted and uplifted, and compressionally deformed during Early Permian than the Donets segment of the DDB. However, the processes that led to this strong inversion are not clearly known. In general, there are two models to explain this inversion and uplifting (Stovba and Stephenson, 1999). First, it is considered that the profound uplift occurred in response to the build-up of stresses coming from the Hercynian Caucasus/Uralian orogens located in the South (Stovba and Stephenson, 1999). The other model suggests that the uplifting occurred in response to the activity of an asthenospheric (mantle) diapir and salt tectonics. Whatever the case, the DDB comprises two separate tectonic units: in the east a regime of undulations with intense tectonic movements leading to the formation of large folds in the DF; and in the central part of the DDB limited uplift probably followed by a resumption of subsidence. Therefore, the project aims at providing additional information to understand the origin of the strong uplift in the DF.
- Another puzzling question came from regional surface geology. The main geological features of the DF and the adjacent Donets segment of the basin are shown in the Cenozoic sub-crop map (see Figure 7.2). Along the seismic survey line, Carboniferous sediments crop out within the axial zone. Near the Ukrainian Shield margin of the DF, pre- and syn-rift Devonian sediments are exposed. Therefore, Permian-Jurassic sediments are almost absent and Upper Cretaceous and Cenozoic sediments are absent along the axial zone of the DF. Due to the absence of much of the sedimentary record younger than Carboniferous, it is difficult to obtain direct evidence about the intensity and the distribution of Early Permian and younger tectonic events in the DF. The post-rift evolution of the Donets segment and the Donbas Foldbelt is highlighted by an excessive post-rift Carboniferous sedimentary succession when compared to the degree of tectonic activity recorded in the stratigraphy and Basin architecture. This post-rift evolution possess puzzling questions about the time of the basin inversion. There are also numerous questions about the Early Permian and younger post-rift tectonic events. These include the precise timing and nature of the complex set of tectonic events leading to major uplift and erosion of the Donbas Foldbelt. Therefore, it is the third objective of the project to elucidate the Permo-Carboniferous and younger evolution of the

DF.

- Another objective of the project is to study the structure of the deeper crust in this area. This is connected to understanding the evolution of the East European Craton as well as the shape of the Moho discontinuity below the DF. It is also aimed at studying what influence asthenospheric activities had in the uplifting of the DF.

To meet with these objectives, the DOBREfraction 1999 and DOBREflection 2000 line was acquired in summer 1999 and 2000 by Ukrgeofisika (a Ukrainian national company). In this thesis only the DOBREflection 2000 line is interpreted. The focus of the study is in the basin sediments. In addition to the seismic data, a surface structural geologic profile was also acquired along a nearby line. The interpretation of geological and geophysical knowledge is aimed to reach the objectives mentioned above. In the Institute of Geophysics, University of Hamburg, the focus of the study is in the basin sediments. The objective is to process the seismic data and construct an accurate velocity/depth model and to produce images in time and particularly in depth of the survey area. While in the GeoForschungsZentrum in Potsdam, the focus is on geologic balancing.

7.2 Data Acquisition

In the survey area both Vibroseis and explosive seismic data were acquired. In the following I will describe only the acquisition parameters for the Vibroseis data. One component geophones were deployed. All recording parameters for the survey are summarised in Table 7.1. Important considerations in the acquisition program included high fold, long receiver array lengths, and an offset range that corresponds to an angle of incidence from 0° to 45° according to the deepest target event. A total number of 877 shots were acquired with uniform shot spacing of 140 m interval. Along the profile the shooting interval was not always constant. There was a shot point gap of 14 km in the axial part of the survey line, due to prohibition of shooting operations within an extensive network of coal mining. Each shot gather was made up of 680 traces with geophone spacing of 35 m.

The acquisition geometry was mainly split-spread configuration but in some areas the configuration was asymmetric split-spread and in other areas it was an end-on spread configuration. The nearest and largest offsets on most shot records were 35 m and 12000 m respectively for each side of the spread (for the end-on spread it was 35 m and 24000 m). The central parts of the survey were covered with an 84 fold coverage and to the ends of the survey the coverage decreases to zero. Many of the traces that contribute to the fold diagram are from very large offsets. Low-fold areas were found to be more susceptible to local noise problems (such as poor geophone coupling and spurious traces) than high-fold areas. The low-fold areas generally produce regions with lower amplitude in the stacked sections. The lack of a uniform distribution, which was related to the patch acquisition, was recognised as a problem and degraded the results in some areas.

7.3 Data Preprocessing

The goal in processing seismic reflection data is to enhance the genuine reflection signal by suppressing unwanted energy in the form of coherent and random ambient noise. This goal is achieved by choosing a number of processing steps which “fit” to the data quality. The main processing steps applied to the data are displayed in Figure 7.5. The processing parameters were mostly space-variant, i.e., the parameters were often adjusted along the profile in response to the continuously changing quality of the data. This is very common for onshore data. Because the data processing is not a major part of this thesis, I will only give a brief description of the processing steps and show the final results on two shot examples (before processing and after processing).

The data were processed using Focus 2D software of Paradigm Geophysical. The first step was setting up the field geometry and field statics. A table of values with field statics and residual statics were provided by Ukrgeofisika, together with a stacking velocity model.

7.3.1 Geometry, Trace Editing and Noise Analysis

The correlated vibrograms were supplied by Ukrgeofisika. Apart of the sampling rate of 2 ms and the number of samples, all the traces had no other header information. Field geometry information (observers records) was supplied in the form of the standard Shell Processing Support (SPS) format. The SPS format is a standard format used in the industry for writing onshore data records (see the SEG homepage for a detailed description, www.seg.org). The SPS files contain shot and receiver locations, field statics, and shot and receiver elevations. The field geometries in the SPS


RECORDING DATA		SPREAD	
Record length	30 s	Type	split spread
Sampling interval	2 ms	Number of stations	681
Channels	681	Station interval	35 m
Geophone/Group	12	Minimum offset	35 m
Geophone-Frequency	10 Hz	Maximum offset	12000 m
VIBROSEIS PATTERN		SPREAD DIAGRAM	
Number of vibrators	4		
Sweep frequency	8-80 Hz		
Sweep length	12 s		
Sweep type	linear		
S.P. position	on half station		
S.P. interval	140 m		
Coverage	85 fold		
Number of vert. stack/V.P.	20		
Recording length	30 s		
DYNAMITE PATTERN			
Total charge size	80 kg TNT		
Average hole depth	30 m		
S.P. interval	variable		
Coverage	4 fold		
Recording length	99 s		

Table 7.1: Seismic data acquisition parameters. The symbol S.P stands for shot point.

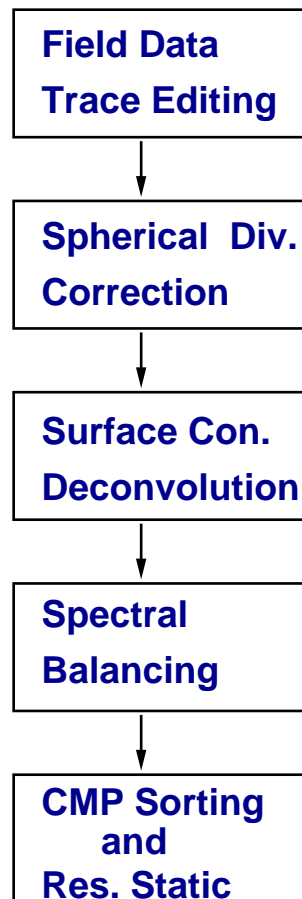


Figure 7.5: Processing flow for the Vibroseis Donbas Foldbelt data.

files were read and inserted onto the traces. From the 30 s recording length, I processed only the first 10 s since this is the part that included the sedimentary basin of major interest. To increase the signal in the seismogram a gain function with large window is applied (Automatic Gain Control AGC 3000 ms). With this large AGC window the amplitude character of the genuine reflection events were not seriously damaged.

7.3.1.1 Incoherent Noise Contamination

In onshore data it is usually required that the traces in each shot gather be edited for the removal of bad traces, dead traces and polarity reversal. The criterium I used is that a good trace exhibit amplitude decay with time while a bad trace is one that manifests a constant status of amplitude with time. Therefore, each shot was edited using this criterium. After trace editing, the next step was to perform noise analysis. To find the optimum tool for noise suppression it was required to know the major type of noise present in the data. All the Vibroseis shot gathers were contaminated by incoherent noise that appeared sometimes at zero offset traces or near zero offset traces at traveltimes between 4 - 6 s. Some of this noise also suddenly appeared at large offsets (> 4000 m). The character of the noise generally looks like uncorrelated noise (see e.g. Okaya et al., 1992; Polom, 1999) and it affects the whole trace record length. In a few cases, the noise spectrum is coloured, presenting dominant frequencies of 34 and 41 Hz. Both the noise power and the noise spectrum are, basically, time invariant. This noise might be from inadequate gain settings of the

seismic group recorder floating-point amplifiers. Another possible source of this noise could be vibrator induced. That is poor vibrator-to-ground coupling can produce resonant-induced energy which propagates with the primary sweep and produces artifacts in the correlated seismogram. This phenomenon was also observed by Okaya et al. (1992) and Polom (1999). I used a notch filter of 34 Hz and 41 Hz in order to remove the dominant noise.

7.3.1.2 Trace Muting and Scaling

The next processing step involved muting of the direct waves and first arrivals from refractions. The mute window was specified separately for each shot with special care taken in order to preserve reflections from steeply dipping horizons. Due to complex tectonic area (steep dipping horizons and overthrusting), the apex of some reflection hyperbola were shifted towards the first arrivals in the shot gather. The process of muting was followed by the application of geometrical spreading correction and the application of exponential gain function. The geometrical spreading correction is expressed as a function of subsurface velocity and travelttime. The average subsurface velocity was estimated and supplied by Ukrgeofiska. After a set of tests a suitable geometrical spreading function of $v^2 t^{3/2}$ was chosen. Next, the trace amplitudes were balanced on a record basis using trace equalisation. This was accomplished by scaling the data to a defined energy level. The Focus 2D routine allows for a separate balancing factor to be computed for each trace. This factor is applied individually to each trace, thereby keeping relative amplitudes through the trace. I used a time variant high pass filter (low-cut) to first suppress the low frequency components of the data. A broad band trapezoid filter of 3/5 - 100/120 Hz was later applied to suppress the high frequency component of the signal. The next major processing steps were surface consistent deconvolution and spectral balancing. However, before passing the Vibroseis data to deconvolution, the mixed phase data had to be transformed to their minimum phase counterpart. This part of the processing is not required for the explosive data because they are already minimum phase.

7.3.2 Minimum Delay Transformation

A seismic trace $w(t)$ is a convolution of the source wavelet $s(t)$, the earth reflectivity $e(t)$ and the receiver and instrument response function $r(t)$ plus a noise component $n(t)$ (Yilmaz, 2001):

$$w(t) = s(t) * e(t) * r(t) + n(t). \quad (7.1)$$

Because $s(t)$ is zero phase (Klauder wavelet), $e(t)$ and $r(t)$ are minimum phase, the seismic signal, $w(t)$, is mixed phase. For a correct application of deconvolution and spectral balancing the seismic data need to be transformed to its minimum phase counterpart. This process of wavelet transformation is usually called wavelet processing as described in Fertig et al. (1999) and Yilmaz (2001).

First, I construct a filter which will convert the Klauder wavelet to its minimum phase counterpart. For this purpose I use the auxiliary traces stored in the first five channels of each shot gather. The auxiliary traces are the sweep signal, the Klauder wavelet, the impulse response of the recording instrument and a vibrogram trace. Note that for Vibroseis data a spike ($\delta - Impulse$) is

assumed as the basic source signal (Fertig et al., 1999). Figures 7.6, 7.7, and 7.8 show the impulse response of the recording instrument, the Klauder wavelet, and its minimum phase equivalent. These Figures also display the corresponding amplitude and phase functions of the signals. Note that the phase spectrum of the impulse response is the most important part because it is responsible for the signal shape at a given amplitude spectrum (Yilmaz, 1987).

The minimum delay transformation is performed following a strategy described by Fertig et al. (1999). First I convolve the sweep signal and the instrument's impulse response to give a filter-sweep signal (FS). Next, the autocorrelation of the filter-sweep is constructed. This is followed by taking the inverse of FS and a zero-phase equivalent of the inverse function ($AK(FS)$). The zero-phase function is stored as a filter in the database. Also constructed is the minimum delay equivalent of the filter-sweep function (MDE). Finally, the minimum delay filter is given as the ratio $MDE/AK(FS)$, i.e. the inverse of the filter-sweep autocorrelation multiplied by the minimum delay equivalent of the filter-sweep. This minimum delay filter is convolved with the mixed phase seismograms to obtain the minimum phase traces. After transforming the traces to their minimum phase equivalent, surface consistent deconvolution follows.

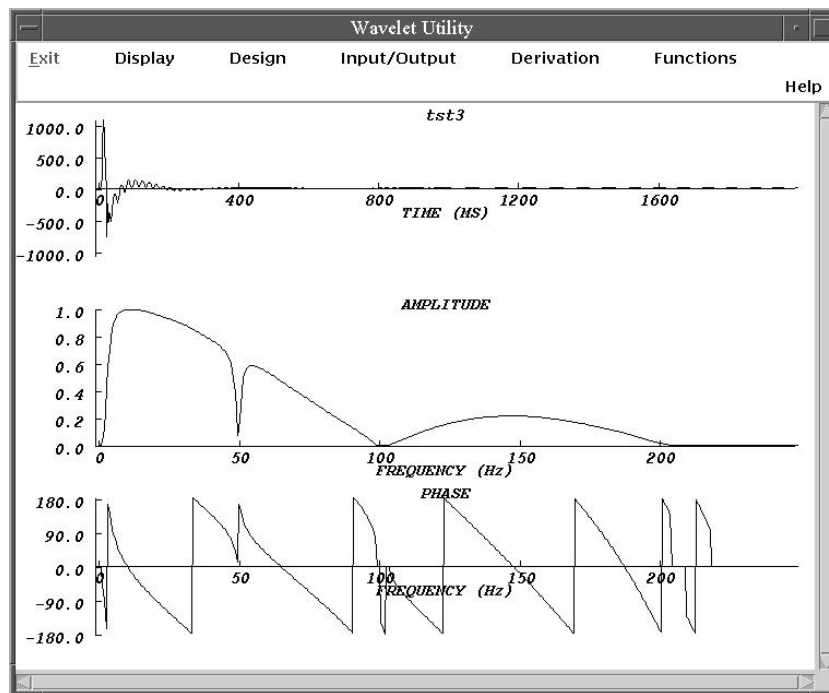


Figure 7.6: Display of the instrument's response and its corresponding amplitude and phase functions. The impulse response is a minimum phase signal with a 50 Hz-Notch filter

7.3.3 Surface Consistent Deconvolution

One of the main processing steps was the application of surface consistent deconvolution (SCDECON) on the data. As shown in Equation 7.1, a seismic trace is a convolution of individual operators that are attributed to the trace's source, receiver, offset, and common depth point location. The decomposition of a seismic wavelet into these four components is usually known as the surface consistent hypothesis (Cambois and Stoffa, 1992; Cary and Lorentz, 1993; Yilmaz, 2001). Cary

and Lorentz (1993) showed that the decomposition model results in obtaining accurate and stable deconvolution filters, as well as obtaining accurate amplitude, phase and statics solutions from the recorded data. The surface consistency hypothesis assumes that the shape of the basic seismic wavelet depends only on the source and receiver locations and not on the details of the raypaths from source to reflector and back to the receivers. Therefore, SCDECON is usually solved with only the source and receiver decomposed components. The essence of applying SCDECON is to compensate for conditions such as irregular shot and receiver coupling, variable shot signatures and attenuation of high frequencies at long offsets along the seismic line. During the deconvolution, the source components collect effects of the source signature and near-source structural effects, while the receiver components collect receiver characteristics and near-receiver structural effects.

In the seismic industry, SCDECON is usually implemented by deriving and applying a shot-consistent operator to the common shot gathers, followed by deriving and applying a receiver-consistent operator to the data after sorting to common receiver gathers (Cary and Lorentz, 1993). Applying this strategy on the Donbas Foldbelt data would require more disk space, since the 11 GB data would automatically require at least 22 GB of disk space. Therefore, to avoid this problem I used the alternative strategy as discussed in Cary and Lorentz (1993). In this strategy a four-component surface consistent deconvolution is performed in two passes: one pass is to solve for the four components, and another pass is to design and apply the deconvolution operators. No data sorting is required. Even though all four components are decomposed, only the source and the receiver components are used.

Autocorrelations of the decomposed shot and receiver components are used to design the deconvolution filters. In a shot gather the autocorrelations are computed over a specified time gate on the traces. Within the shot ensembles there can be more than one time gate, and time gates are interpolated between ensembles not specified. From the autocorrelation function computed for each ensemble, the mean autocorrelations for shot, receiver and offset are stored. Likewise a trace-by-trace amplitude scaling factor is stored. For each shot the autocorrelations are summed and the results are used in designing the deconvolution operator according to the Wiener-Levinson algorithm (see Cary and Lorentz, 1993; Yilmaz, 2001 for more details). The Wiener-Levinson algorithm designs a filter that effectively filters out the predictable signal from the data. Usually a Hanning filter-function is applied to the autocorrelations in order to smooth the undesirable effects on the power spectrum of a trace caused by the sharp truncation that might occur during the time gate selection (Focus 2D Users Guide). For AVO processing the trace-by-trace scaling factors can be used as surface consistent amplitude balancing to correct for amplitude corruption caused by the difference in source and receiver coupling during acquisition.

I applied the bandpass surface consistent spiking deconvolution¹ with an operator length of

¹Surface consistent deconvolution is a multichannel deconvolution in contrast to the single-channel spiking deconvolution which is often used. The multichannel deconvolution does not assume that the reflectivity series is white (Yilmaz, 1987, 2001) and it is not too sensitive to random noise. This is because when designing the deconvolution filter the amplitude spectrum of several traces in a shot gather are averaged.

128 ms and white noise of 0.1 %. The parameters, e.g., the frequency band, were chosen based on the resulting character of the deconvolved data. Filters for shot ensembles and traces not specified were defined by spatial interpolation. Because both high frequency noise and signals were boosted after deconvolution, the data were later filtered with a bandpass filter of 8/10 - 40/60 Hz.

7.3.4 Spectral Balancing

The next main processing step was spectral balancing. Spectral balancing, like coherency filtering, aims at suppressing surface waves such as ground roll. In the Donbas Foldbelt data surface waves covered the important near offset traces and displayed almost the same frequency content as the reflection signals. This was very predominant in the data with the main frequency content of the reflection events being as low as 17 - 20 Hz. Therefore, the objective was to suppress the surface waves in the centre of the shot records without destroying reflection events. After a series of tests, I concluded that frequency filtering (e.g. frequency (f) wavenumber (k) filter) was not an adequate method for suppressing the surface waves. F-k filtering gave smeared results. Instead, I applied zero-phase spectral balancing (Focus 2D Users Guide) to overcome this problem. With spectral balancing the spectra of the individual traces are balanced (similar to AGC) by multiplying the traces by a calculated average amplitude spectrum. As such the spectrum of the shot records are approximately the same. Spectral balancing modifies only the amplitude spectrum while the phase spectrum is left unchanged.

7.3.5 Residual statics and CMP sorting

The final stage of the data processing was the application of residual statics corrections and sorting the data to common midpoint (CMP) gathers. A table with residual static values were supplied by Ukrgeofisika, therefore, I did not pick static values. Figures 7.9 to 7.12 show the first 3 s of some selected shot gathers before and after applying the processing steps described above. In these Figures not all 681 traces within a shot record are displayed. The surface waves, high frequency signals at zero-offset and first arrival refractions are all suppressed. These figures clearly demonstrate that the objective of enhancing the genuine reflection signals by suppressing coherent and random noise is well achieved. After that, the CMP gathers are sorted and are input into the CRS stack algorithm and Geodepth software for prestack depth migration.

The next chapter will focus on applying the CRS method for imaging key areas of the reflection section. These areas are critical in estimating the amount of inversion of the basin.

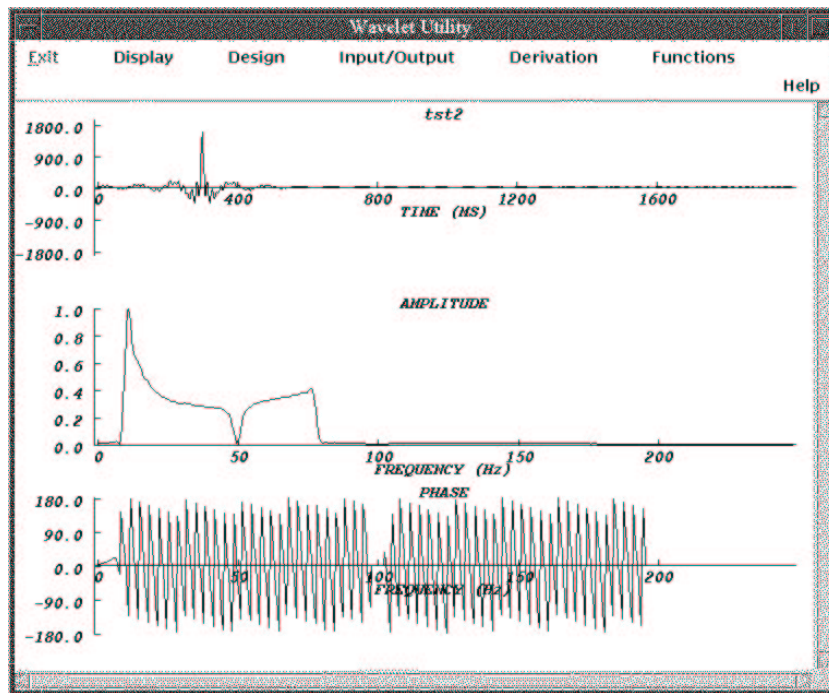


Figure 7.7: Zero phase Klauder wavelet and its corresponding amplitude and phase functions.

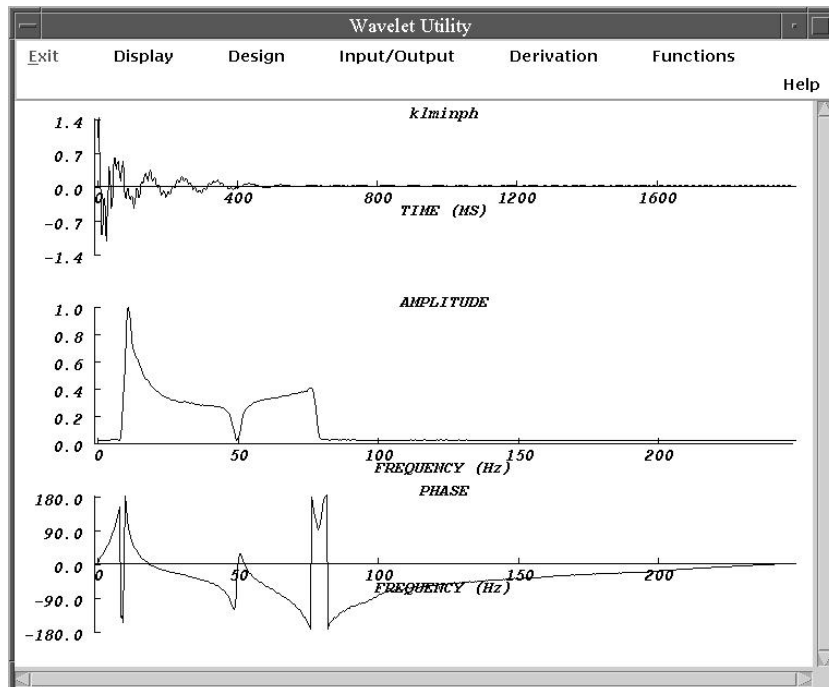


Figure 7.8: Minimum phase equivalent of the Klauder wavelet.

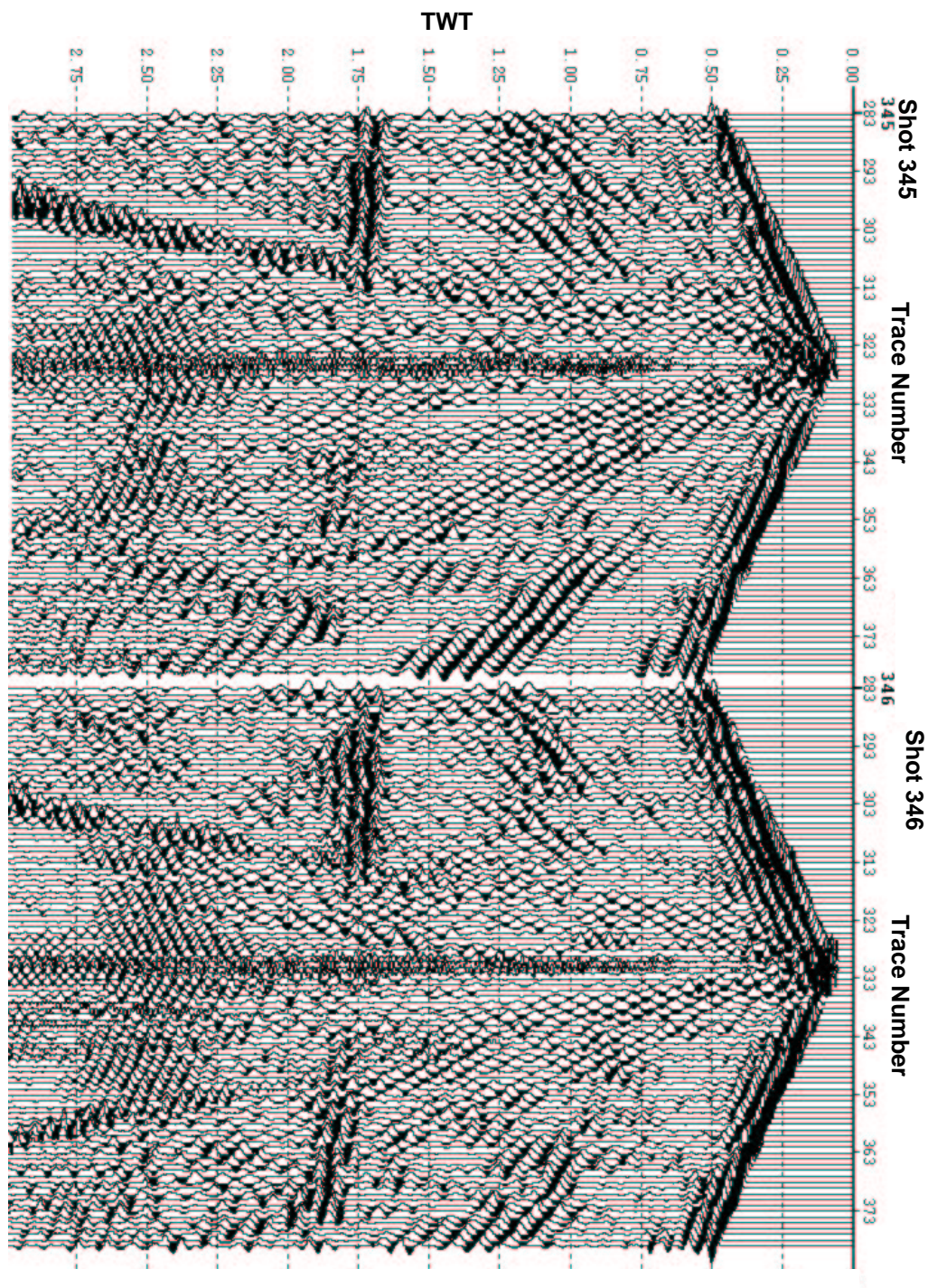


Figure 7.9: Split spread shot gathers of the Vibroseis survey. The gathers are shot numbers 345 and 346 before processing. An AGC with a time window of 1000 ms was applied for display. For shot 345 the source is located between channel 325 and 326 and for shot 346 the source is located between channel 331 and 332.

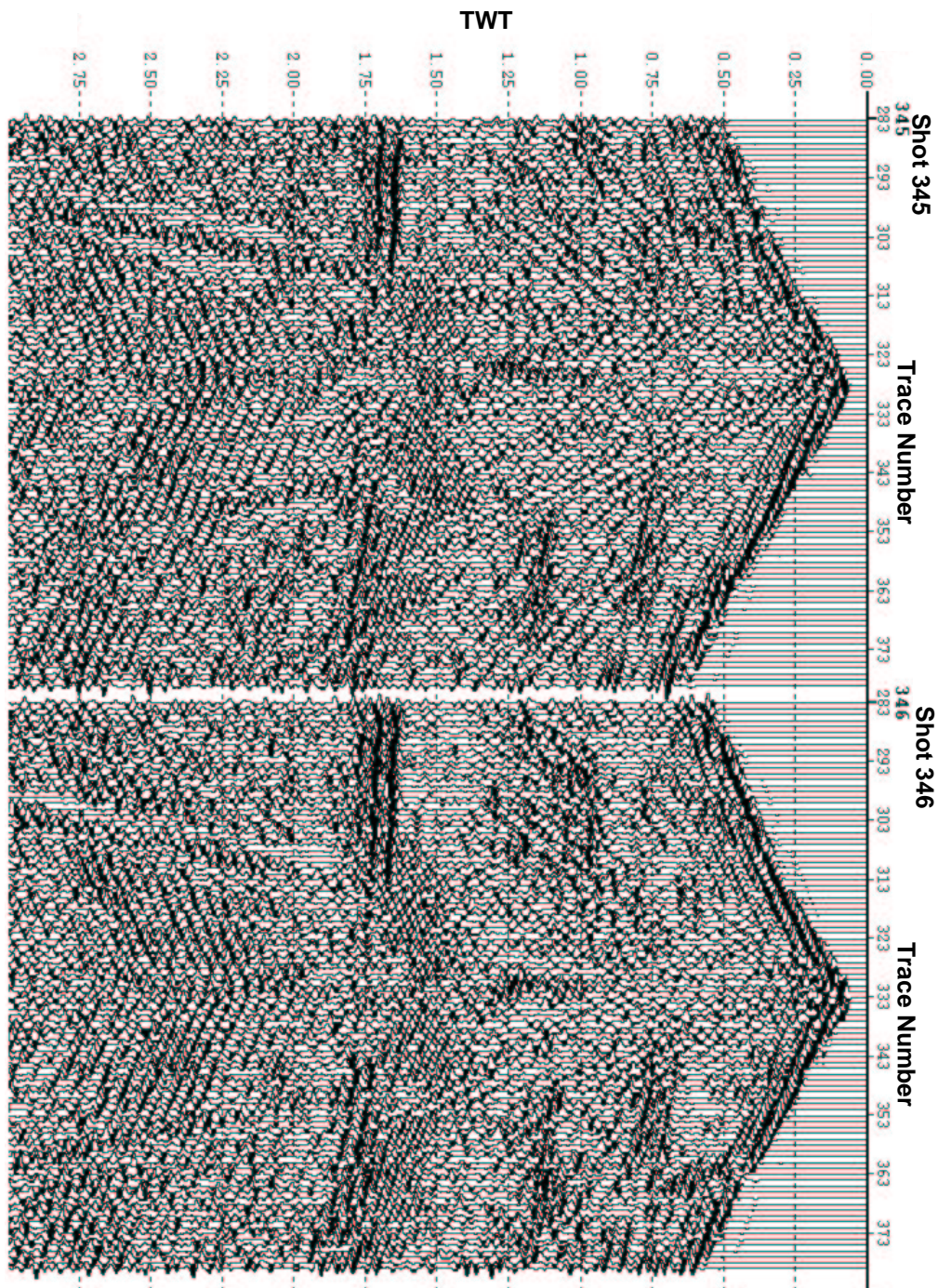


Figure 7.10: Same shot gathers as in Figure 7.9 after processing. Notice the reduction of the surface waves and the high frequency noise in the center.

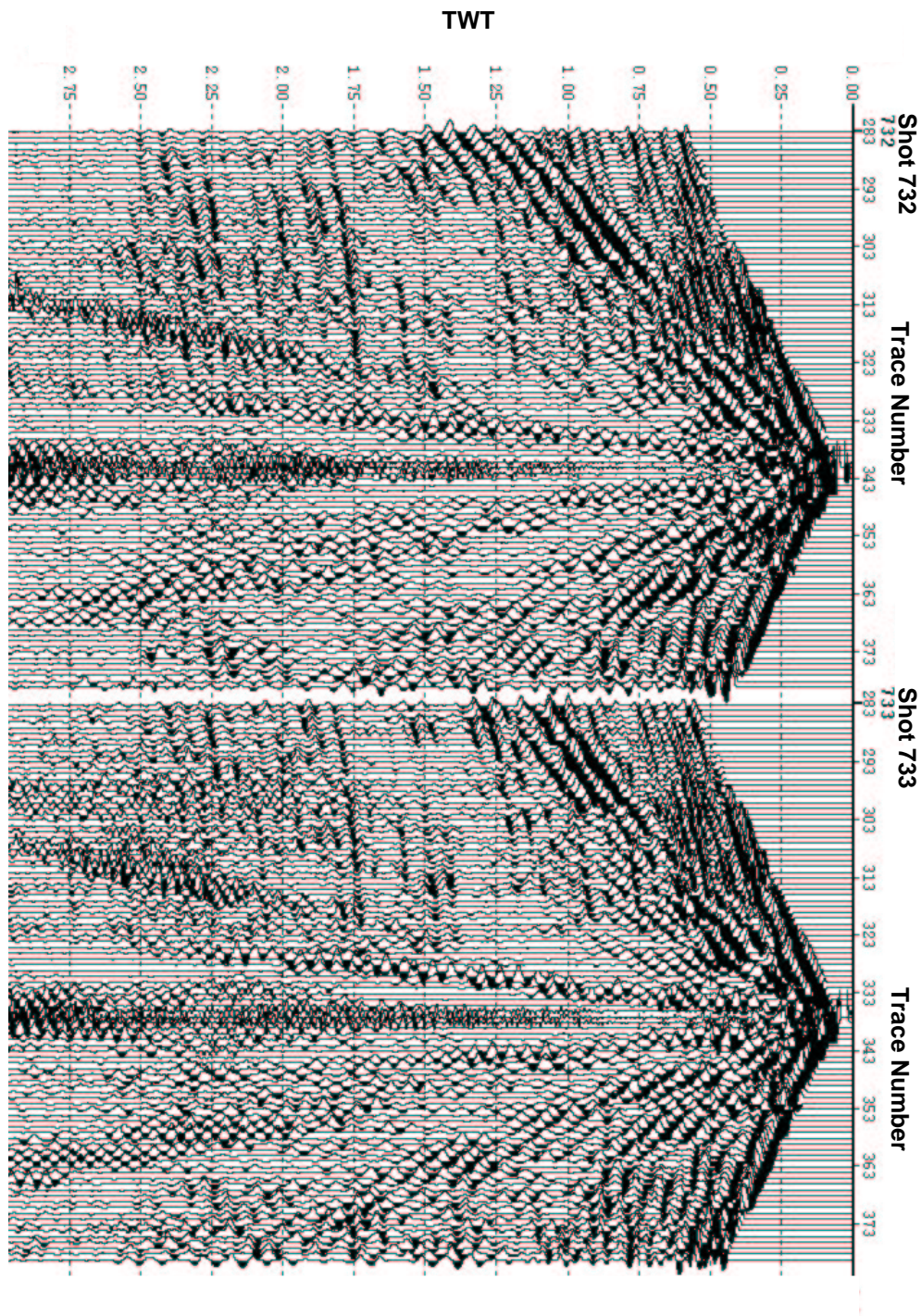


Figure 7.11: Shot numbers 732 and 733 of the Vibroseis profile before processing. AGC of 1000 ms was applied for display purposes. For shot 732 the source is located between channel 340 and 341 and for shot 733 the source is located between channel 339 and 340.

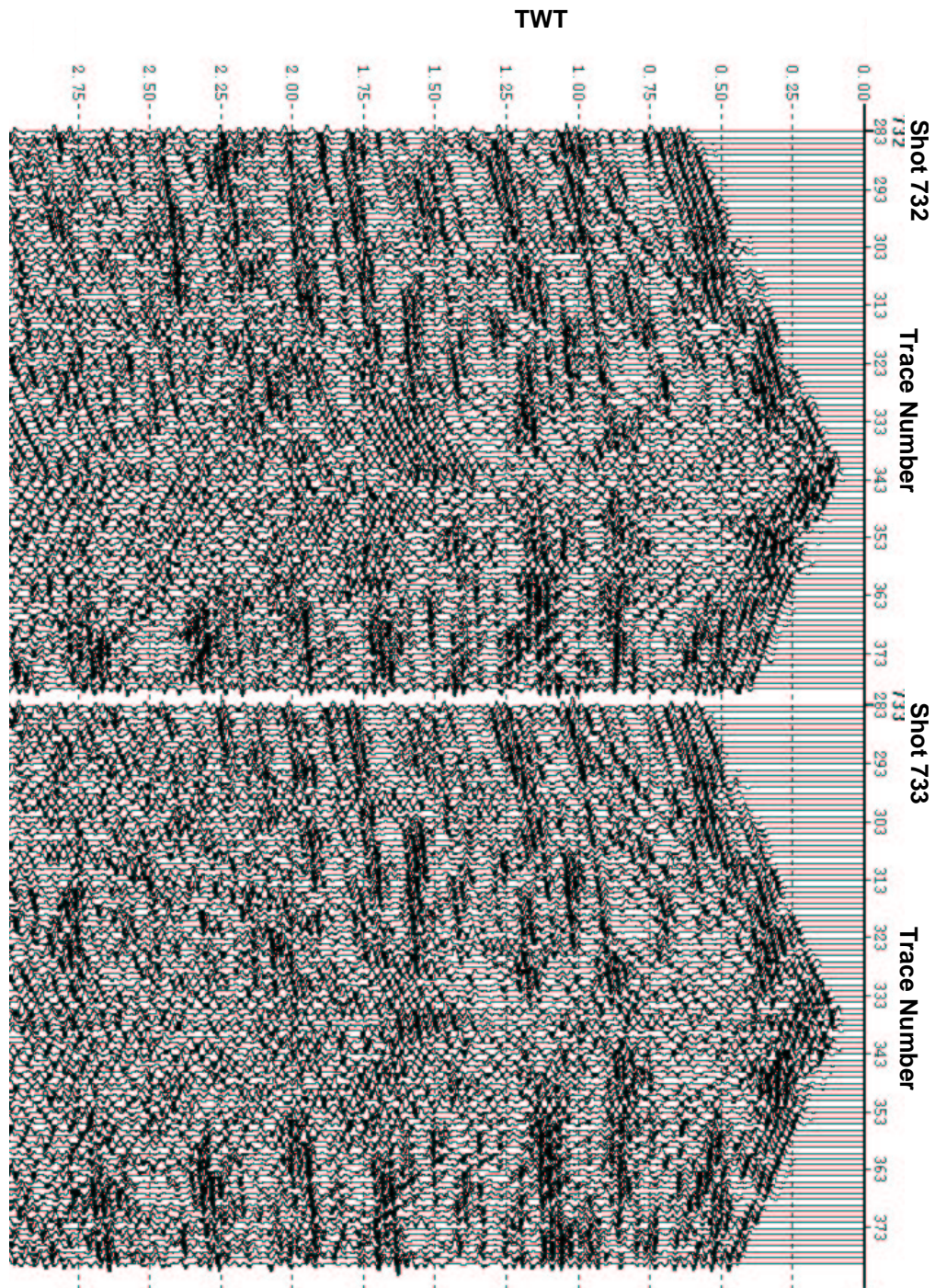


Figure 7.12: Same as in Figure 7.11 after processing. Almost all of the coherent noise are suppressed and genuine reflection events are enhanced.

Chapter 8

Field Data: CRS Stacking and Poststack Time Migration

8.1 Introduction

I have shown with the Picrocol synthetic examples in Chapter 6 that the CRS stack, if correctly applied, leads to major improvements on poststack seismic data. An optimal stacked section is a prerequisite for any poststack migration process. Therefore, for the Donbas Foldbelt data, the objective is to use the advantages of the CRS stack in order to reach maximum improvements on the final stack sections. The following expectations from the CRS stack were made:

- The S/N-ratio should be strongly increased in the CRS stack, since traces from more than one CMP gather can be summed. The surface-wise summation and therefore, increased fold should improve the reflector continuity.
- An improved image of the dipping reflectors and thrust fault boundaries are expected. This is expected because the local dip or orientation of the reflector is directly incorporated in the summation surface.
- Improved images of deeper reflectors is expected. In conventional processing deeper reflectors are usually obscured by noise.

Therefore, in this chapter I discuss the results of applying the CRS stack on the field data and investigate the fulfillment of the above stated expectations. I focus only on some key areas of the reflection section which are critical to estimate the amount of inversion of the basin (see Chapter 7, Section 7.1). The figures in this chapter are displayed using an automatic gain control with a window length of 100 ms.

8.2 Identified Regions on Poststack Time Migrated Sections

The Donbas Foldbelt data were previously stacked after conventional velocity analysis. Kirchhoff poststack time migration was later applied. The unmigrated stacked section from conventional CMP stacking which are displayed in this chapter were generated using the stacking velocity

displayed in Figure 8.1. This velocity field was supplied by Ukrgeofisika (Ukrainian national geophysical company). The migration velocities were derived from the stacking velocities by converting it to root mean square velocities. The rms-velocities were later modified to give the optimum time migrated section (Figure 8.2).

As a next stage, the migrated section was then interpreted (Figure 8.3). The imaging potential of the poststack migration is usually limited by the quality of the stacked section. In the Donbas Foldbelt data low fold areas led to low amplitude areas in the stacked section. Some main reflectors suddenly disappeared and their continuity was unclear. Uncertain reflector continuity can lead to wrong geological interpretation. The continuation of the fault systems from the surface down to the subsurface was poorly delineated. In deeper areas of the basin (TWT 5 - 10 s) where the S/N-ratio was generally poor geological interpretation of the main horizons was even more complicated. In certain areas the first interpretation in Figure 8.3 were questionable. The line drawings were constrained by the surface structural geology and shallow wells (ca. 2 km deep). I attributed the imaging problems to the poor quality of the unmigrated stacked. The key areas on Figure 8.3 which already show substantial basin inversion were selected for imaging with the CRS stack method. These key areas (rectangular boxes in Figure 8.3) show clear indications of the basin inversion and are key for the understanding of the basin evolution. Note that the gap zones with no data were due to lack of shot points in the area. The CRS method was not applied to the complete data set because of the limited computation power at the time.

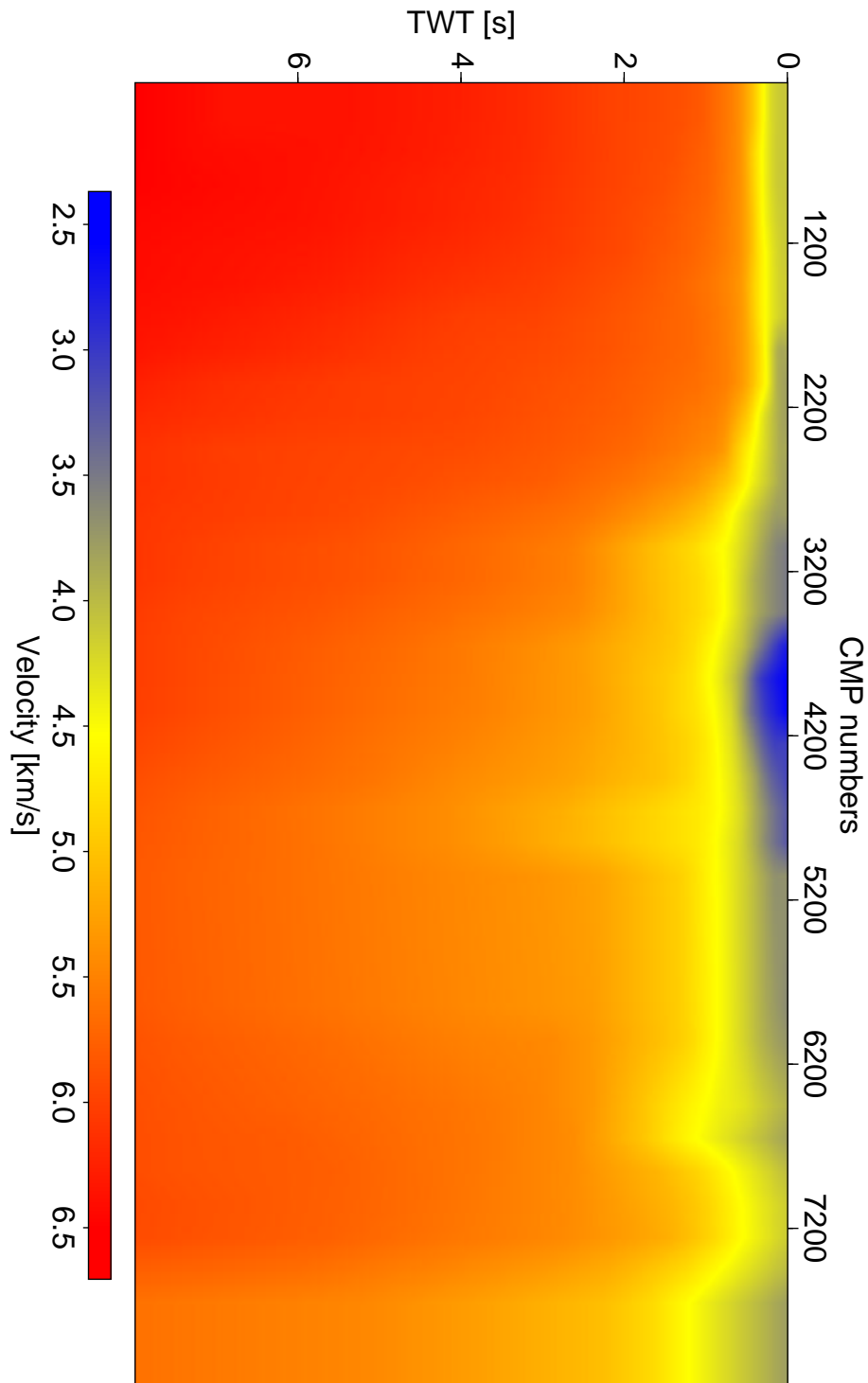


Figure 8.1: Stacking velocity model of the Donbas Foldbelt data. This stacking velocity model was used to obtain the conventional CMP stack results.

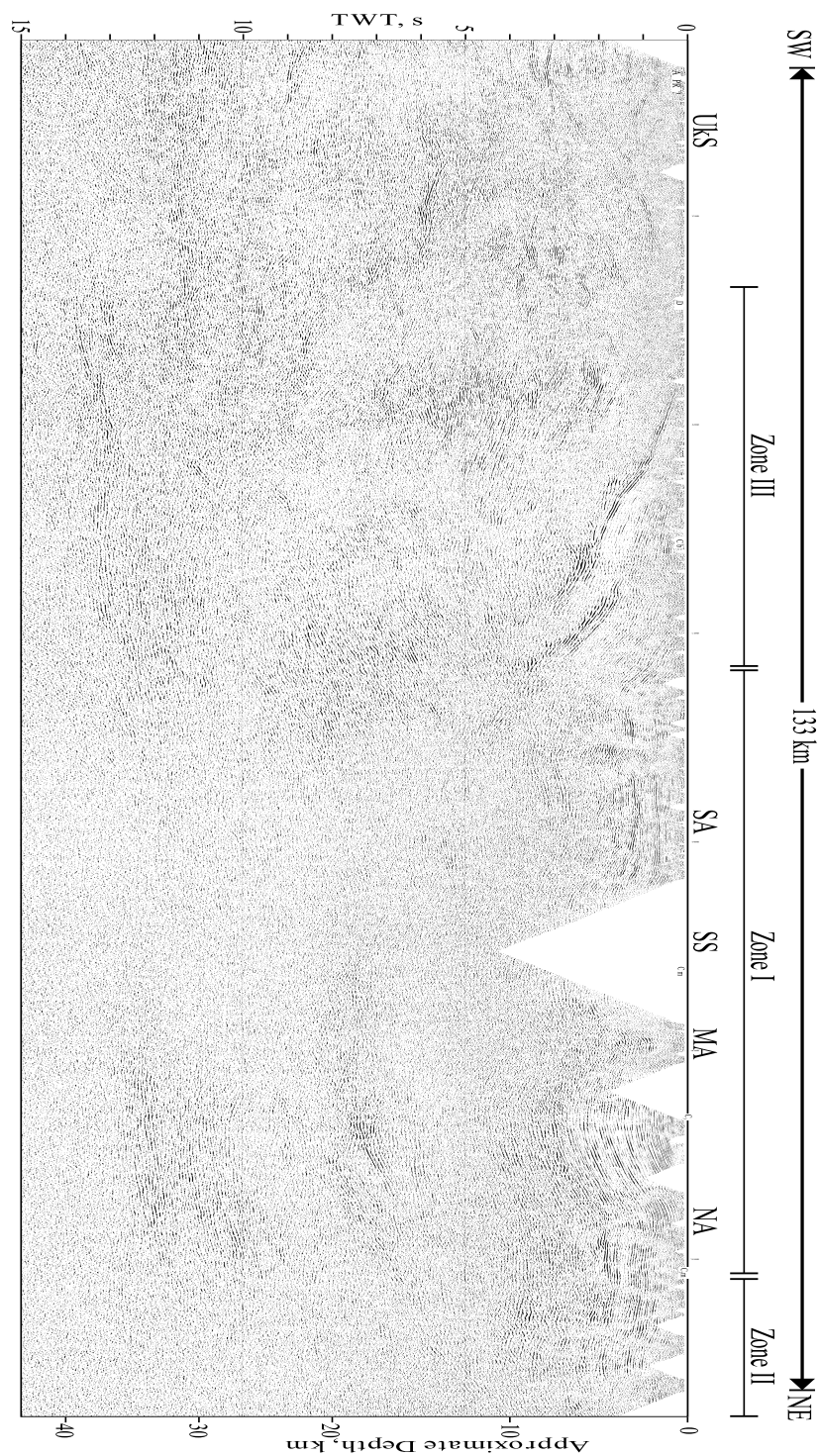


Figure 8.2: Poststack time migration of the complete seismic line. For display only every 10-th trace was plotted.

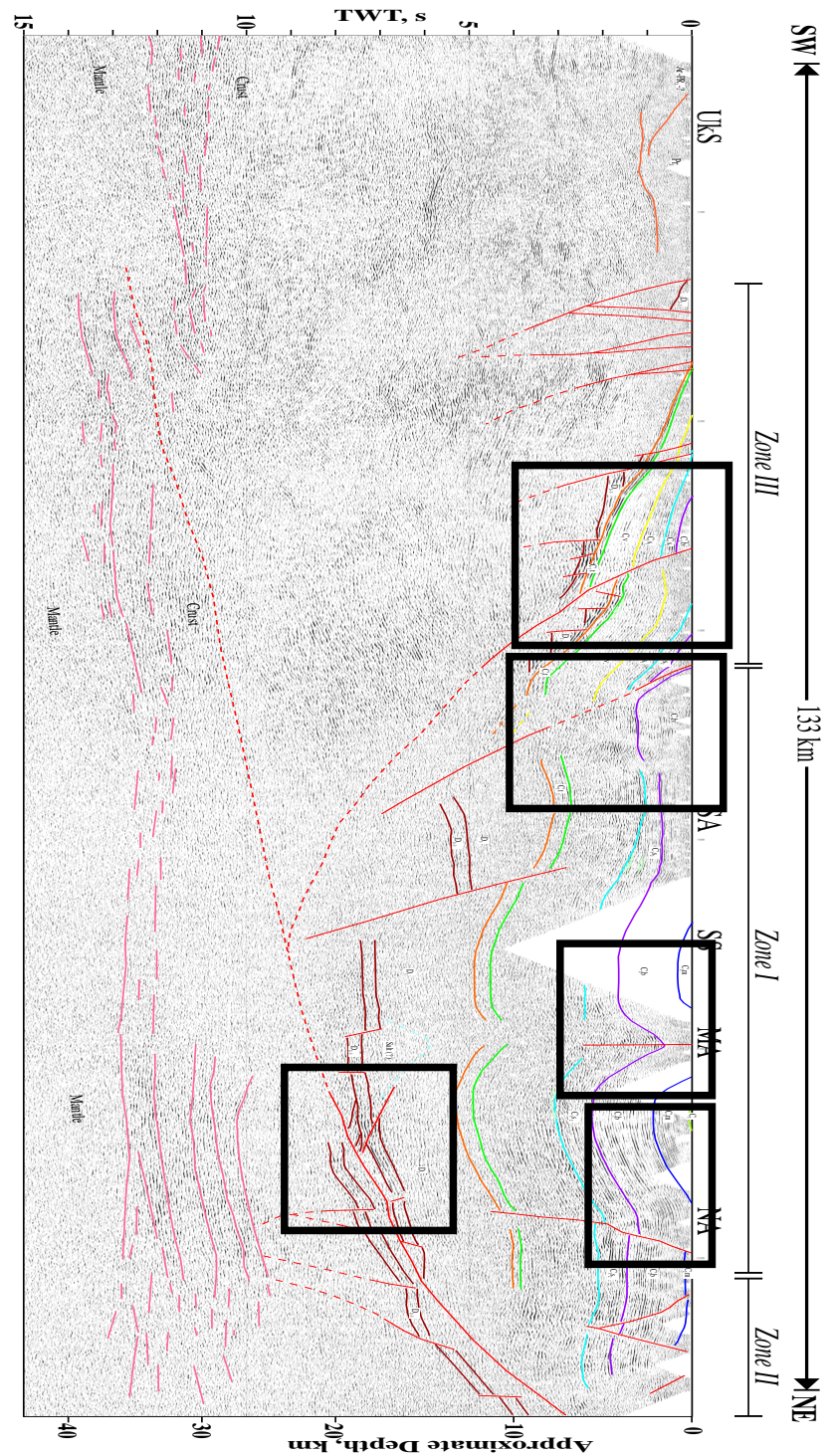


Figure 8.3: Interpreted poststack time migration of the seismic line. The interpretation was constrained using surface structural geology information. The boxes are the identified areas to be imaged with the CRS stack algorithm.

8.2.1 Small Scale Resolution, Dipping Layers and Anticline Flanks

As long as no additional information about the underlying model is available, the automatic CMP stack (see Chapter 6, section 6.4.2.1, page 82) is applied without constraints. If some information about the minimum and maximum stacking velocity of the medium is known, the constrained automatic CMP stack can be applied. The major advantage of using the constrained automatic CMP stack is that it reduces the search range for the optimum stacking velocity. In addition, I observed that much better zero-offset sections were obtained with the constrained automatic CMP stack than without any constraints.

Figures 8.4 and 8.5 represent unmigrated images of an area which cover the main anticline. Figure 8.4 is obtained from conventional stacking while Figure 8.5 results from applying the CRS stack. An obvious difference in the subsurface resolution can be observed. The most remarkable feature is the anticline flank which can be much better interpreted in Figure 8.5. The CRS stack which explicitly incorporates the reflector orientation in the stacking surface, strongly enhances the anticline boundaries and reveals other horizons that are not visible in Figure 8.2. The event between TWT 3 - 4 s in Figure 8.5 is completely absent in Figure 8.4.

8.2.2 Improved Imaging of Deep Reflections with a poor S/N-ratio

A typical problem in onshore prospecting is the imaging of deeper targets, where poor S/N-ratio hardly allows to construct continuous reflections. This was typical in the Donbas data, in the deeper part of the basin between TWT 5 - 10 s (Figure 8.6) and the lower crust. Therefore, it can be very difficult to construct continuous reflections from the conventionally stacked section (Figure 8.6). Figure 8.7 shows the CRS stack version with an interpreted fault line. This fault line probably describes an inclined listric shear zone within the axial part of the basin. The shear zone has also been observed in other parts of the DDB. The suppression of the noise and the amplification of the deep reflector elements by the CRS stack are clearly visible at this depth. The low amplitude areas between trace number 100 to 200 and between trace number 310 to 450 in Figure 8.7 are due to lack of traces in the prestack data. This area is exactly below the gaps seen in Figure 8.3.

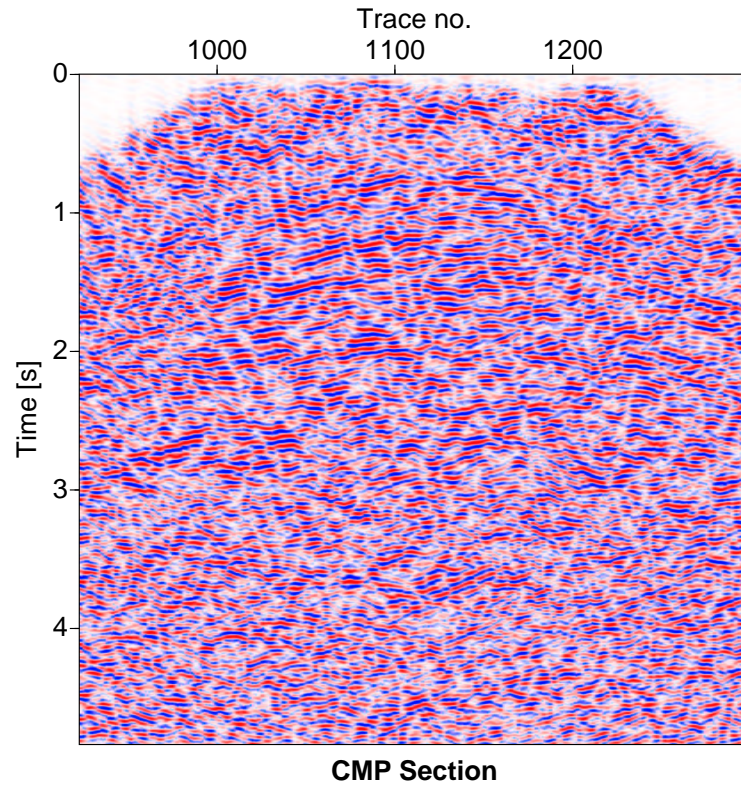


Figure 8.4: Unmigrated stacked section of the main anticline. This section was produced with the velocity section of Figure 8.1, after conventional velocity analysis and stacking

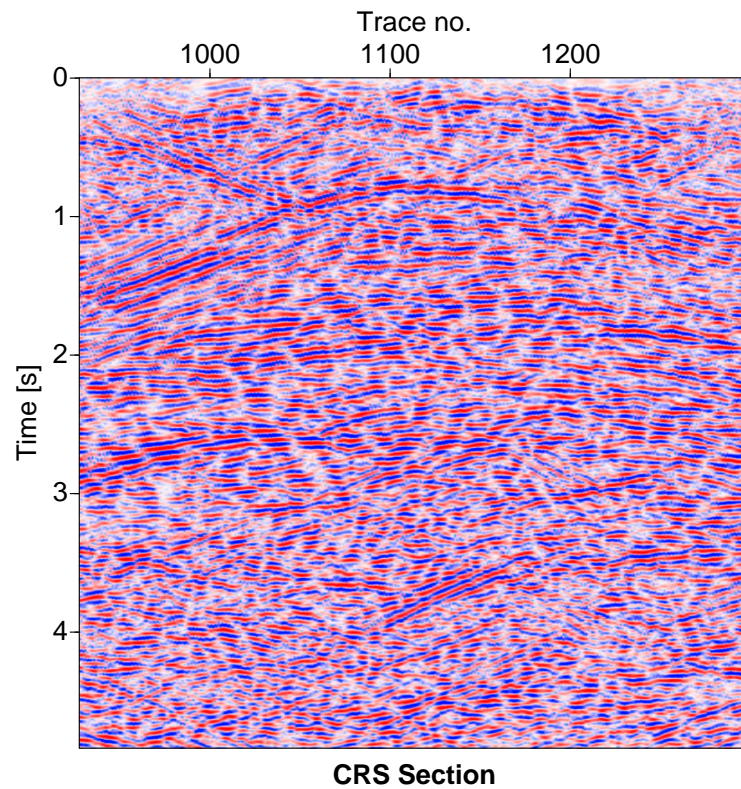


Figure 8.5: Unmigrated part of the main anticline after CRS stacking. The image quality is much improved compared to Figure 8.4

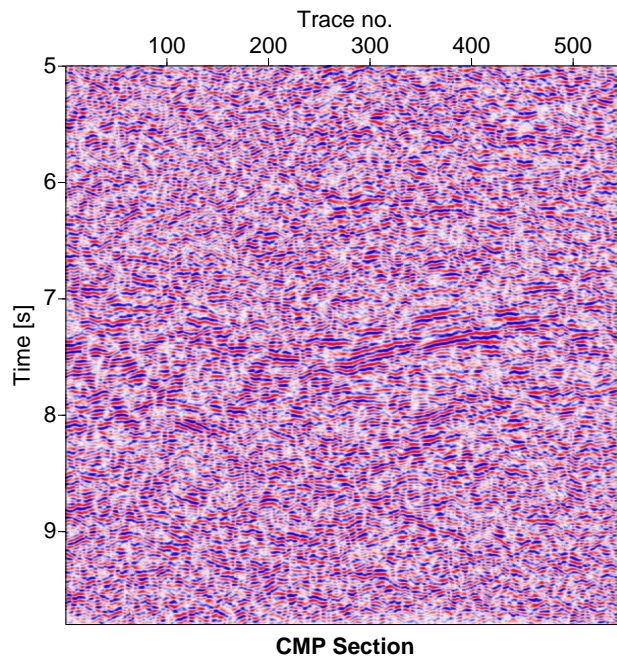


Figure 8.6: Conventional stack section showing the axial part of the basin. At this depth (5-10 s) the S/N-ratio is generally poor.

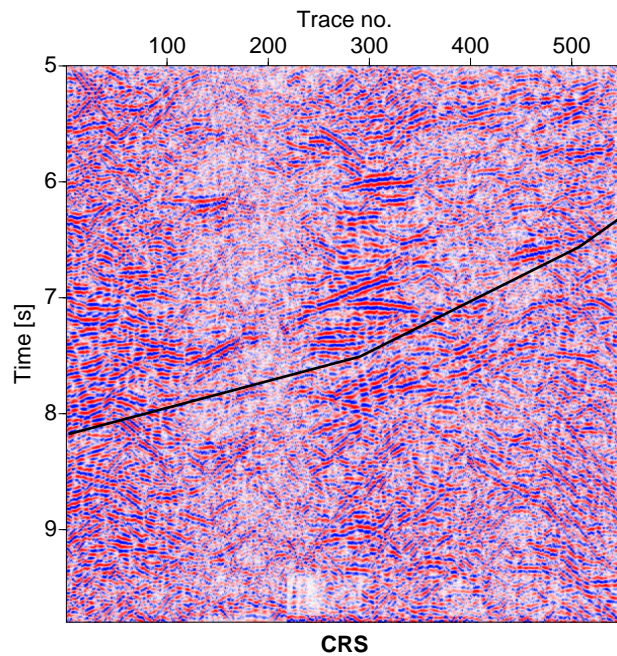


Figure 8.7: CRS stack section of Figure 8.6. Note the improved S/N-ratio as compared to Figure 8.6. The interpreted line shows the listric shear zone.

8.2.3 CRS Stack plus Poststack Time Migration

The CRS stack sections were poststack migrated using the Kirchhoff implementation of Paradigm Geophysical (Geodepth). For a reliable comparison the CRS stack and the CMP stack sections were migrated with the same rms-velocities. Note that because time migration is relatively insensitive to the velocity model, the accuracy of the image depends more on the quality of the unmigrated stack.

Figure 8.8 shows the fragment of the line showing in detail a basement involving backthrust on the southern flank of the DF as an example of the inversion tectonics as described in Chapter 7. In this figure only the main thrust reflector is clearly imaged. This figure was obtained after conventional CMP stacking and poststack time migration. Figure 8.9 shows the corresponding migrated section after CRS stacking. The quality of the migrated CRS data is excellent as compared to Figure 8.8. The S/N-ratio is highly improved and additional reflectors can be seen. Figure 8.9 is marked by a large number of continuous and highly energetic reflectors, which appeared weaker and less coherent in Figure 8.8. Steep dipping events (approximately 40°) not clearly resolved in Figure 8.8 are now enhanced. The change of reflector orientation near the surface indicates the location of the outcrop of the fault line. The surface location of this fault line was also seen in the structural geological section of the area. Note the enhancement of the near surface structure between TWT 0 - 0.7 s and trace numbers 0 - 210. The continuity of the main thrust reflector (TWT 1.5 - 2.2 s) is very well established.

In Figures 8.10 and 8.11 special emphasis is made to the improvement of the reflector continuity. This was one of the most difficult areas along the survey line. Not only the reflector continuity is improved in Figure 8.11 but also detailed reflector structures and their intensity are seen. Figure 8.12 and 8.13 are the result of the main anticline in the northern part of the line after migration. It is difficult to interpret the top and flanks of the anticline using Figure 8.12. In Figure 8.13 the top of the anticline and other reflectors are better imaged. Note that the improved quality of the CRS poststack migrated section is due to the improved quality of the CRS stack section.

The increase of the S/N-ratio is more obvious in Figure 8.15, where the deep subsurface structure can be more easily identified. This figure marks two Carboniferous stratigraphic units. A very strong increase of reflector continuity in the migrated CRS image is observed. As shown in the previous main anticline example, especially the dipping layers especially benefit from the CRS technique. Note that despite the good results, the data in these areas were not of optimum quality due to a number of technical shortcomings (shot positioning restrictions due to intensive coal mining, and coverage difficulties).

8.3 Summary

This chapter showed results of unmigrated and poststack time migrated CRS stack images of the Donbas Foldbelt. I stress that to obtain the stacked sections, no velocity analysis was required as is usually the case in conventional CMP stacking. However, it is necessary that the search parameter

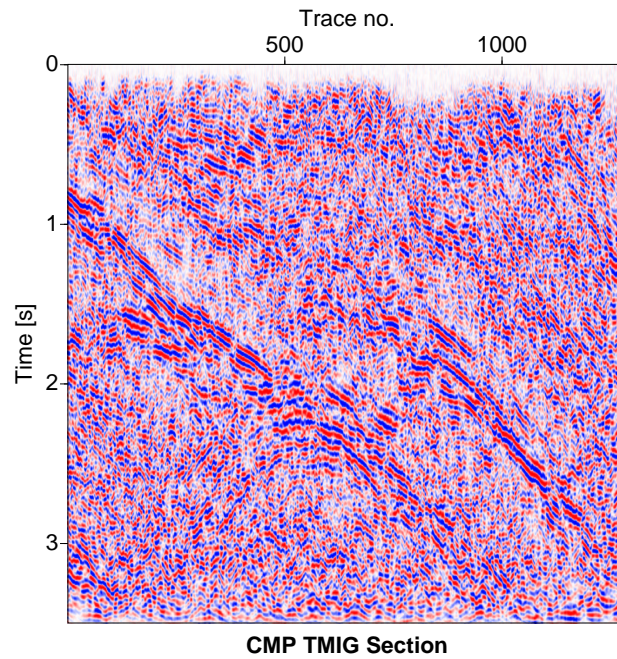


Figure 8.8: Poststack time migrated image of the main marginal fault zone of the basement after conventional CMP stacking. This image shows a backthrust on the southern flank of the DF, i.e. a reverse fault as an example of the inversion tectonics.

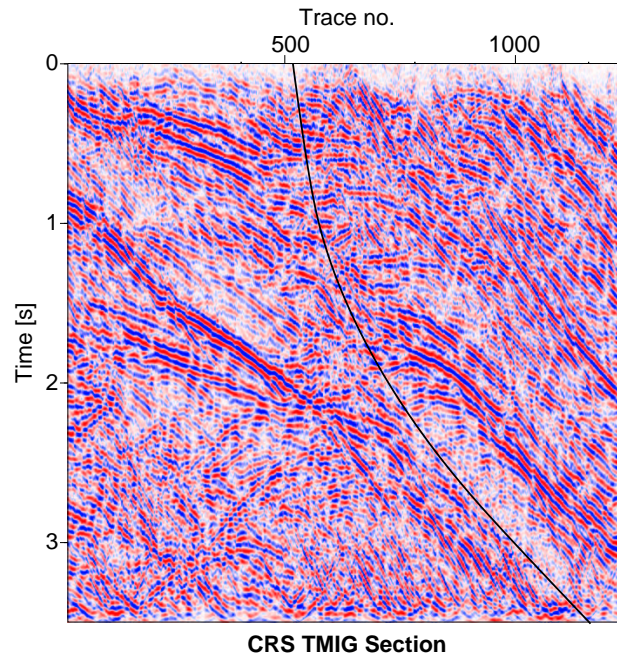


Figure 8.9: Same as in Figure 8.8 above but after applying CRS stack and poststack migration. The change in reflector orientation clearly shows the line of the reverse fault. More dipping reflectors up to the surface are better delineated.

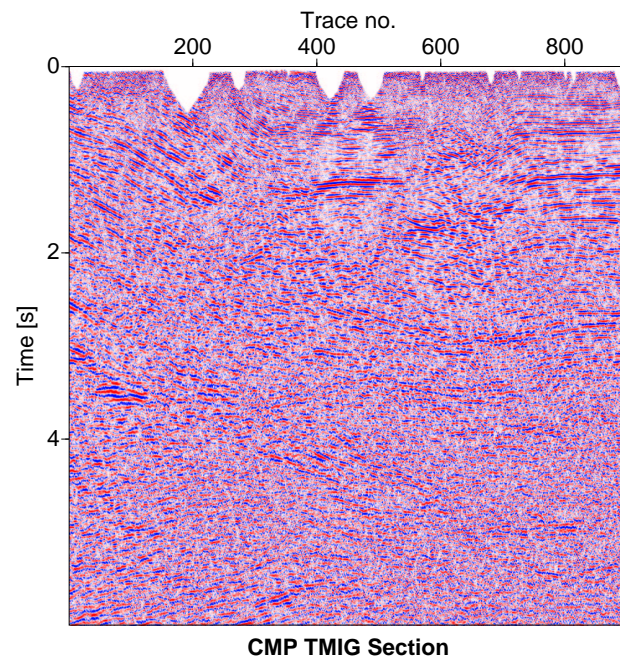


Figure 8.10: Poststack time migrated section after conventional CMP stacking

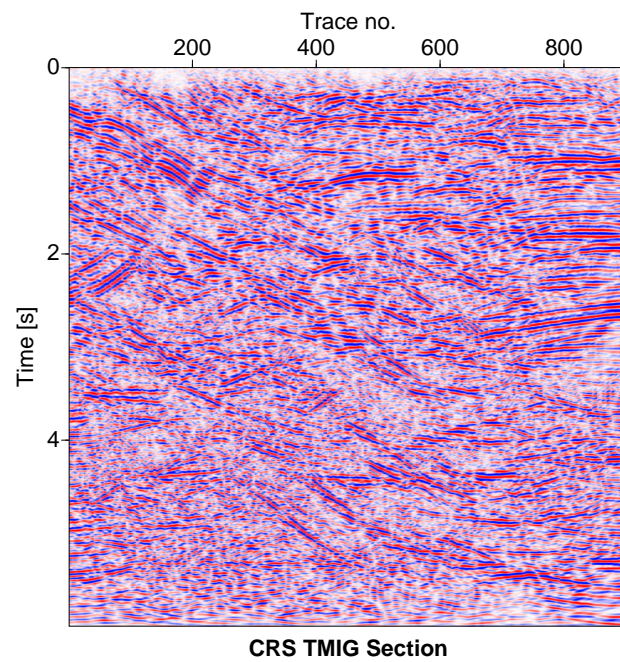


Figure 8.11: Poststack time migrated section after CRS stacking. This section is from the same area as in Figure 8.10.

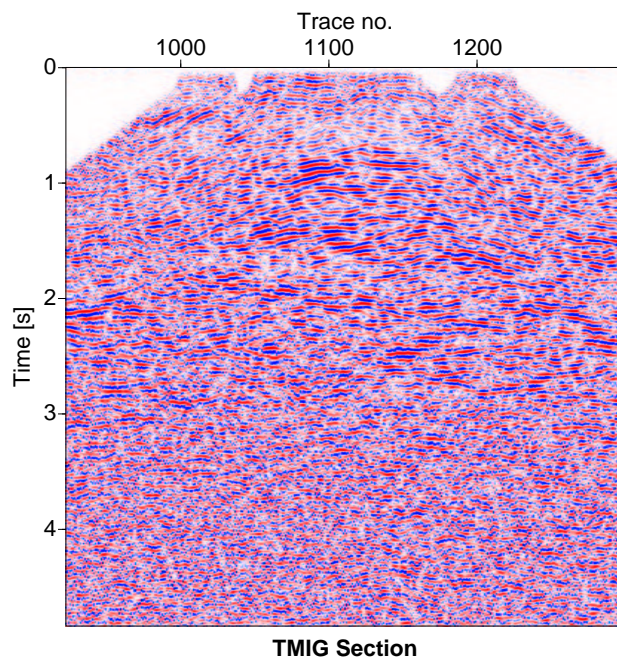


Figure 8.12: Poststack migrated CMP stack section. In this section the upper part of the anticline remains disturbed.

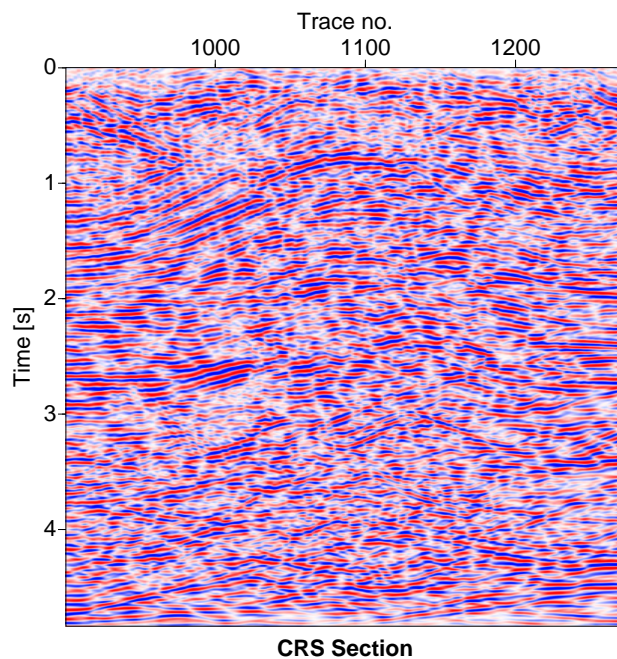


Figure 8.13: Poststack migrated CRS stack section. In this section the upper part of the anticline is more continuous than in Figure 8.12 and some internal reflectors are now clearly observed.

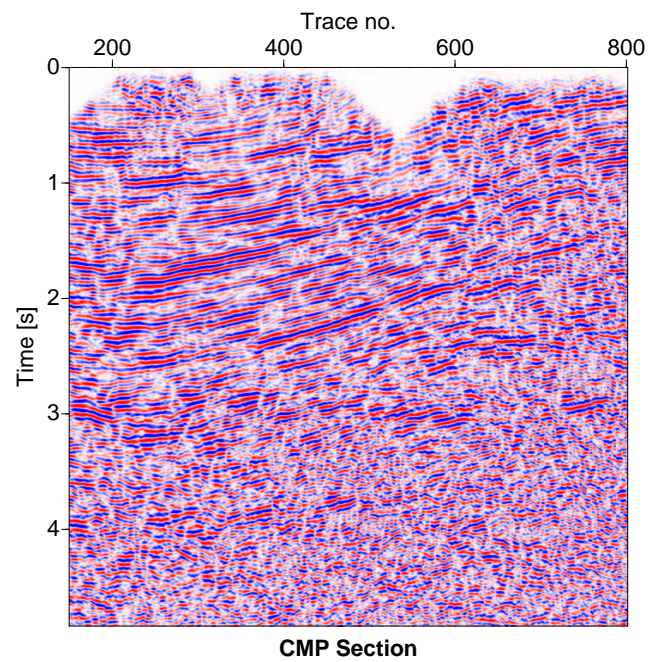


Figure 8.14: Poststack time migrated image after conventional CMP stacking.

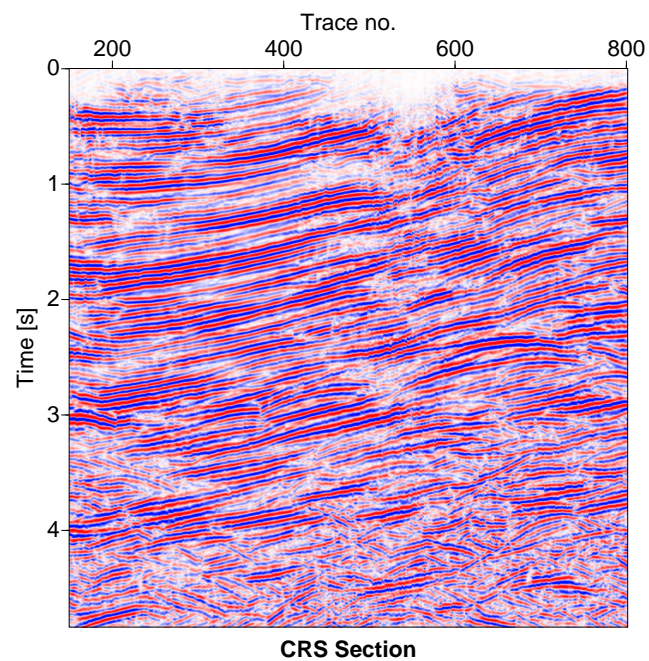


Figure 8.15: Poststack time migration after CRS stacking of the same section as in Figure 8.14.

for the automatic CMP stack be constrained. Using the constrained automatic CMP stack reduces the run time of the algorithm and as described in Chapter 7 allows for a better estimate of the wavefront attributes in the later stages of the flow.

For this data the CRS stacking method has proven to be a valuable supplement to the conventional CMP stacking processing. The three main expectations stated in section 8.1 were satisfactorily fulfilled. Better S/N-ratio, improved poststack image quality and the continuity of the reflectors are substantially better for the CRS time migrated images as compared to the respective results of the conventional CMP stack and CMP from migrated images. The time image of the CRS stack reveals a good definition of the major backthrust fault lines. Other examples presented by Mann et al., (1999) and Trappe et al. (2001) have shown similar results. Therefore, I suggest that in complex geology where CMP stacking (NMO/DMO) and the subsequent poststack migration fails or give poor results, the CRS stacking and poststack migration is a better alternative. The CRS image has a larger fold, since the summation surface extends over several CMP gathers. This leads to the visible increase in S/N-ratio and reflector continuity. The adaptation of the CRS stacking parameters at each point of the prestack data improves the resolution in two respects. First, it compensates for small scale overburden effects of the prestack wavefield. Second, the small scale structures produced by the fault line are resolved much more distinctly. The fault lines are better identified and their offsets can be easily followed into the subsurface. The newly gained information from the migrated CRS stacked section will be interpreted and incorporated in a velocity/depth model building flow in Chapter 9.

Chapter 9

Velocity/Depth Model and Depth Imaging: Donbas Foldbelt Data

9.1 Introduction

In Chapter 8, I showed examples of using the model-independent CRS stack method for imaging the DF data. This model-independent method produces time images. If depth imaging is required, a velocity/depth model is needed. Therefore, the next stage in imaging the DF data is to construct a structural velocity/depth model. The major issue is how to estimate the appropriate velocity model by incorporating all the information from Chapters 7 and 8. In this chapter I will describe the five methodologies which I followed in order to obtain the velocity/depth model. The methodologies are listed as follows:

1. Poststack time migration (CRS and conventional sections) and interpretation of main horizons (see Chapter 8).
2. Prestack depth migration (PSDM) using an initial velocity model obtained from coherency inversion.
3. Iterative and interpretive adjustment of the velocity/depth models for optimising prestack depth migration.
4. Structural interpretation of the prestack migrations during the iterative process.
5. Use of additional information from the migrated CRS images and surface structural geology for the structural interpretation of the depth migrated section.

Following these methodologies (especially step 4 and 5) reveal that an integration of geology and seismics is an important strategy for the success of the results. In the literature the strategy of estimating structural velocity/depth models by integrating information from different disciplines is called a model-based method (Fagin, 1991). An advantage of model-based methods is that it is easy to bring in a priori information about the model in the process. In this work I use interpretational information from the migrated CRS stack images and from structural geology in estimating the velocity/depth model. This shows that PSDM is both a processing and an interpretative tool.

Because the process of migration velocity analysis is iterative and all the shot gathers have to be re-migrated each time, I use first arrival prestack depth migration. First arrival in this sense means, the traveltimes computation method is a finite difference eikonal solver (see Chapter 2, Section 2.4, page 19). To further reduce the run time, a layer-by-layer model updating is applied. To obtain the final depth migrated section, I then apply the maximum energy arrival prestack depth migration.

9.2 Structural Model Building and Updating

9.2.1 Initial Model

The construction of the initial model is performed through coherency inversion (Landa et al., 1988, 1991). Coherency inversion estimates interval velocities directly from the prestack data and it does not require reflection event picking on the prestack data. It uses raytracing to derive a family of moveout curves for a range of “test” interval velocities. The input includes CMP trace gathers and zero-offset traveltimes of principal reflectors. The zero-offset times are given from interpreted time horizons. Usually the time horizons are picked on unmigrated stacked sections and it is assumed that there is no vertical velocity gradient within each layer. However, the velocity can vary laterally. The positions of the time interfaces and velocities within the layers are parametrised by spline functions (Landa et al., 1988).

Coherency inversion is performed in two steps. First, for a given trial constant velocity the n -th unmigrated time horizon (n is the layer number) is mapped to depth by normal incidence ray migration using the picked zero-offset time information. Second, for selected CMP gathers and surface locations along the line nonzero-offset traveltimes are computed by ray tracing through the obtained depth model. Using the modelled moveout curves, semblance values are computed on the selected CMP gathers along the actual prestack reflection events (Landa et al., 1988, 1991). Therefore, for every CMP group a semblance function is computed along the reflection travel-time. During each iteration and for a range of test interval velocities, synthetic traveltimes curves are computed for the interface under consideration. This semblance function reaches a maximum value when the synthetic arrival time curves match the arrival times of the reflection events on the prestack CMP gathers. The semblance functions are interpreted and the velocities with the maximum semblance is assigned to that layer below the CMP location where the inversion is being performed. Therefore, the inversion produces a velocity/depth model that maximises semblance coherency on prestack trace gathers. Note that the semblance computation is analogous to the semblance computation in conventional stacking velocity analysis. In contrast to stacking velocity analysis, in coherency inversion the moveout curves along which semblance is calculated can be non-hyperbolic since ray tracing in a laterally heterogeneous model is performed.

Practically, the inversion is performed either in a continuous mode or local mode. In the continuous mode a range of CMP positions are given and the inversion is performed automatically through all the CMP gathers. The result is a semblance plot which is then interpreted. In local mode each CMP gather is analysed separately and the inversion is performed. The result of this is the NMO corrected CMP gather with a histogram showing the velocity value with the maxi-

mum semblance coherency (see Yilmaz, 2001; Geodepth Users Guide). The coherency inversion is performed layer after layer until the whole model is completed. Before proceeding from one depth horizon to the next, I edited the horizon to remove very unreasonable jumps in the horizon structure.

As indicated above, time horizons on unmigrated stacked sections have to be interpreted. Note that the areas along a reflector horizon which are wrongly interpreted will definitely give wrong interval velocities. Therefore, interpreting or picking the correct horizons, together with the corresponding diffractions, is important for the success of the coherency inversion. Generally, in complex areas like the DF geology it is practically inefficient to interpret the unmigrated stacked section including the whole spread of triplications. Therefore, I suggest to perform poststack Kirchhoff time migration using rms velocities. The rms velocity is obtained from the stacking velocities (Figure 8.1). This is followed by interpreting the migrated section to give a time model. The time model is then demigrated to give the unmigrated interpretation time domain. In this work I constrain the interpretation of the time horizons by surface structural geology. Only the main horizons which show strong velocity contrast are interpreted.

9.2.2 Integrating Migrated CRS Images into Model Building

The interpretation of the time horizons strongly depends on the quality of the poststack time migrated sections. Therefore, in the areas of poor time migrated signal quality, interpretation of time horizons were inefficient and prone to errors. In the areas where poststack time migrated images gave unsatisfactory results, I interpreted the images from the migrated CRS stack section (e.g., Figures 9.1, 9.2, 9.3 and 9.4). I link the poor quality of the migrated CMP stack data to incorrect stacking velocity, poorly picked events for stacking velocity analysis and/or incorrect rms velocity used for poststack time migration. Note that the imaging potential of the poststack time migration depends on the quality of the unmigrated stacked section. Thus, poorly stacked data directly leads to poor migrated images. The model-independent CRS method avoids the problems of wrong stacking velocities and “pushes” the use of velocity only for the depth conversion phase. In addition, because the CRS method is data-driven, errors due to wrong prestack reflection event picking are avoided. For these reasons interpreted migrated CRS images give reliable picks of time horizons (Figures 9.1, 9.2, 9.3 and 9.4). The reflector continuity and high S/N-ratio simplifies the horizon interpretation. Figures 9.3 and 9.4 clearly show in detail the orientation of reflector dips and the main backthrust zone, and the top of the main anticline. Time horizons on the other areas with migrated CRS images are picked. Note that imaging with the CRS method need not be limited only to certain areas, but can be used to image the complete data set. In this work the application of the CRS method was limited only to particular key areas because of computational limitations.

Finally, after interpreting the complete time migrated section, the interpreted time horizons are demigrated via normal incidence rays onto the unmigrated stacked section. The unmigrated horizons are directly used as input into coherency inversion. Therefore, the first stage of integrating

model-independent and model-dependent structural interpretation is performed at this level. At other stages of the model building process it was necessary that the interpretation is supported by the horizon geometry of the migrated CRS images. Figure 9.5 is a summary of the new processing flow for estimating the initial interval velocity/depth model in complex areas such as the Donbas Foldbelt data.

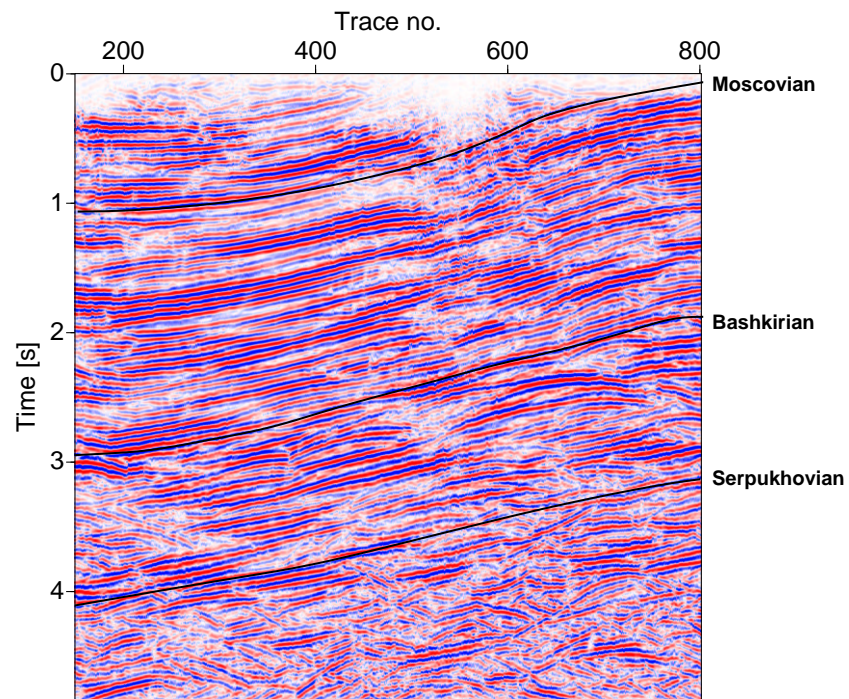


Figure 9.1: Time horizons on a CRS stack migrated section showing three distinct stratigraphic units.

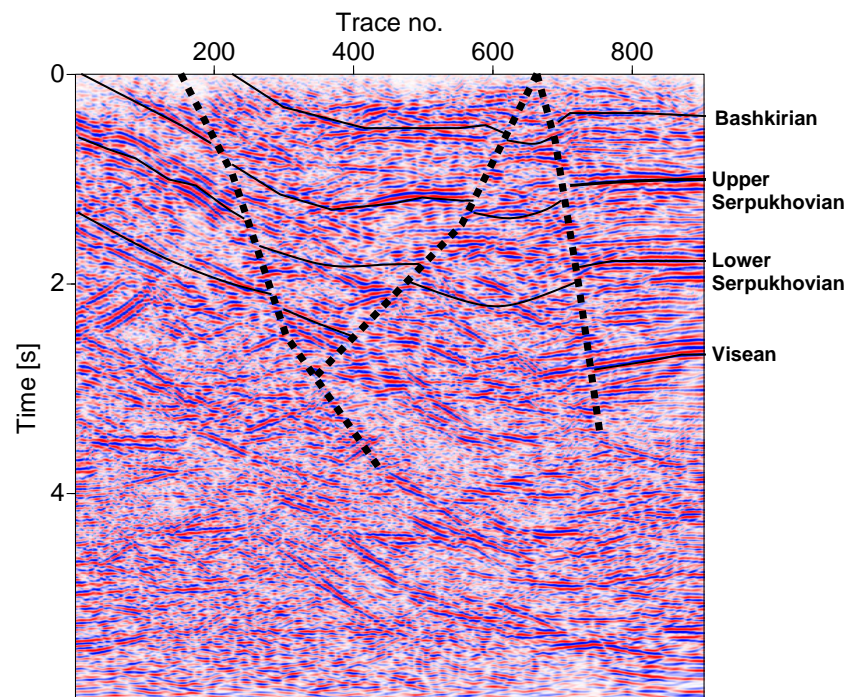


Figure 9.2: Interpretation of CRS time horizons on the structured syncline.

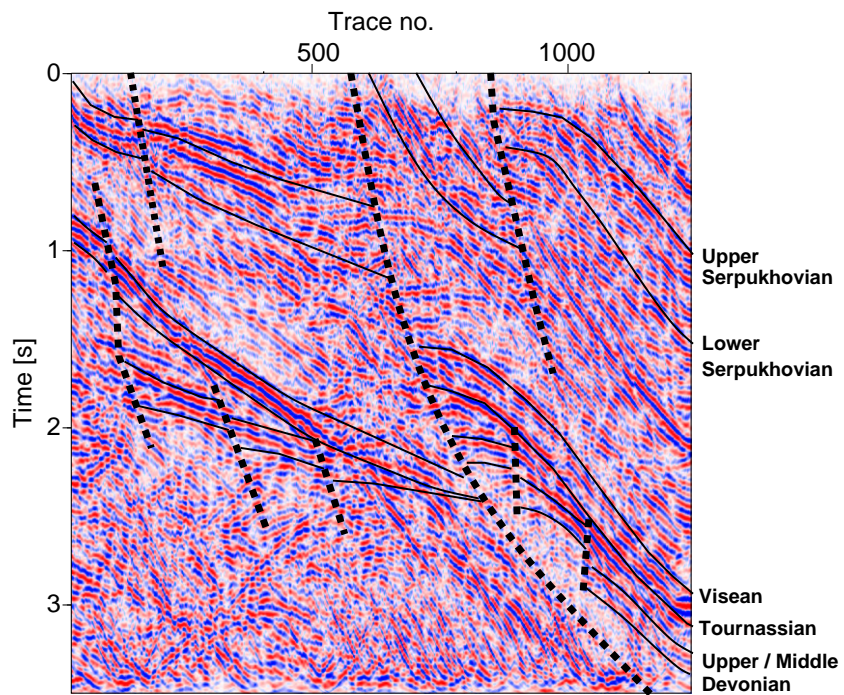


Figure 9.3: Interpreted time horizons on migrated CRS image. This Figure shows details of the basement involving thrust on the southern flank of the DF.

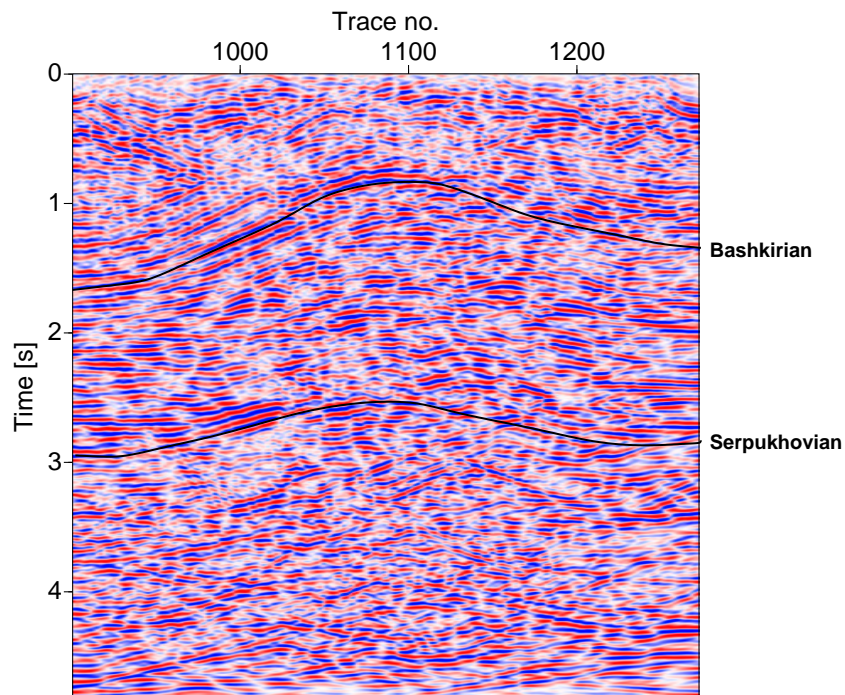


Figure 9.4: Interpretation of migrated CRS time horizons on the main anticline.

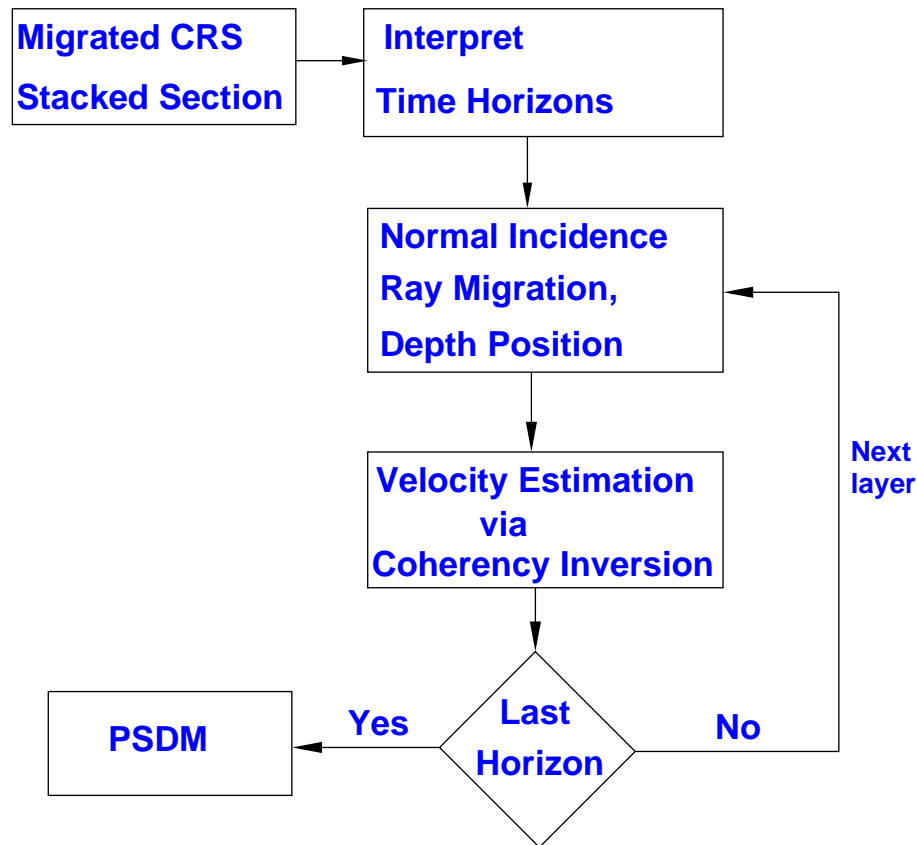


Figure 9.5: A scheme of processing flow for estimating the initial interval velocity/depth model of the Donbas Foldbelt data. Generally, one can completely generate the unmigrated stacked section with the CRS method and later apply poststack time migration. This is recommended because the whole time stacked section would be generated with the same algorithm (completely data driven).

9.2.3 Iterative Prestack Depth Migration and Model Updating

9.2.3.1 Migration Velocity Analysis

The initial velocity/depth model from coherency inversion and CRS stack is used as input into prestack depth migration. After the first PSDM, the velocity/depth model has to be updated. Residual moveout analysis with the CRP gathers and structural interpretation of the migrated section are applied to update the velocity/depth model. Residual moveout analysis identifies the remaining error in interval velocity to flatten the CRP gathers. Therefore, updating the velocity model refers to the process of determining the velocity errors in the CRP gathers and correcting the velocity data.

In residual moveout analysis (also known as coherency analysis) CRP gathers should be independent of source-receiver offset and be flat when the layer velocities are correct (see Chapter 1.5). After the first migration and for a set of CRP gathers, I examine the offset variation of the CRP gathers. Figure 9.6 shows examples of some CRP gathers (CMP numbers 6200, 6400, 6600 and 6800) to the depth of 9 km. The gathers show upward residuals. The upward residuals indicate a too low migration velocity. A downward residual moveout would indicate a too high interval velocity.

Residual moveout analysis on CRP gathers uses semblance sections. For each residual moveout, a theoretical hyperbolic curve is estimated and fitted to the actual CRP event. This curve describes errors in interval velocity. A semblance value is computed for every residual and a semblance section is created (Figure 9.7). Note that the original interval velocity field is used to compute the theoretical residual curves. The semblance plots (Figure 9.7) are interpreted to best reflect the primary residual moveouts. From the interpretation, the model is updated in accordance with the new velocity values. In Figure 9.7 the semblance plot has a positive and a negative axis. A line in the centre (black line in Figure 9.7) defines the zero-error zone (no residual moveout, i.e. CRP events are flat). A deviation from this centre line indicates an error in velocity.

Even though the CRP gathers are in the depth domain, the residual moveout analysis is performed in the time domain. First, the depth migrated CRP gathers are converted to the time scale using the initial interval velocity. In the time domain the residual moveout is given as (similar to NMO equation):

$$\Delta t = \sqrt{t_o^2 + \left(\frac{1}{v_c^2} - \frac{1}{v_o^2} \right) x^2} - t_o, \quad (9.1)$$

where t_o is the reflection time at zero-offset; x is the offset at which the residual is measured; Δt is the time residual, defined as the time difference between the location of the CRP event at zero-offset and the location of x ; v_o is the original rms velocity, which is converted from interval velocity, $v_i(z)$: At first the $v_i(z)$ is converted to time scale, $v_i(t)$, and $v_i(t)$ is then converted to rms velocity, $v_{rms}(t)$, using Dix's formula. v_c is the new corrected rms velocity. The new rms velocity is converted to a new interval velocity as a function of time, $v_{cINT}(t)$ and it is later converted to depth $v_{cINT}(z)$. In time domain CRP gathers also allows for the application of other conventional processing techniques such as mute and filter to improve the appearance of the final migrated section. The updated interval velocity is interpreted and continuous velocity functions are picked along the horizons. Note that the depth structure has not been updated. Note that in Equation 9.1 if v_o is equal to v_c then the residual moveout is zero and the CRP gathers should be flat.

9.2.3.2 Updating Depth Horizons

With the new velocity section, a new prestack depth migration is carried out and the layer geometry for the corresponding layers are determined by picking new depth horizons from the migrated section. The horizon interpretations were based on the migrated section and guided by migrated CRS stack sections and the surface structural geology section. The process of horizon interpretation is crucial because wrong interpretation of horizons lead to a wrong depth model. In addition to the surface structural geology, I use particular characteristics such as reflector pattern, amplitude, lateral continuity and interval velocities in defining the seismic horizons. I superimpose the velocity/depth model onto the migrated section and perform the depth model re-interpretation. The interpretation was tied to the structural geological model which was provided by Ukrgeofisika. The interpretation becomes complicated in regions of low amplitude reflectivity. In the areas of missing shots only geological information is used to continue reflector interpretation. Line drawing of the fault lines (normal and reverse faults) were constrained by the surface geology model.

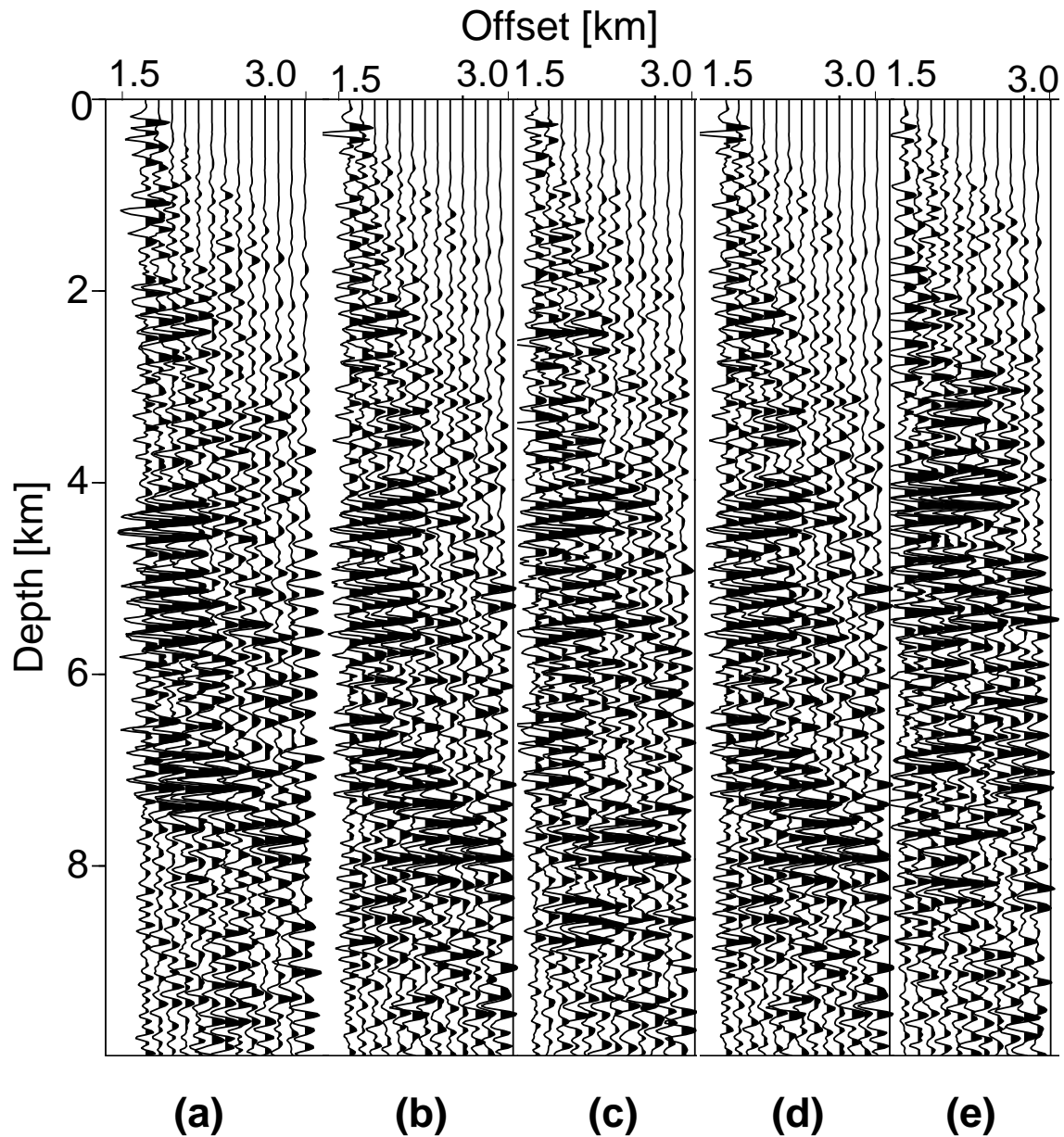


Figure 9.6: CRP gathers showing residual moveout. The upward moveout indicates that the migration velocity is too low. The gathers are CRP numbers 6200, 6400, 6600, 6800 and 7000. From about 7.0 km the gathers show downward curvature.

Well imaged structures in the shallow section were used to constrain the structure of the poorly imaged deeper sections. Fault offsets clearly imaged in the shallow section were carried down to other layers. The position of outcrop of the main fault line onto the surface was supported by the migrated CRS stack image. After re-interpreting the depth horizons, a new velocity/depth section is generated and PSDM is repeated. The layer velocity updating and re-interpretation of the depth horizons are repeated until the velocity/depth model and the migrated section are fairly consistent. A schematic of the processing flow is given in Figure 9.9.

To obtain the final model three iterations with the maximum energy arrival prestack depth mi-

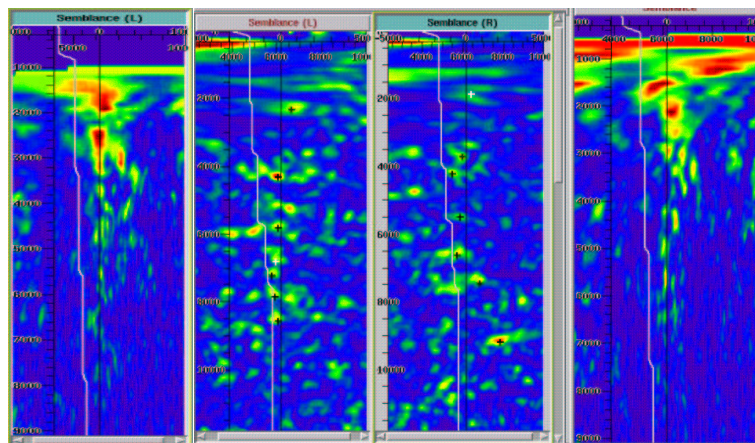


Figure 9.7: Example of semblance analysis for migration velocity. The plot is for the gathers 6200, 6400, 6600, 6800 and 7000 shown in Figure 9.6. The white line on the semblance plot is the velocity profile at the CRP gather location. The black centre line indicates zero residual moveout. The velocities are too low if the semblance maxima are at the left of the line, and velocities are too high if the semblance maxima are to the right of the black line.

gration are performed. In maximum energy arrival migration (also known as ray-based Kirchhoff migration) the method used for traveltimes computation is the wavefront construction algorithm (Vinje et al., 1993; Ettrich and Gajewski, 1996). This method computes proper amplitudes and uses the maximum amplitude arrival for multivalued arrivals. It is superior to the first arrival migration which gives only fastest traveltimes (see Section 9.2.4). Figure 9.8 displays the same CRP gathers as Figure 9.6 after PSDM with the final velocity/depth model. The CRP gathers are sufficiently flat, thus, indicating the correctness of the interval velocities (Figure 9.10). The CRP gathers are muted in order to remove migration artifacts (see Section 4.1.1.1, page 46). After muting the gathers are summed to give the final PSDM section (Figure 9.11). Note that the maximum energy prestack depth migration require that the input velocity/depth model need to be smoothed. Sometimes, even if an accurate structural model is generated, smoothening of the model (which is required for ray tracing) for Kirchhoff PSDM can introduce errors in the velocity model. The degree of smoothening a model can affect the image positioning as well as the strength of the reflectivity (i.e., the amplitude attributes). Other authors (e.g Versteeg, 1994) have shown that care has to be taken when smoothing structural models.

9.2.3.3 Results and some Geologic Discussions

Figure 9.10 shows the final velocity/depth model. In the crystalline part of the model, I use a smooth gradient model, $v(z) = v_o + az$, with the gradient, a , given as 0.038, and $v_o = 5.9 \text{ km/s}$ as the starting velocity from the surface. The depth model ranges from 0 - 21 km with velocities from 4.0 - 6.2 km/s. Figure 9.11 is an image of the complete depth section (i.e, CMP 176 to 8126). Generally, the depth migrated section shows detailed resolution of the basin sediments. The sedimentary cover is expressed as well-defined package of reflectors. The sediments are resolved from the Ukrainian Shield (Zone III) to the axial part of the DF (Zone I) and further towards the northern part (Zone II) of thrusting and folding. In Figure 9.12 - 9.14 particular sections of the depth

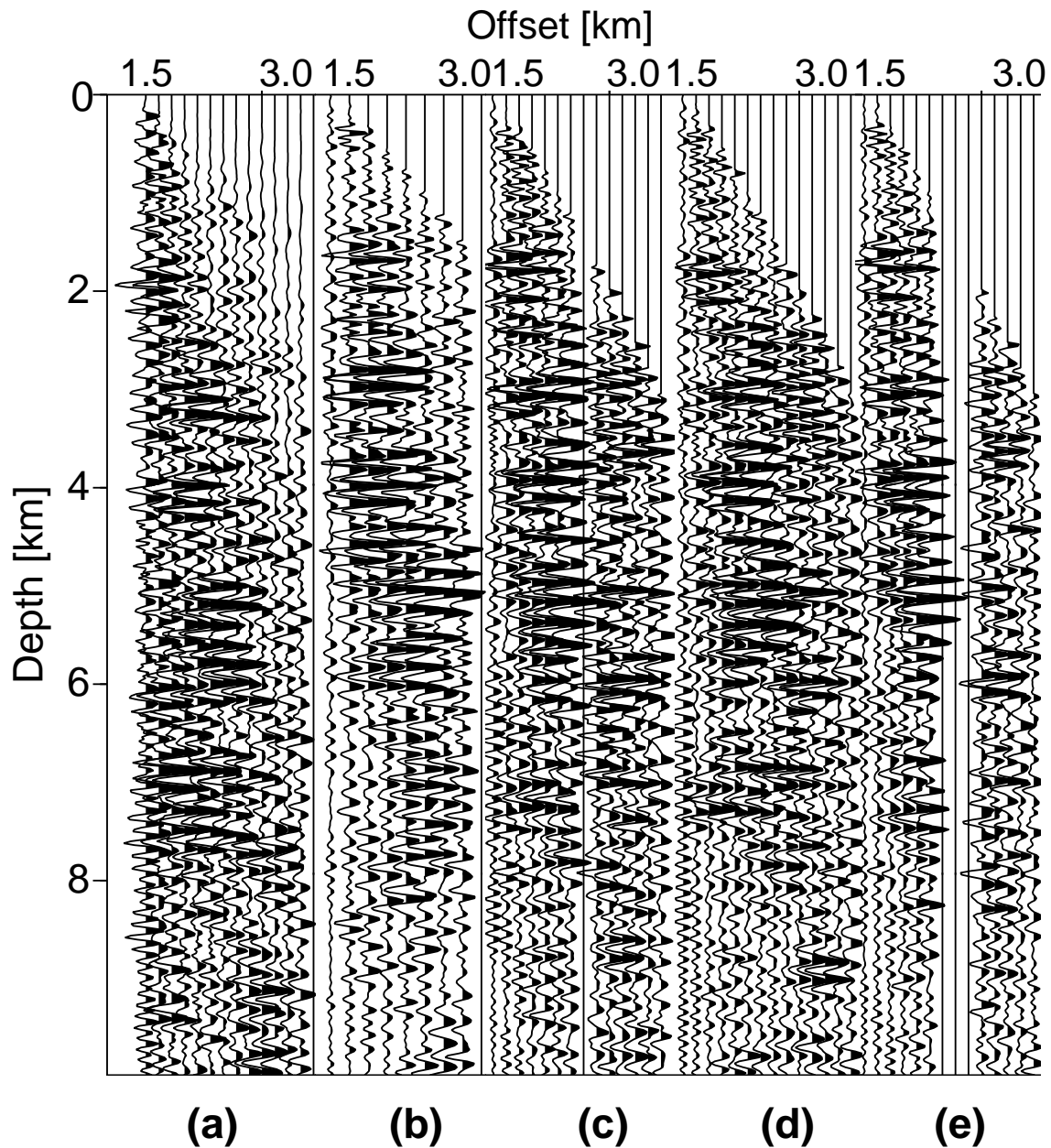


Figure 9.8: The same gathers as in Figure 9.6 with flat events after final model updating.

migrated image are displayed. These sections display characteristics involving the inversion of the basin and its rifting. The Figures are overlaid with the final velocity/depth model. Figure 9.12 is a fragment of the southern part of the basin basement. It is interpreted into four main Carboniferous layers disrupted by the main backthrust fault. This zone of backthrust shows the extent of the basin inversion during Early Permian. The major backthrust fault has an offset of ca. 3 km. The basement of the basin which is of Devonian sediment is disrupted by minor syn-rift fault systems, which later form traps for pre-rift and syn-rift sediments.

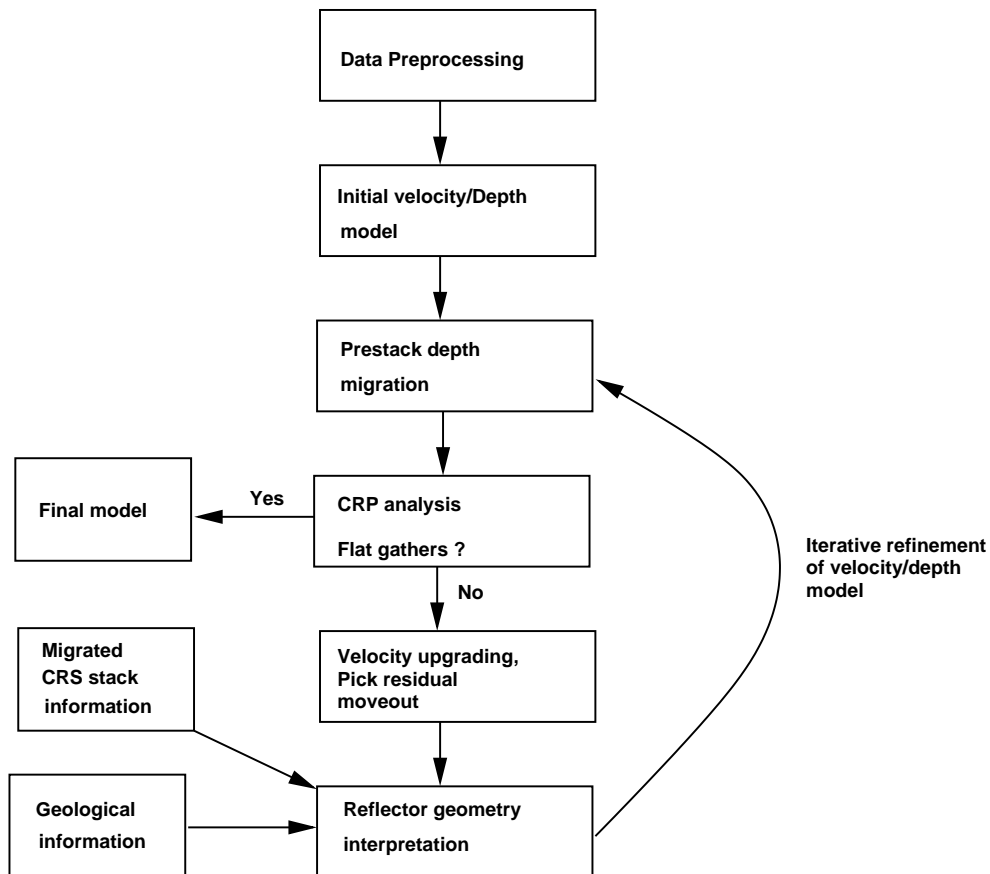


Figure 9.9: Iterative flow steps for obtaining the final velocity/depth structure. PSDM begins with an initial velocity/depth model from coherency inversion. If the CRP gathers are flat then the model was accurate. If the gathers are not flat then the model needs to be updated and the migration is repeated. Reflector geometry from migrated CRS stack images is used in areas where prestack depth migration produced poor results. Informations from structural geology are incorporated to interpret the depth migrated horizons after each re-migration.

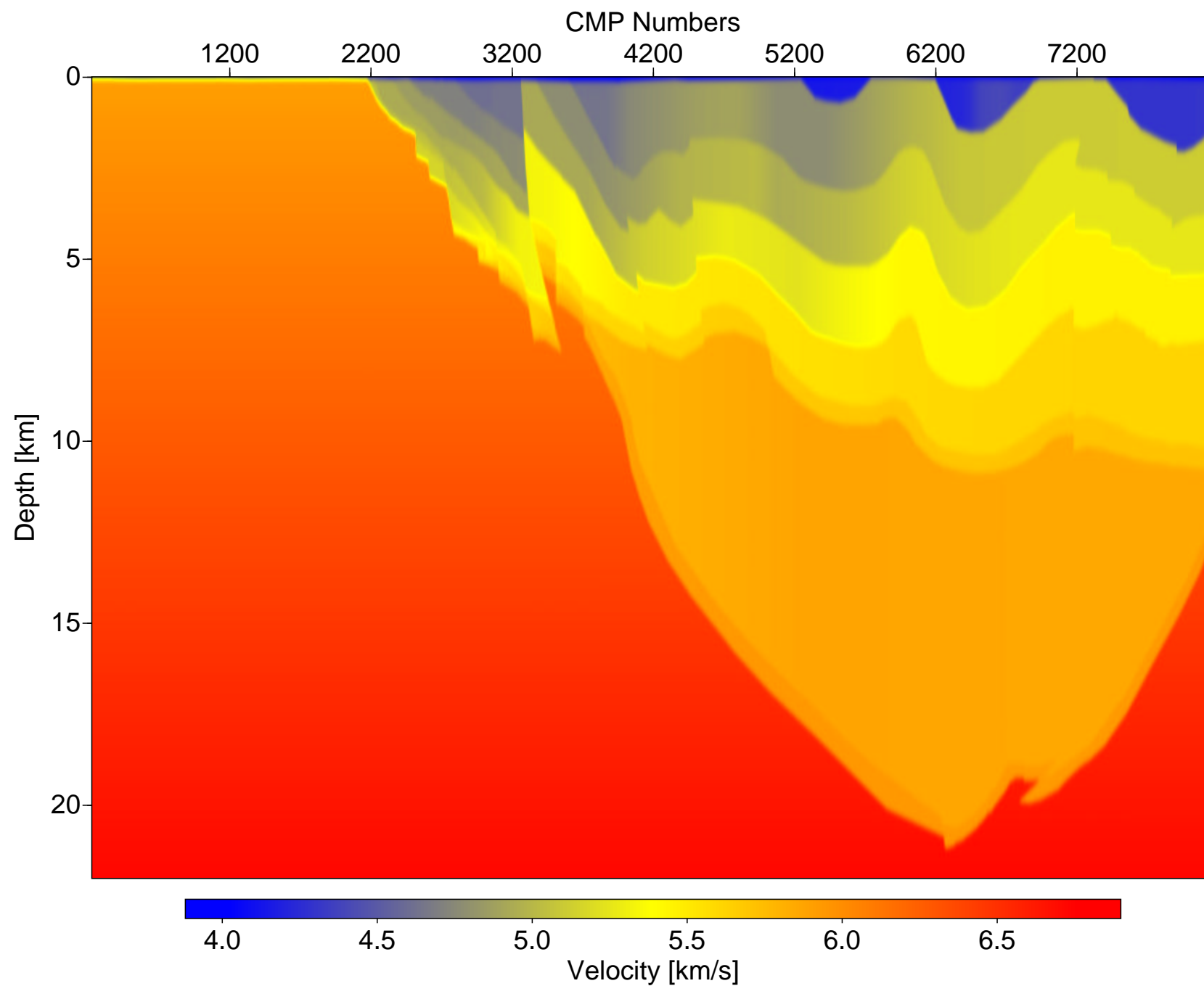


Figure 9.10: Final interval velocity/depth section

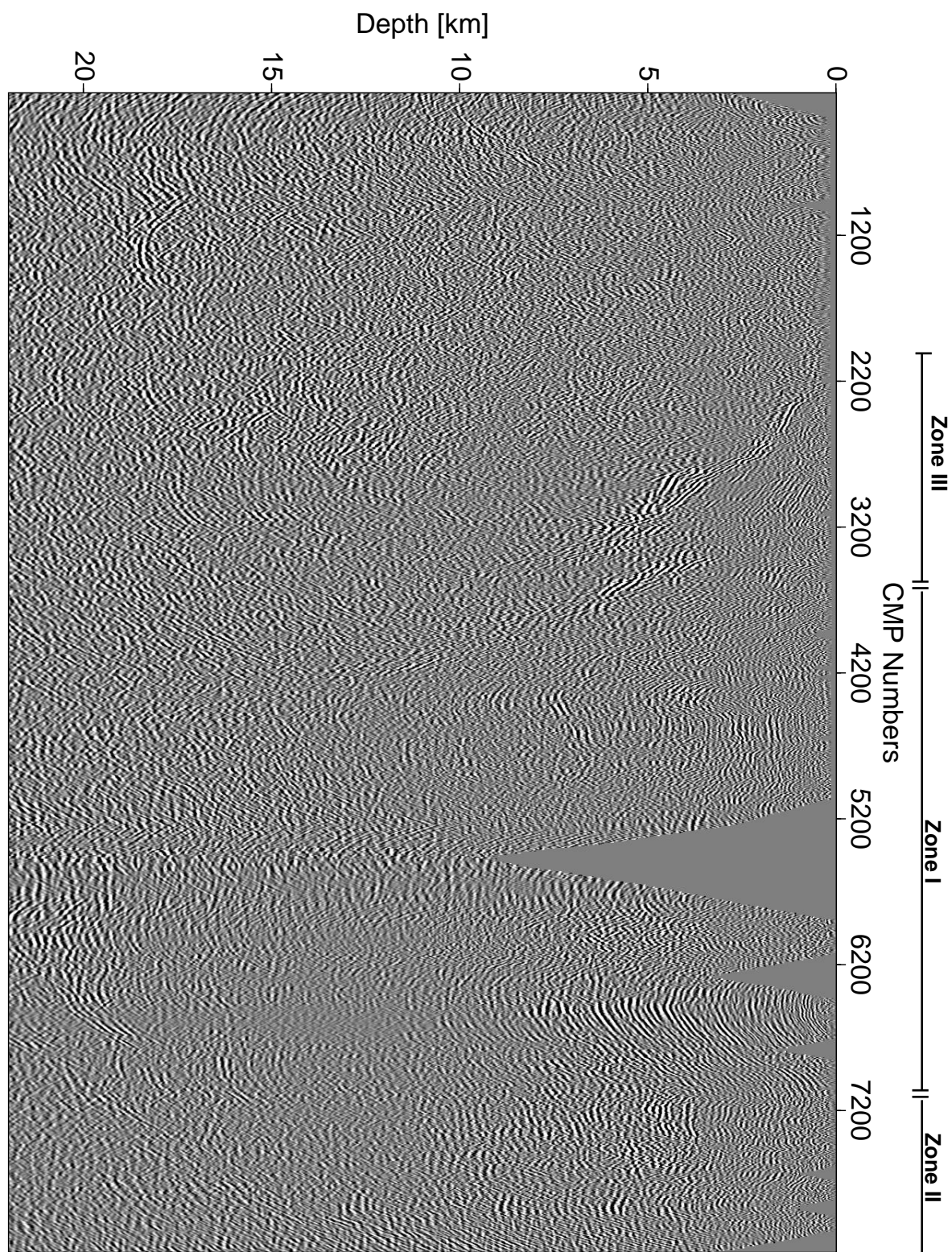


Figure 9.11: Depth section after PSDM using the final interval velocity/depth section (Figure 9.10)

The northern part of the basin is displayed in Figure 9.13, while Figure 9.14 displays the deepest part of the basin. In Figure 9.13 fault systems are interpreted from the surface right into the subsurface. The intense tectonic occurrence in this part is explained by a compressional force originating from the southwest and pushing towards the Russian Shield in the northeast. Figure 9.14 is a fragment of the axial part of the basin, at the depth of about 20 - 21 km. This Figure displays a listric shear zone which also appeared on the surface and extended through the Moho. The outcrop of this fault line to the surface was observed on surface geological sections as well as on the extension of the seismic line (DOBREflection-2001).

The geological interpretation of the complete depth migrated section is shown in Figure 9.15. The basement of the basin is disrupted by the Devonian (D_{2-3}) syn-rift faults (see also Figure 9.12). Some of these faults were reactivated during post-rift extensional tectonic events in Carboniferous and Early Permian times (Sergiy Stovba, personal Communication). A summary of the main tectonic events during rifting and rift-reactivation is shown in Figure 7.4. On the southern part of the profile, a pronounced backthrust affecting the whole sedimentary succession as well as the upper crust is clearly evident. It has horizontal and vertical offsets of about 3.5 km and 2 km, respectively. Most of the folding and reverse faulting occurred during the Late Triassic and Late Cretaceous times (Stovba and Stephenson, 1999). The thickness of the sediments reaches about 20 - 21 km in the axial part of the DF (see also Figures 9.10 and 9.15). The corresponding thickness of Devonian syn-rift sediments is about 14 - 15 km. Note that the younger Mesozoic sediments and a significant portion of the Carboniferous succession were eroded during subsequent inversion of the basin (see Chapter 7). The basin inversion (i.e. compressional deformation) and uplift is mainly displayed as folding and thrusting within the Carboniferous succession while the Devonian sediments appear not to have been affected. It is argued that this pattern is related to decoupling effects of Upper Devonian salt-rich sediments (Stovba, personal communication). However, there was no evidence of salt bodies on the seismic section. The main anticline (indicated as B in Figure 9.15) is the largest and most prominent pervasive fold in the axial part of the DF (Zone I), and it is bounded by the southern (indicated as A) and the northern (indicated as C) synclines (Figure 9.15).

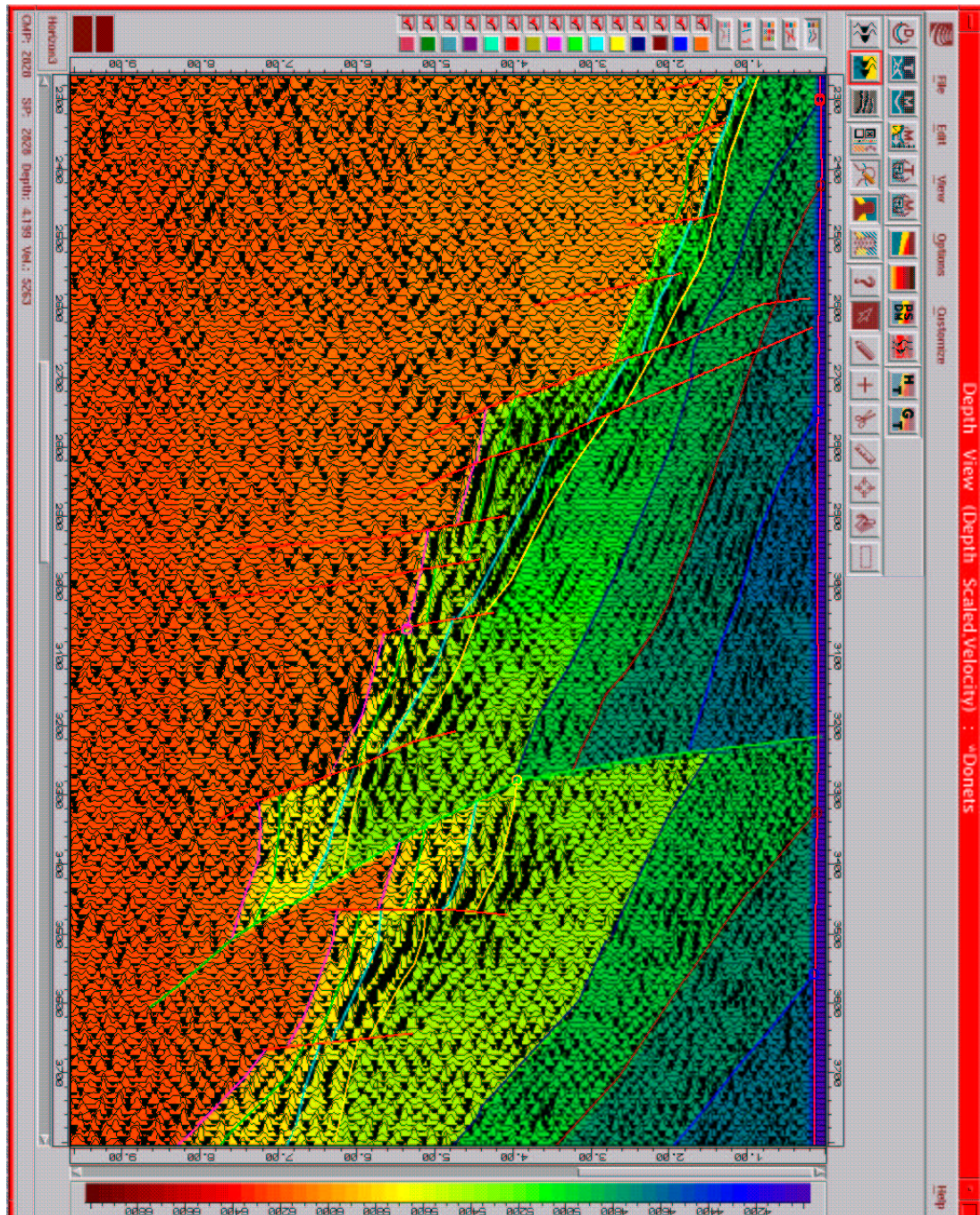


Figure 9.12: PSDM section of the main backthrust fault zone, overlaid with the velocity/depth model. The vertical axis is the depth in km and the horizontal axis displays the CRP number.

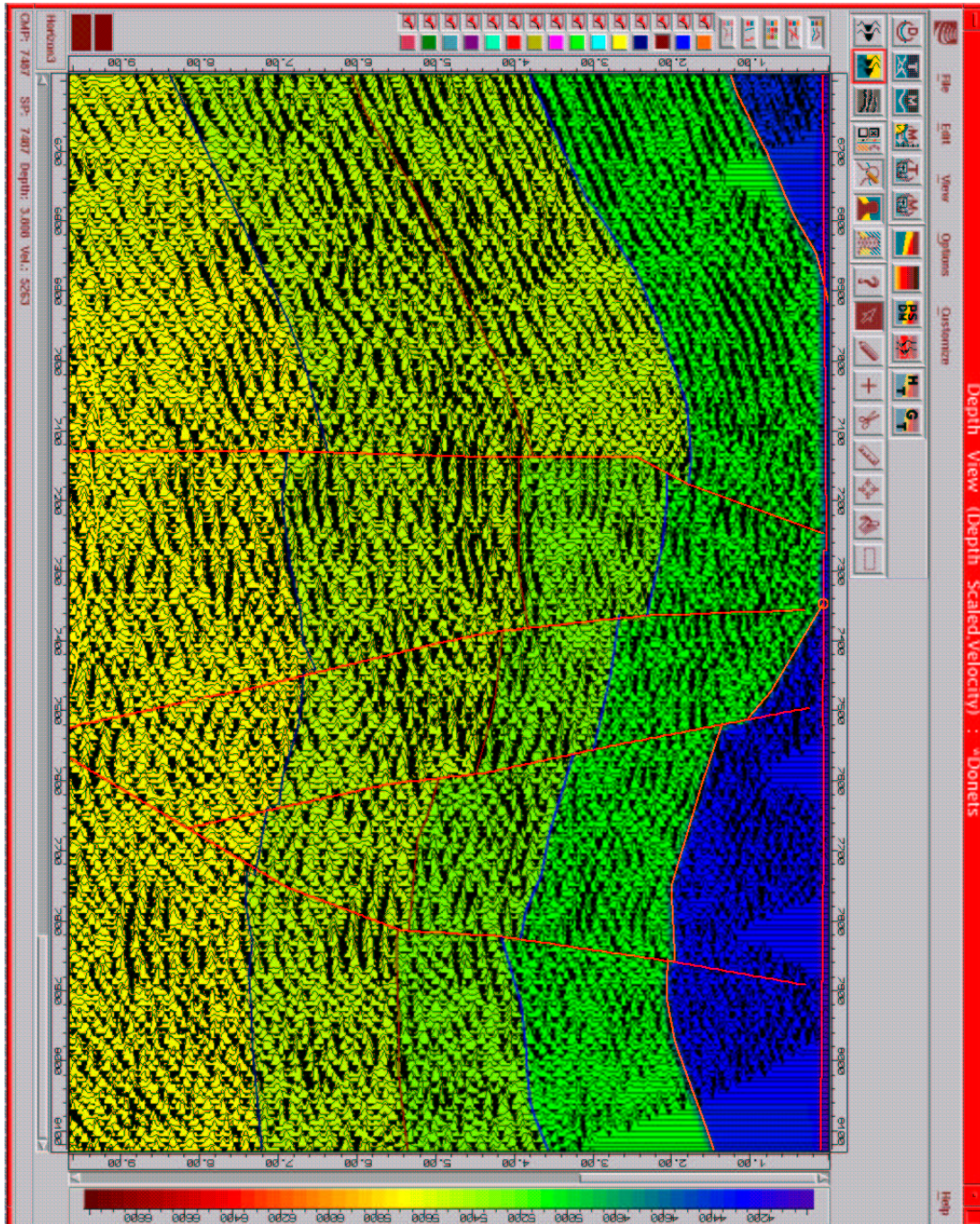


Figure 9.13: PSDM section of the northern part of the profile overlaid with the velocity/depth section. The vertical axis is the depth in km and the horizontal axis displays the CRP number.

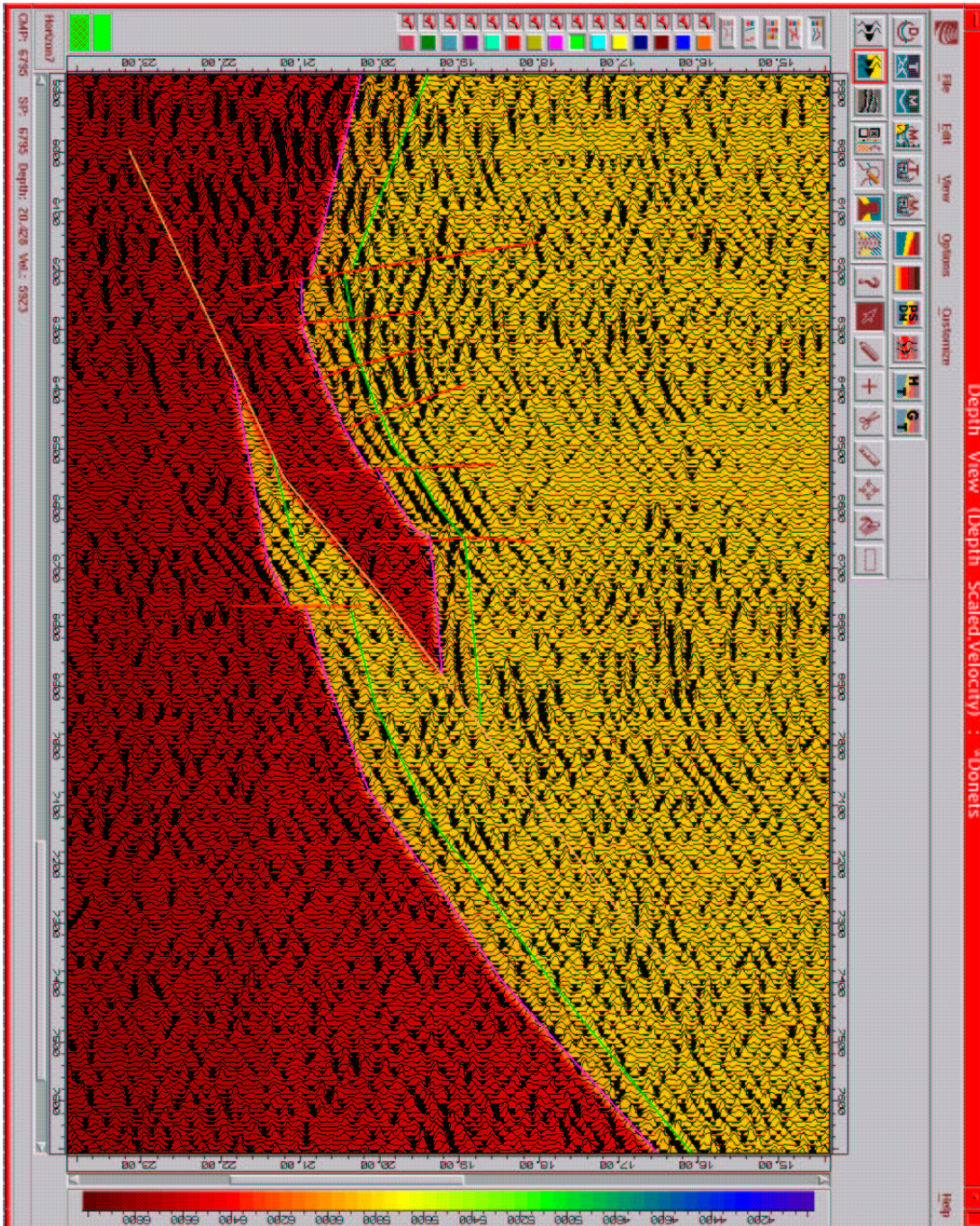


Figure 9.14: Listric shear zone in the axial part of the basin. Maximum depth is ca. 20-21 km. The vertical axis is the depth in km and the horizontal axis display the CRP number.

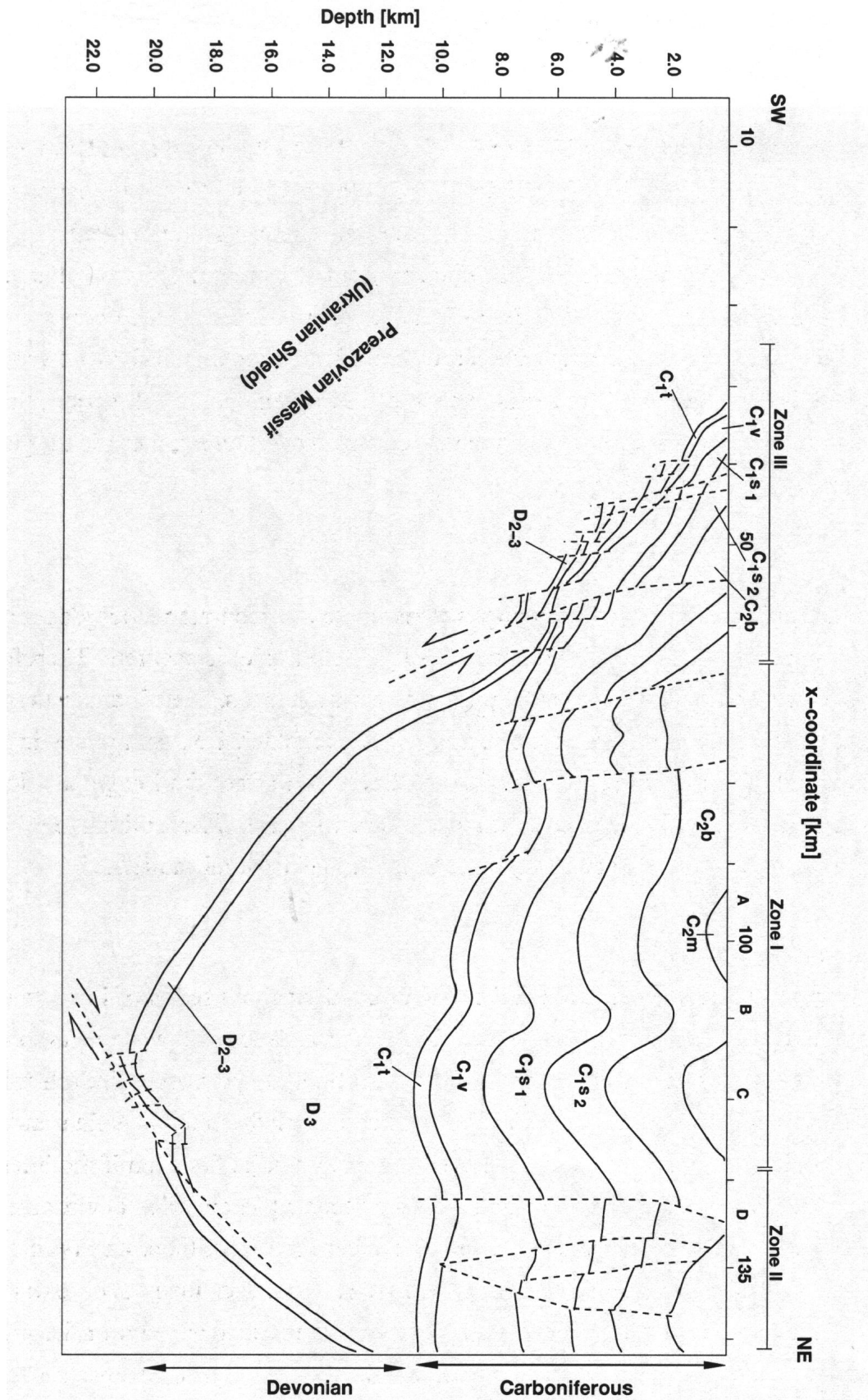


Figure 9.15: 2D structural interpretation of the PSDM section. The stratigraphic interpretation was mainly done by Sergiy Stovba from Ukrgeofisika. The stratigraphic keys include: D_{2-3} – Middle and Upper Devonian; D_3 – Upper Devonian; C_{1t} – Tournassian; C_{1v} – Visean; C_{1s} – Serpukhovian; C_{2b} – Bashkirian; C_{2m} – Moscovian. See Figure 7.4 for the geological times. The symbols A, B, C, and D represent the southern syncline, the main anticline, the main syncline and the northern anticline.

9.2.4 Pitfalls of the Depth Imaging

3D aspects

A general problem with data recorded in Foldbelt and other complex areas is that a 2D imaging will frequently fail to explain 3D effects in the data. In 2D the raypaths for all reflections are assumed to be in the plane of the seismic section. Violations of this assumption are a prominent source of error in 2D depth imaging. Foldbelt data, particularly, are notorious for this problem. Foldbelt structures usually display strong 3D aspects, i.e. there is usually not a prevailing strike and dip direction of the major surfaces over large areas. To reduce this difficulty from the onset, the Foldbelt data analysed in this thesis were shot in the regional dip direction, therefore, reducing the chance of recording out-of-plane reflections. Nevertheless, there is no guarantee that all the events are genuinely in-line.

Migration algorithm

In addition to the accurate velocity model, the migration algorithm used is of importance. The two most commonly applied algorithms are the Kirchhoff migration and wave equation migration (Clearbout, 1985). As shown in this work, for model building purposes Kirchhoff migration with all its flexibility is best for estimating and for verification of the model. However, Nolan and Symes (1996) showed that in complex structures, CRP gathers may not be flat even if the interval velocity/depth model is correct. This is explained by the fact that in complex environments and at large distances from the reflector to the source/receiver locations, there can be many possible travel paths for seismic energy to take as it travels. Whenever many such pairs of rays exist and have the same two-way traveltimes, an inherent ambiguity appears in the migration velocity analysis process. Therefore, all the possible raypaths need to be considered in the algorithm in order to overcome this problem. The Kirchhoff algorithm as implemented in Geodepth assumes that seismic energy propagates only along a single path (first arrival or maximum energy arrival). Multipathing with all possible travel paths is not applied. The implementation of multipathing is not trivial and especially in 3D medium it could be very expensive.

Synthetic data examples have shown that wave equation migrations, on the other hand, can produce accurate and high resolution results than first arrival Kirchhoff migrations (Popovici, 2000). Wave equation migration has the advantage that they are based on the full wave equation and not on the ray theory. In addition, wave equation migration can better handle multipathing, focusing and defocusing effects of velocity variations. However, because its application is computationally intensive it was not applied to this dataset. Moreover, wave equation migration can only be applied only after Kirchhoff migration has been used to obtain an accurate velocity depth model.

Anisotropy

It has been shown by many authors that seismic anisotropy can strongly influence seismic wave propagation. If anisotropy is not considered but present in the real model, then the estimated velocity/depth model will be inaccurate. This will definitely lead to wrong image positioning even if the CRP gathers may be flat. Most often anisotropy causes far offset CRP gathers not to be flat

even after many iterations of velocity updating. The stacking of non-flat CRP gathers definitely leads to defocusing in the stacked section. Fortunately, for the Donbas Foldbelt data the amount of anisotropy was only about 0.5% (Wolfgang Rabbel, personal communication). Such a small percentage of anisotropy has very little effect on P-wave propagation. Therefore, considering an isotropic model is justified.

Inaccurate velocity model

The core problem in imaging the Donbas Foldbelt data lies in the estimation of the velocity/depth model. In some areas, the PSDM section in Figure 9.11 seems to be of poor quality. A possible reason might be an inaccurate velocity/depth model in Figure 9.10 still contain errors, thus PSDM cannot give well focused depth migrated images. While the poststack time migration is relatively insensitive to the accuracy of the migration velocity, PSDM can give focused images only if the input velocity/depth model is correctly defined. RMS velocity fields which are used in time imaging does not contain discontinuities, in contrast to interval velocity/depth models which usually include discontinuities associated with the layer boundaries. The “true” reflector geometry and “true” velocities strongly determines the quality of the depth migrated image.

The incorrectness of the velocity/depth model can be divided into two parts. Either the layer velocities are incorrect or the position of the layer boundaries and reflector geometry are incorrect. As described in Section 9.2.3.2, the interpretation of the layer boundaries was constrained by the surface structural geology map, which was constructed without any well log data. Note that, the structural geological model itself was constrained by external knowledge and geological interpretation about the survey area (Sergiy Stovba, personal Communication). Because in constructing the depth model, the layer boundaries and geometries were strongly tied on the surface structural geology model, I presume that the errors in the layer boundaries and reflector geometries can be the cause of the incorrect velocity/depth model. With such a strong tie on a structural geological model, it is very likely that the resulting velocity/depth model will not be consistent with the true seismic events.

Therefore, a possibility to improve the depth image is to re-construct the velocity/depth model with less geological constraints and re-migrate the data. That is, only major horizons with strong reflectivity need to be interpreted. This will reduce the number of reflectors to be picked and the reflectors will match the seismic events rather than any geological interpretation. As such the final interpretational work will be postponed until the depth image is produced.

Another possibility to improve the image quality is to use prestack depth migration from topography (Wu et al., 1998). Unfortunately migration from topography is not implemented into the Geodepth Software which was used in this work. Provided that the velocity model is accurate, migration from topography can produce improved images because, instead of assuming a flat datum level (via datum static corrections), the migration is performed using the correct source and receiver elevations. In the Donbas Foldbelt area the topography has large elevation changes (about 345 m receiver static over the length of the line), and the thrust belt has considerable near surface

complexity.

Chapter 10

Dissertation Summary

10.1 Part I

The purpose of the first part of this dissertation was to develop a migration algorithm for converted waves, and a tomographic method for estimating an interval shear wave velocity model. The developed algorithm is based on the Kirchhoff formalism.

The elastic Kirchhoff integral and its implementation were discussed and summarised in Chapter 2. The derived migration integral was generalised for all types of multicomponent data. For practical reasons, multicomponent data are decomposed into their corresponding components (z, x, and y components), and the migration is performed separately for each component. Normally it is assumed that the decomposed wave components are free from other wave types. The migration result of each component shows particular characteristics of the subsurface. For example, PS data give the shear wave characteristics of the subsurface.

Chapter 2 also discussed the finite difference eikonal solver for computing seismic traveltimes, and the incorporation of the perturbation method into the traveltime algorithm. The perturbation method allows for a simultaneous migration of PS data with a given range of P- and S-wave velocity models. This simultaneous migration is important for iterative PS migration velocity analysis. The first arrival traveltimes computed by the FD method are accurate enough to perform a fast target oriented prestack depth migration.

In addition to the accuracy of the traveltime algorithms, the success of prestack depth migration strongly depends on the accuracy of the interval velocity model. Conventional one component migration velocity analysis works on the principle of flat CRP gathers, if the corresponding input migration velocity is correct. For PS data this is not always true. PS CRP gathers may be flat, even if the interval S-wave velocity model is incorrect. Therefore, if flatness of PS CRP gathers is the only criterium for velocity correctness, this may lead to wrong velocity interpretation. Chapter 3 described a new tomographic approach for updating interval S-wave velocities and v_p/v_s -ratios. The function to be minimised in the tomography were depth shifts between PS and PP CRP gathers. The depth shifts are converted to time differences, and the time differences are input into the tomographic inversion. The validity of the algorithm was tested on synthetic and field data in

Chapter 4.

The examples showed that the proposed method led to a correct S-wave velocity model in which both PS and PP depth gathers were tied in depth positions. Good reflection continuity and event character were observed on both PP and PS data sets, and reliable correlations could be made between the P- and S-wave data. The proposed tomographic method is stable because reflector depths are not updated. The depth positions are previously estimated from the PP data section. Note that the method is different from conventional reflection tomography because reflection events are picked after depth migration, i.e., in the stacked domain with improved S/N-ratio.

The following points can be concluded from this part of the thesis.

1. Prestack depth migration is the most accurate method for imaging of converted waves. Imaging in the depth domain reveals no lateral shift in the image position between PP and PS events as is usually observed in time domain processing.
2. If flatness of CRP gathers is the only criterium for estimating the correct PS migration velocities, then PS and PP depth positions from the same reflection horizon can be different.
3. The PS CRP gathers can be flat even if the migration S-wave velocity is incorrect.
4. A necessary and sufficient criterion for PS migration velocity analysis is to assure flatness and depth tie of PS and PP CRP gathers. If both PS and PP data correctly match then the derived interval P- and S-wave velocities can provide a direct measurement of physical properties of the rocks.

10.1.1 Future Work

The tomographic approach described in Chapter 3 is a very useful tool for 2D data. Its application to other complicated data sets and especially in a 3D data still has to be validated. Furthermore, in its present form, the algorithm does not consider anisotropic effects in the model. Anisotropy is always present in nature and can affect PS data more than PP data. Therefore, more research is needed to expand the algorithm to estimate anisotropic parameters through tomography.

The tomographic method in Chapter 3 assumes a previous knowledge of a PP velocity/depth model. However, the PP velocity/depth model can be inaccurate. In such a situation both P- and S-wave velocities have to be jointly updated. Therefore, research still has to be done for the case where both P- and S-wave velocities are incorrect. In this respect, the P-wave velocity model obtained from PP data can be used as an initial model for further updating during PS migration velocity analysis.

10.2 Part II

The second part of this work was devoted to integrating model-independent and model-dependent seismic imaging methods in a single workflow in order to construct a velocity/depth model and a

depth migrated section of the Donbas Foldbelt data. The estimation of the model required the integration of the different methodologies and disciplines, each of which gave different information on the subsurface. The model-independent method involved the common reflection surface (CRS) stack method, which give a high quality zero-offset stacked section. The model-dependent method involved Kirchhoff prestack depth migration (PSDM). The integrated workflow for estimating the velocity/depth model was made up of the following:

- Generate a high quality unmigrated stacked section with the CRS method.
- Interpret the main time horizons on the CRS section.
- Using the time horizons, perform coherency inversion to generate an initial model.
- Perform iterative PSDM, starting with the initial model and interpret the migrated stacked section.

Before applying the CRS method to the field data, the algorithm was tested on a synthetic data generated from the Picrocol model (Chapter 6). The synthetic test showed that the CRS algorithm requires readjustment of some input parameters. These input parameters control the quality of the stacked section. The unmigrated CRS stacked section accurately represents a zero-offset image which is a requirement for accurate poststack imaging. Apart from the zero-offset stacked section, other attributes such as a high density stacking velocity section and the wavefield attribute sections are produced. The wavefield attributes are the angle of emergence of the hypothetical wavefronts at the surface, the radius of curvature, R_{NIP} , of the NIP-wavefront and the radius of curvature, R_N , of the N-wavefront. These additional sections can be further used for other inversion purposes to describe the subsurface model. For example the correct geometry of the reflector can be directly estimated from the R_N -section.

The application of the CRS method on the field data revealed improved image quality in areas which previously showed poor image quality on conventionally CMP stacked sections. Even though the CRS method was applied only to particular key zones of the Donbas profile, it could equally be applied to image the complete section. Time horizons on the migrated CRS stacked section were easily interpreted due to the high image quality. Because imaging with CRS does not depend upon the stacking velocity model, errors due to a wrong stacking velocity model were avoided. Furthermore, any error due to the processors mal-picking of prestack reflection events during stacking velocity analysis was also avoided. This implies that all the reflection events in the stacked section were purely data-driven. These events were interpreted and given as input into the model-dependent part of the imaging.

The model-dependent imaging begins with the generation of an initial velocity/depth model through coherency inversion. For this purpose, time horizons from the migrated CRS sections are used as input into coherency inversion. In complex geology, like the Donbas Foldbelt area, I suggest to pick time horizons on poststack migrated sections. This is because picking of time horizons on unmigrated stacked sections, including the complete spread of triplications, is not at all trivial. Note that the accuracy of the coherency inversion result depends on the correctness of the time

picks. The generated initial model from the coherency inversion is used for PSDM.

The initial model from CRS stacking and coherency inversion is iteratively updated and re-used in PSDM until a consistency is achieved between the input model and the depth migrated section. The criteria for the correctness of the velocity model are based on flatness of migrated CRP gathers along the profile. For the Donbas Foldbelt data, CRP gathers were analysed every 200 m. This was dense enough to resolve lateral velocity variations within the layers. Structural geological information was important for interpreting the depth migrated section. After each migration iteration, the depth horizons were re-interpreted to give a new depth model. In this way, additional information from geology and CRS images were easily incorporated into the model updating flow. Therefore, an understanding of the geology of the area was required for accurate interpretation.

This research work has demonstrated that incorporating information from model-independent imaging, model-dependent imaging, and surface structural geology can lead to an accurate estimation of structural velocity/depth models in complex environments.

10.2.1 Future Work

The model-independent imaging was applied only to certain key zones which demonstrated the extent of the basin inversion. With new computer capacity and performance, future work can involve the application of the method to the whole section. This might lead to further imaging of other reflectors which are missing, maybe due to wrong stacking velocities.

Likewise, a future research work is required to investigate the use of the CRS stack wavefield attributes for further inversions. For example, the wavefield attribute sections can be used for inverting for interval velocity, accurate estimation of reflector curvature, estimation of statics and suppression of multiples. The high density, high resolution CRS stacking velocity section can be converted to interval velocities via Dix's formula. This velocity can then be used for poststack depth migration of the CRS stacked sections and PSDM can be used to verify the correctness and upgrading of the interval velocity model.

Another research work will be to develop a PSDM algorithm which take into consideration the true topography of the survey area. In this way I presume that the quality of the depth migrated section can be further improved.

Appendix A

Some Assumptions in Kirchhoff Integral

In seismic data processing, algorithms of the form given in Equation (2.4) are often called “Kirchhoff Migration” or Kirchhoff Imaging algorithms. Indeed, integrals of this form are derived from the Kirchhoff integral. In this appendix, I give some assumptions which are usually made in deriving the Kirchhoff integral. First, I state the physical meaning of the Kirchhoff integral.

“The Kirchhoff formalism gives the wave field of a *point* in space as an integral over a *closed surface* surrounding that point, i.e, the wave field that would be present on the *tangent plane* at that point” (Pao and Varantharjulu, 1976).

This formalism requires certain assumptions to be fulfilled:

1. The data are in the far field, i.e. for an infinitely extended region.
2. The medium parameters are known, i.e., an accurate background medium through which the wavefield propagates is assumed.
3. The wavefield scatterers are point scatterers and their locations are known, i.e., the process of focusing at an image point assumes that the image point is a scatterer.
4. The summation in the Kirchhoff integral is considered to be over a smooth medium. This is justified because the divergence theorem (Gauss theorem) is implied in deriving the Kirchhoff integral.

In implementing the Kirchhoff integral in the seismic world it is usually assumed that these requirements are fulfilled.

Appendix B

Raypath for a constant P/S-velocity ratio

In this appendix I show that if v_p/v_s -ratio is constant then P- and S-waves propagate along the same raypaths for fixed source and receiver positions. For this purpose I use the kinematic ray tracing (KRT) equations. The statement to be proven is that, if the P- and S-raypaths are the same then it should be possible to derive KRT equations for S-waves from those of P-waves as well as Snell's law. The KRT equations for P-wave are given as (Aki and Richards, 1980):

$$\frac{d\vec{x}}{d\tau} = v_p^2 \vec{p}, \quad \frac{d\vec{p}}{d\tau} = -\frac{1}{v_p} \nabla v_p, \quad (10.1)$$

where \vec{p} is slowness vector, v_p is P-wave velocity, τ is travelttime and \vec{x} corresponds to the position vector of the ray. Now we set:

$$\frac{v_p}{v_s} = \text{const.} = \gamma. \quad (10.2)$$

If I insert Equation (10.2) inserting this into Equation (10.1), I obtain for the first set of ray tracing equations:

$$\frac{d\vec{x}}{d\tau} = v_s^2 \vec{p} \gamma^2, \quad (10.3)$$

which then gives, apart of the constant, the first part of the KRT equation for S-waves. This constant does not affect the path through which the ray travels. For the second part of the KRT equation, I have:

$$\nabla v_p = \gamma \nabla v_s, \quad \frac{d\vec{p}}{d\tau} = -\frac{1}{\gamma v_s} \gamma \nabla v_s. \quad (10.4)$$

This implies:

$$\frac{d\vec{p}}{d\tau} = -\frac{1}{v_p} \nabla v_p = -\frac{1}{v_s} \nabla v_s. \quad (10.5)$$

Equation (10.5) is another form of Snell's law for which the ray parameter is constant. Thus, from the above derivations it is shown that when the v_p/v_s -ratio is constant the transmission angles for P-wave and S-wave are equal. On the other hand, if γ is a function of \vec{x} , then Equation (10.4) will be different since I will then have:

$$\frac{d\vec{p}}{d\tau} = -\frac{1}{\gamma v_s} \nabla(\gamma v_s) = -\left(\frac{1}{\gamma} \nabla \gamma + \frac{1}{v_s} \nabla v_s\right). \quad (10.6)$$

Now I expand the first term on the right hand side of Equation (10.6) and show that this will give second order terms which can be neglected. To first order the perturbed velocity ratio γ can be written as:

$$\gamma = \gamma_o + \Delta\gamma, \quad (10.7)$$

such that:

$$|\Delta\gamma| \ll \gamma_o,$$

where γ_o is the constant unperturbed ratio and $\Delta\gamma$ is the velocity ratio difference. Inserting Equation (10.7) into Equation (10.6) and retaining only the first term of the right hand side result in second order terms:

$$-\frac{1}{\gamma_o + \Delta\gamma} \nabla(\gamma_o + \Delta\gamma) = -\frac{1}{\gamma_o + \Delta\gamma} \underbrace{\nabla\gamma_o}_{=0} + \underbrace{\nabla(\Delta\gamma)}_{2^{nd}-order}. \quad (10.8)$$

The symbol Δ indicates difference and should not be confused with the Laplace operator. Similar insertion of Equation (10.7) into Equation (10.3) will result also in second order terms. The idea of a common raypath for both P and S-rays is used in Chapter 2 for a simultaneous computation of P- and S-wave traveltime tables, which is important for PS migration velocity analysis.

Appendix C

PS mode offset-limit

This appendix discusses some practical reasons why short spread limits are often preferred for PS processing. Generally, long spread acquisition is important for migration velocity analysis because the curvature of the residual moveout curve is a function of offset. In practice, long spread PS data are not usually acquired.

When recording PP and PS data, for a given offset x , the angles of incidence, respectively θ_p and θ_{ps} , are different (Figure 10.1a). Beyond the point of maximum reflection amplitude, the PS reflectivity decreases drastically and vanishes. Behind this point the amplitude increases again but the phase of the signal has a different polarity (see Figure 4.2). The rectangular boxes in Figure 10.1a and Figure 10.1b indicates the zones in which the polarity of PS reflections can be uncertain. The offset location of the sign change depends on the elastic parameters of the medium as well as on the depth of the reflector. Therefore, it is difficult to predict this zone (zone of uncertain PS polarity).

An example of such a phase reversal is seen in the PS shot record in Figure 4.2 at an offset of 800 m (the first reflector). The existence of a gradient in the elastic parameters affect the offset at which the phase reversal appears. For weak interfaces (i.e. the jump in the elastic parameters is small) the offset for phase reversal is far from the source point, whereas for strong interfaces (i.e. large differences between the elastic parameters) the offset is nearer towards the source. If PS data with mixed phase polarity are stacked, this will lead to destructive interference and poor PS image quality. Therefore, to avoid stacking signals of opposite polarity, the PS maximum offset (x_{ps}) is usually limited during acquisition in order to avoid the PS incidence range of uncertain polarity (i.e angles beyond θ_L in Figure 10.1). This offset is usually shorter than the PP-wave optimal offset, or x_p , as in Figure 10.1b. Therefore, only short spread PS data are usually acquired.

However, if a phase reversal does exist in the shot gathers, it is usually removed in the processing centre. The simplest way to remove it in the processing stage is by muting those parts of the signals with phase reversal. This means using only the sub-critical wave field (*PS mode offset-limit*) for imaging. This of course will reduce the extent of the images. If the complete reflection signal (i.e., without muting) is to be used for imaging, I suggest to correct the phase reversal by taking the absolute value of each migrated CRP gather for the affected layer before stacking. This was tested on synthetic data but the results are not shown in this work. In the examples presented in

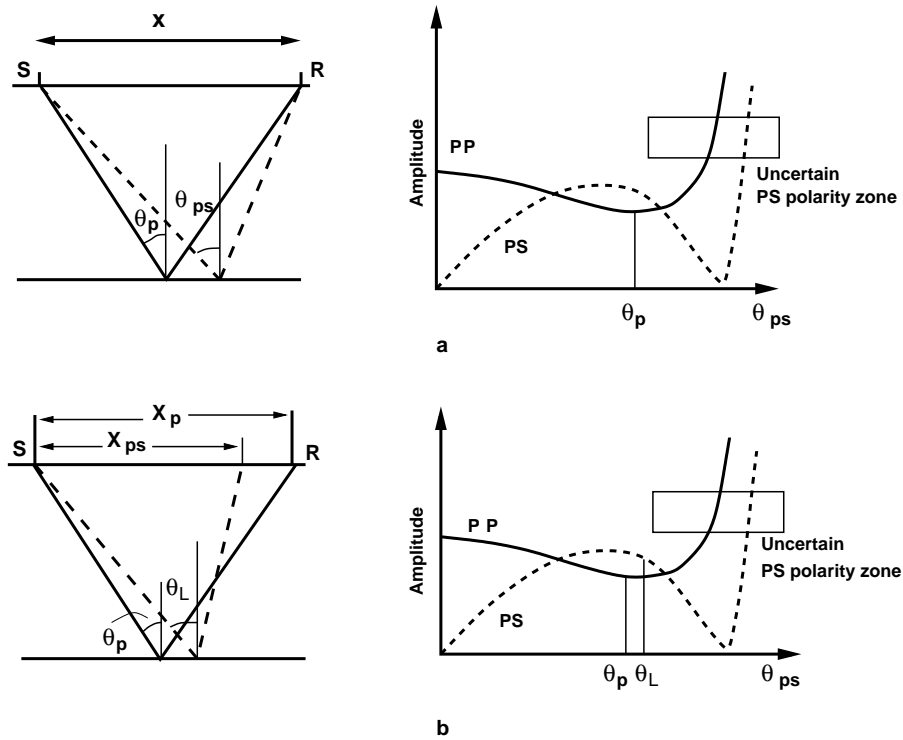


Figure 10.1: Amplitude variation with angle of PP and PS data illustrating the zone of uncertain polarity (rectangular boxes). In this zone the PS reflection usually change sign. The dashed curve are for PS data. θ_p and θ_{ps} are the PP and PS angle of incidence (a), θ_L is the PS angle of incidence for which no polarity reversal will be recorded (b). Note that the offset x_{ps} is less than x_p for the angle of incidence θ_L .

this work I did not apply this approach. For the field data example in Chapter 4, the phase reversal were removed in the preprocessing stage, therefore, only data from the PS mode offset-limit were used.

The phase reversal described above should not be confused with polarity reversal that occurs at zero-offset crossing in a split-spread geometry (Figure 10.2). If in Figure 10.1a the negative angles are considered in the plot of the PS reflection amplitude versus angles, then the amplitude curve crosses zero and continues in the negative axis to a maximum. At this zero-crossing a phase reversal also occurs. Correcting this type of phase polarity change is carried by multiplying the positive offset traces by -1.

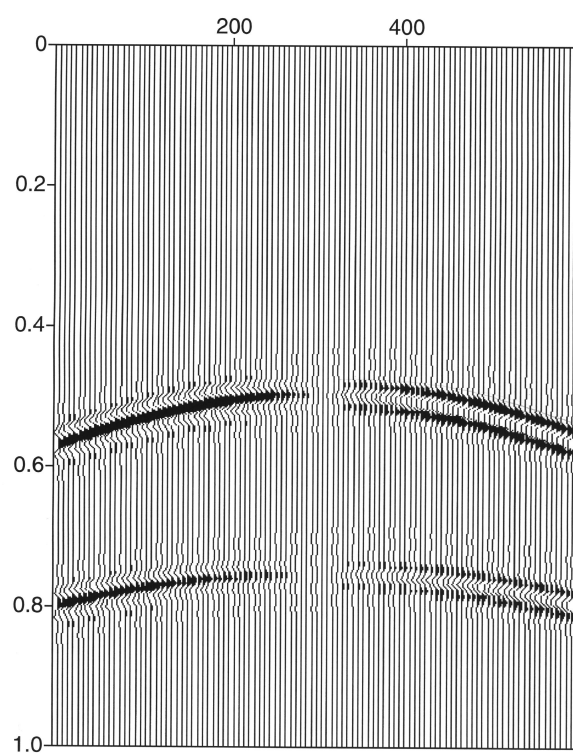


Figure 10.2: An example of polarity reversal at zero-offset crossing in a split spread geometry.

Bibliography

- [1] Aki, K., and Richards, P. G., 1980. Quantitative seismology: Theory and methods, W. H. Freeman and Co.
- [2] Al-Yahya, K. M., 1989. Velocity analysis by iterative profile migration, *Geophysics* **54**, 718-729.
- [3] Audebert, F., Nichols, D., Rekdal, T., Biondi, B., Lumley, D. E., and Urdaneta, H., 1997. Imaging complex geologic structure with single-arrival Kirchhoff prestack depth migration. *Geophysics*, 62, 1533-1543.
- [4] Audebert, F., Granger, P. Y., and Herrenschmidt, A., 1999. CCP-Scan technique: True common conversion point sorting and converted wave velocity analysis solved by PP and PS prestack depth migration, *69-th Ann. Internat. Mtg., Soc. Expl. Geophys.*, Expanded Abstracts, 1186-1189.
- [5] Behle, A., and Dohr, G., 1985. Converted waves in exploration seismics, in Dohr, G., Ed., *Seismic shear waves, Part B: Applications: Geophys. Press*, **15B**, 178-223.
- [6] Bishop, T. N., Bube, K. P., Cutler, R. T., Love, P. L., Resnick, J. R., Shuey, R. T., Spindler, D. A., and Wyld, H. W., 1985. Tomographic determination of velocity and depth in laterally varying media. *Geophysics* **50**, 903-923.
- [7] Bleistein, N., 1987. On the imaging of reflectors in the Earth, *Geophysics* **52**, 931-942.
- [8] Bording, R. P., Gersztenkorn, A., Lines, L. R., Scales, J. A., and Treitel, S., 1987. Applications of seismic travelt-time tomography. *Geophys. J. R. astr. Soc.* **90**, 285-303.
- [9] Brokešov, J., Dekker, S., and Duijndam, A., 1994. Applicability of high-frequency asymptotic methods for the model PICROCOL. 64th Annual Int. SEG Meeting, Expanded Abstracts, 783-786.
- [10] Caldwell, J., 1999. Marine multicomponent seismology, *The Leading Edge*, **18**, No. 11., 1274-1282.
- [11] Cambois, G., and Stoffa, P. L., 1992. Surface-consistent deconvolution in the log/Fourier domain. *Geophysics*, **57**, 823-840.
- [12] Cary, P. W., and Lorentz, G. A., 1993. Four-component surface-consistent deconvolution. *Geophysics*, **58**, 383-392.

- [13] Castagna, J. P., 1993. AVO analysis - tutorial and review: in Offset-dependent reflectivity - theory and practice, Soc. Expl. Geophys.
- [14] Červený, V., 2001. Seismic ray theory. Cambridge University press.
- [15] Červený, V., and Pšenčík, I., 1984. Numerical modeling of seismic wavefields in 2D laterally varying layered structures by the ray method, in: Engdahl, E., Ed., *Documentation of Earthquake Algorithm*: World Data Center for Solid Earth Geophysicists, Rep. SE-35, 36-40.
- [16] Chekunov, A. V., Gavrish, V. K., Kutas, R. I., Ryabchun, L. I., 1992. Dniepr-Donets paleorift. In: Ziegler, P. A. (Ed), *Geodynamics of Rifting*, Vol. I. Case History Studies on Rifts, Europe and Asia. *Tectonophysics* **208**, p. 257-272.
- [17] Chui Stephen, K. L., and Stewart Robert R., 1987. Tomographic determination of three-dimensional seismic velocity structure using well logs, vertical seismic profiles and surface seismic data. *Geophysics*, **52**, 1085-1098.
- [18] Claerbout, J. F., 1985. Imaging the Earth's interior: Blackwell Scientific Publications.
- [19] Coman, R., and Gajewski, D., 2001. Estimation of multivalued arrivals in 3D models using wavefront ray tracing. 71-th Ann. Internat. Mtg., Soc. Expl. Geophys., Expanded Abstracts.
- [20] Dankbaar, J. W. M. Separation of P- and S-waves, *Geophysical Prospecting* **33**, 970-986.
- [21] Deregowski, S. M., 1990. Common-offset migrations and velocity analysis: *First Break*, **8** 224-235.
- [22] Dix, C. H., 1955. Seismic velocities from surface measurements. *Geophysics*, **20**, 68-86.
- [23] Egozi, U., 1998. Efficient development of velocity models over the Gulf of Mexico salt structures, In Model-based depth imaging Ed. by Stuart Fagin; Society of Exploration Geophysics, Course Notes Series, No. 10, Tulsa.
- [24] Ettrich, N., and Gajewski, D., 1996. Wavefront construction in smooth media for prestack depth migration: *Pageoph*, **148**, 481-502.
- [25] Ettrich, N., 1997. Schnelle Laufzeitberechnungen mit Anwendungen auf die Prestack-Kirchhoff-Migration. *PhD Thesis*, University of Hamburg, Germany.
- [26] Ettrich, N., and Gajewski, D., 1998. Traveltime computation by perturbation with FD-eikonal solvers in isotropic and weakly anisotropic media, *Geophysics* **63**, 1066-1078.
- [27] Fagin, S., 1998. Model-Based Depth Imaging. Society of Exploration Geophysics, Course Notes Series, No. 10, Tulsa.
- [28] Faye, J. P., and Jeannot, J. P., 1986. Prestack migration velocities from focusing depth analysis: *56th Annual Intl. SEG Meeting*, Expanded Abstract, 438-440.
- [29] Fertig, J, Thomas M., Thomas, R., 1999. How to remedy non-optimal seismic data by seismic processing, in Gajewski D. and Rabbel W. (Ed.) *Seismic exploration of the deep continental crust*. Reprint from Pure and Applied Geophysics vol. 156, Birkhäuser Verlag.

- [30] Gaiser, J. E., 1996. Multicomponent v_p/v_s correlation analysis, *Geophysics* **61**, 1137-1149.
- [31] Gaiser, J. E., 2000. Advantages of 3D PS-wave data to unravel S-wave birefringence for fracture detection. *70th Annual Intl. SEG Meeting*, Expanded Abstract, 1201-1204.
- [32] Gardner, 1985 (Ed.), Migration of seismic data: Geophysics reprint series, **4**, Society of Exploration Geophysicists.
- [33] Garotta, R. 1985. Observation of shear waves and correlation with P events, in Dohr, G., (Ed.), Seismic shear waves, Part B: Applications: Geophys. Press, **15B**, 1-86.
- [34] Gelchinsky, B., Keydar, S., 1999a. Homeomorphic imaging approach: theory and practice. *J. Appl. Geophysics* **42**, pp 169-228.
- [35] Gelchinsky, B., Berkovitch, A., Keydar, S., 1999b. Multifocusing Homeomorphic Imaging: Part 1. Basic concepts and formulae. *Journal of Applied Geophysics* **42**, 229-242.
- [36] Gelchinsky, B., Berkovitch, A., Keydar, S., 1999c. Multifocusing Homeomorphic Imaging: Part 2. Multifold data set and multifocusing. *Journal of Applied Geophysics* **42**, 243-260.
- [37] Geoltrain, J., and Brac, S., 1993. Can we image complex structures with first-arrival travel-time?: *Geophysics*, **58**, 564-575.
- [38] Gray, S. H., Etgen, J., Dellinger, J., and Whitmore, D., 2002. Seismic problems and solutions. *Geophysics*, **66** 1622-1640.
- [39] Hanitzsch, C., Schleicher, J., and Hubral, P., 1994. True-amplitude migration of 2-D synthetic data. *Geophysical Prospecting*, **42**, 445-462.
- [40] Hanitzsch, C., 1997. Comparison of weights in prestack amplitude-preserving Kirchhoff depth migration. *Geophysics*, **62**, 1812-1816.
- [41] Helbig, K., and Mesdag, C. S., 1982. The potential of shear-wave observation, *Geophysical Prospecting*, **30**, 413-431
- [42] Hubral, P., 1983. Computing true amplitude reflections in a laterally inhomogeneous Earth. *Geophysics* **48**, 1051-1062.
- [43] Hubral, P., Höcht, G., Jäger, R., 1998. An introduction to the common reflection surface stack, EAGE 60th meeting and technical exhibition. Leipzig, Extended Abstracts, 1-19.
- [44] Hubral, P and Krey, Th., 1980. Interval velocities from seismic reflection time measurements: *SEG monograph* no. **3**, Tulsa, Ed. by K. L. Lerner.
- [45] Inoue, H., 1986. A least-squares smooth fitting for irregularly spaced data: Finite-element approach using the cubic B-spline basis. *Geophysics* **51**, 2051-2066
- [46] Jäger, R., Mann, J., Höcht, G., and Hubral, P., 2001. Common-reflection surface stack: Image and attributes. *Geophysics*, **66**, 97-109

- [47] Keho, T. H., and Wu, R. S., 1987. Kirchhoff migration for vertical seismic profiles, 54th Ann. Internat. Mtg., Soc. Expl. Geophys., Expanded Abstracts, 774-776.
- [48] Keho, T. H., Beydoun, W. B., 1988. Paraxial ray Kirchhoff migration, *Geophysics* **53**, 1540-1546.
- [49] Kosloff, D., Sherwood, J., Koren, Z., Machet, E. and Falkovitz, Y., 1996. Velocity and interface determination by tomography of depth migrated gathers, *Geophysics* **61**, 1511-1523.
- [50] Landa, E., Kosloff, D., Keydar S., Koren, Z. and Reshef, M., 1988. A method for determination of velocity and depth from seismic reflection data, *Geophysical Prospecting*, **36**, 223-243.
- [51] Landa, E., Thore, P., Sorin, V., and Koren, Z., 1991. Interpretation of velocity estimates from coherency inversion, *Geophysics*, **56**, 1377-1383.
- [52] Landa, E., Gurevich, B., Keydar, S., and Trachtman, P., 1999. Application of multifocusing method for subsurface imaging, *Journal of Applied Geophysics*, **42**, 283-300
- [53] Leidenfrost, A., 1998. Fast Computation of Seismic Travel Times in Two and Three Dimensions. *PhD Thesis*, University of Hamburg, Germany.
- [54] Mann, J., Jäger, R., Müller, T., Höcht, G. and Hubral, P., 1999. Common-reflection-surface stack - a real data example. *Journal of Applied Geophysics* **42**, 301-318.
- [55] Menyoli, E., and Gajewski, D., 1999. Simultaneous computation of P- and S-traveltimes for pre-stack migration of P-S converted waves. Wave Inversion Technology Annual Report.
- [56] Müller, T., 1998. Common reflection surface stack versus NMO/stack and NMO/DMO/stack. 60th Mtg. Eur. Assoc. Expl. Geophys., Extended Abstracts, 1-20.
- [57] Müller, T., 1999. The common Reflection surface Stack method-seismic imaging without explicit knowledge of the velocity model. *PhD Thesis*, University of Karlsruhe, Germany.
- [58] Newmann, G., 1981. Determination of lateral inhomogeneities in reflection seismics by inversion of traveltime residuals, *Geophysical Prospecting* **29**, 161-177.
- [59] Nolan, C. J., and Symes, W., 1996. Imaging and coherency in complex structures, 66th Annual Internat. Mtg., Soc. Expl. Geophys., Expanded Abstracts, 359-362.
- [60] Okaya, D., Karageorgi, E., McEvelly, T. V., and Malin, P. E., 1992. Removing vibrator-induced correlation artifacts by filtering in frequency-uncorrelated time space, *Geophysics*, **57**, 916-926.
- [61] Paige, C. C., and Saunders, M. A., M. A., 1982. LSQR: An algorithm for sparse linear equations and sparse least squares: *ACM Transactions on Mathematical Software*, **8** 43-71
- [62] Pao, Y. H., and Varatharajulu, V., 1976. Huygens' principle, radiation conditions, and integral formulas for the scattering of elastic waves, *Journal of Acoustic Soc. Am.* **58**, 1361-1371

- [63] Perroud, H., Hubral, P. and Hoecht, G., 1999. Common-reflection-point stacking in laterally inhomogeneous media. *Geophysical Prospecting*, **47**, 1-24.
- [64] Polom, U., 1999. Elimination of noise caused by spikes and burst in vibroseis data, in Gajewski D. and Rabbel W. (Ed.) Seismic exploration of the deep continental crust. Reprint from Pure and Applied Geophysics vol. 156, Birkhäuser Verlag.
- [65] Popovici, A. M., 2000. 3-D wave-equation prestack depth migration, 70th Annual Internat. Mtg., Soc. Expl. Geophys., Expanded Abstracts, 493-496.
- [66] Reshef, M., and Kosloff, D., 1986. Migration of common shot gathers, *Geophysics*, **51**, 324-331.
- [67] Schleicher, J., Tygel, M., and Hubral, P., 1993a. 3D true-amplitude finite-offset migration, *Geophysics*, **58**, 1112-1126.
- [68] Schleicher, J., Tygel, M., and Hubral, P., 1993b. Parabolic and hyperbolic paraxial two-point traveltimes in 3D media, *Geophysical Prospecting*, **41**, 495-513.
- [69] Schneider, W. A., 1978. Integral formulation for migration in two and three dimensions, *Geophysics*, **43**, 49-76
- [70] Sheriff, P., and Geldart, L. p., 1982. Exploration seismology: Cambridge University Press.
- [71] Smith, G. C. and Gidlow, P. W., 1987. Weighted stacking for rock property estimation and detection of gas, *Geophysical Prospecting*, **35**, 993-1014.
- [72] Stork, C., 1992. Reflection tomography for the post migrated domain, *Geophysics* **57**, 680-692.
- [73] Stork, C., and Clayton, R. W., 1991. Linear aspects of tomographic velocity analysis, *Geophysics*, **56**, 483-495.
- [74] Stork, C., and Clayton R. W., 1987. Application of tomography to two data sets containing lateral velocity variations. 57th Annual SEG Meeting extended abstract, 839-842.
- [75] Stovba, S. M., and Stephenson, R. A. 1999. The Donbas Foldbelt: Its relationship with the uninverted Donets segment of the Dniepr-Donets Basin, Ukraine. *Tectonophysics*, **313**, 59-83
- [76] Stovba, S. M., Stephenson, R. A., Kivshik, M., 1996. Structural features and evolution of the Dnieper-Donets Basin, Ukraine, from regional seismic reflection profiles, *Tectonophysics* **268**, 127-147
- [77] Taner, M. T. and Koehler, F., 1969. Velocity spectra – digital computer derivation and applications of velocity functions. *Geophysics* **34**, 859-881.
- [78] Tarantola, A., 1984a. Linearized inversion of seismic reflection data, *Geophysical Prospecting*, **32**, 998-1015

- [79] Tarantola, A., 1984b. Inversion of seismic reflection data in the acoustic approximation, *Geophysics*, **51**, 1893-1903
- [80] Tatham, R. H., and McCormack, M. D., 1991. Multicomponent seismology in petroleum exploration: Investigations in Geophysics series **6**, Society of Exploration Geophysicists, Tulsa.
- [81] Tessmer, G. and Behle, A. 1988. Common reflection point data stacking technique for converted waves, *Geophysical Prospecting*. **36**, 671-688.
- [82] Tessmer, G., Krajewski, P., Fertig, J., and Behle, A. 1990. Processing of PS-reflection data applying a common conversion-point stacking technique, *Geophysical Prospecting*. **38**, 267-286.
- [83] Trappe, H., Gierse, G., and Prüssmann J., 2001. Case studies show potential of common reflection surface stack-structural resolution in the time domain beyond the conventional NMO/DMO stack, *First break*, **19** 625-633.
- [84] Tygel, M., Müller, T., Hubral, P., Schleicher, J., 1997. Eigenwave based multiparameter traveltime expansions. 67th Annual Internat. Mtg., Soc. Expl. Geophys., Expanded Abstract, 1770-1773.
- [85] Ulmishek, G. F., Bogino, V. A., Keller, M. B., Poznyakevich, Z. L., 1994. Structure, stratigraphy and petroleum geology of the Pripyat and Dniepr-Donets basins, Belarus and Ukraine. In: Landon, S. M. (Ed.), Interior Rift Basins. Am. Assoc. Pet. Geol. Mem. **59**, 125-156.
- [86] van Trier, J., 1990. Structural velocity analysis, *PhD thesis*, Stanford University, Palo Alto, CA, USA.
- [87] Versteeg, R., and Grau, G., 1991. The Marmousi experience. *1990 EAGE workshop on Practical Aspects of Seismic Data Inversion*, EAGE, Zeist, The Netherlands.
- [88] Versteeg, R., and Roelof, J., 1993. Sensitivity of prestack depth migration to the velocity model, *Geophysics* **58**, 873-882.
- [89] Vidale, J. E., 1988, Finite-difference calculation of traveltime, *Bull. Seis. Soc. Am.* **78**, 2062-2076.
- [90] Vinje, V., Iversen, E., and Gjoystdal, H., 1993, Traveltime and amplitude estimation using wavefront construction. *Geophysics*, **58**, 1157-1166.
- [91] Williamson, P. R., 1990. Tomographic inversion in reflection seismology, *Geophysical Journal International*, **100**, 255-274.
- [92] Woodward, N. B., Boyer, S. E. and Suppe, J., 1989. Balanced Geological Cross-Sections: An Essential Technique in Geological Research and Exploration, *AGU, Short Course in Geology*, **6**, Washington.

-
- [93] Wu, W. J., Lines, L., Burton, A., Lu, H. X., Zhu, J., Jamison, W., Bording R. P., 1998. Prestack depth migration of an Alberta Foothills data set - The Husky experience. *Geophysics*, **63**, 392-398.
- [94] Yilmaz, Ö., 1987. Seismic data processing. Tulsa, Society of Exploration Geophysicists.
- [95] Yilmaz, Ö., 2001. Seismic data analysis: Processing, Inversion and interpretation of seismic data, **I** and **II**. Tulsa, Society of Exploration Geophysicist.
- [96] Zaske, J., Keydar, S., and Landa, E., 1999. Estimation of kinematic wavefront characteristics and their use for multiple attenuation, *Journal of Applied Geophysics*, **42**, 333-346.
- [97] Zhang, Y., Bergler, S., and Hubral, P., 2001. Common-reflection-surface (CRS) stack for common offset. *Geophysical Prospecting*, **49**, 709-718.